UNIVERSITY OF OKLAHOMA

GRADUATE COLLEGE

THE ORIGINS AND IMPACTS OF MAGNETIC FIELDS IN WHITE DWARFS

A DISSERTATION

SUBMITTED TO THE GRADUATE FACULTY

in partial fulfillment of the requirements for the

Degree of

DOCTOR OF PHILOSOPHY

By

ADAM G MOSS
Norman, Oklahoma
2025

THE ORIGINS AND IMPACTS OF MAGNETIC FIELDS IN WHITE DWARFS

A DISSERTATION APPROVED FOR THE
HOMER L. DODGE DEPARTMENT OF PHYSICS AND ASTRONOMY

BY THE COMMITTEE CONSISTING OF

Dr. Mukremin Kilic, Chair

Dr. Edward Baron

Dr. Sean Matt

Dr. Doerte Blume

Dr. Trina Hope

To my Father;

Forever in my heart.

Acknowledgements

In my first semester of college at Embry-Riddle, I had room in my schedule for an elective. Since I came in as an Engineering major, I wanted to explore other areas of interest, so I signed up for Introductory Astronomy with Dr. Saurav Dhital. By the following semester, I had swapped my major to Astronomy, and I was graciously invited to observe at Kitt Peak National Observatory by Dr. Terry Oswalt. The next year I received my first glimpse into research with Dr. Tomomi Otani, and I steadily gained the knowledge and experience needed to continue my education in science. The guidance of my professors at this early education stage were critical in my development, and I am so grateful for their support.

By my senior year, Dr. Ted von Hippel had returned from sabbatical. While I had met him during my freshman year, the timing had not quite worked out for me to join his research group. But I think I always knew that I wanted to work with him, so his return to campus was my chance. It was under his excellent mentorship that I truly began my career path as an astronomer. I attended conferences, gave presentations, met new people, published my first paper, and most importantly I fell in love with the stars. I felt like I finally had a path toward studying the universe. And throughout all the self-doubt on whether I had what it took to pursue a career in this field, Ted was always there to reassure and guide me. I could not have asked for a better advisor during this stage of my life.

Astronomy is a small field, and I soon found myself attending graduate school with one of Ted's former PhD students as my advisor, Dr. Mukremin Kilic. I have known Mukremin now for six years, and a lot can happen in such a short time frame. In those first two years of graduate school, I struggled with classes and the shift to remote work, often contemplating dropping out, not understanding the value of my research, and believing that I could not make it through the program. Now here I am feeling more confident about the future and myself than at any other point in my life. Mukremin has challenged me to work harder, think deeper, and to push myself beyond what I thought I was capable of. An entire world of opportunity has been opened thanks to his leadership. I can state with full confidence that the past few years have been the best of my life thanks to him, as I grow into the type of scientist I have always admired. But to say he made me a better scientist would be an understatement. Over these last six years, I have become a better man. Thank you Muk.

I also want to thank all of my collaborators, in particular Dr. Pierre Bergeron and Dr. Warren Brown for making so much of my work possible. Obtaining interesting spectra does not mean much if you cannot model what you see, and Pierre's contributions have provided immense insight into the physical mechanisms that produce our data. And while our APO and Gemini data have been great, it is hard to beat the spectra quality from the MMT. Thank you Warren for staying up late and obtaining some of the best looking spectra out there.

A special thanks to all the teachers in my life that never receive enough credit for what they do. I am especially grateful for Glenn Nakamura and Peggy Frisbie for being incredible math teachers, Kenneth Webb for introducing me to the world of physics and astronomy, Chris Guice for being a great mentor and friend, and Darryl Johnson, Kent Kesler, and Jon Eckman for showing me the power of music.

I am also so thankful for all the friends I have met while in graduate school. I feel like I finally found my people here, with everyone bonding over the struggles of coursework and research. Coming out of the pandemic, it was difficult to return to normal and resume in-person activities. But I think our efforts to socialize, attend events, and go back to "normal" have been well worth it. I wish you all the best wherever life takes you after graduate school.

Of course, I would not be here today without the incredible support from my family. Louis, you have been the brother I never had. Thank you for being the one who never gets tired of listening to me drone on about science, politics, or whatever is on my mind. Amanda, there is nobody in the world who has been happier about my success than you. Even when we have our spats, we never let them get in the way. Thank you for being the best sister in the world. And mom, you have been the calming voice throughout all my ups and downs. How many times did you convince me not to drop out of graduate school? Turns out, you are actually smarter than me. I love you all so much.

Finally, I want to thank my dad. He passed away about a month before my 18th birthday. I never really got to know him as an adult. But I will always remember him as a strong family man, who loved us more than he loved himself. I will remember him as a father who was always proud of me, even if I did not feel proud of myself. He was not exactly the most scientifically literate person out there. I remember in middle school I was riding in the car with him, and he asked me some questions like "Why can we not recycle light from light bulbs like we recycle plastic?", and "Why do we need to constantly refill our cars with gasoline but not our bodies with blood?". Of course at the time I did not have good answers for him. I wish I could have had more time to discuss these complicated topics, and more importantly to say how much I love him. I hope that one day, despite all odds, I am able to see him again.

Adam Moss

Contents

Abstract **ix**

1 Introduction **1**
- 1.1 White Dwarfs: The Stellar Graveyard . . . 1
- 1.2 White Dwarf Atmospheres . . . 3
- 1.3 Spectral Evolution: Wait, White Dwarfs can Change? . . . 5
- 1.4 Magnetism: More Complications . . . 9
  - 1.4.1 Creating the Field . . . 9
  - 1.4.2 Detecting the Field . . . 11
  - 1.4.3 Modeling the Field . . . 14
- 1.5 My Dissertation . . . 16

2 Magnetic White Dwarfs in the SDSS 100 pc Sample **18**
- 2.1 New Insights . . . 18
- 2.2 The 100 pc Sample in the SDSS Footprint . . . 19
- 2.3 Sample Selection and Observations . . . 19
- 2.4 Model Atmosphere Analysis . . . 21
- 2.5 Results . . . 27
  - 2.5.1 Effective Temperature . . . 27
  - 2.5.2 Mass . . . 28
  - 2.5.3 Cooling Age . . . 30
  - 2.5.4 Rotation Periods . . . 32
  - 2.5.5 Tangential Velocities . . . 39
- 2.6 Evidence of Two Populations . . . 41
  - 2.6.1 Kolmogorov-Smirnov Tests . . . 41
  - 2.6.2 A Gaussian Mixture Model Approach . . . 44
- 2.7 Discussion . . . 45
  - 2.7.1 Biases in our Sample . . . 47
  - 2.7.2 The Young, Massive, Strong-Field White Dwarfs . . . 48
  - 2.7.3 The Old, Average Mass, Weak-Field White Dwarfs . . . 51
- 2.8 Conclusion . . . 52

3 Discovery of a Magnetic Double-Faced White Dwarf **60**
- 3.1 Exotic White Dwarfs with Inhomogeneous Atmospheres . . . 60
- 3.2 The Case of SDSS J0910+2105 . . . 63
- 3.3 Observations . . . 68
- 3.4 Analysis . . . 70
  - 3.4.1 The Rotation Period . . . 70

3.4.2 Modelling the Emergent Fluxes . . . 74
3.4.3 Model Fits to the Time-Resolved Spectra . . . 81
3.5 Discussion . . . 82
3.5.1 The Patchy Atmosphere . . . 82
3.5.2 The Rotation Period and Magnetic Field . . . 85
3.5.3 Comparison with other Patchy Atmosphere White Dwarfs . . . 86
3.6 Conclusion . . . 88

4 Cool Double-Faced White Dwarfs **89**
4.1 Unresolved Binaries? Or Single Stars? . . . 89
4.2 Observations . . . 92
4.3 Results . . . 94
4.3.1 LHS 1243 . . . 95
4.3.2 LHS 2273 . . . 98
4.3.3 PM J15164+2803 . . . 100
4.3.4 G62-46 . . . 102
4.3.5 The Rest . . . 102
4.4 Discussion . . . 107
4.4.1 Rotational Variability . . . 107
4.4.2 Patchy Atmospheres . . . 107
4.4.3 Source of Magnetism . . . 108
4.5 Conclusion . . . 112

5 The Emerging Class of Double-Faced White Dwarfs **114**
5.1 Finding More Targets . . . 114
5.2 Observations and Target Selection . . . 114
5.3 Analysis . . . 117
5.3.1 SDSS J084716.21+484220.40 . . . 121
5.3.2 SDSS J085618.94+161103.6 . . . 122
5.3.3 Non-Variable Objects . . . 126
5.4 Discussion . . . 126
5.4.1 The Class of Double-faced White Dwarfs . . . 126
5.4.2 The Role of Magnetism in Double-Faced White Dwarfs . . . 128
5.4.3 Cooler Double-Faced White Dwarfs . . . 130
5.5 Conclusion . . . 132

6 Conclusions and Future Work **134**
6.1 Summary of this Dissertation . . . 134
6.2 The Future . . . 135
6.3 Final Thoughts . . . 137

Abstract

White dwarfs are the final product of stellar evolution for the overwhelming majority of stars in our Galaxy. These "dead stars" radiate their residual thermal energy into space and cool down over billions of years, as they can no longer produce energy via nuclear fusion to sustain themselves. Despite this lack of an internal energy source, multiple physical processes arise on the white dwarf cooling sequence that complicate the otherwise static, relatively unchanging picture of white dwarf evolution. The first is spectral evolution, in which the elements that make up a white dwarf's atmosphere completely change as the object cools due to internal motion of material. The second is magnetism, which requires a dynamo to be spun up and similarly implies some sort of internal mechanism to generate the magnetic field. The source of these fields, and their impacts on the processes that lead to spectral evolution, have been poorly understood until now.

Three primary channels have been proposed as the source of magnetic fields in white dwarfs: a fossil origin, crystallization, and binary evolution. All three channels have their own specific problems, with no one channel able to explain the occurrence of all magnetic white dwarfs. Recent work has discovered two distinct populations of magnetic white dwarfs that form through two unique channels based on their physical properties. In order to further test this hypothesis, we conducted a survey of all white dwarfs in the Sloan Digital Sky Survey (SDSS) footprint and within 100 pc of the Sun, and identified 163 magnetic white dwarfs in this sample, 87 of which are new discoveries. We analyzed trends in field strength, mass, and cooling age, and provided statistical evidence of the existence of two populations using Kolmogorov-Smirnov tests and a Gaussian mixture model. The high mass, young, high field strength group is likely dominated by binary evolution products, while the low mass, old, weak field group is dominated by fields that form via crystallization or on the main-sequence. However, when accounting for the breakout timescales of a crystallization-induced dynamo, we find that a main-sequence dynamo can account for the incidence of magnetism in many more of our old, low mass population.

We discovered a hot mixed-atmosphere white dwarf that shows strong variations in its spectral line profiles as it rotates. We do not detect radial velocity shifts, hence this object is not in a binary system, and the object has a confirmed magnetic field based on the Zeeman-splitting of Hα. Homogeneous atmosphere models, in which the distribution of hydrogen and helium in the atmosphere is assumed to be constant across the surface, completely fail to reproduce our optical spectra. Instead, we employ an inhomogeneous model with hydrogen polar caps and a helium equatorial belt, which yields excellent fits to our time-resolved spectra. Following this discovery,

we detected similarly significant variations in a second hot mixed-atmosphere white dwarf, and conducted extensive follow-up on a third object with known variability and a confirmed magnetic field. Our polar cap model successfully reproduces our spectra for these targets as well, whereas homogeneous models once again fail. These three targets are part of the class of eight double-faced white dwarfs that show spectral variations as they rotate. We defined this class for the first time, and linked the inhomogeneities to the effects of magnetism on convective dilution. This dilution process normally causes the switch from a hydrogen to helium atmosphere during spectral evolution, but the fields in these objects greatly inhibit convective motion at the poles. This results in the hydrogen atmosphere remaining intact at the poles, while the equatorial regions switch to helium as convective dilution is not as inhibited in these regions.

This dilution process occurs at high effective temperatures, while a second process called convective mixing occurs at cooler temperatures. The mixing process similarly swaps a hydrogen atmosphere to helium, hence we should be able to detect double-faced targets at cool temperatures in which homogeneous atmosphere models fail to reproduce their spectra. We led an observing program to obtain time-resolved spectroscopy on seven cool magnetic white dwarfs that were initially proposed to be in binary systems due to the inability to fit their spectra with homogeneous models. All seven targets are strongly magnetic, and none of them show radial velocity shifts. Once again, our polar cap model successfully yields excellent fits to our spectra. Four of the seven objects also show variations in the position of their Zeeman-split absorption profiles due to the rotation of the strong magnetic fields. We use an offset dipole model to determine the geometry and field strength of each system, and we obtain rotation periods on the order of minutes for three of the four objects that show line position variations. The rapid rotation and/or low masses in six of our targets point to binary evolution as the source of their magnetic fields.

Chapter 1

Introduction

Like humans, all stars eventually die. Thankfully for us, our own local star, the Sun, is very much alive. It is alive in the sense that it continues to radiate tremendous amounts of energy into space, some of which reaches Earth and allows life to flourish. The source of this energy comes from deep within the Sun, in the central core where the temperatures and pressures are significantly higher than anywhere you would find on Earth. The conditions are extreme enough that nuclear fusion takes place, in which hydrogen atoms are smashed together to form a helium atom. Any star that is undergoing nuclear fusion in the core is labeled a "main-sequence" star. The relevant by-product for us is the energy that comes from this process, which makes its way to the surface of the Sun and into space. Without this hydrogen in the core and the energy created by fusion, we would not be here today.

Unfortunately for the Sun (and us), this reservoir of hydrogen is finite. In about 5 billion years or so, the Sun will run out of hydrogen in the core, leading to dramatic changes. The Sun's core will begin to contract, as the energy produced via fusion was once able to support the Sun against gravitational collapse, but that energy source is no longer present. As it contracts, the temperatures and pressures increase, which will spark fusion in a layer surrounding the core. This causes the outer layers to greatly expand, and the Sun is now a red giant. The Sun is now so large that it has engulfed Mercury, Venus, and potentially Earth.

While this expansion of the outer layers occurs, the core continues to contract until it is hot enough to ignite helium fusion, which produces a combination of carbon and oxygen. The Sun is not massive enough to ignite fusion beyond this point in the core. Meanwhile the outer layers are so loosely bound to the core that significant mass loss takes place, as the Sun sheds its outer layers into space. After enough time, the entirety of the outer layers are gone, leaving only the inert carbon-oxygen core as a fossil. The Sun, once a beacon of light and an object of worship and reverence for countless prior civilizations, has become a small, dim, white dwarf.

1.1. White Dwarfs: The Stellar Graveyard

Though the Sun will turn into a white dwarf at the end of its life, this fate is not guaranteed for every star. Some stars will turn into exotic neutron stars or even black holes. However, the eventual fate is dependent on the mass of the star when it originally formed. Stars between $\sim 0.07M_{\odot}$ and $\sim 8M_{\odot}$ will become white dwarfs once they exhaust their fuel (Fontaine et al., 2001), though this process will take trillions of years for the lowest mass stars. This mass range encompasses about 98% of all stars in the Milky Way. Thus white dwarfs are incredibly important for studying not just how stars evolve, but how the Galaxy changes over time as well.

Perhaps the most defining characteristic of white dwarfs is their size. Since these objects are the contracted cores of stars, they are much smaller than the original star they came from. The typical white dwarf size is $\sim 0.01 R_{\odot}$ (Shipman, 1979), or roughly the size of Earth. Despite their relatively hot temperatures, which translates to high amounts of thermal energy released over a given area, this small size means the total surface area that emits this energy greatly limits how bright these objects appear to us on Earth. For example, Sirius A is the brightest star visible in the night sky due to its large size, high temperature, and proximity to Earth. Its companion, Sirius B, is a white dwarf that is approximately ten-thousand times fainter than Sirius A (Adams, 1915), all because of the size difference. This makes studying white dwarfs in detail a challenge, with the number of white dwarfs with known spectral classification on the order of $\sim 100,000$ compared to millions of stars.

As they say though, size is not everything, as these objects are quite massive despite their small frame. While significant mass loss occurs during the giant stages of stellar evolution, the majority of the star's mass is retained in the core. The typical white dwarf has a mass of $\sim 0.6 M_{\odot}$ (Liebert et al., 2005a; Kepler et al., 2007; Tremblay & Bergeron, 2009; Kleinman et al., 2013; Kilic et al., 2025). So we have effectively taken about half the Sun's mass and squished it down into a sphere of only a hundredth the radius of the Sun. In general, gravity pulls mass towards a central point. On the main-sequence, the Sun is able to counteract this gravitational collapse via the radiation released from nuclear fusion. But now that nuclear fusion has ceased, nothing can prevent the contraction of the stellar core into these extremely dense and stable white dwarfs.

So what prevents these white dwarfs from collapsing even further if there is no traditional force to balance against gravity? The answer is electron degeneracy pressure. Electrons, the negatively charged particles that comprise atoms, obey the Pauli exclusion principle. This principle states that no two electrons can occupy the same quantum state. In English, this means that as you force atoms closer and closer together under high densities (like in white dwarfs), electrons run out of space and cannot be forced closer together. The high-energy electrons thus move at speeds close to the speed of light, and carry enough momentum to push back against gravitational collapse. This electron degeneracy pressure thus allows white dwarfs to live fairly stable lives as they cool over billions of years. Of course, even this pressure has its limits. If the white dwarf mass exceeds $1.4 M_{\odot}$ (Chandrasekhar, 1931), this pressure is unable to support the object against gravitational collapse. Hence why more massive stars form neutron stars and black holes rather than white dwarfs, as their cores are more massive than the Chandrasekhar limit.

1.2. White Dwarf Atmospheres

The strong gravities of white dwarfs result in relatively simple internal structures. Heavier elements have stronger forces acted upon them, thus the central regions of white dwarf consist almost exclusively of carbon and oxygen (or helium for the lowest mass white dwarfs and oxygen plus neon for the most massive white dwarfs). Hydrogen and helium though, as the most common elements in the universe, are still present in these objects but in the outer layers rather than the core. Similar to stars and Earth, white dwarfs possess atmospheres that comprise the thin, outermost region of the objects. Since these atmospheres are at the surface of the white dwarf, they are exclusively dominated by hydrogen or helium (or both), though heavier elements can still be present on occasion.

We can determine the atmospheric composition by taking spectra of the white dwarf. Without an atmosphere, the spectrum would look like that of a blackbody. But the atmosphere will absorb some of the emitted light, and since atomic energy levels are quantized, light is absorbed at specific wavelengths depending on which element is present. We thus classify white dwarfs based on the absorption lines detected in their spectra. The high pressures at the surface create extremely broad line profiles compared to those seen in the spectra of stars. The two spectral types that will be most relevant for this thesis are those that show hydrogen or helium lines. We label a white dwarf that shows hydrogen lines in its spectrum as a “DA”, while helium lines earn the moniker “DB”. If both hydrogen and helium lines are present (so the atmosphere has both elements in the atmosphere), we use “DAB” or “DBA” depending on which lines are strongest. Figure 1.1 shows the spectra of a typical DA and DB white dwarf. If the white dwarf is at a sufficiently high $T_{\rm eff}$ such that we observe ionized helium lines in the spectra, we use the label “DO” instead of DB.

While the spectra are useful for determining atmospheric composition, there is still the task of determining fundamental stellar parameters such as mass, effective temperature ($T_{\rm eff}$), etc. In the model atmosphere analysis discussed throughout this thesis, we use a technique detailed in Bergeron et al. (1997), Genest-Beaulieu & Bergeron (2019a), and Bergeron et al. (2019). We leverage photometric data of each target, which is how bright an object is in a given wavelength filter. We select the Panoramic Survey Telescope and Rapid Response System (Pan-STARRS, Chambers et al. 2016) $grizy$ filters and the Sloan Digital Sky Survey (SDSS, York et al. 2000) u filter, as well as the Galaxy Evolution Explorer (GALEX, Martin et al. 2005) FUV and NUV if they are available. The Pan-STARRS values are available for almost the entire sky visible from Hawaii, while the inclusion of the SDSS u filter gives us superior constraints at shorter wavelengths in the analysis. These values are given in magnitudes rather than fluxes, which we convert using the relation

$$m_\nu = -2.5 \log f_\nu^m + c_m \tag{1.1}$$

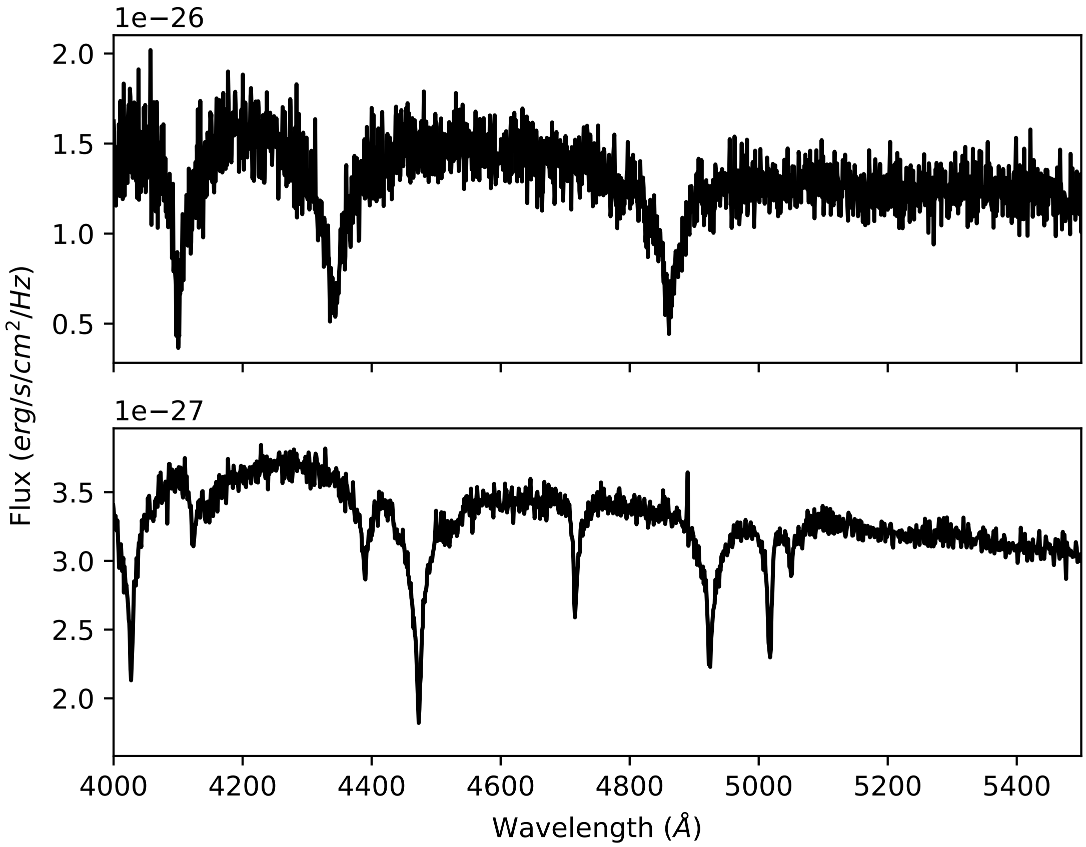

Figure 1.1: Optical spectra of a DA white dwarf (top) and a DB (bottom). The wavelength position and amount of absorption lines are different due to the presence of either hydrogen or helium in the atmosphere.

where

$$f_\nu^m = \frac{\int f_\nu S_m(\nu) d\log\nu}{\int S_m(\nu) d\log\nu} \tag{1.2}$$

and f_ν is the observed monochromatic flux from the white dwarf received at Earth, S_m is the total system response which incorporates factors such as atmospheric transmission and mirror reflectance, and c_m is a constant that is calculated based on the standard star, Vega. Our model atmospheres generate synthetic monochromatic fluxes, H_ν, which need to be converted to average fluxes, H_ν^m. This is done by substituting f_ν in Equation 1.2 for H_ν,the monochromatic Eddington flux. The relation between the average observed and synthetic fluxes is

$$f_\nu^m = 4\pi(R/D)^2 H_\nu^m \tag{1.3}$$

where R/D is the ratio between the radius of the white dwarf and its distance to Earth. We then minimize the χ^2 using the Levenberg-Marquardt algorithm (Press et al., 1986) by allowing $T_{\rm eff}$ and the solid angle, $\pi(R/D)^2$ to vary in the fits. The distance, D, is known by using the superb trigonometric parallaxes from the Gaia mission (Gaia Collaboration et al., 2016, 2018), so we effectively fit for the radius R. We assume an initial surface gravity of $\log g = 8.0$, and then use evolutionary models to determine the mass M and a new value for the $\log g$. An example of this technique is show in Figure 1.2.

With the combination of photometry and spectroscopy, we can learn a great deal about white dwarfs: their temperature, size, mass, composition, etc. But conducting a model atmosphere analysis on a single object gives us little information on the population of white dwarfs as a whole. For this, we need to conduct large surveys on thousands of white dwarfs at different stages in their cooling, perform the analysis on each target, and see what trends emerge. These can help us answer more fundamental problems such as the frequency of old/young white dwarfs, how fast do white dwarfs cool off, the distribution of white dwarf masses, and so on. As it turns out, these large surveys can often yield surprising results.

1.3. Spectral Evolution: Wait, White Dwarfs can Change?

When a white dwarf is born, it almost exclusively possesses either a hydrogen or helium-dominated atmosphere. To constrain the fraction of white dwarfs that begin their lives with a specific atmosphere, Bédard et al. (2020) conducted a model atmosphere analysis of 1806 hot ($T_{\rm eff} \geq 30,000$ K) white dwarfs and found that ∼75% are DAs and the remaining ∼25% are DOs. Given that white dwarfs are thought of as static, dead objects, one may naively think that whichever atmosphere type a white dwarf begins with should thus remain for the rest of the white dwarf's life. This would imply that no matter what $T_{\rm eff}$ range is observed, the fraction of DAs should always be

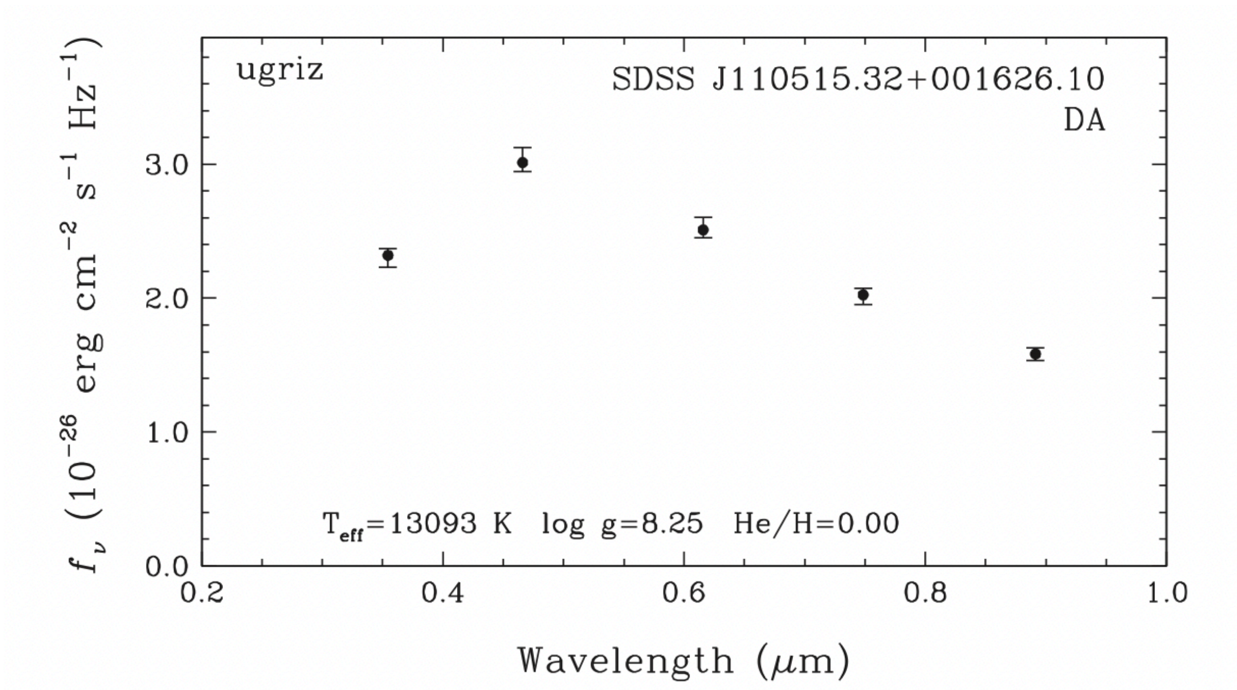

Figure 1.2: Example photometric fit of a DA white dwarf (Genest-Beaulieu & Bergeron, 2019a). Note that this fit uses the SDSS $ugriz$ filters and the Gaia DR2 parallax. Black circles are the model fluxes while the error bars are the observed fluxes.

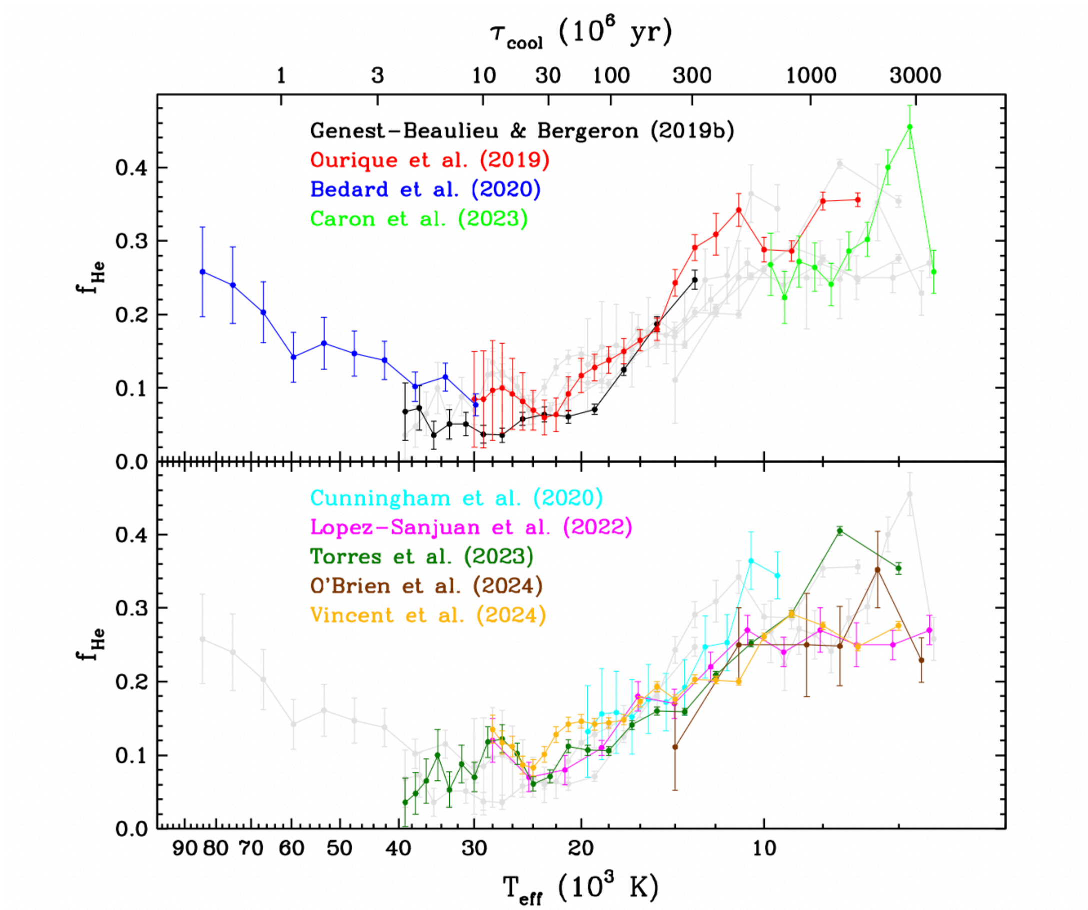

Figure 1.3: Fraction of helium-dominated atmosphere white dwarfs as a function of T_{eff} and cooling age from several model-atmosphere studies (Bédard, 2024). There is a clear decrease in the fraction from 90,000 K to ∼30,000 K, followed by a notable increase at lower temperatures.

∼75%. Of course like many things in life, the reality is more complicated.

Figure 1.3 shows a summary plot from Bédard (2024) of the fraction of helium-dominated atmosphere white dwarfs across T_{eff} (and by proxy, cooling age) from multiple studies: Genest-Beaulieu & Bergeron (2019b); Ourique et al. (2019); Bédard et al. (2020); Caron et al. (2023); Cunningham et al. (2020); López-Sanjuan et al. (2022); Torres et al. (2023); O'Brien et al. (2024); Vincent et al. (2024). There is a clear V-shape in this plot: the fraction of helium-dominated atmospheres begins to decrease starting at ∼90,000 K until reaching a minimum between ∼30,000 and ∼20,000 K. The trend then reverses as the fraction begins to increase before stabilizing below ∼10,000 K. Unless we have a significant bias in detecting these atmospheres at very specific temperatures, there must be some mechanism that leads to this evolution of spectral types.

The decrease in the helium-dominated atmosphere fraction at high T_{eff} is attributed to the float-up process. Due to strong gravitational settling, hydrogen gradually floats up to the outermost layers as the newly formed white dwarf cools. This leads to a switch from a DO to DA provided there is enough hydrogen in the interior (Fontaine & Wesemael, 1987; Bédard, 2024). The location on the cooling sequence where this transition occurs depends on the initial hydrogen content, with higher mass fractions leading to transitions at hotter temperatures. For example, an initial mass fraction of $X_{\rm H} = 10^{-3}$ in the outer $10^{-4}\ M_\star$ leads to a DO-DA transition at $T_{\rm eff} = 70,000$ K, whereas $X_{\rm H} = 10^{-6}$ results in a transition much later, when the star cools down to $T_{\rm eff} = 35,000$ K (Bédard, 2024).

Clearly the float-up process is not the end of the story since the fraction of helium-dominated atmospheres goes back up over time. This rise is due to a combination of two separate process: convective dilution and convective mixing. The new exterior hydrogen layer that formed from the float-up process is relatively thin, such that it can be eroded by the underlying helium convective zone, resulting in a DB or DBA. This convective dilution process is thought to occur between $30,000$ K $\gtrsim T_{\rm eff} \gtrsim 14,000$ K depending on the hydrogen layer mass (MacDonald & Vennes, 1991; Rolland et al., 2018, 2020; Bédard et al., 2023).

However, this switch from a DA to DB can be delayed if the exterior hydrogen layer is massive enough, such that the hydrogen atmosphere is maintained for longer. If the hydrogen layer is thicker than the outer $\sim 10^{-14}\ M_\star$ (Bédard, 2024), then dilution is unable to cause an atmosphere change. However, a convection zone appears at about $T_{\rm eff} = 18,000$ K (Cunningham et al., 2019), and it expands significantly below 12,000 K to include a large portion of the underlying helium envelope. This leads to efficient transport of helium up to the outer layers, resulting in a switch from a hydrogen-dominated to helium-dominated atmosphere. This convective mixing process is expected to occur between $14,000$ K $\gtrsim T_{\rm eff} \gtrsim 6,000$ K (Tremblay & Bergeron, 2008; Chen & Hansen, 2011; Rolland et al., 2018; Cunningham et al., 2020; Bédard et al., 2022b; Bergeron et al., 2022).

Ultimately, most white dwarfs do not undergo this spectral evolution. The $\sim$75% of objects that are born as DAs will not switch atmospheres, as hydrogen is the lightest element, the hydrogen layers are relatively thick, and the convection zone in these objects never reaches deep enough to pull helium to the surface. But for the remaining $\sim$25% of targets that begin as DOs, $\sim$60% of them have enough residual hydrogen in their interiors to begin the float-up process followed by either convective dilution or mixing. In fact, 60%$-$75% of all DB white dwarfs are specifically DBAs (Koester & Kepler, 2015; Rolland et al., 2018; Genest-Beaulieu & Bergeron, 2019b). Hence for this population of white dwarfs that begin as DOs, analyzing these complicated interior processes is vital for understanding white dwarf evolution. But beneath the surface, something far more sinister than convection lurks in the depths.

1.4. Magnetism: More Complications

Earth has a magnetic field generated by the internal motion of iron and nickel in Earth's outer core. At the surface, this field is relatively weak at only $\sim$0.5 G. Thankfully this field generates a magnetosphere that is sufficient for shielding the Earth from the Sun's radiation pressure, which would otherwise strip the atmosphere from Earth over time (look how well that worked out for Mars). The Sun also has a magnetic field though it is roughly twice the strength of Earth's, and is similarly generated through the internal motion of material throughout the star.

Perhaps then it is no surprise that we detect magnetic fields in white dwarfs as well. Unsurprisingly however, our knowledge of these fields is much more limited due to biases in detection methods and the diversity of magnetic objects detected. The big question that needs to be addressed is: where do these fields come from? After all, if a magnetic field is generated through some sort of internal motion of material, why do only $\sim$20% of these dead stars host a field (Bagnulo & Landstreet, 2021)?

1.4.1. Creating the Field

There are three primary explanations for the source of magnetism in white dwarfs, each with their own strengths and weaknesses. The first and perhaps simplest is a fossil origin, meaning the magnetic field formed during prior evolution stages such as on the main-sequence or during the giant stages. This field would then survive all the way to the white dwarf phase. This formation mechanism has historically not been given much favor, namely due to the difficulty of detecting magnetic fields in many main-sequence stars (Shorlin et al., 2002; Bagnulo et al., 2006; Fossati et al., 2015). While there is a subclass of highly magnetic stars with spectral types Ap and Bp that could certainly form magnetic white dwarfs at the end of their lives, there are not nearly enough of them to explain all magnetic white dwarfs (Wickramasinghe & Ferrario, 2005).

While we cannot seem to find many magnetic fields at the surface of stars, an interesting alternative is that the fields are simply buried in the cores of these stars and thus cannot be detected via traditional methods. Simulations have shown that strong convection in stellar interiors can in fact spin up a field (Brun et al., 2005; Augustson et al., 2016; Hidalgo et al., 2024), and that this field can emerge to the surface during the white dwarf stage (Camisassa et al., 2024). Fields have even been detected in the cores of red giant stars using asteroseismology (Li et al., 2022, 2023; Deheuvels et al., 2023; Hatt et al., 2024). So this origin certainly cannot be disregarded.

The second proposed mechanism for generating fields is via crystallization. As white dwarfs cool, their interiors solidify similar to how steam will eventually turn to ice if it cools down sufficiently. Since the white dwarf core is composed of both carbon and oxygen, phase separation occurs as the solid phase becomes enriched with the heavier oxygen while the carbon-oxygen mixture remains above the core (Stevenson, 1980; Mochkovitch, 1983; Isern et al., 1997). The convective motion of this material has thus been proposed to be able to spin up a magnetic dynamo (Isern et al., 2017), similar to how Earth's own field is generated.

From an observational perspective, this is an attractive solution because the occurrence of magnetic white dwarfs often coincides with the onset of crystallization (Bagnulo & Landstreet, 2021, 2022). Recent theoretical calculations however have cast doubt on the feasibility of this origin. Some have determined that the convective velocities are fast enough to sustain this dynamo (Isern et al., 2017; Ginzburg et al., 2022), while others have found that they are too slow (Montgomery & Dunlap, 2024). In addition, once the field forms in the interior, it does not simply become immediately detectable at the surface. Instead, it takes time to propagate to the surface. Blatman & Ginzburg (2024) found that this timescale is on the order of billions of years. Due to this additional delay by the breakout time, many magnetic white dwarfs in the 20 and 40 pc volume actually cannot be well-explained by crystallization (Blatman & Ginzburg, 2024). While this channel cannot be ruled out, it has perhaps lost some value in recent years.

The final proposed mechanism to generate a magnetic field is via binary evolution and mergers. Binary systems are quite common among stars (Offner et al., 2023), and assuming the companions are not too widely separated, the stars can interact and influence each other as they evolve. The more massive star will evolve faster, and thus become a giant star while its companion remains on the main-sequence. Provided the stars are close enough, the giant star will begin mass transfer onto the lower mass companion. As the more massive star grows, mass is lost faster than it can be accreted by the companion, and a common envelope forms in which both stars are contained within a large volume of mass. Over time, the orbits shrink due to drag forces as orbital angular momentum is transferred to the envelope. If enough is transferred, the envelope can be ejected. Otherwise, the orbit will continue to decay and the two stars will merge.

This example is for binary evolution of two stars, but mergers between two white dwarfs are also quite common. As two white dwarfs orbit each other, they emit gravitational waves. This radiation actually causes their orbital distance to decrease over time, such that they end up merging. The final product is higher mass than the two original stars, and it is predicted that $30-50\%$ of all massive white dwarfs come from mergers (Temmink et al., 2020).

Both mechanisms have been found possible of generating a dynamo. In the double white dwarf merger case, the final product has a hot, convective, differentially rotating corona that is capable of generating strong fields that are confined to the surface (so the fields are immediately detectable) rather than buried in the interior (García-Berro et al., 2012). For objects that have undergone common envelope evolution, differential rotation similarly produces this dynamo (Tout et al., 2008; Briggs et al., 2018a). These two sources involving binary evolution are supported by the fact that magnetic white dwarfs tend to be more massive than non-magnetic ones (Kepler et al., 2013; Amorim et al., 2023), and they have shorter rotation periods (Hermes et al., 2017b; Hernandez et al., 2024; Oliveira da Rosa et al., 2024). In addition, there are effectively no high-field magnetic white dwarfs in detached binaries where the companion is a nondegenerate star (Liebert et al., 2005b, 2015). Hence it appears that binary evolution is required in some capacity, otherwise the fraction of isolated magnetic white dwarfs should be similar to that in these non-interacting binary systems.

However, it is unlikely that every single magnetic white dwarf has undergone binary evolution of some form, a combination of formation channels is likely necessary. Disentangling the source of these fields requires large-number studies of magnetic white dwarf populations and comparing them to their non-magnetic counterparts. So how are these magnetic fields detected in the first place?

1.4.2. Detecting the Field

There are two ways to detect stellar magnetic fields. The first, which we do not conduct in our work but is still highly relevant for discussion, is via spectropolarimetry. This technique specifically leverages the polarization of light when in the presence of a magnetic field. If you are familiar with polarized glasses, you already have some experience with this. Light is an electromagnetic wave, such that it consists of coupled oscillating electric and magnetic fields that travel perpendicular to one another. In the case of direct sunlight, these fields oscillate randomly in all directions around the direction of propagation, so the light is unpolarized. But what happens when this sunlight scatters off a surface such as water? The surface reflects light that oscillates parallel to the surface more efficiently than light that oscillates perpendicular to the surface. This introduces glare, which results in these surfaces appearing brighter than their surroundings. By using a filter that specifically blocks this “horizontal” light, the glare is eliminated.

In the case of magnetic white dwarfs, the magnetic field circularly polarizes the light received here on Earth. In this case, the electric and magnetic field vectors have a constant magnitude but a varying phase angle. The electric field vector can rotate either clockwise or anti-clockwise, and the net polarization can be determined by measuring the intensity of both the clockwise and anti-clockwise polarized light. A more detailed summary of spectropolarimetry is provided by Landstreet (2015). The beauty of this technique is that it can detect very weak magnetic fields, down to $\sim$1 G, with stronger magnetic fields leading to stronger net polarization. The downside is that this method requires vast amounts of light to detect net polarizations that are often on the order of $\sim 1\%$. This means it is typically limited to brighter objects, and as we have discussed previously, white dwarfs are stubbornly faint.

The second and more common method is through Zeeman-splitting of absorption lines. As shown in Figure 1.1, electrons in the white dwarf atmosphere normally absorb energy at specific wavelengths, which leads to predictable line profiles in their spectra. Each energy level has an associated magnetic moment, so when an atom is placed in a magnetic field, these default energy levels (E_{i0}) become split. This introduces the possibility of new transitions between the magnetic sublevels, whose energies are

$$E_i = E_{i0} + g_i(eh/4\pi mc)Bm_J \tag{1.4}$$

where g_i is the Landé factor, e is the electron charge, m is the electron mass, c is the speed of light, h is Planck's constant, B is the magnetic field strength, and m_J is the magnetic quantum number. With these new energy levels, the associated wavelength shifts relative to the default wavelength of these transitions follow as

$$\Delta\lambda_{ij} = \frac{e\lambda_0^2}{4\pi mc}(g_i m_{Ji} - g_j m_{Jj}) = (4.67 \times 10^{-13})\lambda_0^2 B(g_i m_{Ji} - g_j m_{Jj}) \tag{1.5}$$

Hence measuring the observed wavelength splitting of a given absorption line can be used to obtain the magnetic field strength, with larger field strengths producing greater wavelength shifts. Figure 1.4 shows the predicted wavelength position of the Balmer series for a given field strength and an example optical spectrum of a magnetic DA white dwarf. Unlike the magnetic fields of the Earth and Sun, field strengths on the order of MG are quite common in white dwarfs. For field strength less than ~100 MG, the shifted line positions are relatively well-behaved especially for Hα since there are no nearby absorption lines. Above this threshold, the line positions behave non-linearly and will often smear out due to blending of multiple lines, which makes determining the field strength much more difficult. We label magnetic white dwarfs with an "H", so a magnetic DA is now a DAH, a magnetic DB is a DBH, etc. The split features are typically denoted as the σ components while the central line is the π component.

The main advantage of using Zeeman-splitting to find magnetic white dwarfs is the wide availability of spectra. With large surveys such as SDSS (York et al., 2000), spectra for thousands of white dwarfs can quickly be downloaded and inspected for splitting of the absorption lines. The tradeoff is that below ~1 MG, the splitting becomes extremely weak which makes detecting the splitting extremely difficult with low-resolution spectroscopy (Kepler et al., 2013). High-resolution spectroscopy can help alleviate this to some degree, but this comes at the cost of signal-to-noise. And above ~100 MG, all of the absorption features can be smeared out such that the spectrum is featureless. Non-magnetic white dwarfs have featureless spectra below ~11,000 K with a helium-dominated atmosphere and below ~5,000 K with a hydrogen-dominated atmosphere, as there is not enough thermal energy to cause transitions. Hence these strong field magnetic white dwarfs at cooler temperatures can be conflated with non-magnetic objects, making their identification difficult as well. Spectropolarimetry can solve both of these problems, but only if the target is bright enough.

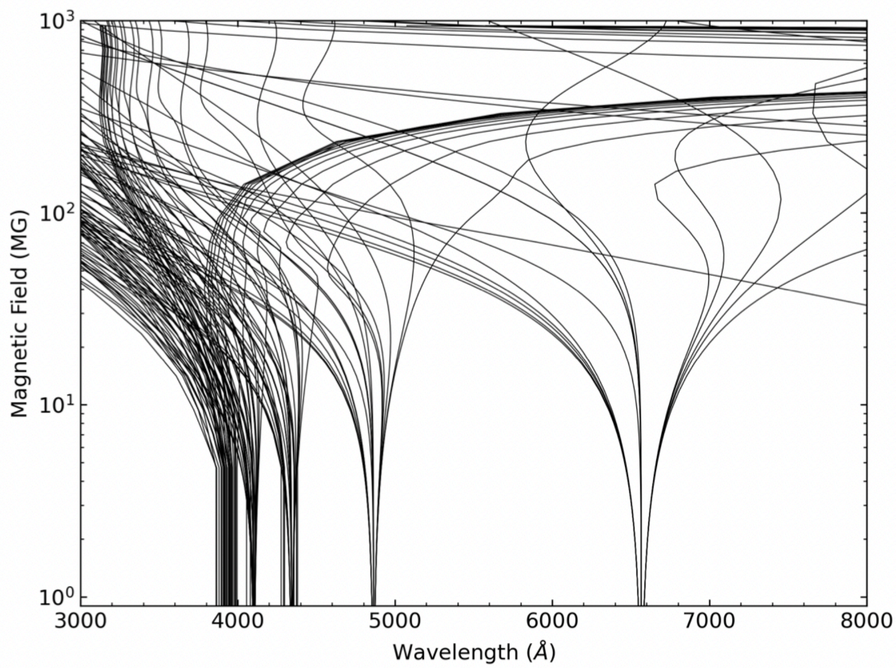

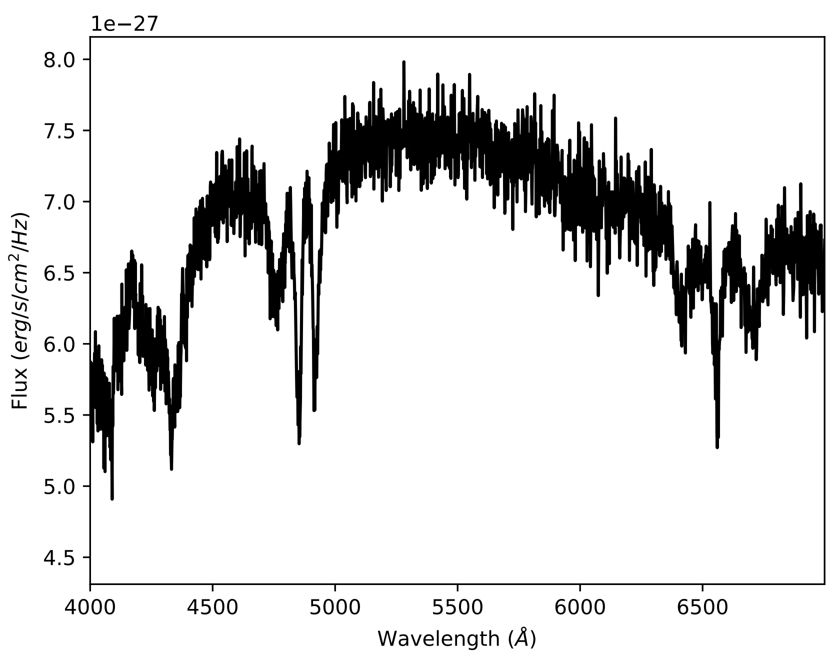

Figure 1.4: *Top*: Predicted wavelength positions of the Balmer series in the presence of a magnetic field (Hardy et al., 2023a). *Bottom*: Spectrum of a DAH white dwarf. Zeeman-splitting is clear in both Hβ and Hα.

1.4.3. Modeling the Field

Determining the parameters of magnetic fields comes with its own set of challenges. An initial geometry must be assumed, where the simplest case is a dipole model similar to that of Earth's field. In this geometry, there is a distinct north and south pole with field lines looping from the north to the south. A more complicated source of the field for example would be a magnetic quadrupole, which in some cases yields a better fit to observed data. Euchner et al. (2005) conducted phase-resolved spectropolarimetry of a magnetic DA white dwarf and found that the field structure is dominated by a quadrupole with additional dipole and octupole contributions. However, the dipole model is often sufficient for fitting magnetic spectra, so it is the most commonly used model and will be the focus of this section.

While this dipole model is fairly straightforward, there is an additional variable to consider, which is the location of the dipole within the white dwarf. The dipole that generates Earth's field is at the center of our planet, however this centered dipole model has not been fully successful at reproducing observed spectra of magnetic white dwarfs. Instead, an offset dipole model, in which the dipole origin is shifted along some arbitrary axis, has been successful in matching the observations where the centered model has failed (Wickramasinghe, 1987; Achilleos & Wickramasinghe, 1989; Bergeron et al., 1992).

The strength of the field at a given point on the white dwarf surface using this offset dipole model is given by Achilleos et al. (1992):

$$B(x, y, z) = \frac{B_d(r^2 + 3(z - a_z)^2)^{1/2}}{2r^4} \tag{1.6}$$

where

$$r^2 = x^2 + y^2 + (z - a_z)^2 \tag{1.7}$$

and B_d is the dipolar field strength and a_z is the offset of the dipole along the z-axis measured in radii of the white dwarf. While the choice of axis to shift the dipole is arbitrary, shifting the dipole parallel to the magnetic axis simplifies the calculations (Martin & Wickramasinghe, 1984). Figure 1.5 shows a diagram for this field geometry. In this diagram, the dipole is offset along the x, y, and z axes for clarity. There is also an additional parameter, i, to consider when trying to reproduce the magnetic spectra. This viewing angle, while not intrinsic to the field itself, does impact the spectrum that we obtain when observing the white dwarf.

Figure 1.6 shows how the synthetic spectra change when varying the field strength, z-offset, and viewing angle. The relation between the field strength and the position of the split lines has already been discussed, with higher field strengths leading to larger wavelength shifts. A positive

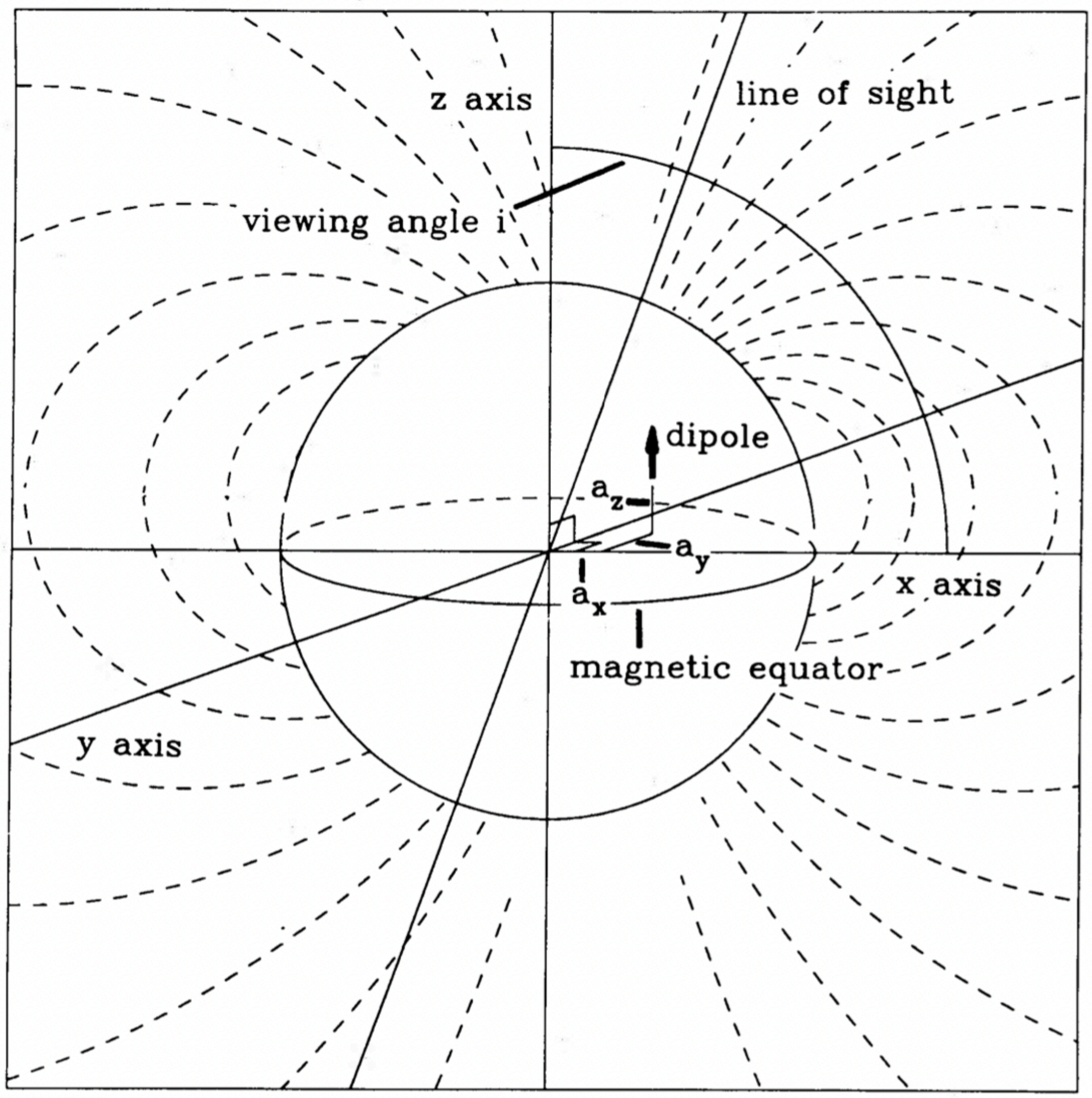

Figure 1.5: Diagram of the magnetic field geometry using an offset dipole model (Achilleos & Wickramasinghe, 1989). Here the dipole is offset along each axis, however we set the x and y offsets to 0 when generating fits.

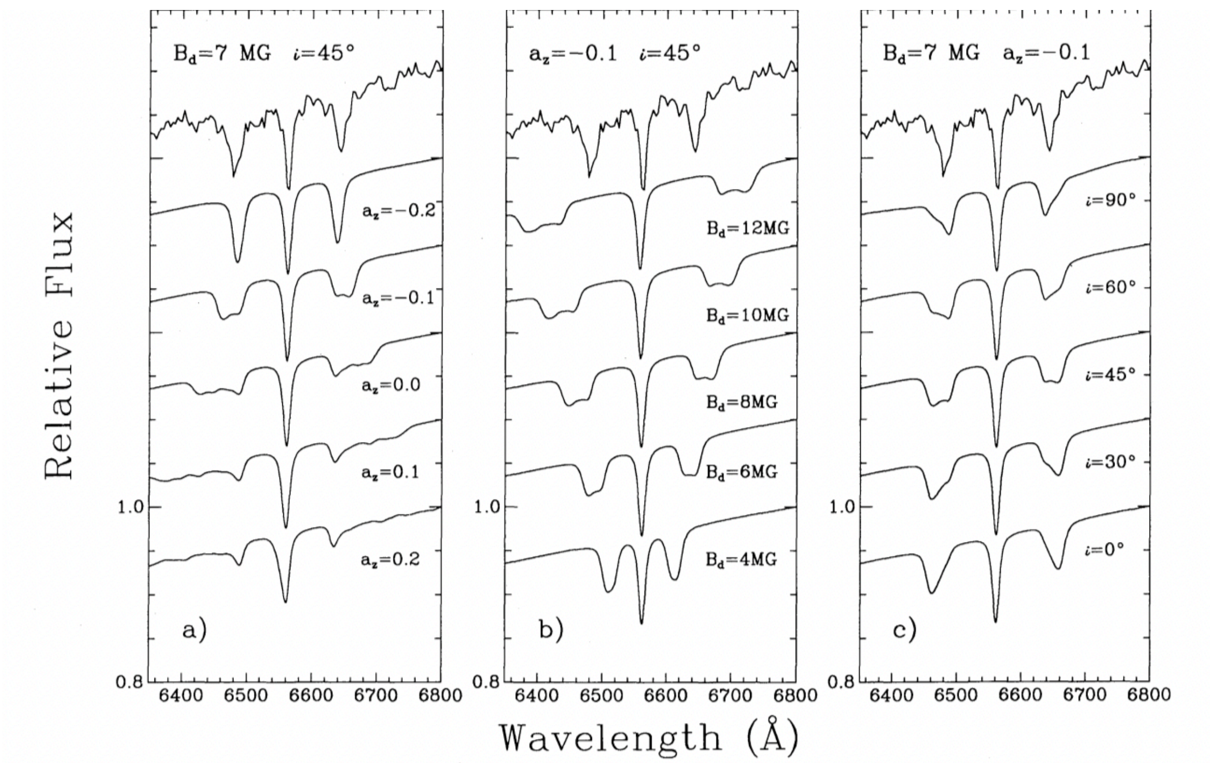

Figure 1.6: Example calculations of Hα using the offset dipole model (Bergeron et al., 1992). Each panel holds two parameters constant while allowing the third to vary, which affects how the Hα profile appears. The left panel holds the field strength and viewing angle fixed at 7 MG and 45° respectively, the middle panel holds the z-offset constant at -0.1 in addition to the viewing angle, while the right panel holds the field strength and z-offset fixed. At the top of each panel is the spectrum of a DAH, LHS 1734. The synthetic spectra are offset for clarity.

z-offset leads to shallower σ components while a negative one produces deeper, narrow components. The viewing angle's effects are much more subtle, affecting only the shape of the σ components. With low signal-to-noise spectra, constraining the viewing angle can thus be very difficult. It is not uncommon to allow B_d and a_z to vary as free parameters during the spectral fitting process, while selecting specific i values and manually inspecting which ones best fit the data.

1.5. My Dissertation

When I arrived in Oklahoma in the summer of 2019, Mukremin gave me a project that I do not even remember the details of because it ultimately did not appear feasible after a month or so working on it. Shortly after, he brought up one of his previous papers that analyzed a variable magnetic dwarf. Despite electrodynamics being my worst subject in physics, I was very interested in variable stars, and this was a chance to gain more experience with observational data. What initially began as a study on a handful of peculiar magnetic white dwarfs has expanded into investigating the impacts of magnetism on spectral evolution in addition to determining the source of magnetism with the largest volume-limited sample of magnetic white dwarfs ever conducted. The organization of my dissertation is as follows:

Chapter 2 describes our analysis of the magnetic white dwarfs in the SDSS 100 pc sample. I discuss the sample, the modeling of the objects, and how a statistical analysis of the stellar parameters shows evidence of two populations of magnetic white dwarfs which form via separate channels. This text is based on a paper that will be published in The Astrophysical Journal by Moss et al. (2025b).

Chapter 3 describes the study of a new magnetic white dwarf that shows clear variations in the depth of its hydrogen lines in time-resolved spectra. This object likely has an inhomogeneous distribution of hydrogen and helium in its atmosphere due to the effects of the magnetic field on convective dilution. The text is based on a paper published in Monthly Notices of the Royal Astronomical Society by Moss et al. (2024).

Chapter 4 discusses a sample of magnetic white dwarfs that have likely undergone binary evolution based on a combination of fast rotation periods and low masses. These targets require an unresolved companion to match the shallow absorption profiles, however the lack of Doppler shifts in their spectra suggests they are single objects with inhomogeneous atmospheres due to the effects of the magnetic fields on convective mixing. This text is based on a paper published in Monthly Notices of the Royal Astronomical Society by Moss et al. (2023).

Chapter 5 describes the discovery of two additional objects with varying absorption profiles in their spectra, once again pointing to inhomogeneous atmospheres due to magnetism. With the growing number of these variable targets, we describe the class of these exotic objects for the first time and make the connection between magnetism and spectral evolution that causes these unique atmospheres. This text is based on a paper published in The Astrophysical Journal by Moss et al. (2025a).

Finally, in Chapter 6 I conclude with a summary of this work and discuss future projects to further our understanding of magnetic white dwarfs.

CHAPTER 2

Magnetic White Dwarfs in the SDSS 100 pc Sample

2.1. New Insights

The origin of magnetic fields in white dwarfs has been notoriously difficult to constrain. Recent work however has taken advantage of volume-limited surveys to obtain a holistic view of the magnetic white dwarf population. Bagnulo & Landstreet (2021) obtained new spectropolarimetric observations of 85 white dwarfs within 20 pc of the Sun. Combined with literature data, they checked 149 of the 152 white dwarfs in this volume for magnetic fields, with sensitivies down to 1kG for DAs and 1 MG for DCs. Of these 149 objects, 33 are magnetic, for a magnetic fraction of 22%. However, there is a notable lack of magnetic white dwarfs younger than 0.5 Gyr in this sample. Bagnulo & Landstreet (2022) thus obtained spectropolarimetric observations of 85 white dwarfs younger than 0.6 Gyr and between 20 and 40 pc from the Sun in order to better understand the incidence of magnetism among young white dwarfs.

Figure 2.1 shows the age-mass diagram for the white dwarfs in the 20 pc sample, and white dwarfs younger than 0.6 Gyr within 40 pc from Bagnulo & Landstreet (2022). Several key findings emerge from this particular sample of white dwarfs. The first is that among white dwarfs younger than 0.6 Gyr, high mass white dwarfs ($M \geq 1.1\ M_{\odot}$) are almost exclusively magnetic (∼85%). In contrast, young white dwarfs below 0.75 $M_{\odot}$ are rarely magnetic ($\lesssim$2.5%). Additionally, these massive magnetic white dwarfs have strong fields on the order of 100 MG, whereas the few average mass ones have weak fields on the order of 10 kG. When looking at older ages, namely beyond 2 Gyr, there are virtually no high mass white dwarfs, while magnetism among the average mass objects becomes more common. These old, average mass magnetic white dwarfs also have notably strong fields compared to their younger counterparts.

These trends provide valuable insight into where the fields come from. The high mass population of magnetic white dwarfs likely come from binary evolution, as they are massive, young, and have high field strengths. Given their young age, the magnetic fields emerge quickly (within hundreds of Myr) at the surface once the cooling phase begins. The average mass white dwarfs likely come from single-star evolution, thus their magnetic fields likely come from either crystallization or an earlier stage of stellar evolution. More specifically, both the strength and frequency of magnetic fields in these objects grow over time. Hence there appears to be two distinct populations of magnetic white dwarfs that form from unique channels. These two populations were initially proposed by Valyavin & Fabrika (1999), but could not be confirmed until a sufficiently large volume-limited survey could be conducted.

2.2. The 100 pc Sample in the SDSS Footprint

To obtain an unbiased view of the white dwarf population, Kilic et al. (2020) conducted a model atmosphere analysis on the white dwarfs within 100 pc. This project involved obtaining spectroscopic follow-up observations for objects with unconstrained atmospheric compositions, so the sample focused on targets within the SDSS observational window, and the follow-up was limited to targets hotter than 6000 K. Below this limit, it becomes increasingly difficult to constrain the atmospheric composition as the hydrogen lines become weaker. Kilic et al. (2025) then extended the follow-up observations to targets hotter than 5000 K in order to analyze important processes that occur at low temperatures such as convective mixing. In total, Kilic et al. (2025) has spectral classifications for 3146 out of 4214 white dwarfs.

Unsurprisingly, some of these white dwarfs in this sample are magnetic. Hence it is beneficial to analyze the magnetic white dwarfs within this sample, as we are able to obtain improved statistics by analyzing the magnetic white dwarfs within 100 pc. Specifically, we can further test the idea that there are two distinct groups of magnetic white dwarfs that form via different channels with this large, volume-limited sample. We discuss our observations and sample selection in Section 3, followed by our model atmosphere analysis in Section 4. In Section 5 we discuss the results with respect to various physical features such as magnetic field strength, photometric variability, cooling age, etc. In Section 6 we show statistical evidence for two populations of magnetic white dwarfs in our sample, and then discuss our findings with regards to the unsettled questions in white dwarf magnetism in Section 7. We then conclude in Section 8.

2.3. Sample Selection and Observations

As described in Kilic et al. (2025), there are 3146 white dwarfs with spectral classifications out of 4214 in the entire SDSS 100 pc sample. These 3146 targets consist of 2306 white dwarfs with spectral classification from the literature, and 840 obtained from follow-up optical spectroscopy. The spectroscopic follow-up is 86% complete for targets with $T_{\rm eff} \geq 5000$ K and 91% for targets with $T_{\rm eff} \geq 6000$ K. The follow-up observations were conducted using the 1.5m Fred Lawrence Whipple Observatory (FLWO), MDM Hiltner 2.4m, Apache Point Observatory (APO) 3.5m, 6.5m MMT, 6.5m Magellan, and 8m Gemini South telescopes between 2020 October and 2024 May. MDM observations were obtained as part of the OSMOS queue, and Gemini data were taken as part of the queue programs GS-2022B-Q- 304, GS-2023A-Q-227, and GS-2023A-Q-327.

We primarily identify magnetic targets based on Zeeman-splitting of optical absorption lines. Since a high magnetic field strength ($\sim$100 MG) can smear out absorption lines, we can also detect fields if a target has a featureless spectrum and if it is at a sufficiently high effective temperature

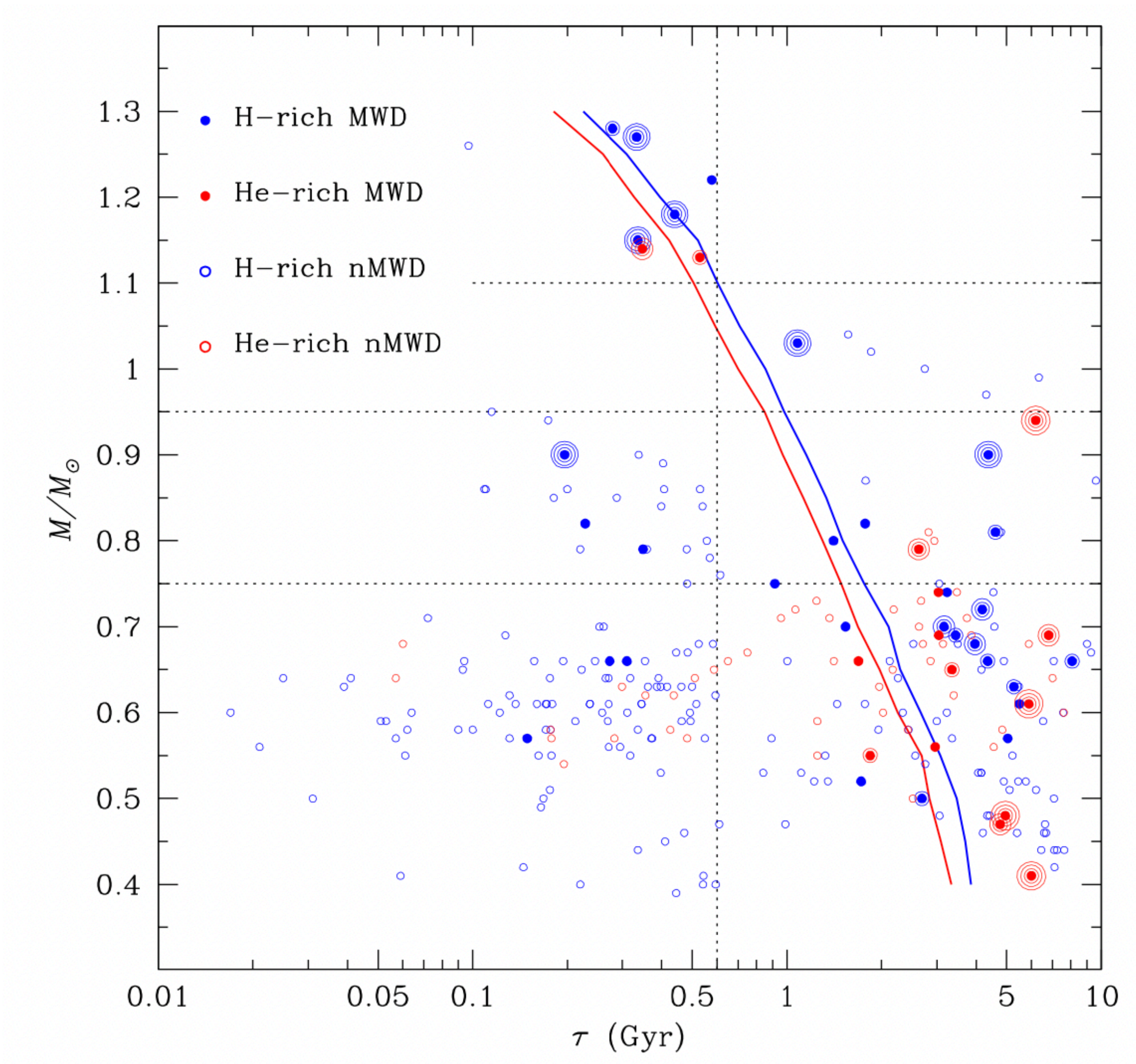

Figure 2.1: Age-mass diagram of the white dwarfs within 20 pc and those younger than 0.6 Gyr within 40 pc (Bagnulo & Landstreet, 2022). Blue points are for hydrogen-rich atmosphere white dwarfs, while red points are for helium. The point sizes correspond to their field strengths: unfilled points are non-magnetic, filled have fields weaker than 1 MG, one circle corresponds to a field between 1 and 10 MG, two circles is between 10 and 100 MG, and three is above 100 MG. The red and blue tracks mark the onset of crystallization based on thin and thick hydrogen layer models (Bédard et al., 2020) respectively.

such that we would expect to see H or He lines. We do not conduct spectropolarimetry in our observations, thus we are biased against objects with very weak fields ($B < 1$ MG) and DCs at lower effective temperatures that could harbor high field strengths ($B > 100$ MG).

From this sample, we identify 163 total magnetic white dwarfs, 149 of which have hydrogen-dominated atmospheres (91%). This sample is thus the largest volume-limited sample of magnetic white dwarfs to date. The magnetic fraction however is notably lower (5.2%) than both Bagnulo & Landstreet (2021) and Bagnulo & Landstreet (2022), who obtained a magnetic fraction of 22% for the local 20 pc volume and ~10% of white dwarfs younger than 0.6 Gyr and within 40 pc. This is not surprising given the limitations of using optical spectroscopy only to detect magnetic fields. If we only consider objects with field strengths $1 \leq B \leq 100$ MG from Bagnulo & Landstreet (2022), the magnetic fraction drops to 5.9%. Hence our magnetic fraction is consistent given our biases against very weak and very strong fields. Note that there are two objects with Zeeman-split Balmer lines in emission (DAHe) in the 100 pc sample. Since the origin of these targets is unclear (Manser et al., 2023), we do not include them in our analysis.

Figure 2.2 shows the Gaia color-magnitude diagram of the 100 pc sample with the magnetic targets highlighted and the evolutionary sequences for a $0.6 M_{\odot}$ and $0.8 M_{\odot}$ white dwarf with pure H atmospheres (Tremblay et al., 2011; Blouin et al., 2019; Bédard et al., 2020). We immediately see an above-average mass tendency in hotter magnetic white dwarfs, while the cooler ones are more concentrated among average mass white dwarfs. This is in line with the results from Bagnulo & Landstreet (2022), who found that the mass of magnetic white dwarfs with cooling age ≥ 2 Gyrs is similar to the mass of normal white dwarfs. We also see a lack of magnetic white dwarfs redder than $G_{BP} - G_{RP} \approx 1.0$ in our sample. This corresponds to $T_{\rm eff} = 5000$ K, below which H lines disappear. We cannot detect magnetism in white dwarfs redder than this limit through optical spectroscopy alone, so we are biased against the oldest and coolest magnetic white dwarfs. Thus our observations provide a robust lower limit on the number of magnetic white dwarfs in the sample.

2.4. Model Atmosphere Analysis

Of the 149 magnetic white dwarfs with hydrogen-dominated atmospheres, 81 of these are new discoveries while 2 were found by Berdyugin et al. (2024) with no field estimate provided. For these 83 targets, we use offset dipole models to obtain fits to our spectra. We start by using the photometric technique described by Bergeron et al. (2019) to constrain the effective temperature and solid angle, and thus the radius and mass. We obtain these parameters for all 163 magnetic white dwarfs in our sample. For the 83 new objects, we construct a grid of magnetic spectra to determine the viewing angle i ($i = 0°$ means viewing the white dwarf "pole-on"), magnetic field strength B_d, and dipole offset a_z (see Figure 1 of Achilleos & Wickramasinghe 1989 for the 3D model of this geometry and Figure 4 of Bergeron et al. 1992 for example synthetic spectra). We do

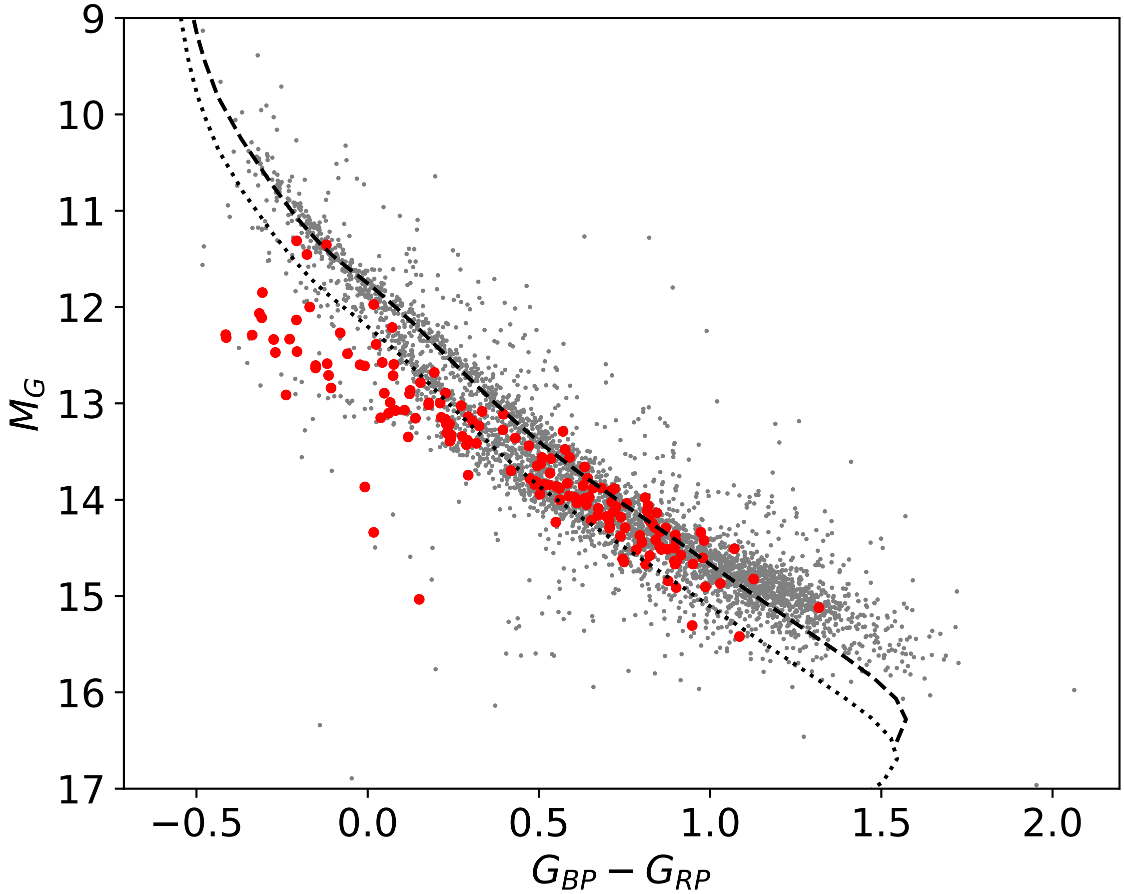

Figure 2.2: Gaia color-magnitude diagram of the 100 pc sample in the SDSS footprint (gray points) with the magnetic white dwarfs marked by red points. The dashed and dotted lines are the cooling tracks for a $0.6M_\odot$ and $0.8M_\odot$ white dwarf respectively with pure H atmospheres, which go down to $T_{\rm eff} = 3000$ K in this figure.

not provide model fits for the 6 newly found non-DAs (2 DQHs and 4 DZHs).

The total line opacity is calculated as the sum of the individual Stark-broadened Zeeman components. The line displacements and oscillator strengths of the Zeeman components of Hα through Hδ are kindly provided by S. Jordan (see also Hardy et al. 2023a). The total line opacity is normalized to that resulting from the zero-field solution. The specific intensities at the surface, $I(\nu, \mu, \tau_\nu = 0)$, are obtained by solving the radiative transfer equation for various field strengths and values of μ ($\mu = \cos\theta$, where θ is the angle between the propagation of light and the normal to the surface of the star). Further details of these magnetic models are provided in Moss et al. (2024).

We typically obtain excellent fits for field strengths 2 MG $\lesssim B_d \lesssim$ 100 MG. Above 100 MG, the absorption lines tend to smear out or become distorted, which makes determining the specific geometry difficult. Figure 2.3 shows an example fit to the Hα line of a DAH with an average magnetic field strength. We obtain a field strength of 5.0 MG for this target, which yields an excellent fit to the central Hα line and the Zeeman-split components. Thus we are confident that the field strength and geometry for this object are well constrained.

Figure 2.4 shows the fits to two targets where we obtain field strengths above 100 MG. For J0800+0655, the absorption features are shifted but still prominent. We are thus able to obtain an excellent fit with a field strength of 317 MG, and we consider this field strength accurately constrained. In contrast, the absorption features of J0818+4144 are more smeared out, likely due to the high strength and geometry of the field. While the field strength is likely above 100 MG, we consider this value questionable as we are not confident that 143 MG is the exact field strength of this object based on the quality of our fit.

Below a few MG, the Zeeman-split components are not shifted far from the central Hα line, making them hard to distinguish when fitting the spectra. However, we can infer the presence of a field based on the non-magnetic fit to Hα. Figure 2.5 shows an example non-magnetic and magnetic fit to an object with a field strength on the order of 1 MG. Here we do not see obvious Zeeman-splitting, but the shape of the Hα line is clearly distorted from what we would expect from a DA. Hence we classify this target as magnetic, but we mark the field strength as questionable.

We also identify a DAP in our sample, SDSSJ000728.91+340341.4. This target was previously classified as a DCP (Berdyugin et al., 2024), however we detect a weak Hα feature in the optical spectrum from Limoges et al. (2015). Hence we classify this object now as a DAP. We use the spectrum obtained by Limoges et al. (2015) to constrain the magnetic field strength. We obtain a magnetic field strength of $B_d = 62$ MG in our fit, shown in Figure 2.6.

Of the 81 new discoveries, there are 13 in which the presence of a magnetic field is likely but unclear, which we classify as "DAH:". There are also 9 targets where we are unsure of the atmospheric composition, which we label as "DAH?". We consider the field strengths in these spectral types preliminary. We also have 14 magnetic non-DAs in our sample, including 1 DBH, 1 DBAH, 1 DCP, 4 DQH, and 7 DZH white dwarfs. 4 of the DZHs are new identifications, and their spectra are shown in Kilic et al. (2025). The DCP, SDSSJ074842.48+112502.0, was recently identified as magnetic by Berdyugin et al. (2024) using broadband polarimetry. However, no magnetic field estimate was given in that study, so we provide a fit assuming a hydrogen-dominated atmosphere. Given the lack of strong absorption lines, we provide a tentative fit which yields a field strength of $B_d = 112$ MG. The exact field strength is likely much higher. The fits to the newly identified magnetic white dwarfs, as well as the two DAP and DCP white dwarfs, can be found on Zenodo, which can be accessed via the DOI https://doi.org/10.5281/zenodo.15163601.

We have magnetic field strength estimates for 152 of the 163 objects in the sample. 83 (81

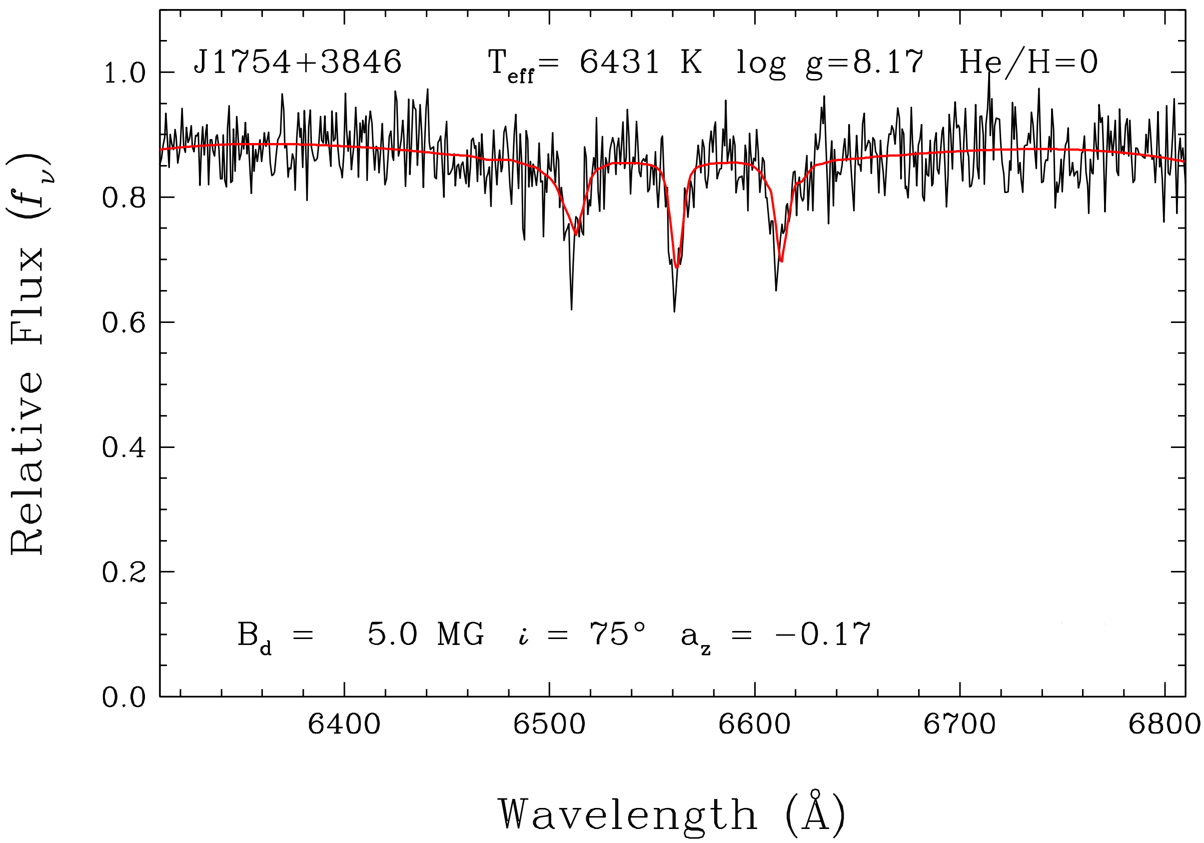

Figure 2.3: Offset dipole fit to the Hα line of a DAH, J1754+3846. We obtain an excellent fit with a magnetic field strength of 5.0 MG.

new DAHs, 1 DAP and 1 DCP) of these come from our own analysis, while the remaining are taken from the literature. We list the physical parameters for all 163 magnetic white dwarfs in Table 2.3. We inspect each of our fits and note the dipole parameters that we consider preliminary from our analysis with an "X" in the final column. We do not expect this to affect our results, which depend more on the order of magnitude of the field strengths rather than the specific values themselves. However, the fits in these cases are not sufficient enough for us to conclude that the parameters we obtain represent the exact geometry of the objects. We also do not make a distinction between different types of field measurements in our analysis. For example, we use the mean field modulus $\langle |B| \rangle$ obtained by Bagnulo & Landstreet (2024) for SDSSJ162157.77+043218.8, while our model atmosphere analysis and most of the estimates in the literature use the dipole field strength B_d. Similar to our preliminary fits, we do not expect this lack of distinction to impact our final results. Lastly, our theoretical framework follows that of Hardy et al. (2023a), who found relative uncertainties of 5% in the field strengths, 20% for the viewing angle, and 50% for the dipole offset. These uncertainties were determined by varying the parameters until the resulting synthetic

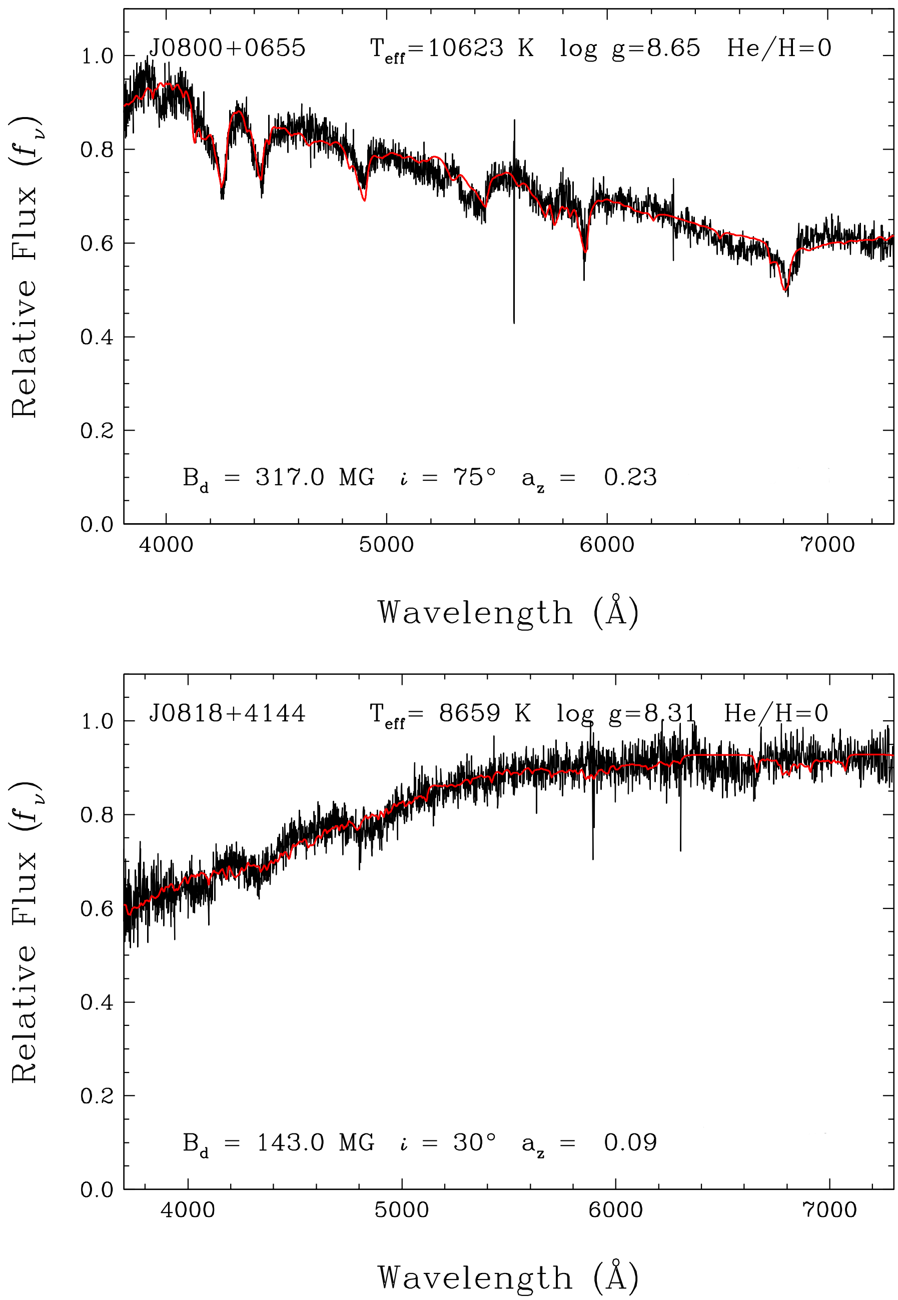

Figure 2.4: Fits to two targets that possess some of the highest field strengths in our sample. For J0800+0655 (top), absorption lines are present but significantly shifted from their zero-field positions. In contrast, the lines appear mostly smeared out for J0818+4144 (bottom).

spectrum significantly diverged from the observed spectrum. Hence we do not report exact error estimates for these parameters in Table 2.3.

Figure 2.7 shows the distribution of field strengths. Our sample is dominated by lower field objects, specifically those between 1 and 10 MG. There is a sharp decline in the number of objects

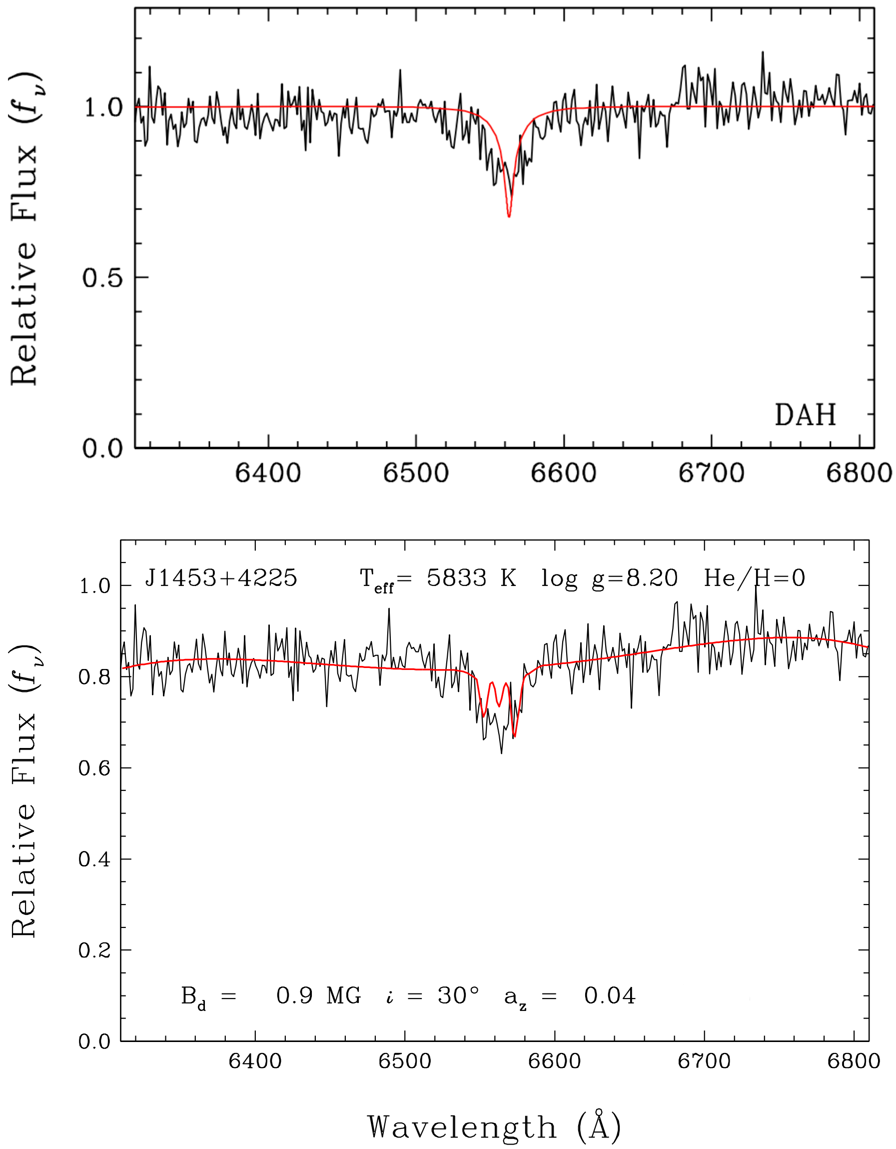

Figure 2.5: An example fit to a target with a low field strength (< 1 MG). While Zeeman-splitting is not obvious, the shape of the line profile compared to that of a typical DA suggests the presence of a magnetic field.

below 1 MG, which is a bias in our sample. Since we primarily identify targets as magnetic based on Zeeman-splitting, and many of the objects do not have spectropolarimetry observations in the literature, we are biased against the weakest fields ($B < 1$ MG). A summary of the magnetic white dwarfs in our sample is presented in Table 2.1.

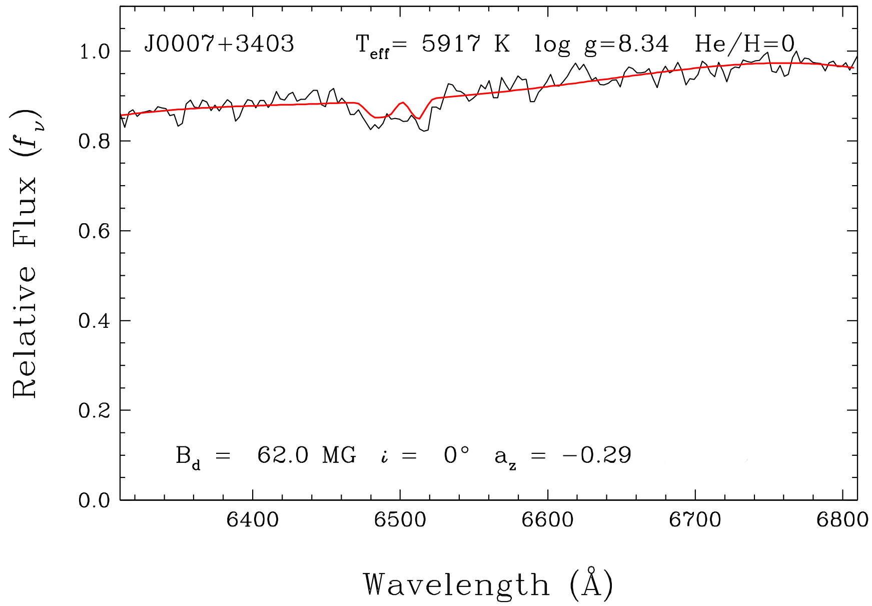

Figure 2.6: Offset dipole fit to a DAP in our sample, which was recently classified as a DCP. The Hα line is weak but noticeable.

2.5. Results

2.5.1. Effective Temperature

Our goal is to analyze the trends in magnetism across multiple parameters in order to constrain the formation channel and evolution of magnetic fields in white dwarfs. Figure 2.8 shows the stellar masses as a function of effective temperature of the 100 pc sample. The magnetic white dwarfs are marked with large circles, and we indicate their field strength measurements by color. There appears to be a clear trend in the occurrence of magnetism and the onset of crystallization, with $\approx$2/3 of the magnetic objects having begun core crystallization. The exact start of crystallization depends on the oxygen abundance in the core. These evolutionary models assume equal amounts of C and O. However, a higher oxygen abundance (e.g. $\sim$0.8, Giammichele et al., 2018, 2022) would shift the onset to higher temperatures, which would result in a larger fraction of our magnetic sample undergoing crystallization.

We also see a loose trend in the field strengths, with weaker fields becoming prevalent at low mass and effective temperature. This becomes more apparent in Figure 2.9 where we plot the magnetic field strength vs effective temperature and indicate mass by color. We can visually see two possible populations of magnetic white dwarfs: those cooler than $\sim$8000 K that tend to have field strengths weaker than $\sim$10 MG, and those at hotter temperatures that have a wide range of field strengths including some of the strongest in our sample. In addition, the targets at lower temperatures exclusively have lower masses. These lower mass targets do not show evidence of

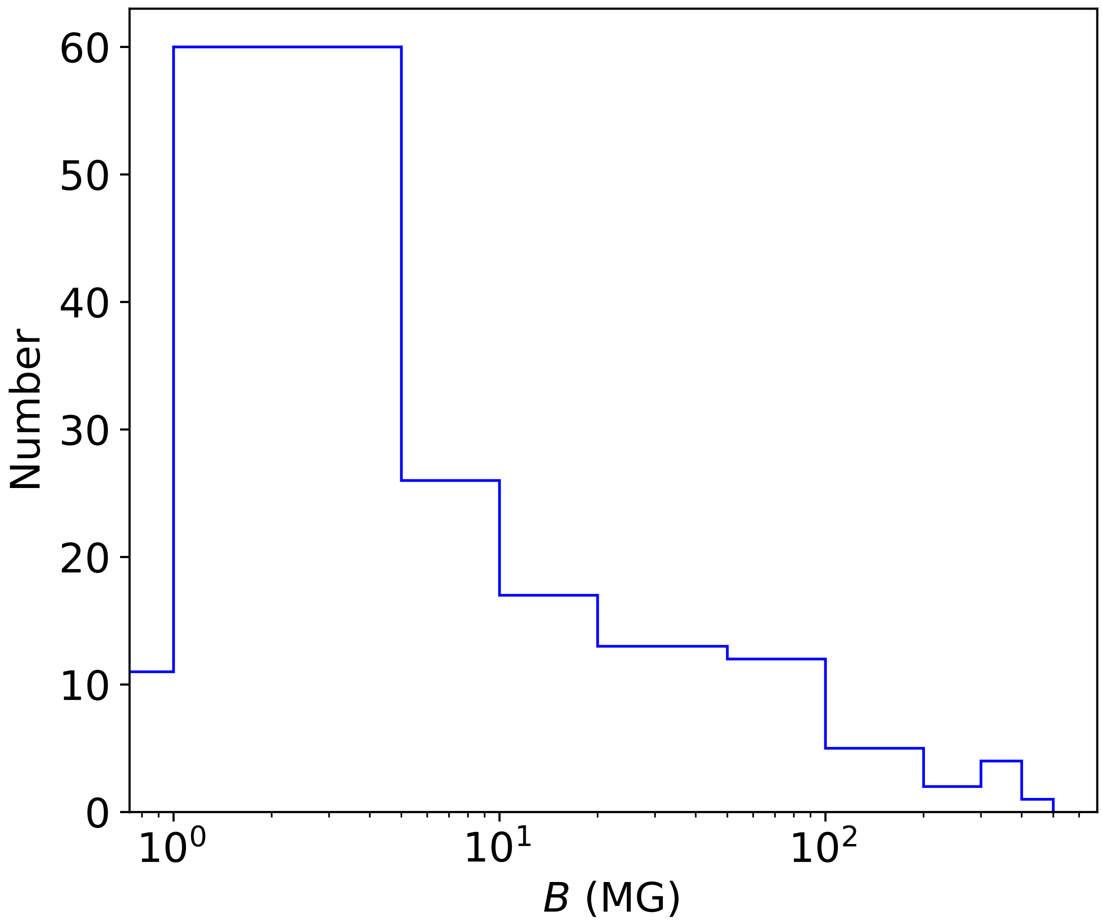

Figure 2.7: Distribution of field strengths in the SDSS 100 pc sample. The sample is dominated by intermediate fields between 1 and 10 MG, with a median field strength of 5.2 MG. The sharp decline below 1 MG is likely an observational bias in our sample which relies on low-resolution spectroscopy.

magnetic fields at young age/high $T_{\rm eff}$, but the field strength and frequency grow over time (Bagnulo & Landstreet, 2022).

2.5.2. Mass

Figure 2.10 shows the mass distribution of the non-magnetic and magnetic white dwarfs with hydrogen-dominated atmospheres. As shown in many previous studies, the magnetic objects have higher masses on average than the non-magnetic targets (Liebert et al., 2003; Kepler et al., 2013; Ferrario et al., 2015; McCleery et al., 2020; Amorim et al., 2023; Hardy et al., 2023a; O'Brien et al., 2024). While the peak of the magnetic distribution occurs at 0.7 $M_{\odot}$, we see a high mass

Table 2.1. Summary of our magnetic white dwarf numbers for a given category.

Category	Number
Total	163
Hydrogen-dominated Atmospheres	149
Non-DA	14
Field Strength Measurements	152
Newly Discovered Objects	87
New Field Measurements	83
Preliminary Fits	47
DAH:	13
DAH?	9

tail which consists of many likely merger remnants. Temmink et al. (2020) performed a population synthesis study on the single white dwarfs within 100 pc and found that 30−50% of massive white dwarfs originate from binary mergers, but only 10−30% for white dwarfs of all masses. Jewett et al. (2024) analyzed all white dwarfs greater than $0.9M_{\odot}$ in the Pan-STARRS footprint within 100 pc and found that the merger fraction ranges from 25% to 78% for different masses. Hence mergers are a more common source of these high mass magnetic white dwarfs compared to those at lower mass.

In order to see how the fraction of magnetic white dwarfs changes with mass, we divide the sample into equal width bins and calculate the fraction of magnetic objects in each bin. We calculate the errors in the fraction using the binomial probability distribution discussed in Burgasser et al. (2003). Figure 2.11 shows the calculated magnetic fractions as a function of mass for our sample in addition to the ultramassive sample (Jewett et al., 2024) and the 40 pc sample (O'Brien et al., 2024). We see a clear increase in the magnetic fraction as mass increases. Regardless of the source of magnetism, whether it is mergers, crystallization, or a fossil field, the incidence of magnetism is favored in higher mass objects. Binary interactions inherently result in higher mass white dwarfs, while more massive white dwarfs crystallize earlier on the cooling sequence and then likely suffer from long cooling delays due to ^{22}Ne distillation. Magnetic fields also reach the surface in more massive white dwarfs faster than lower mass ones (Blatman & Ginzburg, 2024; Camisassa et al., 2024) regardless of if these fields come from crystallization or from earlier evolutionary stages. While the exact nature of where magnetic fields come from has been a complex problem to solve, the trend in mass is quite clear.

Given that we do not have spectropolarimetric observations for many of the cooler objects, our measurements present a firm lower limit. There can only be more magnetic white dwarfs if spectropolarimetric observations were available. While the 40 pc sample shows a similar decreasing

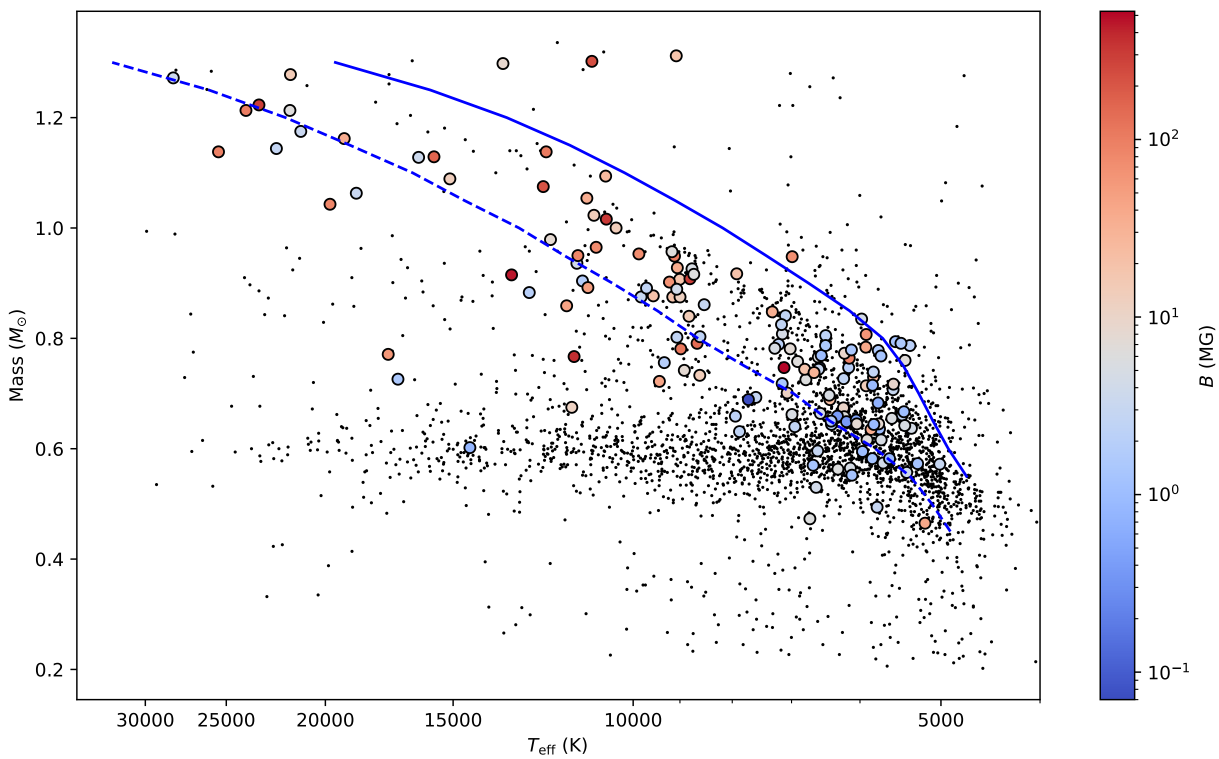

Figure 2.8: Stellar masses as a function of effective temperature for all spectroscopically confirmed white dwarfs in the SDSS 100 pc sample. Objects that are classified as magnetic in the literature and in this work are colored by field strength. We have field strength measurements for 152 of the 163 magnetic white dwarfs in the sample. The blue tracks correspond to the onset of crystallization (dashed line) and 80% core crystallization (solid line) assuming a carbon-oxygen core composition.

trend in the magnetic fraction at lower mass, O'Brien et al. (2024) finds a higher fraction than our sample at these lower masses. This is likely due to their sample having a higher fraction of spectropolarimetry data, which become increasingly difficult to acquire with decreasing brightness (and thus distance).

2.5.3. Cooling Age

In Figure 2.12 we plot mass and field strength as a function of cooling age to see if we detect a distinction in the sample based on cooling age. Interestingly, we do not detect any field strengths larger than 100 MG beyond a cooling age of ∼2.5 Gyr. The object with the strongest field, SDSSJ002128.60+150223.8, has a field strength of 527 MG (Külebi et al., 2009) and a cooling age of 2.4 Gyr. In addition, we have 98 total objects with field strengths less than 10 MG, of which 54 (55%) are older than 2.5 Gyr, and 67 (68%) are older than 2 Gyr. We see that white dwarfs older

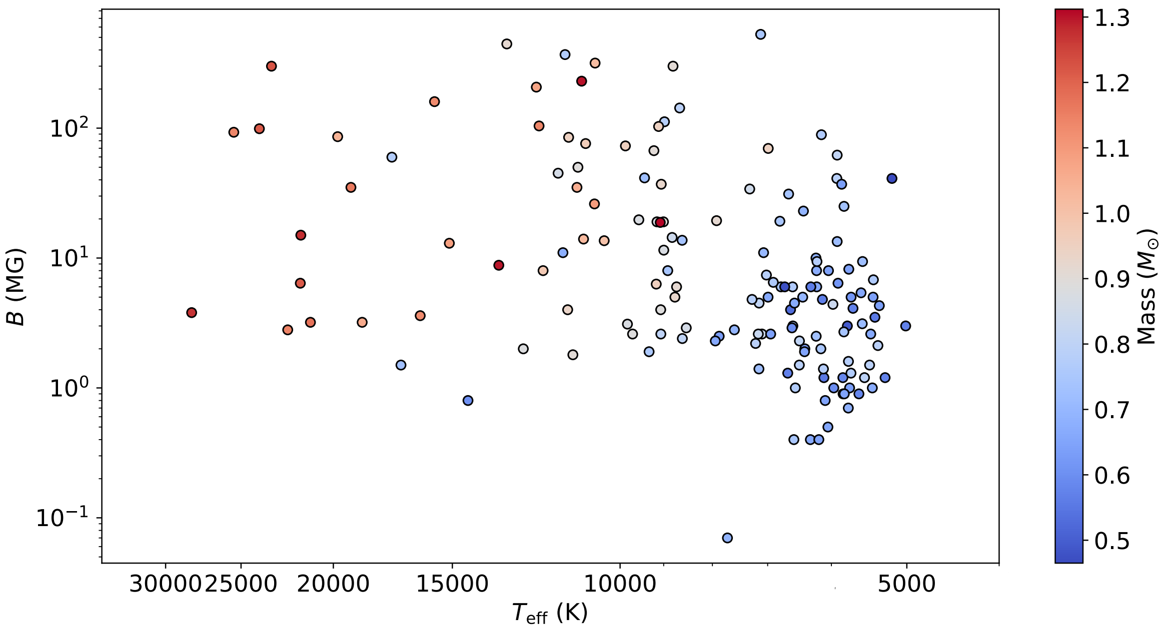

Figure 2.9: Field strength as a function of effective temperature, with mass indicated by color. There is a noticeable distinction between objects that are hotter/colder than ~8000 K, with cooler objects having lower mass than hotter objects.

than ~2 Gyr consistently have lower masses and weaker field strengths than those younger than 2 Gyr. While there are several objects at older ages with larger field strengths, these cases are the exception rather than the norm.

Bagnulo & Landstreet (2022) found an increase in the fraction of average-mass magnetic white dwarfs ($M < 0.75 M_\odot$) with cooling age out to ~4 Gyr, followed by a decline after ~4−6 Gyr. These average-mass magnetic white dwarfs likely come from single-star evolution, and thus their magnetic fields likely come from crystallization or a previous stage of stellar evolution. Hence the observed variations in the magnetic fraction could indicate a slow relaxation of the field from the interior to the surface. We calculate the magnetic fraction as a function of cooling age shown in Figure 2.13 using the same mass cutoff from (Bagnulo & Landstreet, 2022). Jewett et al. (2024) used 0.9 $M_\odot$ as the cutoff in their ultramassive sample since mergers contribute to a significant fraction of these white dwarfs (Temmink et al., 2020). Hence we also look at the trend in magnetic fraction as a function of cooling age for magnetic white dwarfs below 0.9 $M_\odot$.

Similar to Bagnulo & Landstreet (2022), we see an increase in the magnetic fraction with age. However, we find tighter error bars for the youngest objects given our larger sample size. The magnetic fraction in our sample peaks at a slightly younger age (2−3 Gyr), which could simply be

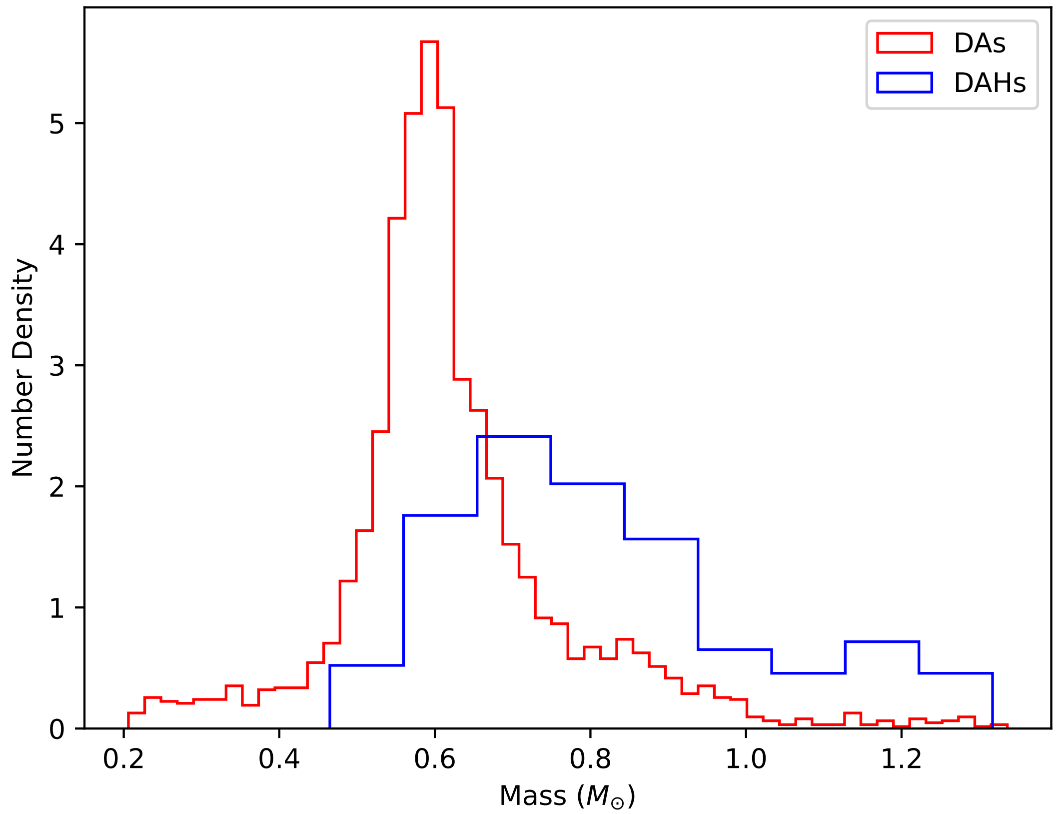

Figure 2.10: Mass distributions of the hydrogen-dominated atmosphere white dwarfs in the 100 pc sample. The non-magnetic distribution peaks at 0.59 $M_\odot$ with a broad shoulder, while the magnetic distribution peaks at 0.7 $M_\odot$ and has a high mass tail.

due to our lack of spectropolarimetry and thus our inability to reliably detect fields in older objects. Beyond this peak, we see a leveling off in the magnetic fraction for objects below 0.75 $M_\odot$ and for objects less than 0.90 $M_\odot$. The decline in the fraction for older objects could be potentially due to ohmic decay, however it is more likely caused by the inherent difficulties of detecting fields in featureless white dwarfs (Bagnulo & Landstreet, 2022). The uncertainties for our 5−6 and 6−7 Gyr bins are also large given that we have only 6 and 3 magnetic white dwarfs in each bin respectively. Since magnetism occurs more frequently in higher mass white dwarfs, the magnetic fraction for objects below 0.9 $M_\odot$ is larger at all ages than for those below 0.75 $M_\odot$, particularly at the oldest ages where we do not detect any magnetic white dwarfs below 0.75 $M_\odot$ and older than 6 Gyr.

2.5.4. Rotation Periods

The fact that magnetic white dwarfs typically have shorter rotation periods than non-magnetic objects is well known (Brinkworth et al., 2013; Kawaler, 2015; Hermes et al., 2017b; Kawka, 2020;

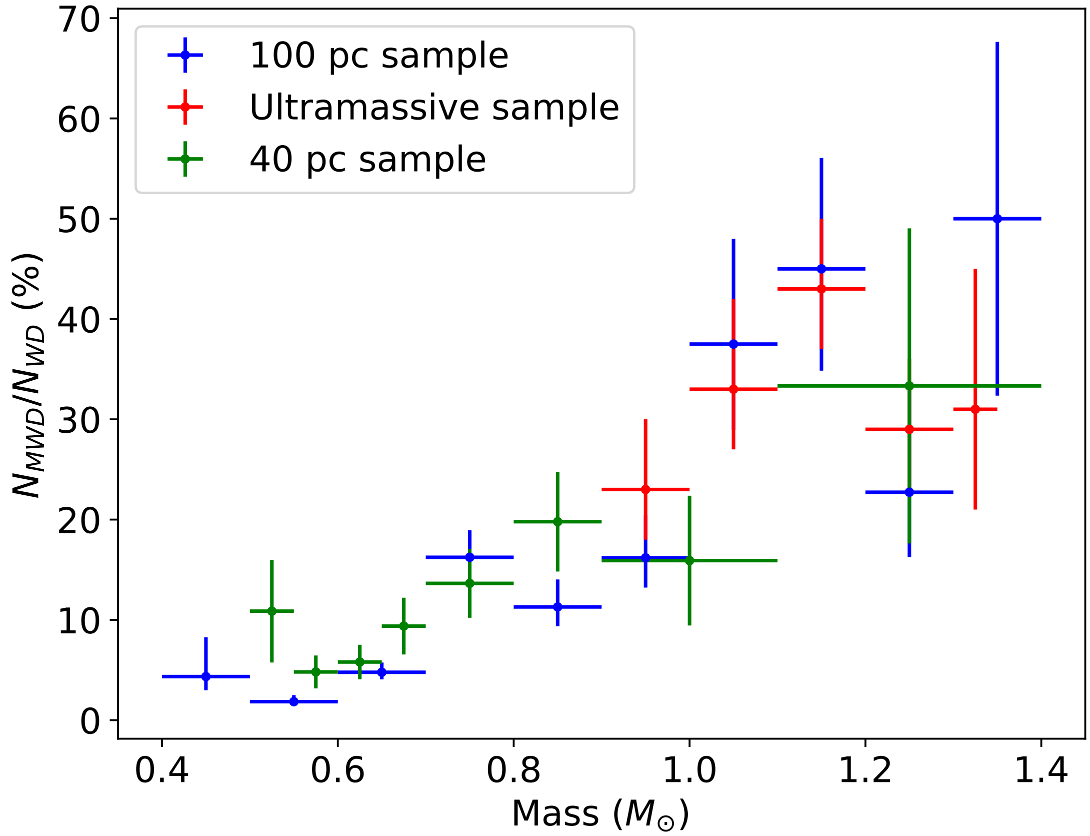

Figure 2.11: The fraction of magnetic white dwarfs as a function of mass. Each mass bin is 0.1 $M_\odot$ wide. The trend in magnetic fraction is similar across each sample.

Hernandez et al., 2024; Oliveira da Rosa et al., 2024). A merger remnant from two CO white dwarfs is predicted to rotate on the order of minutes (Schwab, 2021), while crystallization could induce a dynamo independent of the white dwarf's rotation rate during efficient convective mixing (Fuentes et al., 2024). Hence any known periods in our sample could lend insight into the mechanism that generates the magnetic fields.

We search for photometric variability in our sample using the Transiting Exoplanet Survey Satellite (TESS) and Zwicky Transient Facility (ZTF). For the TESS data, we check the 20 sec and 2 min cadence light curves available on the Mikulski Archive for Space Telescopes (MAST), as well as the Full Frame Images (FFI) for targets that do not have short cadence light curves available. We use TESSExtractor (Brasseur et al., 2019; Serna et al., 2021) to extract the light curves from the FFIs. We generate Lomb-Scargle periodograms to determine if there is a strong signal in each light curve, and we report the photometric rotation periods only if our results satisfy multiple criteria: the signal must be above the 1% False Alarm Probability; the signal occurs in multiple TESS sectors or

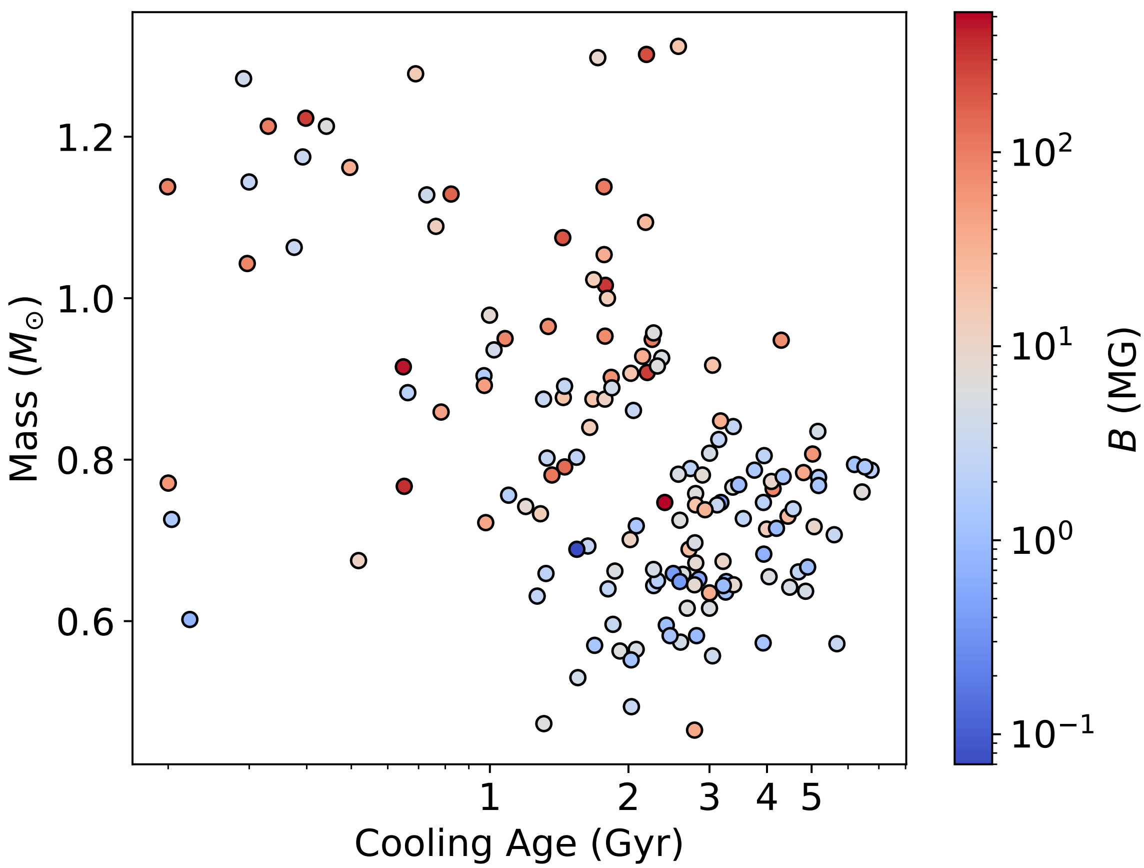

Figure 2.12: Mass as a function of cooling age colored by field strength. We see evidence of 2 distinct populations of magnetic white dwarfs, with lower mass objects possessing lower field strengths typically having longer cooling ages.

in ZTF; there is little aliasing or any potential aliasing can be explained as harmonics of the true signal; and the period for a given object must closely match values reported in the literature. We also report the rotation period if it has been previously obtained through a separate method such as spectropolarimetry or time-series spectroscopy.

Figure 2.14 shows an example TESS light curve and periodogram for a variable DAH, SDSS J015342.00+180857.9 (J0153+1808). There is a significant signal at 1.69 hours in 2 TESS sectors, and (Oliveira da Rosa et al., 2024) obtains the same period. While we do not detect a signal for this object in ZTF, there is little data available so this is not surprising. Hence we adopt the 1.69 hour value. Figure 2.15 shows the ZTF light curve and periodogram for SDSSJ185218.63+183355.4 (J1852+1833). This object shows significant variability both in ZTF and TESS but at different periods. The ZTF light curve favors a very short rotation period of 0.48 hours, while TESS shows

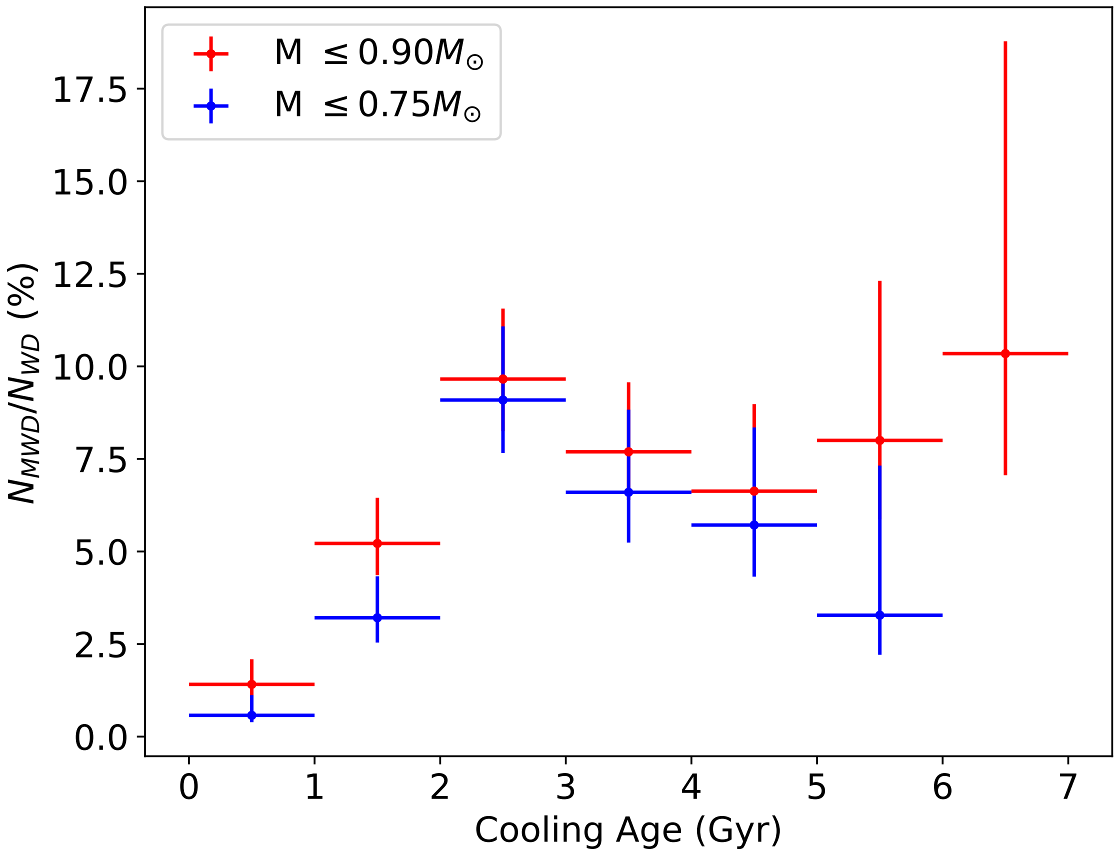

Figure 2.13: The fraction of magnetic white dwarfs as a function of cooling age. Each age bin is 1 Gyr wide. We see a clear increase in the magnetic fraction out to 2−3 Gyr, followed by a leveling off after 2−3 Gyr regardless of mass cutoff. Tighter constraints are needed for the oldest objects to verify the trend at older ages.

convincing evidence of a 6.7 hour period. This target lies in a particularly dense field with many nearby sources. Given the large pixel sizes in TESS that leads to source blending, we adopt the ZTF signal.

Of our 163 magnetic white dwarfs, we have confident rotation period measurements for 26 of them (16%). We report these values in Table 2.2. We do not detect significant variability in the objects with only TESS FFIs available. Many of our objects have been previously identified by Oliveira da Rosa et al. (2024) who conducted a wide TESS search of variable magnetic white dwarfs. Our fraction of photometrically variable targets is slightly lower than the 20% obtained for the 20 pc volume by Farihi et al. (2024). One object from the literature we exclude is SDSSJ125715.54+341439.4, which does not show significant variability in our TESS light curves, while Oliveira da Rosa et al. (2024) found a period of 0.092 hours. They only detected variability in

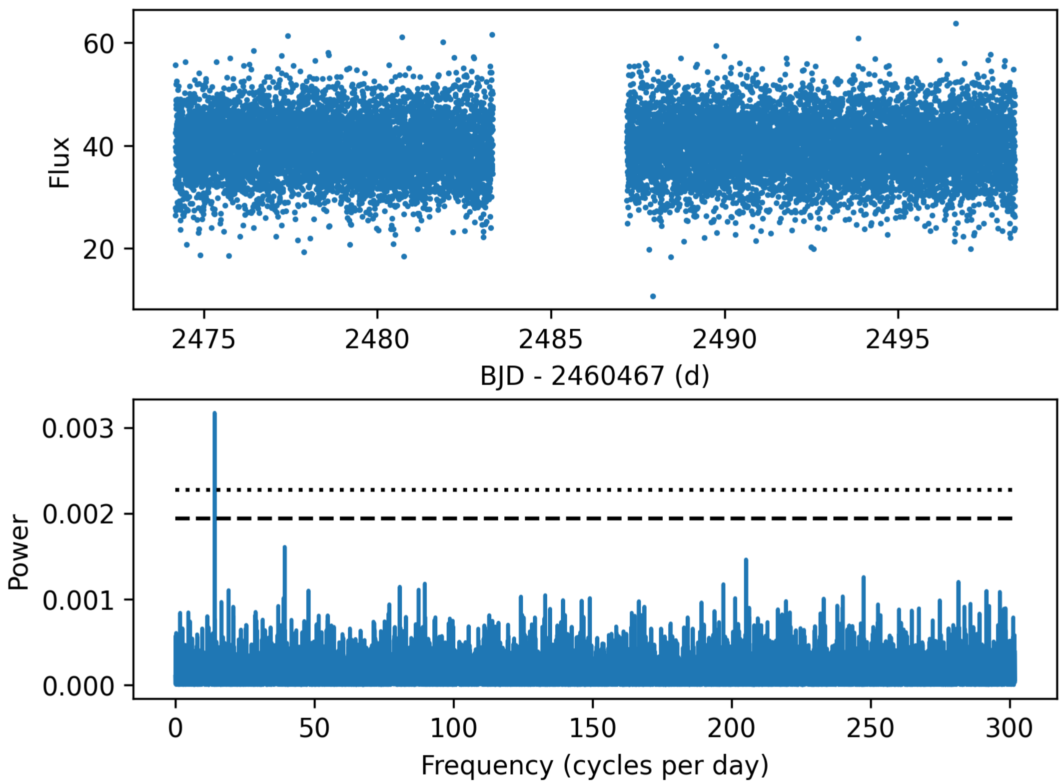

Figure 2.14: TESS light curve and Lomb-Scargle for J0153+1808. The dashed and dotted lines represent the 10% and 1% False-Alarm Probabilities. We detect a significant signal in two sectors at 1.69 hours, which matches the result from Oliveira da Rosa et al. (2024).

one sector for this target, so we do not include it here. We also exclude SDSSJ133250.73+011706.3, which has confirmed spectroscopic variations (Moss et al., 2023) but an unconstrained period. We do not detect photometric variability in this target, and there is no reported value in the literature.

The median period for our 26 objects is 0.69 hours. This result is notably shorter than the results found by Hernandez et al. (2024) and Oliveira da Rosa et al. (2024), who found median values of 6.2 and 3.5 hours respectively for their TESS samples. We do not detect strong trends in the period with either mass or field strength, similar to previous work (Brinkworth et al., 2013; Jewett et al., 2024; Hernandez et al., 2024; Oliveira da Rosa et al., 2024). However, we do see that the objects with known periods tend to have higher masses and lower cooling ages as shown in Figure 2.16. Of the 26 objects with known periods, only five are older than 2 Gyr. The median mass and field strength for our variable objects is $0.97 M_{\odot}$ and 15 MG respectively. Since these variable objects

Table 2.2. Known rotation periods in our sample.

Object	Period (hrs)	Source
J0006+3104	0.386	TESS, ZTF, Oliveira da Rosa et al. (2024)
J0050-0326	0.672	Jewett et al. (2024); Oliveira da Rosa et al. (2024)
J0150+2835	0.288	ZTF
J0153+1808	1.69	TESS, Oliveira da Rosa et al. (2024)
J0718+3731	0.188	TESS, ZTF, Oliveira da Rosa et al. (2024)
J0748+1125	0.192	ZTF
J0835+5332	2.16	Steen et al. (2024)
J0856+1611	5.70	TESS, ZTF, Hermes et al. (2017b); Oliveira da Rosa et al. (2024)
J1018+0111	1.65	TESS, ZTF, Hernandez et al. (2024)
J1029+1127	0.681	TESS, ZTF, Moss et al. (2023); Oliveira da Rosa et al. (2024)
J1039-0325	0.501	TESS, Oliveira da Rosa et al. (2024)
J1105+5225	1.92	ZTF
J1516+2803	0.576	Moss et al. (2023)
J1543+3021	1.31	TESS, ZTF, Oliveira da Rosa et al. (2024)
J1621+0432	0.672	Bagnulo & Landstreet (2024)
J1628+2332	5.3	TESS
J1630+2724	14.86	ZTF
J1659+4401	0.704	Jewett et al. (2024); Oliveira da Rosa et al. (2024)
J1707+3532	0.576	ZTF, Jewett et al. (2024)
J1852+1833	0.480	ZTF
J1956-0102	34.78	TESS, Valyavin et al. (2011)
J2211+1136	0.0192	Kilic et al. (2021)
J2223+2319	1.42	ZTF
J2257+0755	0.37	ZTF, Williams et al. (2022)
J2318+1236	428.54	Schmidt & Norsworthy (1991)
J2332+2658	2.77	Brinkworth et al. (2013)

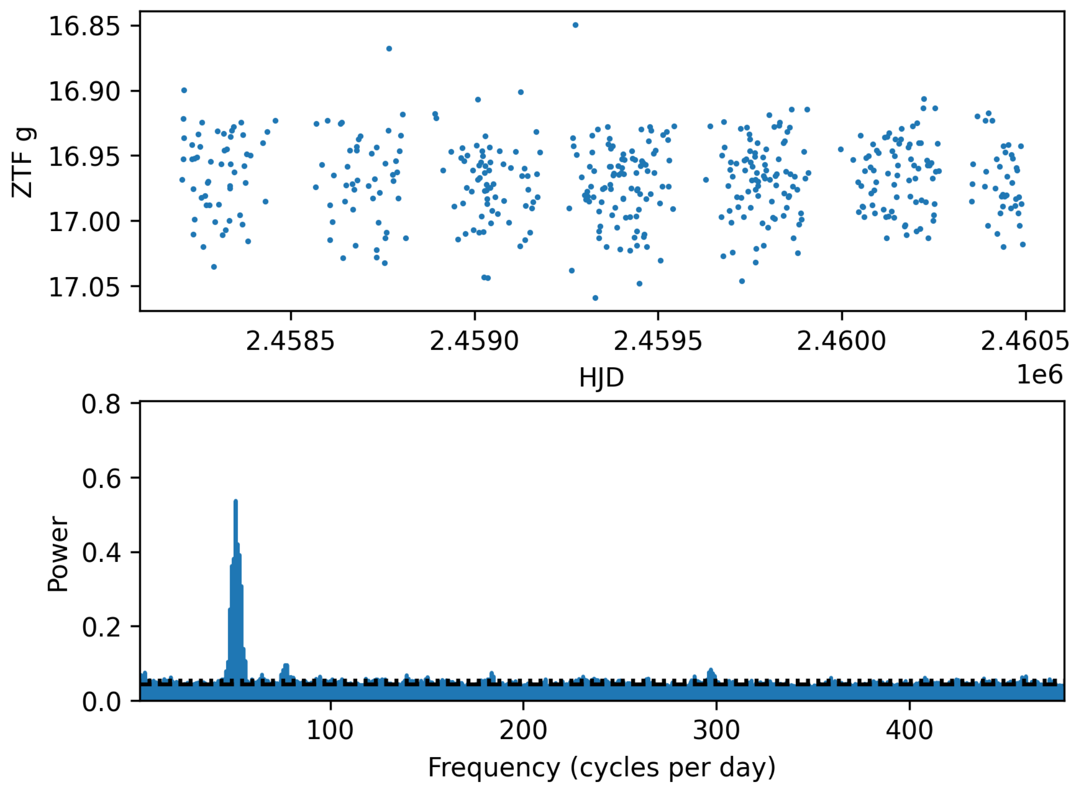

Figure 2.15: ZTF light curve and Lomb-Scargle for J1852+1833. There is a significant signal at 0.48 hours.

tend to have higher mass and field strengths than the entire sample, in addition to having short rotation periods, photometric variability tends to be more common among likely merger remnants.

Bagnulo & Landstreet (2024) found that 16 of 17 normal-mass magnetic white dwarfs older than 2 Gyrs and possess strong fields ($B \geq 10$ MG) are non-variable. However, they found that 4 of 8 magnetic white dwarfs in the same mass and age range but with intermediate field strengths ($1 < B < 10$ MG) are non-variable. Of our 89 targets that are older than 2 Gyr and have field measurements, only 23 have fields stronger than 10 MG, and 57 of our old targets have intermediate field strengths, of which a sizable fraction should have variable fields. Since we do not conduct spectropolarimetry, we are unable to determine rotation periods for many of these older objects.

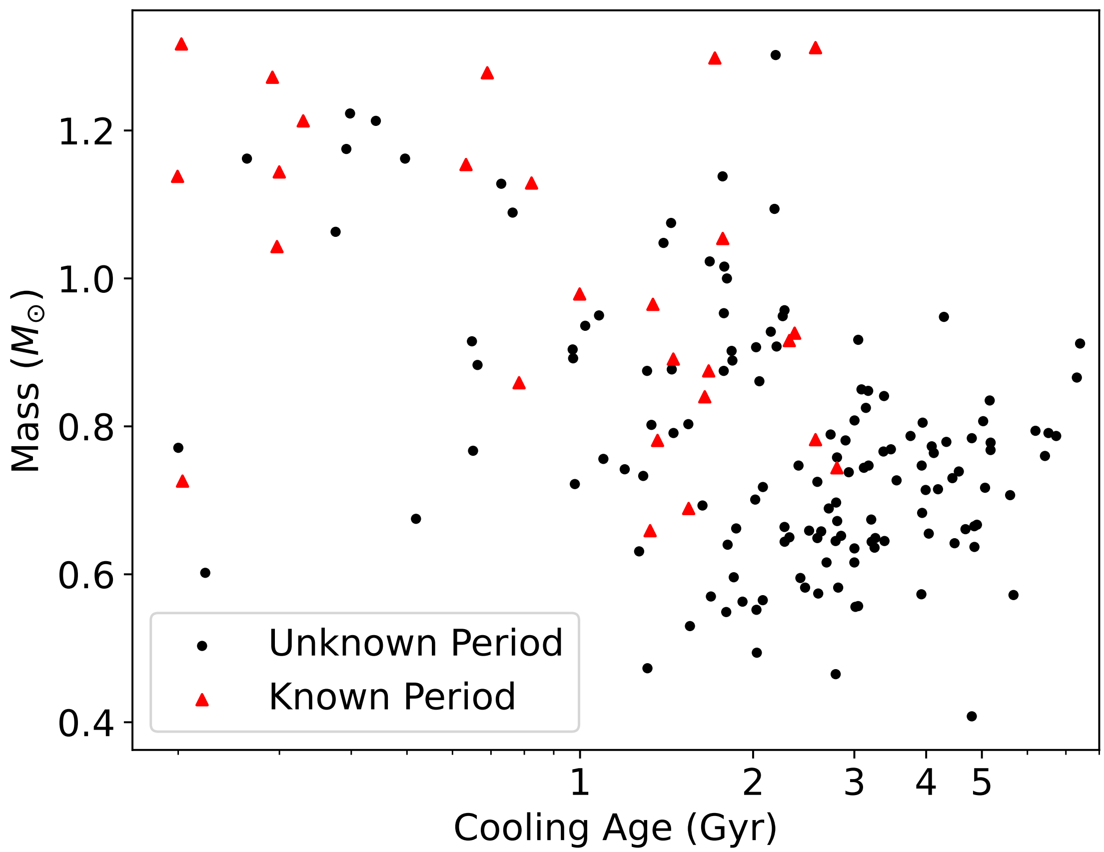

Figure 2.16: Mass-age distribution of our sample with the objects that have known rotation periods marked with red triangles. The majority of our objects with known periods are young and high mass.

2.5.5. Tangential Velocities

High tangential velocities ($v_{\rm tan} > 50$ km/s, Wegg & Phinney 2012) can be an indicator of a merger event if the white dwarf's cooling age is fairly young. Velocity dispersion increases with age (Nordström et al., 2004), but a merger event resets the cooling age, making the product appear younger than its actual age. However, using just the velocity to identify mergers is difficult given that not all likely merger products have high velocities. Wegg & Phinney (2012) found that the velocity dispersion of white dwarfs decreases with mass, and concluded that their high-mass ($M > 0.95 M_\odot$) targets came from single-star evolution given that none of these targets had high tangential velocities. But Cheng et al. (2020) found that ∼30% of their targets with masses $> 1 M_\odot$ come from mergers. Among the ultramassive white dwarfs in the 100 pc sample, Jewett et al. (2024) found that only five out of 66 magnetic white dwarfs had high velocities, despite classifying the remaining 61 as likely merger remnants.

To determine if our magnetic objects are kinematic outliers, we calculate the tangential velocities of our sample using the Gaia DR3 proper motions and parallaxes. Figure 2.17 shows the tangential velocities for the DAHs in our sample. The velocity dispersion increases with age as expected, with few targets possessing high velocities before 2 Gyr. Interestingly, our high mass targets have some of the lowest velocities in the sample despite being likely merger remnants based on their masses and field strengths. Of the 26 objects with known rotation periods, 23 have periods shorter than 6 hrs. Of these 23 fast-spinning objects, 15 have masses $> 0.9 M_\odot$. These 15 objects are thus likely merger remnants. For these 15 objects, only four have tangential velocities > 50 km/s. Hence not all merger remnants can be identified based on their kinematics alone.

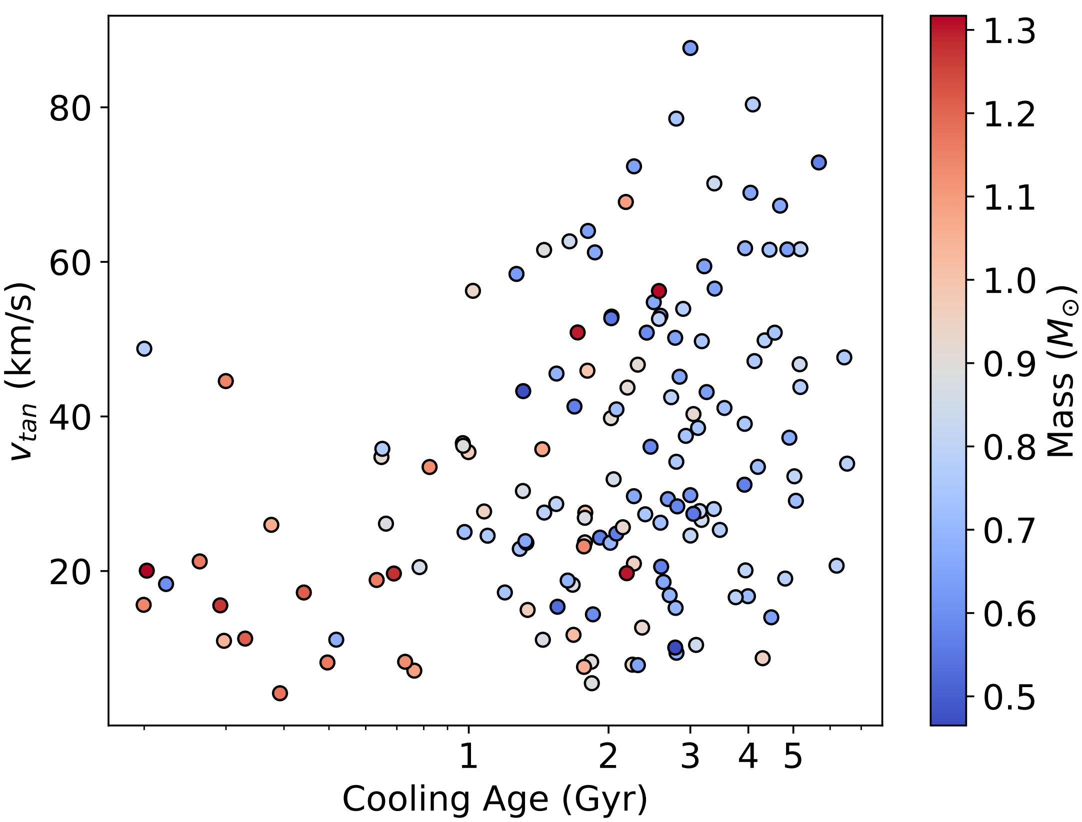

Figure 2.17: Tangential velocity distribution for the DAHs in our sample. The high-mass magnetic white dwarfs in our sample have velocities almost exclusively below 50 km/s, while more average mass and older magnetic white dwarfs show a large dispersion in their velocities.

2.6. Evidence of Two Populations

2.6.1. Kolmogorov-Smirnov Tests

The primary goal of this study is to test the two population hypothesis initially proposed by Valyavin & Fabrika (1999) and confirmed by Bagnulo & Landstreet (2022) with a large, volume-limited survey. In Figure 2.12, we can already see evidence of these two populations: young objects tend to be more massive and have stronger fields, while older objects are less massive and have weaker fields. These populations have distinct masses and field strengths, which indicate two separate formation channels that lead to different magnetic white dwarfs. To investigate these channels, we split the magnetic objects into two groups based on cooling age: those that are older and younger than 2 Gyr.

While the exact age cutoff we choose is somewhat flexible as we will show, the important distinction is that one group is comprised of relatively young magnetic white dwarfs, while the other group contains older objects. Bagnulo & Landstreet (2022) found that magnetic white dwarfs older than 2 Gyr have similar masses to those of non-magnetic white dwarfs, and that the lower mass white dwarfs do not show evidence of magnetism until roughly 2 Gyr in cooling age. In addition, Bagnulo & Landstreet (2024) found that magnetic white dwarfs across all masses and older than 2 Gyr with high field strengths ($B \geq 10$ MG) show little polarimetric variability, which could be an indicator of their field origin. Hence we conclude that a 2 Gyr age cutoff is sufficient to study the possible separate formation channels in these magnetic white dwarfs.

We first perform nonparametric two-sample Kolmogorov-Smirnov (K-S) tests (Kolmogorov, 1933; Smirnov, 1939) on the field strengths and masses of these two age groups. These tests are utilized to determine if two samples, in our case objects younger and older than 2 Gyr, belong to the same underlying distribution. The statistical significance we provide here is in the form of a two-tailed p-value, and we compare it to a significance level of $\alpha = 0.05$ to show evidence against our null hypothesis, which is that any magnetic white dwarfs younger or older than 2 Gyr belong to the same population. Figure 2.18 shows the cumulative distribution of the field strengths for each age group. We see a clear difference in the field strengths based on cooling age, with younger objects clearly possessing stronger fields than older objects. Performing a two-sample K-S test on these separate field strength groups yields a p-value of 0.01. Hence we reject the null hypothesis that the field strengths in our two samples originate from the same parent distribution.

The discrepancy in field strength between ages could at least partly be explained by the biases in our sample. Average mass magnetic white dwarfs are expected to have weak fields at young ages which then grow over time (Bagnulo & Landstreet, 2022). In general, we are not sensitive to magnetic fields below $\sim$1 MG, so many of the hot, average-mass white dwarfs we classify as non-magnetic could simply have weak fields. Additionally, as these white dwarfs cool off sufficiently,

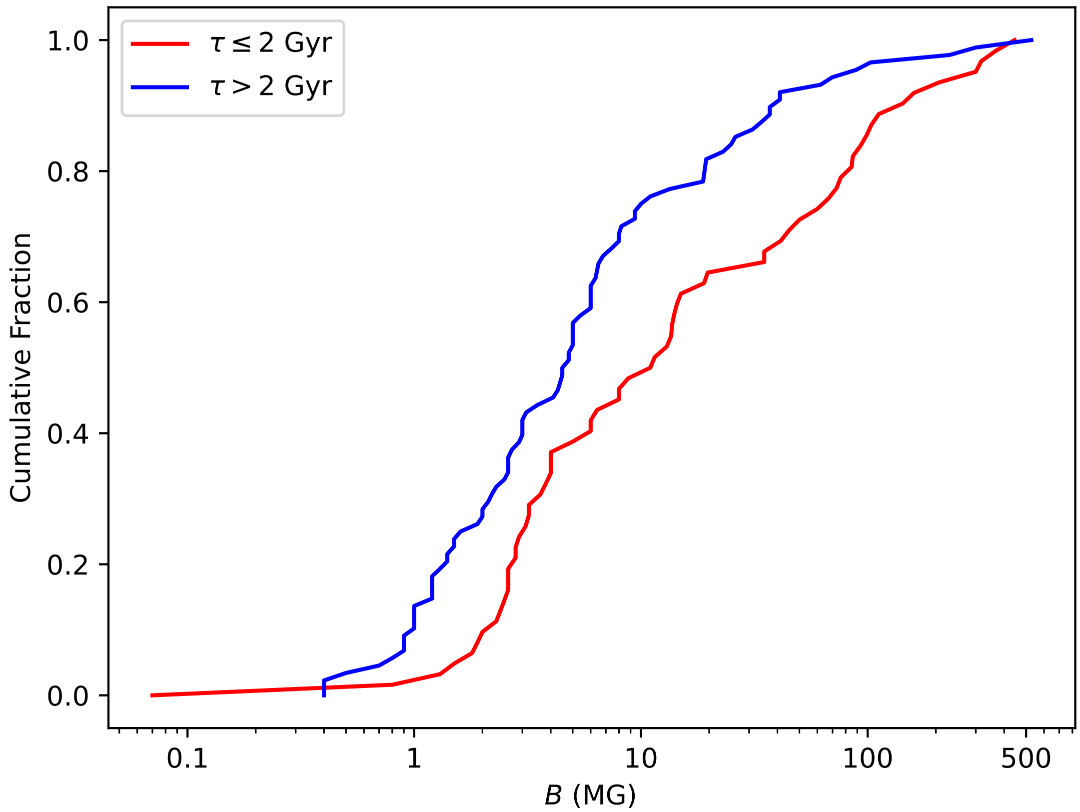

Figure 2.18: Cumulative distribution of magnetic field strengths for the old ($\tau > 2$ Gyr, blue line) population and young ($\tau \leq 2$ Gyr, red line) population. There is a clear separation between the two distributions, with younger objects possessing stronger fields than older objects.

their spectral lines vanish so we would be unable to detect the potential strong fields at old ages. Hence the $\tau \leq 2$ Gyr distribution could be missing weak fields, while the $\tau > 2$ Gyr distribution could be missing strong fields. We discuss these biases in detail in Section 2.7.1.

Mergers are expected to produce some of the strongest fields among magnetic white dwarfs, and these fields should instantly appear at the surface (García-Berro et al., 2012). Naturally, a group of white dwarfs that originate from mergers should also be more massive than those that come from single-star evolution (Temmink et al., 2020). Figure 2.19 shows the cumulative distributions for the masses using our 2 Gyr age cutoff for both the magnetic and non-magnetic objects in the 100 pc sample. The young magnetic targets are notably more massive than the older targets, while the distributions of the non-magnetic targets seem to show the opposite. Performing the K-S tests for the masses of the magnetic and non-magnetic objects yields p-values of 2.3×10^{-8} and 7.7×10^{-18} respectively, so we again reject the null hypothesis. For both field strength and mass separated by younger and older magnetic white dwarfs, the two-sample K-S test has provided evidence with 95% certainty that these two groups are observationally distinct groups of magnetic white dwarfs.

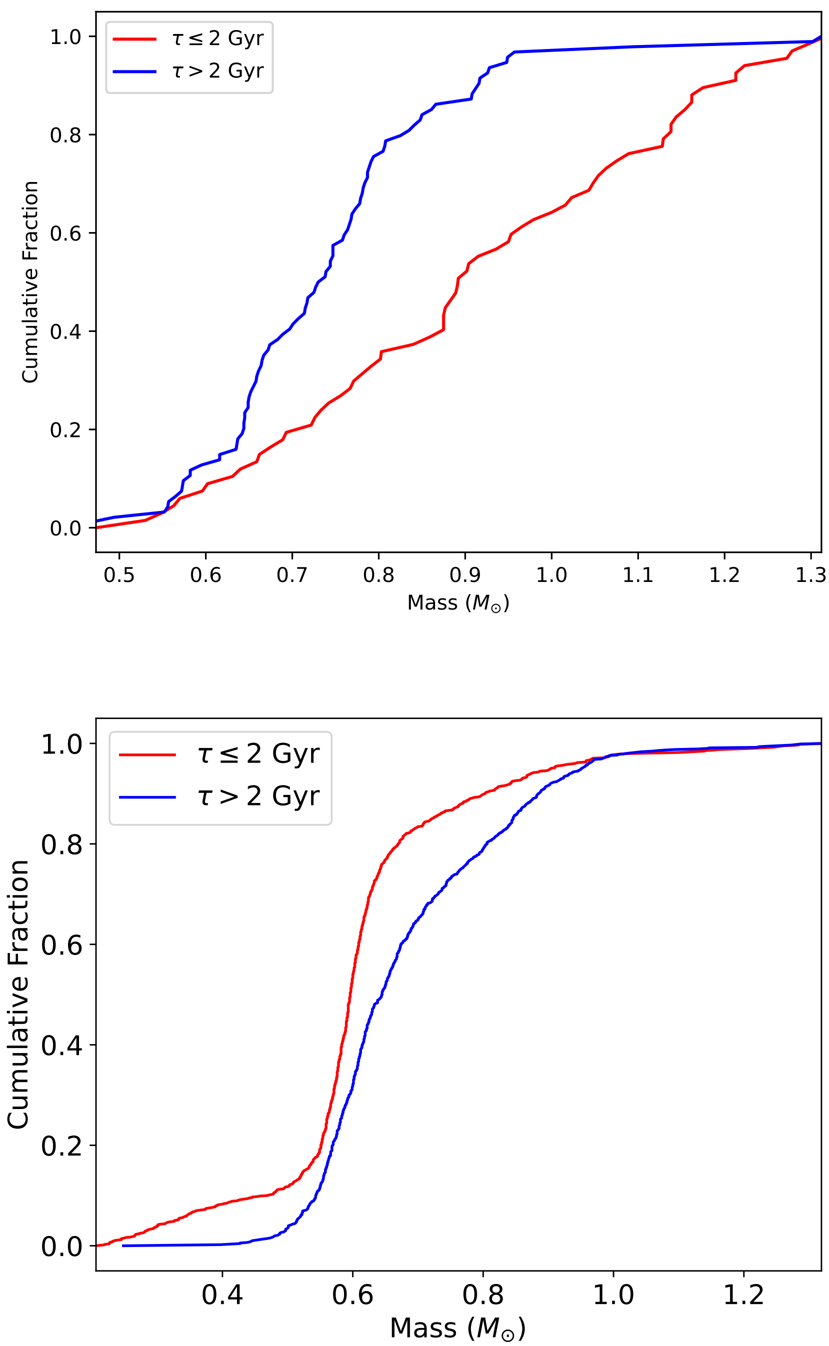

Figure 2.19: Cumulative distribution of stellar masses separated by cooling age for the magnetic white dwarfs (top panel) and the non-magnetic DA white dwarfs (bottom panel). Older magnetic white dwarfs tend to have lower masses than younger magnetic white dwarfs, while the non-magnetic DAs show the opposite trend.

While we choose a 2 Gyr age cutoff in these tests, we can achieve similar statistical significance for a small range of cooling ages. We perform multiple K-S tests with age cutoffs every 0.5 Gyr ranging from 0.5 to 4.0 Gyr. While the difference in mass among the magnetic white dwarfs is statistically significant regardless of what age we choose, we only obtain p-values less than 0.05 between 1.0 and 3.5 Gyr for the field strengths, with our lowest p-value occurring at 2.5 Gyr.

2.6.2. A Gaussian Mixture Model Approach

To further confirm the existence of two distinct populations in our sample, we use a Gaussian mixture model (GMM) with 2 components to group objects together based on similar parameters (Day, 1969; McLachlan & Peel, 2000). A GMM is an algorithm that calculates the parameters to a set of multivariate Gaussian distributions, such that the likelihood of data being described by those distributions is maximized. In this case, this data is the set of magnetic field strengths, cooling ages, and masses observed, and we want to show that this data can be described by two Gaussian distributions in a 3-dimensional space. In this way, we are looking to find evidence of these two populations being more distinct in higher-dimensional space. We make this calculation using `scikit-learn`'s `GaussianMixture` model (Pedregosa et al., 2011), which provides the optimal values of means and covariance matrices for the two Gaussian distributions that describe our groups. This method is advantageous for our sample as there is clear overlap between the two visually proposed groups, which necessitates the use of a clustering method based on probability as opposed to direct assignment (e.g. k-means clustering). With GMMs, a probability of each object belonging to either group can be determined, and therefore group assignment can be decided based on the group with a higher probability.

Figure 2.20 shows the calculated clusters and a visual representation of 1-, 2-, and 3σ intervals projected onto the axes of the figure given by the covariance matrix of the GMM (see Burrow et al., 2020, for more details) The algorithm detects two groups at low and high mass (and correspondingly, old/young age) with little overlap at the 1σ level. The center of each cluster occurs at 2.9 Gyr, 0.71 $M_\odot$, 3.7 MG and 1.8 Gyr, 0.96 $M_\odot$, 84 MG respectively. This result combined with the K-S tests provide clear and strong evidence that there exists two formation channels that lead to magnetic dynamos at different evolution stages and field strengths based on our sample. It is important to note that these clusters represent only the magnetic white dwarfs in our 100 pc sample, and not necessarily the true distribution of magnetic white dwarfs. The GMM cannot account for the young, average mass, weak field objects nor the old, average mass, strong field objects that we are likely missing.

Figure 2.21 shows the same mass-cooling age plot but with the points marked by which cluster the GMM assigns each point to. For example, there are 3 points at $\sim$0.8 $M_\odot$ and $\sim$5 Gyr, but they have field strengths larger than 10 MG, so the algorithm classifies them as belonging to the young

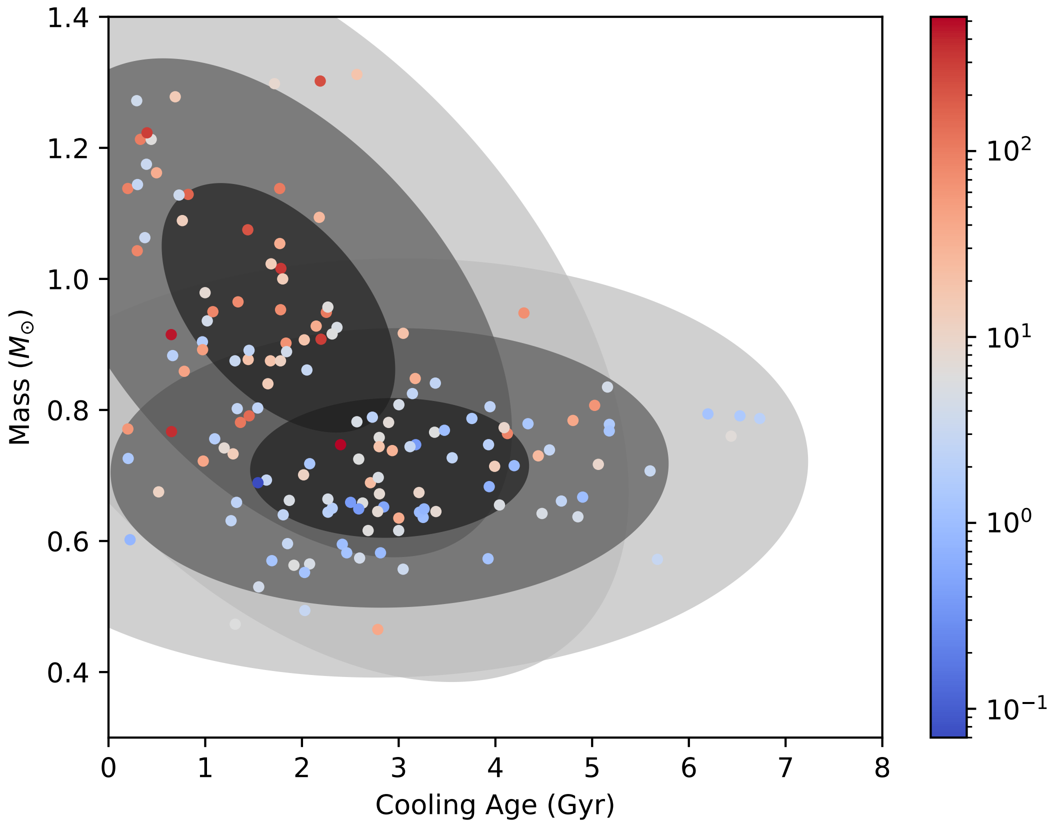

Figure 2.20: Similar to Figure 2.12 but including the clusters from our GMM analysis. The shaded regions represent the 1, 2, and 3σ intervals from dark to light gray respectively.

population. These "outlier" targets could realistically belong to either group, so confirming the formation channel in these is naturally difficult. However, looking at the sample holistically, the measurements suggest that two formation channels lead to two distinct groups of magnetic white dwarfs.

2.7. Discussion

We provide further evidence of the existence of two distinct magnetic white dwarf populations created by two distinct formation mechanisms. These populations were initially proposed by Valyavin & Fabrika (1999) based on $T_{\rm eff}$ and mass estimates for 49 and 35 magnetic white dwarfs respectively. They found that the incidence of magnetism is approximately seven times higher in white dwarfs with mass $> 1.1\ M_\odot$ than in white dwarfs below this mass. Additionally, 70% of these ultramassive white dwarfs have field strengths > 100 MG, while none of the magnetic white dwarfs below this mass possess such high field strengths. Hence Valyavin & Fabrika (1999) predicted that

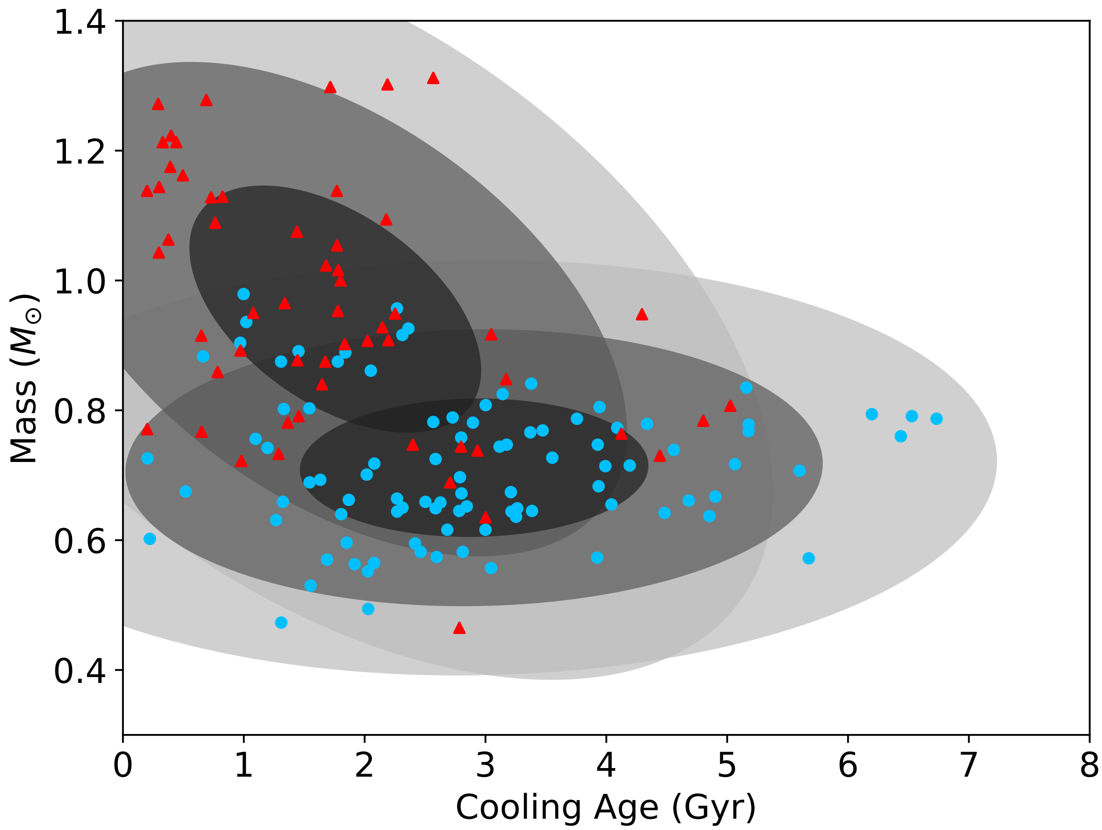

Figure 2.21: Mass as a function of cooling age with each point marked by which cluster the GMM method assigns them to. Red points are assigned to the young, high mass, strong field cluster while blue points are assigned to the old, low mass, weak field cluster.

these ultramassive highly magnetic white dwarfs come from binary evolution.

Bagnulo & Landstreet (2022) confirmed these populations based on the analysis of all white dwarfs within the 20 pc volume (see Bagnulo & Landstreet 2021) and white dwarfs younger than 0.6 Gyr within 40 pc. The authors made several key findings, including a clear increase over time in the magnetic fraction of white dwarfs with mass $< 0.75\ M_\odot$. Additionally, among the white dwarfs younger than 0.6 Gyr, ∼85% with masses $> 1.1\ M_\odot$ are magnetic compared to $\lesssim 2.5\%$ for masses $< 0.75\ M_\odot$. Their mass distribution also provides important insights: the average mass of their young magnetic white dwarfs is 0.98 $M_\odot$ compared to 0.65 $M_\odot$ for objects older than 2 Gyr. The high-mass magnetic white dwarfs have high field strengths on the order of MG while comparable fields do not appear in in the lower mass magnetic white dwarfs until after 2 Gyr of cooling. Hence there are two populations of magnetic white dwarfs that arise from different formation mechanisms. We now discuss these two populations with respect to our 100 pc sample.

2.7.1. Biases in our Sample

The low-resolution spectra from SDSS leads to difficulties in detecting magnetic objects with field strengths weaker than ∼1 MG (Kepler et al., 2013), as well as in older white dwarfs that lose their spectral features as reach cool effective temperatures ($T_{\rm eff}$ $\lesssim$11,000 K for He-dominated atmospheres, $\lesssim$5,000 K for H-dominated). We can analyze these biases and their effects on our sample with regards to the two magnetic populations put forth by (Valyavin & Fabrika, 1999) and (Bagnulo & Landstreet, 2022). The young, massive, strong magnetic white dwarfs should not be significantly affected by these biases. Even though strong field strengths can wipe out absorption features ($B \gtrsim 100$ MG), these objects are almost exclusively at hotter temperatures, such that we can infer the presence of a strong magnetic if no absorption lines are detected. Polarimetric measurements would certainly aid in further constraining the field strength, but otherwise are not needed to detect a field for these targets.

The group of average mass, older, weakly magnetic objects is a different story. Bagnulo & Landstreet (2022) found that there is an evolutionary trend in the average mass magnetic white dwarf population. At young ages, magnetism is rare and the fields that are present are fairly weak. For white dwarfs younger than 0.6 Gyr, less massive than 0.75 $M_{\odot}$ and within 40 pc, $\lesssim 2.5\%$ of them are magnetic. In addition, the few magnetic white dwarfs within this age and mass range have field strengths less than 1 MG. Hence while these young, average mass magnetic white dwarfs are quite rare, we would likely not detect them given our bias against such weak fields. At older ages, both the frequency of magnetic white dwarfs and strength of their fields increase. The first average mass magnetic white dwarf with a MG field does not appear until approximately 2 Gyr, but 11 of 64 magnetic white dwarfs older than 3 Gyr and $M \leq 0.75\ M_{\odot}$ have field strengths comparable to the young, high mass population. While we do detect magnetic white dwarfs beyond 3 Gyr, it certainly does become more challenging. Thus it is almost guaranteed that we are underestimating the number of average mass magnetic white dwarfs both at very young ages where the fields are too weak to detect and at older ages where spectral lines vanish.

To better understand what field strengths we are not sensitive to, we plot synthetic spectra convolved with a $4\mathring{A}$ width Gaussian profile. We set the $\log g = 8.15$ and implement a typical geometry with $i = 45°$ and $a_z = -0.1$. We vary the field strength, checking low field strengths at high temperature and high field strengths at low temperatures. Figure 2.22 shows our synthetic spectra at various $T_{\rm eff}$ and B_d. At $T_{\rm eff} = 10,000$ K, it is very unlikely that we could detect field strengths below ∼0.5 MG. But around 0.5 MG, the line core begins to flatten, even though the individual σ components would not be resolved (see for example the spectrum and fit for J1139+2613). At $T_{\rm eff} = 8,000$ K, we can reliably detect field strengths up to ∼100 MG, as the Hα feature has not completely vanished assuming our geometry. At $T_{\rm eff} = 6,000$ K, both the π and σ

become very weak above 40 MG. Below this threshold, it is possible we can still detect fields based on the shape of the central line, however the absence of the split components would likely lead to a degeneracy between a weak and strong field strength.

Of the 3146 total objects in the SDSS 100 pc sample, 397 of them have masses of $M \leq 0.75\ M_{\odot}$ and are younger than 0.6 Gyr. If we assume an optimistic magnetic fraction of 2.5% from Bagnulo & Landstreet (2022), we would expect $\sim$10 magnetic white dwarfs in this mass and age range. It is perhaps worth noting that of the three magnetic white dwarfs in Bagnulo & Landstreet (2022) that are in this age and mass range, two are DAH+dM systems and one is a "DAH?". We would expect these 10 potentially missing targets in our sample to have weak fields on the order of tens of kG. We can test if the inclusion of these objects would affect our K-S analysis by simply adding these 10 additional magnetic white dwarfs to the list of magnetic white dwarfs that are younger than 2 Gyr. For simplicity, we assume these 10 objects have field strengths of 50 kG. Running the K-S test on the field strengths with these simulated young, average mass, weak field objects yields a p-value of 0.079. Hence we would not be able to reject the null hypothesis that the magnetic white dwarfs younger and older than 2 Gyr come from the same distribution. If we included additional high field objects at old ages that we are likely missing, the p-value would further increase in this test, as the old age group is currently dominated by low-field objects. If we make the age cutoff at 2.5 Gyr where our initial p-value was the lowest, we now obtain a p-value of 0.037 with the simulated missing objects. However the age cutoff itself is not physical, rather it is simply used in an attempt to distinguish between the magnetic white dwarfs that come from separate formation channels.

2.7.2. The Young, Massive, Strong-Field White Dwarfs

The GMM implies there is a population of young, high field, massive magnetic white dwarfs but provides no physical constraint on their origin. It is unlikely that every single object in this population is a merger remnant, but rather mergers are the dominant formation channel for this population. Hence high mass single-star evolution could in principle produce some of these objects (Richer et al., 2019; Caiazzo et al., 2020).

Camisassa et al. (2024) showed that a main-sequence dynamo could generate a field that would reach the surface of the white dwarf within $\sim$1 Gyr of cooling in ultramassive white dwarfs. However there is currently no clear picture from an observational standpoint as to why the fields in these higher mass white dwarfs are clearly stronger than those in more average mass white dwarfs. Wickramasinghe & Ferrario (2005) calculated mass distributions and space densities using different assumptions about the IFMR, and found that there are too few strongly-magnetic Ap and Bp main-sequence stars to explain the number of high-field magnetic white dwarfs ($B > 1$ MG). Instead, they propose that if 40% of main-sequence stars that are more massive than $\sim$4.5$M_{\odot}$ become high-field magnetic white dwarfs, this could reproduce the mass distribution and fraction of

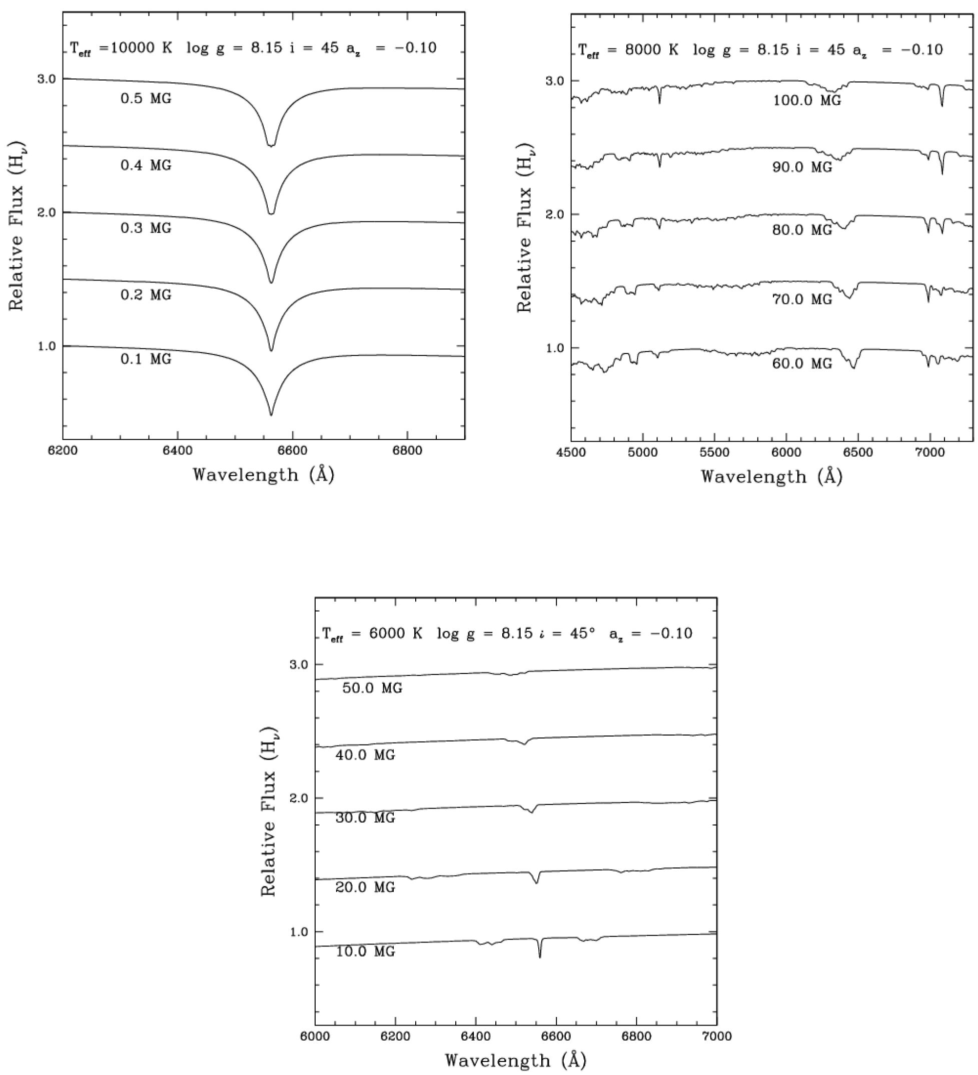

Figure 2.22: Synthetic spectra for a 0.75 $M_{\odot}$ white dwarf and fixed magnetic field geometry. The left, middle, and right panels show $T_{\rm eff} = 10,000, 8,000, 6,000$ K respectively. Each spectrum is labeled with its field strength, with weaker fields at the bottom of each panel.

high-field magnetic white dwarfs. However, this would require that these stars have field strengths from 10−100 G. Bagnulo et al. (2006) conducted a spectropolarimetric survey on 235 A and B stars, of which 97 are Ap and Bp stars. For the remaining 138 normal stars, none had detectable magnetic fields, though the median error in these measurements was 136 G. Shorlin et al. (2002) similarly conducted a spectropolarimetric survey and found no field detection in any of their 22 normal B, A, and F stars. Fossati et al. (2015) searched for fields in 50 O and B stars and only detected fields in 3 of them. Hence there does not appear to be a sufficient amount of magnetic stars that could explain the majority of our high mass, high field population, at least based on detectable surface fields in stars. Additionally, there would need to be an explanation as to why many ultramassive white dwarfs are not magnetic. Only ∼32% of the ultramassive sample from Jewett et al. (2024) is magnetic, so some factor would need to generate a dynamo in certain high mass main-sequence stars but not in others.

Theoretical modeling however does show some evidence of a relation between the mass of the star and the field strength buried within the stellar core. Brun et al. (2005) conducted magnetohydrodynamic simulations on the inner 30% of a $2M_\odot$ main-sequence star, and found that strong convection is able to generate a field on the order of ∼60 kG. Similarly, Hidalgo et al. (2024) performed simulations on the inner 20% of a $2.2M_\odot$ and also obtained field strengths of ∼60 kG. Augustson et al. (2016) meanwhile obtained field strengths exceeding 1 MG based on simulations of the inner 23% of a $10M_\odot$ star. Future modeling on a wide range of stellar masses as well as core rotation rates will be valuable for establishing a strong connection between the field generated in the core and the final white dwarf field.

Since we cannot measure the rotation periods in many of these objects, the tangential velocities could potentially identify merger products. However as we show in Figure 2.17, very few of the young, high mass objects have large tangential velocities. This is similar to the findings of Jewett et al. (2024), who detected large velocities in only five of their magnetic objects, and only 15% of the total sample. Hence it does not appear that tangential velocities by themselves can isolate merger products, particularly in samples dominated by white dwarfs in the thin disk such as the 100 pc sample.

Bagnulo & Landstreet (2024) found that young, massive magnetic white dwarfs show no preference toward symmetric or non-symmetric fields about their rotation axes. This could be due to a number of variables, such as contributions from dynamos generated through mergers and single-star evolution, the initial geometry of the individual white dwarfs during a merger, and the inability to measure extremely fast rotation periods with long spectropolarimetric cadences. They also found a clear lack of variability among the old, average mass targets with fields stronger than 10 MG. We have rotation period estimates for 12 of 27 (44%) objects in our sample that are more massive than $1M_\odot$, but only 13 of 135 (9.6%) for everything below this mass. 82 of our 116 magnetic white dwarfs that do not have confirmed periods are less massive than $1M_\odot$ and have fields weaker than 10 MG. So at least through photometry, either the high mass white dwarfs tend to be more variable than lower mass objects, or the lower mass white dwarfs have longer periods that are simply harder to detect.

2.7.3. The Old, Average Mass, Weak-Field White Dwarfs

Our second population of magnetic white dwarfs is more interesting as the exact dynamo origin is unclear beyond the fact that these objects likely come from single-star evolution. The first question to answer is if the crystallization process can generate a magnetic field. Multiple theoretical studies have been conducted to address this, primarily by investigating the ability of convection during C/O phase separation to generate velocities capable of generating a dynamo. Montgomery & Dunlap (2024) found that the resulting velocities are lower than those found by Isern et al. (2017) and Ginzburg et al. (2022), and thus could not form a dynamo. This could be resolved by fast rotation rates (Schreiber et al., 2021), however Bagnulo & Landstreet (2024) found that these average-mass crystallized magnetic white dwarfs typically do not show variable fields, which makes it difficult (if not impossible) to determine the rotation periods of these objects. Other studies have shown that a dynamo could be generated but only at the onset of crystallization when efficient convection is present and before thermohaline convection becomes dominant (Castro-Tapia et al., 2024; Fuentes et al., 2023, 2024).

As shown in Figure 2.8, while many of our magnetic targets have begun core-crystallization, a non-negligible fraction has not. Of our 163 magnetic white dwarfs, the models suggest that about 47 (or 29%) have not begun crystallization, 40 of which are less massive than $1M_\odot$. Hence even if crystallization can spin up a dynamo, this mechanism alone cannot explain the source of magnetism in all of our lower mass objects. We assume an equal fraction of C and O in the core, which impacts the T_{eff} that white dwarfs begin crystallizing. Assuming a higher O abundance leads to earlier crystallization times due to a larger coupling constant and average ion charge. However O'Brien et al. (2024) found that several magnetic white dwarfs in the 40 pc sample have not begun crystallizing despite using an O fraction of 0.8. Similarly, Hernandez et al. (2024) found multiple magnetic white dwarfs with long rotation periods and typical masses that had not begun crystallizing. Hence it is unlikely that changing the oxygen abundance will allow a crystallization dynamo to explain all of our low mass magnetic white dwarfs, even if a crystallization-driven dynamo is plausible.

A second issue arises with regards to when the magnetic field from a crystallization dynamo reaches the surface. The diffusion of the dynamo from the convective boundary to the surface is expected to take several Gyr (Isern et al., 2017; Ginzburg et al., 2022). Blatman & Ginzburg (2024) calculated this diffusion time as a function of mass and compared this result to the cooling ages of magnetic white dwarfs within the volume-limited sample from Bagnulo & Landstreet (2022). While several magnetic white dwarfs that have fields strengths > 1 MG first appear after the breakout time, many magnetic white dwarfs still appear before the breakout should happen. They also assumed that the field starts to diffuse right at the crystallization onset from a convective boundary close to the surface. Castro-Tapia et al. (2024) on the other hand found that the convective boundary is located deeper within the white dwarf, leading to significantly longer breakout times. Hence the calculation from Blatman & Ginzburg (2024) is actually a "best-case" scenario. So it seems that when accounting for the breakout time, crystallization by itself is insufficient.

On the other hand, core-convective fields that are trapped within main-sequence stars should reach the surface faster than a crystallization-driven dynamo by several Gyr depending on the mass (Camisassa et al., 2024). While uncertainties in the input physics results in large uncertainties in the emergence time, this provides a promising alternative to the crystallization dynamo which appears to fail for at least some of the low mass magnetic white dwarfs. Camisassa et al. (2024) compared their predicted emergence timescales to the volume-limited sample of magnetic white dwarfs (Bagnulo & Landstreet, 2022) and found that a significantly higher fraction could be explained by this core-convective dynamo rather than the crystallization dynamo.

In Figure 2.23 we plot the mass-age distribution with points colored by field strength, along with the emergence times expected from a crystallization and core-convective dynamo found by Blatman & Ginzburg (2024) and Camisassa et al. (2024) respectively. It is clear from these plots that the core-convective dynamo can explain at least some of the magnetic white dwarfs that crystallization cannot. Only 21 of our 101 magnetic white dwarfs with field estimates and that are less than $0.85 M_{\odot}$ lie to the right of the crystallization dynamo breakout line, while an additional 22 lie to the right of the core-convective dynamo emergence line. Many of the objects below $\sim 0.7 M_{\odot}$ and younger than $\sim$4 Gyr could also be explained by the core-convective dynamo given the uncertainties found by Camisassa et al. (2024). This mechanism could also explain some of the high mass magnetic white dwarfs if they in fact do not come from mergers.

2.8. Conclusion

We have performed a model atmosphere analysis on the magnetic white dwarfs in the SDSS 100 pc sample (Kilic et al., 2025). Our sample contains 163 magnetic white dwarfs, 87 of which are new discoveries. We have magnetic field estimates either from our model fits or from the literature for 152 of the 163 magnetic white dwarfs. This analysis is thus the largest volume-limited survey of magnetic white dwarfs to date. To explore the two formation channel hypothesis in our sample, we split our sample into two groups based on cooling age: one that contains targets younger than 2 Gyr, and one for targets older than 2 Gyrs. We find statistically significant evidence of two separate populations of magnetic white dwarfs through the use of K-S tests and a GMM. Our K-S tests

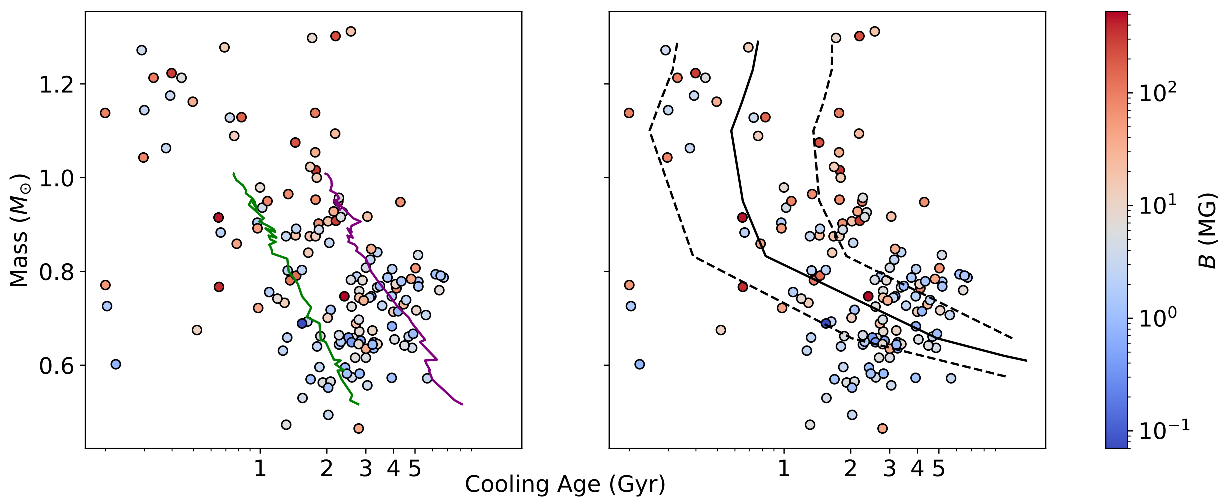

Figure 2.23: Mass as a function of a cooling age with points colored by field strength. The left panel shows the onset of crystallization (green line) and the breakout time for a crystallization-induced dynamo (purple line) as calculated by (Blatman & Ginzburg, 2024). The right panel shows the emergence of a core-convection generated dynamo produced on the main sequence (black solid line) as calculated by Camisassa et al. (2024). The dashed lines represent an error of ± 0.3 dex. The majority of our low-mass objects are not old enough for a hypothetical crystallization dynamo to have reached the surface. The main sequence dynamo on the other hand almost splits the low-mass population down the middle, with many objects within the errors. Hence it can potentially explain the occurrence of magnetism for more of our low-mass targets.

provide low p-values (< 0.05) when comparing the field strengths of each age group provided we use an age cutoff between 1.0 and 3.5 Gyr. Our GMM analysis finds two populations centered at 2.9 Gyr, 0.71 $M_{\odot}$, 3.7 MG and 1.8 Gyr, 0.96 $M_{\odot}$, 84 MG respectively.

These populations show clear differences in their physical properties because they are dominated by magnetic white dwarfs that come from two distinct formation channels. The young, high mass, high field strength population is dominated by merger remnants, while the old, average mass, weak field strength population is dominated by targets formed through single-star evolution. Although there is little overlap at the 1σ level in the populations based on our GMM analysis, we cannot completely rule out single-star evolution products in our high mass population or binary evolution products in the low mass population. The presence of two populations was proposed by Valyavin & Fabrika (1999) and confirmed by Bagnulo & Landstreet (2022). This work further provides statistically significant evidence of these distinct populations with the use of a large and robust sample size.

In addition to the masses, cooling ages, and field strengths of our magnetic white dwarfs, we use rotation periods and tangential velocities to provide further insight into the formation channel. We have rotation periods for 26 targets using data from TESS, ZTF, and values reported in the literature, 23 of which are shorter than 6 hrs and 15 have masses $> 0.9 M_{\odot}$. These high mass, fast-spinning objects are thus extremely likely merger products. However, only 4 of these 15 have tangential velocities $>$ 50 km/s, and the sample shows a typical increase in velocity dispersion for older targets. Hence we are unable to use kinematics to identify merger remnants for this thin disk dominated sample.

While binary evolution can likely explain the majority of the young population, some ambiguity remains for the old population. These objects likely come from single-star evolution, but whether these dynamos come from crystallization or from earlier stellar evolution stages is still up for debate. However, when accounting for breakout times, a noticeably larger fraction of our older targets can be explained through a dynamo that forms on the main-sequence rather than crystallization. This result is in strong agreement with the findings of Blatman & Ginzburg (2024) and Camisassa et al. (2024). Uncertainties in the treatment of convective boundaries and the IFMR leads to large uncertainties in the breakout times for this core-convective dynamo. Nevertheless, crystallization itself seems unlikely to generate the magnetic fields we see in many of our low mass magnetic white dwarfs given the long breakout times for this dynamo.

The primary bias in our survey is against objects with fields too weak to produce clear Zeeman-splitting and white dwarfs that do not show absorption features in their spectra. The latter group consists of He-dominated atmosphere white dwarfs cooler than ∼11,000 K, and H-dominated atmosphere white dwarfs cooler than ∼5000 K. If we expect to see absorption features based on the atmosphere composition and T_{eff} but do not, we can infer the presence of a strong field.

Otherwise, these white dwarfs with featureless spectra cannot be confirmed as magnetic without spectropolarimetry. Hence we are biased against older white dwarfs with field strengths greater than 100 MG, and all magnetic white dwarfs with field strengths weaker than $\sim$1 MG. However, the lack of these objects should not affect our statistical analysis, as these targets should almost exclusively belong to the old, low mass, weak field population. While we may obtain better statistics with the inclusion of these targets, the evidence is clear even without them.

This work has been dedicated to understanding the origins of magnetic fields in white dwarfs by analyzing trends in a large, volume-limited survey. The observing strategy for such a survey is limited to single or dual exposures per target in order to sufficiently observe the thousands of targets. In doing so, we obtain only a snapshot of the white dwarf at a given time. This is perfectly reasonable given the goals of this study, but it fails to inform us on how the magnetic field may impact the white dwarf itself. In particular, it would be useful to understand how the fields impact the surface of the white dwarf, similar to how local fields impact the surface of our Sun. To better understand this process, multiple spectra on a single target are needed at different points in the object's rotation to sample the surface and look for changes. This requires a tradeoff in which we focus on fewer targets for much longer durations. In doing so, we are able to obtain a clearer picture of how the magnetic field interacts with the white dwarf.

Table 2.3. Physical parameters for our magnetic white dwarf sample. An "X" in the final column means the dipole parameters are tentative based on the quality of our fit to that object.

SDSS ID	Composition	Spectral Type	$T_{\rm eff}$	Mass (K)	Cooling Age ($M_\odot$)	B (Gyr)	i (MG)	a_z (°)	Source (R/R_*)	Note
J000603.80+075514.4	H	DAH	8607	0.733	1.288	13.7	48	0.30	7	
J000637.93+310415.7	H	DAH?	25442	1.138	0.200	93.0	0	0.50	1	X
J000728.91+340341.4	H	DAP	5917	0.807	5.026	62.0	0	-0.29	1	X
J001328.72+074844.6	H	DAH	6219	0.672	2.801	8.0	45	-0.13	1	
J002128.60+150223.8	H	DAH	7119	0.747	2.399	527.3	28	0.16	10	
J005045.81-032655.6	H	DAH?	23916	1.213	0.330	99.0	15	0.23	1	X
J005233.73+150916.5	H	DAH	5742	0.636	3.253	1.0	0	0.23	1	X
J010624.44+150626.4	H	DAH:	5758	0.778	5.178	1.6	60	0.03	1	X
J015013.17+283556.2	H	DAH	12046	0.979	0.999	8.0	60	0.30	9	
J015342.00+180857.9	H	DAH	9147	0.875	1.674	19.0	45	0.49	1	
J015453.71+253739.3	H	DAH	6778	0.725	2.587	6.0	90	0.48	1	
J021148.21+211548.2	H	DAH	12244	1.075	1.440	207	45	0.4	9	
J021407.27-050548.1	H	DAH	9005	0.907	2.024	19.0	15	0.47	1	
J022742.58+442444.1	H	DAH:	14444	0.602	0.223	0.8	90	-0.04	1	X
J025506.14-071551.4	H	DAH	7149	0.718	2.080	1.4	7	-0.28	2	
J025930.85+034058.6	H	DAH:	5695	0.574	2.596	4.1	60	-0.07	1	X
J030350.63+060749.0	H	DAH?	13150	0.915	0.649	445	90	-0.45	1	X
J031613.91-081637.5	H	DAH:	6482	0.805	3.944	2.3	90	0.41	1	X
J032619.23+133108.6	H	DAH	11351	0.936	1.021	4.0	15	0.30	9	
J035324.54+103728.0	H	DAH?	5922	0.784	4.802	41.0	75	-0.09	1	X
J035734.99+191549.3	H	DAH	5905	0.616	2.684	6.4	0	-0.22	1	
J042229.75+165706.5	H	DAH	6623	0.530	1.553	4.0	60	0.42	1	
J052054.17+011442.2	H	DAH	6590	0.766	3.371	6.0	75	0.43	1	
J055119.47-001021.4	log(C/He) = -6.07	DQH	6228	0.674	3.210	10	NA	NA	4	
J060755.76+341526.1	H	DAH	21139	1.175	0.392	3.2	45	0.3	9	
J064400.57+092605.1	H	DAH	6217	0.658	2.627	6.0	60	-0.11	1	
J065757.54+660505.7	H	DAH:	5183	0.465	2.784	41.0	60	-0.25	1	X
J071816.41+373139.1	H	DAH?	33942	1.317	0.203	NA	NA	NA	9	
J074213.37+315703.4	H	DAH	9426	0.722	0.979	41.4	11	-0.16	2	
J074402.82+154442.7	H	DAH:	5270	0.573	3.924	1.2	15	-0.35	1	X
J074842.48+112502.0	log(H/He) = -4.20	DCP	8983	0.781	1.364	112.0	45	0.10	1	X
J075636.88-004525.4	H	DAH:	5966	0.595	2.417	1.0	15	0.06	1	X
J080042.46+065542.1	H	DAH	10623	1.016	1.782	317.0	75	0.23	1	
J080323.83+163356.9	H	DAH	5456	0.661	4.682	2.6	75	0.33	1	
J080359.94+122944.0	H	DAH	19168	1.162	0.496	35.0	15	0.30	9	
J080643.94+405837.7	log(Ca/He) = -9.16, log(He/H) = 3.0	DZH	6091	0.649	3.263	0.8	NA	NA	8	
J081802.74+414410.2	H	DAH	8659	0.791	1.454	143.0	30	0.09	1	X
J083531.17+533230.9	H	DAH	8818	0.840	1.648	14.4	10	-0.46	2	
J084155.74+022350.6	H	DAH	6905	0.758	2.799	6.5	51	0.30	7	
J084214.99-022226.7	H	DAH?	23910	1.162	0.263	NA	NA	NA	9	
J084452.43+103537.5	H	DAH:	6313	0.659	2.503	0.4	15	0.22	1	X
J085106.12+120157.8	H	DAH	11209	0.904	0.971	1.8	60	0.3	9	
J085618.94+161103.6	log(H/He) = -5.50	DBAH	16984	0.726	0.204	1.50	0	-0.40	7	
J085649.67+253441.1	H	DAH	11325	0.950	1.079	85.0	19	-0.20	2	

Table 2.3 (cont'd)

SDSS ID	Composition	Spectral Type	$T_{\rm eff}$	Mass (K)	Cooling Age ($M_\odot$)	B (Gyr)	i (MG)	a_z ($^\circ$)	Source (R/R_*)	Note
J085830.85+412635.0	H	DAH	7097	0.841	3.379	2.6	41	0.3	7	
J092213.46+050438.3	H	DAH	5760	0.683	3.936	0.7	30	0.19	1	X
J092433.23+052106.8	H	DAH:	6185	0.649	2.587	0.4	15	0.23	1	X
J094122.18+071617.9	H	DAH:	5917	0.714	3.992	13.4	0	-0.24	1	X
J100759.81+162349.6	H	DAH	10392	1.000	1.801	13.6	42	0.30	7	
J101131.94+372713.1	H	DAH:	6398	0.644	2.269	2.0	30	0.49	1	X
J101145.20+495834.3	H	DAH	6155	0.747	3.929	2.0	60	-0.23	1	
J101529.62+090703.7	H	DAH	7146	0.808	3.002	4.5	47	0.30	7	
J101631.72+181754.7	H	DAH?	7310	0.848	3.171	34.0	30	0.01	1	X
J101805.04+011123.6	H	DAH	10869	0.965	1.339	76.1	16	0.05	7	
J102054.11+362647.1	H	DAH	17361	0.771	0.200	59.8	69	0.15	7	
J102837.65+145101.8	H	DAH	5836	0.582	2.463	1.2	60	0.00	1	X
J102907.55+112718.3	H	DAH	6796	0.744	2.798	19.2	46	0.30	7	
J103430.16+032736.4	H	DAH	15110	1.089	0.763	13.0	75	0.30	9	
J103532.53+212603.6	H	DAH	6949	0.640	1.806	2.6	48	0.30	7	
J103941.53-032534.2	H	DAH?	19792	1.043	0.297	86.0	15	0.49	1	X
J105320.18-232926.0	H	DAH:	5344	0.637	4.853	4.3	15	-0.17	1	X
J105544.90+211105.0	H	DAH	6051	0.652	2.845	0.5	7	-0.25	2	
J105556.77+252556.1	H	DAH	7069	0.701	2.017	11.0	30	0.50	1	X
J105607.14+385257.6	H	DAH:	5820	0.730	4.443	25.0	45	-0.16	1	
J105709.82+041130.4	H	DAH	7870	0.631	1.267	2.5	41	0.38	10	
J110505.75+522522.2	H	DAH?	17588	1.154	0.633	NA	NA	NA	9	
J111638.37+311921.2	H	DAH	5539	0.794	6.197	1.2	0	0.05	1	X
J112328.49+095619.4	H	DAH	9323	0.756	1.098	1.9	70	0.30	7	
J112605.90+090628.9	H	DAH	10639	1.094	2.179	26.1	2	0.28	7	
J111341.32+014641.7	log(C/He) = -6.50	DQH	5226	0.866	7.314	NA	NA	NA	1	
J113756.51+574022.4	H	DAH	7586	0.693	1.633	2.8	0	0.17	10	
J113926.44+261320.5	H	DAH:	6570	0.747	3.176	0.4	0	0.25	1	X
J114207.26+662443.3	H	DAH:	5435	0.667	4.902	1.0	45	0.22	1	X
J114439.54+662928.5	H	DAH	6717	0.473	1.310	6.0	75	0.50	1	
J120125.41+084800.5	H	DAH	7207	0.789	2.728	2.2	12	-0.1	2	
J120327.49+420602.6	H	DAH	5773	0.494	2.030	3.0	30	-0.49	1	X
J120332.77+591011.5	H	DAH?	9872	0.953	1.779	73.0	15	0.50	1	X
J121033.23+221402.6	H	DAH	12636	0.883	0.663	2.0	86	-0.30	7	
J121456.38-023402.9	log(Ca/He) = -8.26, log(He/H) = 1.0	DZH	5362	0.787	6.733	2.12	NA	NA	8	
J121548.73-005637.5	H	DAH	6586	0.744	3.117	3.0	90	0.00	1	
J121735.25+082810.1	H	DAH	18654	1.063	0.376	3.2	60	0.30	9	
J122920.15+412611.5	H	DAH	6306	0.563	1.917	6.0	45	-0.49	1	
J124004.84-100242.1	H	DAH	5721	0.616	3.000	5.0	30	-0.50	1	X
J124146.05-150629.4	H	DAH	7920	0.917	3.047	19.4	0	0.42	1	X
J125446.22+491818.9	H	DAH	6547	0.769	3.473	1.0	15	0.04	1	
J125715.54+341439.4	H	DAH	9557	0.877	1.444	19.7	72	0.29	7	
J130033.46+590406.9	H	DAH	6132	0.565	2.079	4.8	35	-0.01	7	
J131426.37+173228.0	H	DAH	7160	0.825	3.142	2.6	14	-0.35	2	

Table 2.3 (cont'd)

SDSS ID	Composition	Spectral Type	$T_{\rm eff}$	Mass (K)	Cooling Age ($M_{\odot}$)	B (Gyr)	i (MG)	a_z (°)	Source (R/R_{*})	Note
J133250.73+011706.3	H	DAH	7021	0.781	2.896	7.4	60	-0.07	5	
J133359.84+001655.0	log(C/He) = -6.32	DQH	5180	0.912	7.409	NA	NA	NA	1	
J133431.97+602815.6	H	DAH	5853	0.635	3.001	37.0	90	-0.26	1	
J135118.59+171943.9	H	DAH	9111	0.949	2.252	103.0	60	0.37	1	
J135141.13+541947.3	H	DAH	11423	0.767	0.652	368.5	34	0.07	7	
J140640.31+222456.2	log(Ca/He) = -8.40, log(He/H) = -30.0	DZH	5664	0.665	4.850	NA	NA	NA	1	
J141737.99+180537.8	H	DAH	9053	0.928	2.147	37.0	45	0.28	1	
J141857.13+193530.3	H	DAH?	6147	0.764	4.124	89.0	0	-0.11	1	X
J141906.19+254356.5	H	DAH	9062	0.802	1.331	2.6	55	0.38	10	
J141938.91+544313.3	H	DAH:	5978	0.835	5.159	4.4	0	-0.12	1	X
J143019.05+281100.9	H	DAH	9163	0.957	2.268	6.3	6	0.16	10	
J143352.48+510058.2	H	DAH	5585	0.655	4.042	5.4	60	-0.41	1	X
J144921.34+205421.9	H	DAH:	5723	0.768	5.177	1.3	15	-0.39	1	X
J145335.93+422524.6	H	DAH:	5833	0.715	4.194	0.9	30	0.04	1	X
J150356.96+462721.1	H	DAH	6110	0.552	2.027	1.2	0	0.15	1	X
J150613.45+215051.5	H	DAZH	5614	0.582	2.812	0.9	0	0.13	1	X
J150942.07+141121.3	H	DAH	6403	0.650	2.313	1.9	60	-0.03	1	
J151130.17+422023.0	H	DAH	10924	1.023	1.681	14.0	40	0.30	7	
J151625.07+280320.9	H	DAH	7944	0.659	1.324	2.3	33	0.00	2	
J153843.10+084238.3	H	DAH	8998	0.875	1.778	11.5	49	0.29	7	
J154020.79+042421.0	H	DAH:	5471	0.791	6.528	1.5	15	-0.47	1	X
J154315.10+302133.6	H	DAH	15661	1.129	0.824	160	15	0.30	9	
J154345.65-024741.2	log(Ca/He) = -8.99, log(He/H) = 30.0	DZH	6585	0.549	1.796	NA	NA	NA	1	
J154855.05+245113.0	H	DAH	21662	1.213	0.441	6.4	60	0.2	9	
J155857.69+041704.9	H	DAH	6990	0.948	4.295	69.8	10	-0.16	2	
J160437.35+490809.2	H	DAH	9215	0.902	1.835	67.1	40	0.30	7	
J160604.03+550925.5	H	DAH	5753	0.645	3.385	8.2	15	-0.50	1	
J160833.28+311230.8	H	DAH	6420	0.689	2.708	23.0	60	0.35	1	
J161043.52+132704.9	H	DAH	6600	0.596	1.851	2.9	75	0.06	1	
J161249.16+325536.0	H	DAH	11482	0.675	0.518	11.0	30	0.48	1	
J162157.77+043218.8	H	DAH	21636	1.278	0.690	15	NA	NA	4	
J162608.75+055239.9	H	DAH	8912	0.742	1.196	8.0	90	-0.37	1	X
J162808.39+233254.2	H	DAH	7269	0.782	2.568	4.8	19	-0.21	2	
J163036.80+272451.5	H	DAH	11099	1.054	1.771	35.0	45	0.30	9	
J163917.46+103605.0	H	DAH	6484	0.787	3.757	1.5	17	-0.21	2	
J164358.80+443855.5	H	DAH	5014	0.572	5.675	3.0	45	-0.30	1	X
J165101.72+424955.5	log(Ca/He) = -8.03, log(He/H) = 30.0	DZH	5569	0.707	5.599	3.12	NA	NA	8	
J165200.66+411030.0	H	DAH	11073	0.892	0.973	50.0	75	0.36	1	
J165948.41+440104.5	H	DAH	28170	1.272	0.292	3.8	60	0.30	9	
J170751.92+353239.4	H	DAH	22332	1.144	0.300	2.8	60	0.30	9	
J171236.24+392110.1	H	DAH	6043	0.645	2.783	8.0	0	-0.48	1	
J174826.81+005210.0	H	DAH	9065	0.889	1.841	4.0	75	0.50	1	

Table 2.3 (cont'd)

SDSS ID	Composition	Spectral Type	$T_{\rm eff}$	Mass (K)	Cooling Age ($M_\odot$)	B (Gyr)	i (MG)	a_z ($^\circ$)	Source (R/R_*)	Note
J175438.38+384644.6	H	DAH	6431	0.697	2.789	5.0	75	-0.17	1	
J180147.08+652136.7	H	DAH	5425	0.642	4.482	5.0	0	-0.15	1	
J180603.12+464003.2	H	DAH	5816	0.644	3.215	0.9	15	0.05	1	X
J184926.23+645811.1	log(H/He) = -3.29	DQH?	12059	1.048	1.397	NA	NA	NA	9	
J185218.63+183355.4	H	DAH	8759	0.926	2.362	5.0	45	0.49	1	X
J195629.08-010236.0	H	DAH	7714	0.689	1.545	0.07	NA	NA	11	
J201222.28+311349.5	log(H/He) = -6.00	DBH	23226	1.223	0.398	300	NA	NA	4	
J201438.48+111157.0	H	DAH	5401	0.557	3.046	3.5	75	-0.12	1	X
J203305.00-183127.2	H	DAH	6225	0.727	3.553	2.5	0	-0.41	1	X
J203524.31-183515.9	H	DAH	12164	1.138	1.770	104.0	15	-0.10	9	
J204400.72+403006.0	H	DAH	7393	0.850	3.087	NA	NA	NA	3	
J204626.15-071036.9	H	DAH	8603	0.803	1.543	2.4	64	0.30	7	
J205129.58+035800.8	H	DAH	6993	0.662	1.869	5.0	90	0.40	1	
J210515.02+090057.4	log(Ca/He) = -8.99, log(He/H) = -30.0	DZH	4427	0.408	4.802	NA	NA	NA	1	
J211125.84+110219.7	H	DAH	16212	1.128	0.729	3.6	60	0.30	9	
J211504.84+040009.5	H	DAH	6560	0.664	2.268	4.5	6	-0.23	2	
J212232.19-091609.3	H	DAH	6213	0.773	4.090	9.4	15	-0.35	1	
J213148.70+065930.1	H	DAH	6654	0.738	2.934	31.1	9	-0.25	2	
J215135.01+003140.1	H	DAH	8799	0.908	2.197	300	NA	NA	13	
J215843.44+052741.5	H	DAH	9824	0.875	1.308	3.1	60	0.26	1	
J221141.81+113604.4	H	DAH	9075	1.312	2.568	18.8	22	-0.35	2	
J222109.87-011122.4	H	DAH	5565	0.717	5.064	9.4	0	-0.34	1	
J222348.45+231909.3	H	DAH	8724	0.916	2.312	6.0	15	-0.50	2	
J222740.49+175320.6	H	DAZH	6668	0.570	1.689	1.3	40	0.29	7	
J223001.91+384630.8	H	DAH	8522	0.861	2.051	2.9	90	0.07	1	
J225513.49+071001.0	H	DAH	10974	1.302	2.189	230.0	0	0.21	9	
J225726.05+075541.7	H	DAH	13407	1.298	1.716	8.8	0	0.10	9	
J225929.73-082822.6	H	DAH	6117	0.779	4.337	1.4	0	0.16	1	X
J231845.17+123602.7	H	DAH	11616	0.859	0.783	45	80	0.05	12	
J233203.85+265846.5	H	DAH	9703	0.891	1.453	2.6	57	0.30	7	
J235006.49-041920.1	H	DAH	5822	0.739	4.559	2.7	0	0.00	1	
J235032.38-075157.8	H	DAH	5421	0.760	6.437	6.8	15	-0.32	1	X
J235741.37+274727.1	log(Ca/He) = -8.51, log(He/H) = 1.0	DZH	5750	0.556	3.013	NA	NA	NA	1	

References. — (1) This Work (2) Amorim et al. (2023) (3) Andrews et al. (2015) (4) Bagnulo & Landstreet (2024) (5) Bergeron et al. (1993) (6) Ferrario et al. (2015) (7) Hardy et al. (2023a) (8) Hollands et al. (2017) (9) Jewett et al. (2024) (10) Külebi et al. (2009) (11) Maxted et al. (2000) (12) Putney & Jordan (1995) (13) Schmidt et al. (2003)

CHAPTER 3

Discovery of a Magnetic Double-Faced White Dwarf

3.1. Exotic White Dwarfs with Inhomogeneous Atmospheres

The isotropic nature of gravity leads to the compact, stratified structure of white dwarfs. Matter is pulled inwards equally from all directions, such that there should not be two separate regions equidistant from the center where the gravitational force is unequal. This logic extends from the core all the way to the outer atmosphere. It follows then that white dwarfs should have homogeneous atmospheres, meaning the distribution of elements across the surface is constant. No matter what region of the surface you observe, the abundances should be the same as a different region. Even in the case of mixed atmosphere white dwarfs (i.e. DABs or DBAs) where both hydrogen and helium are present, the elements are thoroughly mixed throughout such that the ratio of abundances is constant across the surface.

For the vast majority of white dwarfs, this paradigm holds true. Yet there are a handful of white dwarfs that seem to break this mold, each with their own unique properties. The first one to be found was Feige 7 (Achilleos et al., 1992). High-resolution spectra of this target show variations in the line profiles of both hydrogen and helium. Interestingly, this target is also magnetic, with a high field strength of 35 MG (Achilleos et al., 1992). In addition, polarimetric observations show that this object has a rotation period of 131.6 minutes (Liebert et al., 1977), and similarly shows photometric variability with the same period (Achilleos et al., 1992). Hence this object shows significant variability regardless of observation method.

To reproduce their spectra at different rotation phases, Achilleos et al. (1992) used an inhomogeneous atmosphere model with varying He:H ratios. They initially tested a cap model in which patches, centered at the magnetic poles, could possess a pure H, pure He, or an intermediate He:H = 100:1 composition. However, caps of different sizes and compositions were ultimately required at different phases. Instead, the authors employed a ring model shown in Figure 3.1. This model has a cap of pure helium, followed by a small ring of pure hydrogen, and then the aforementioned mixed composition. The authors attribute this complex distribution of elements to the magnetic field: Feige 7 is at an effective temperature ($T_{\rm eff} = 18381 \pm 371$ K, Jewett et al. 2024) in which it likely has undergone convective dilution. Normally this would switch a DA to a DB or DBA with a homogeneous atmosphere, but the magnetic field inhibits this convective process at certain regions. Achilleos et al. (1992) state that this dilution would continue to be efficient at the poles, where the field lines are radial to the surface, and inefficient at the equatorial regions. Hence the

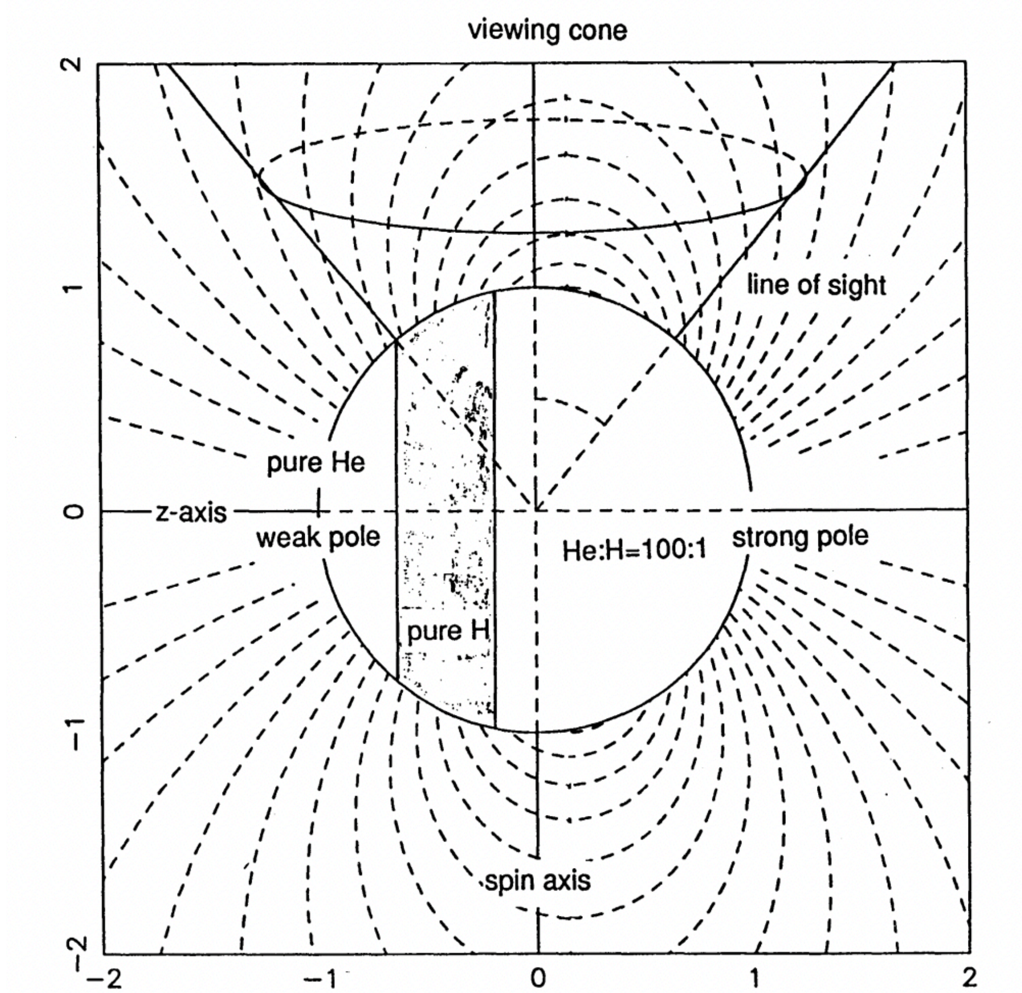

Figure 3.1: Model geometry of Feige 7 from Achilleos et al. (1992). There are three distinct regions with varying elemental abundances. The x and y axes are labeled in units of white dwarf radius.

poles should be dominated by helium and the equatorial region by hydrogen, which matches their model geometry.

A more extreme example of a variable white dwarf is ZTF J203349.8+322901.1 (referred to as "Janus" from here on). Figure 3.2 shows several phase-resolved spectra of this target from Caiazzo et al. (2023). The hydrogen and helium lines disappear and reappear out of phase with each other, indicating that this target actually has one side dominated by hydrogen and the other by helium. This "double-faced" object is quite unique in that the variations are so extreme, however the mechanism that generates this odd atmosphere is likely similar to that of Feige 7. Caiazzo et al. (2023) found that $T_{\rm eff} \approx 35,000$ K, so Janus could be undergoing a DO-DA or DA-DBA transition. While Zeeman-splitting is not detected, a weak magnetic field could still be strong enough to inhibit

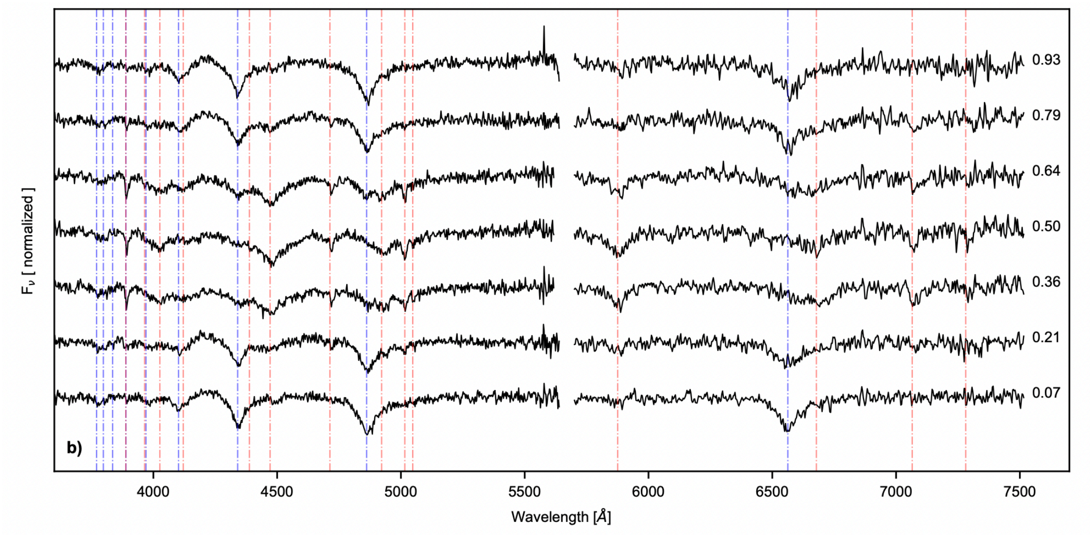

Figure 3.2: Phase resolved spectra of Janus. The red vertical lines mark the position of helium features, while the blue lines mark the position of hydrogen features. Each spectrum is marked with the phase on the right. At phase = 0.07, hydrogen lines are clearly visible while helium is effectively nonexistent. As Janus rotates, the hydrogen features become much weaker while the helium lines strengthen at phase = 0.50. By phase = 0.93, the hydrogen lines come back and helium is gone once again (Caiazzo et al., 2023).

these processes (Tremblay et al., 2015) and generate the observed distribution of elements. While recent work has shown that Janus actually has a thin layer of hydrogen across the entire surface (Bédard & Tremblay, 2025), some mechanism would need to cause this layer to be optically thin on the side where helium is observed.

Three more of these variable white dwarfs have been found (Pereira et al., 2005; Wesemael et al., 2001; Cheng et al., 2024), two of which have confirmed magnetic fields. These objects are incredibly valuable to study for two important reasons. The first is that it is very difficult to study these evolution processes observationally. The processes that govern spectral evolution, particularly the float-up process, are fairly short relative to white dwarf cooling ages (millions vs. billions of years, Bédard et al. 2022b, 2023; Bédard 2024). In addition, these processes should in principal globally affect the white dwarf such that you cannot necessarily tell from a spectrum when a target is undergoing evolution. These double-faced systems are unique in that they have left behind markers of spectral evolution, which gives us opportunity to better understand the evolution process. The second reason is they allow us to study the impacts of magnetism on the internal motion of material. Each target effectively becomes a laboratory where we can determine how the field shapes the distribution of elements in the atmosphere. Given that $\sim$20% of white dwarfs are magnetic (Bagnulo & Landstreet, 2021), and many more white dwarfs could have fields that simply have not been detected, it is important to understand how the fields affect the white dwarf.

If you have been keeping tally, you may notice that so far we have five double-faced white dwarfs. If you are skeptical of the conclusions drawn about these objects from such a small sample, I would not blame you. A larger sample of targets would help answer several questions such as the range of possible atmosphere geometries, the possible $T_{\rm eff}$ range that we find these objects in, the frequency (and thus necessity) of magnetism, etc. If only we had more targets...

3.2. The Case of SDSS J0910+2105

SDSS J091016.43+210554.2 (referred to as J0910+2105 from here on) had been classified as an unresolved DA+DB binary by Genest-Beaulieu & Bergeron (2019b). Fits obtained using homogeneous DBA model spectra predicted H and He lines that were totally inconsistent with the observed spectrum (see also below). By using a double degenerate model composed of a DA+DB white dwarf, the H lines match up much better (see the online version of their Figure 25.4). While the theoretical He lines are still too deep, this fit is a significant improvement over the single-star model.

Figure 3.3 shows two separate SDSS spectra taken on MJD 53700 and 56003. The inset shows the region around Hα. We immediately see signs of a magnetic field via Zeeman-splitting in both the Hα and He I λ6678 lines. Additionally, the depth of the H lines is noticeably deeper in the top spectrum compared to the bottom, particularly in Hβ and Hγ. An unresolved DA+DB binary system would not produce these spectroscopic variations: the H lines vary in depth but the He lines remain constant. Even if this were a binary, both targets would need to be magnetic given the observed Zeeman-splitting in both sets of lines.

While spectroscopic variations seem likely, photometric variations can provide insight into the rotation period and can be checked using the Transiting Exoplanet Survey Satellite (TESS). J0910+2105 (TIC 85911578) has 20-second and 2-minute cadence data from sectors 44, 45, and 46. We search for frequencies ranging from 5 to 1098 minutes in the 2-minute cadence data, and 1 minute to 1098 minutes for the 20-second cadence. For both sets we used 8 million equally spaced frequency bins. Figure 3.4 shows the results from our TESS search. We do not see signs of periodic photometric variability in either set of data, but this does not rule out the possibility of spectroscopic variations. Robinson & Winget (1983) showed that GD 323 does not exhibit photometric variations despite having clear spectroscopic variations (Pereira et al., 2005).

Table 5.1 shows J0910+2105's parameters from Gaia DR3. In addition, the SEGUE Stellar Parameters Pipeline (Lee et al., 2008) provides a radial velocity measurement of 61.5 ± 34.2 km

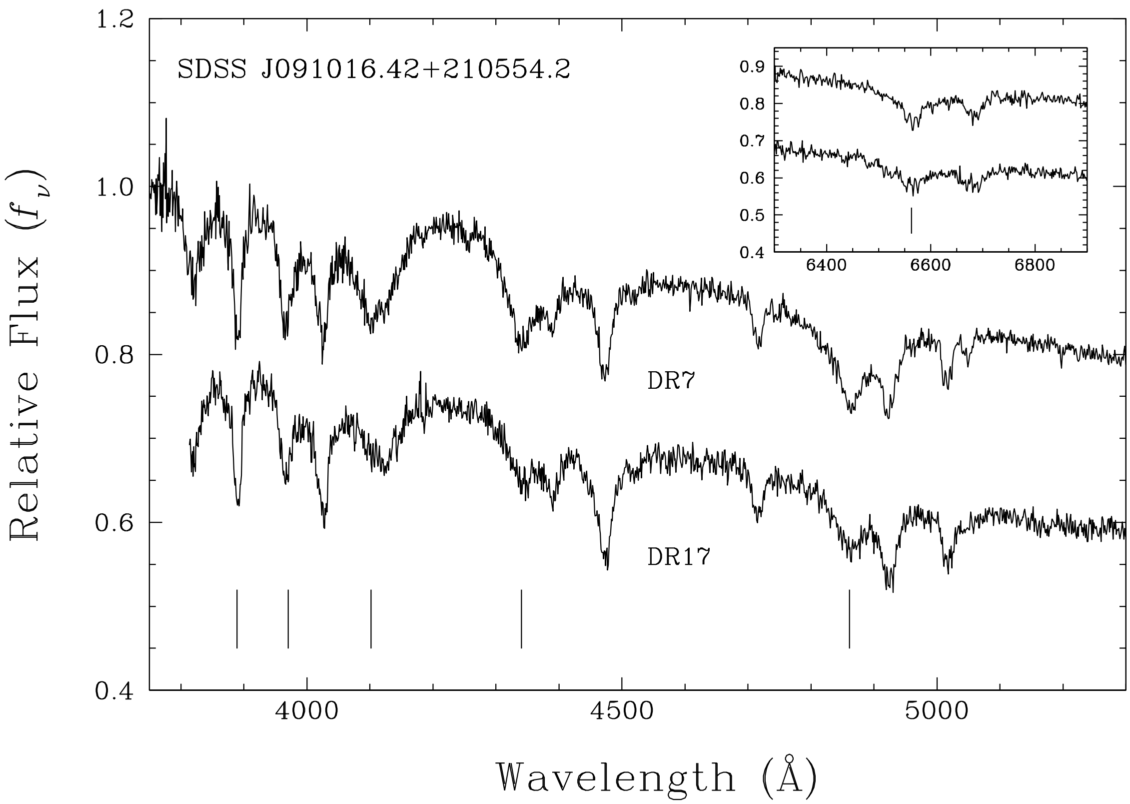

Figure 3.3: SDSS spectra of J0910+2105. Spectra are offset for clarity. Tick marks indicate the locations of the H lines. The top spectrum shows notably deeper Hβ and Hγ lines compared to the bottom. The inset shows the Hα region where Zeeman-splitting is clearly detected. The exposures are 45 and 48 min long, respectively.

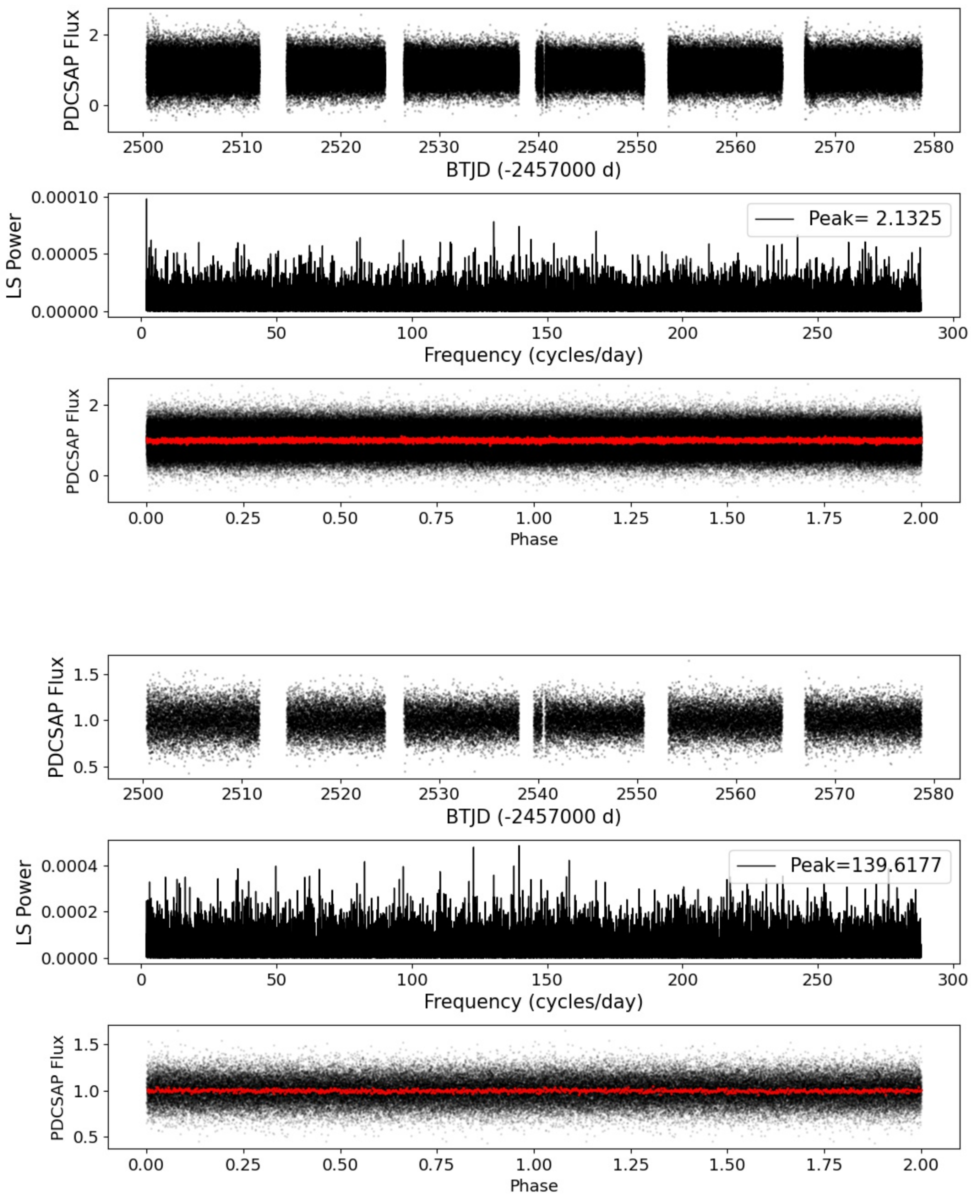

Figure 3.4: *Top*: Light curve, Lomb-Scargle periodogram, and phase-folded light curve based on the highest peak in the periodogram for the 20-s cadence data from TESS. Red data points represent the original data binned by 100. *Bottom*: Similar to the top but for the 2-minute cadence data. Neither cadence shows signs of significant photometric variability.

Table 3.1 Astrometric and photometric data from Gaia DR3 for J0910+2105.

Gaia DR3 ID	637142391019402880
RA (J2000)	09:10:16.444
Dec. (J2000)	+21:05:54.197
π (mas)	10.381 ± 0.069
μ_α (mas/yr)	-31.883 ± 0.074
μ_δ (mas/yr)	7.268 ± 0.066
G (mag)	16.359 ± 0.003
$G_{\rm BP}$ (mag)	16.306 ± 0.006
$G_{\rm RP}$ (mag)	16.463 ± 0.007

s^{-1} for J0910+2105 based on the spectrum obtained on MJD 53700. Using the astrometry provided by Gaia DR3 and the radial velocity obtained by the SDSS, we obtain Galactic space velocities of $U = -53 \pm 23, V = -18 \pm 12$, and $W = 29 \pm 22$ km s^{-1}. These values are consistent with the disk population (Fuhrmann, 2004).

We use the Gaia DR3 distance, GALEX FUV and NUV, SDSS u, and Pan-STARRS $griz$ photometry to obtain a photometric fit of J0910+2105. Figure 3.5 shows our best photometric and spectroscopic fits using homogeneous H/He atmosphere models. While both fits are obtained independently, the H abundance used in the photometric fit is set to the value obtained from the spectroscopic solution. Our photometric solution ($T_{\rm eff} = 16747 \pm 170$ K, $M = 0.778 \pm 0.011\ M_\odot$, $\log g = 8.299 \pm 0.013$) indicates a fairly cool and massive DBA star. Not only is our spectroscopic solution ($T_{\rm eff} = 14620 \pm 120$ K, $M = 0.430 \pm 0.055\ M_\odot$, $\log g = 7.690 \pm 0.135$, $\log {\rm H/He} = -4.50 \pm 0.09$) completely inconsistent with the photometric solution, the model spectrum is also clearly at odds with the observations, as previously concluded by Genest-Beaulieu & Bergeron (2019b). Indeed, the resulting model predicts notably deeper He lines and shallower H lines than what is observed, a discrepancy which is also responsible for the large uncertainties in the derived parameters. Note that this model does not take magnetism into account, however including this would only help with fitting the Zeeman-split components and not significantly affect the overall line strengths. Hence, fits using a homogeneous atmosphere fail to match the spectrum of this target.

Spectroscopic follow-up is necessary to confirm if J0910+2105 is indeed an unresolved double degenerate binary, or if it is a single star with an inhomogeneous atmosphere. In addition, we can analyze several key features of this unique object: the magnetic field strength, the rotation period, and the distribution of H and He in the atmosphere. We present the results from our observations of J0910+2105 in the next section.

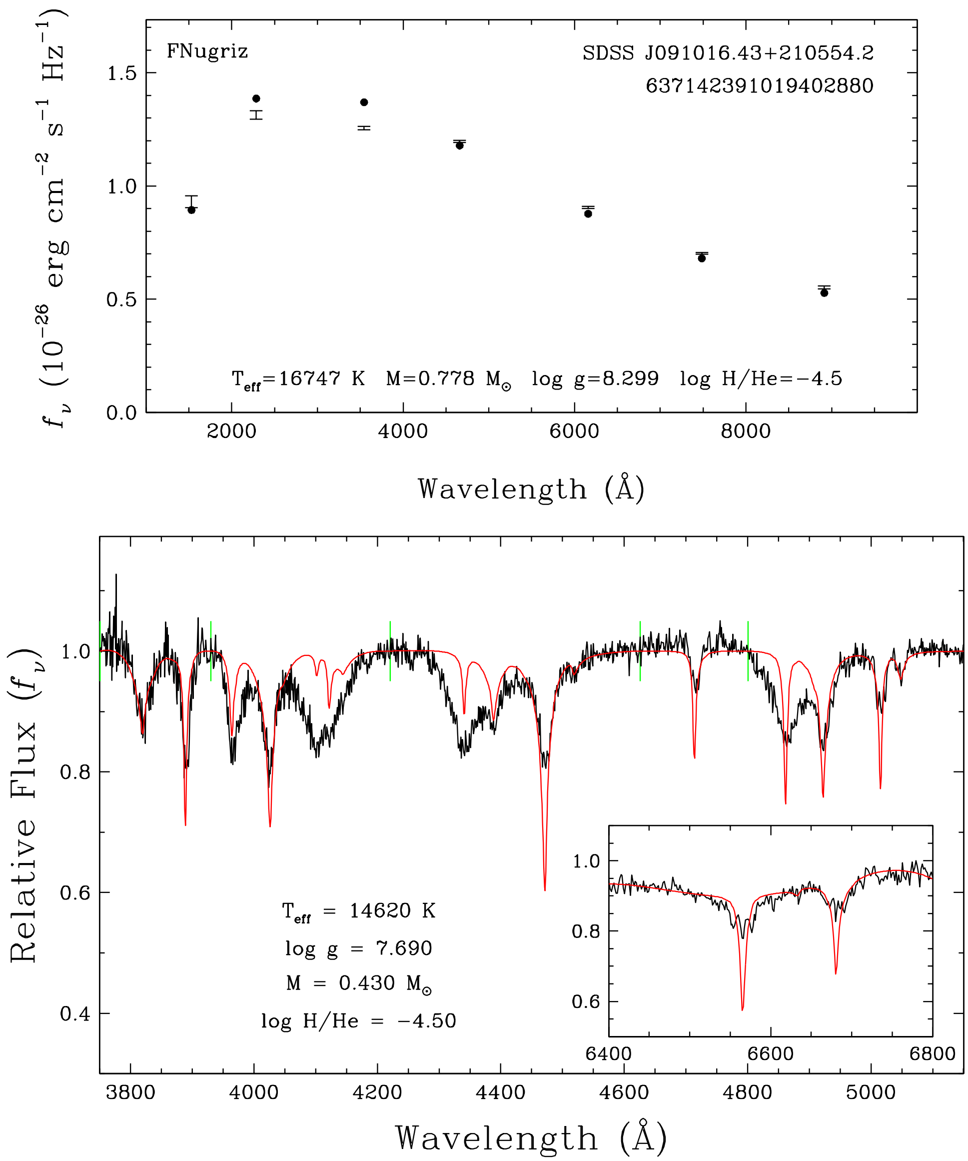

Figure 3.5: *Top*: Best photometric fit using GALEX + SDSS + Pan-STARRS photometry. *Bottom*: Best spectroscopic fit to the SDSS DR17 spectrum. Both fits assume homogeneous H/He models. The predicted line strengths are either too shallow or too deep for most of the absorption features in the observed spectrum.

3.3. Observations

We obtained time-series spectroscopy of J0910+2105 using the Apache Point Observatory (APO) 3.5m telescope equipped with the Kitt Peak Ohio State Multi-Object Spectrograph (KOSMOS) over multiple nights. Our first sequence comprised of 42×5 min long back-to-back exposures on UT 2023 April 13. We increased the exposure time for our second sequence (25×10 min on UT 2023 Apr 17) after analyzing the first night of data and confirming that the target's rotation period is longer than a few hours. On UT 2023 April 24 we attempted our third sequence, however poor weather conditions restricted us to only two 10 min exposures. Our last set of APO observations were taken on UT 2023 May 26 with 9×10 min exposures. All of our APO data were taken using the Blue grism and the 2.1" slit. On UT 2023 April 13 we used the high slit position which provides wavelength coverage from 4150 $-$ 7050Å and a resolution of 1.4 Å per pixel. For the remaining APO observations we used the center slit position which changes the wavelength range to 3800 $-$ 6600Å.

Given the target's hour-scale rotation period, we obtained six additional exposures across four nights (UT 2023 April 22 $-$ 25) using the 6.5m MMT with the Blue Channel Spectrograph. We used the 1.25" slit with the 500 $\mathrm{l\,mm^{-1}}$ grating which yields a resolution of 1.2 Å per pixel.

We reduced all of our data using the standard IRAF routines. Figure 3.6 shows example exposures from the beginning, middle, and end of the first two nights at APO. All of our spectra are available in the online journal, as well as the UT times at the middle of each exposure. Note that certain exposures are combined. We use the time at the middle of the combined exposure for these. The changes in the Hβ and Hγ lines are most noticeable in these exposures given the longer baseline. On UT 2023 April 13 (top panels), the H lines are very weak at the beginning of our run. After about seven exposures, the line becomes more pronounced, appearing very clearly by the end of the night at a strength similar to the He lines. Interestingly, the He lines appear constant across all spectra. This suggests the variations in the Hβ line are due to rotation of the white dwarf, with an inhomogeneous distribution of H in the atmosphere.

Since we did not observe a corresponding decrease in the Hβ line on UT 2023 April 13, it was clear that the rotation period is longer than our initial baseline. Hence we increased our exposure time to 10 minutes to boost the signal-to-noise (S/N) ratio of each spectrum on UT 2023 April 17. Here the Hβ line begins strong (bottom panel in Figure 3.6), but becomes diminished towards the end of the night. This set of observations confirmed the variations in the Hβ feature are caused by rotation.

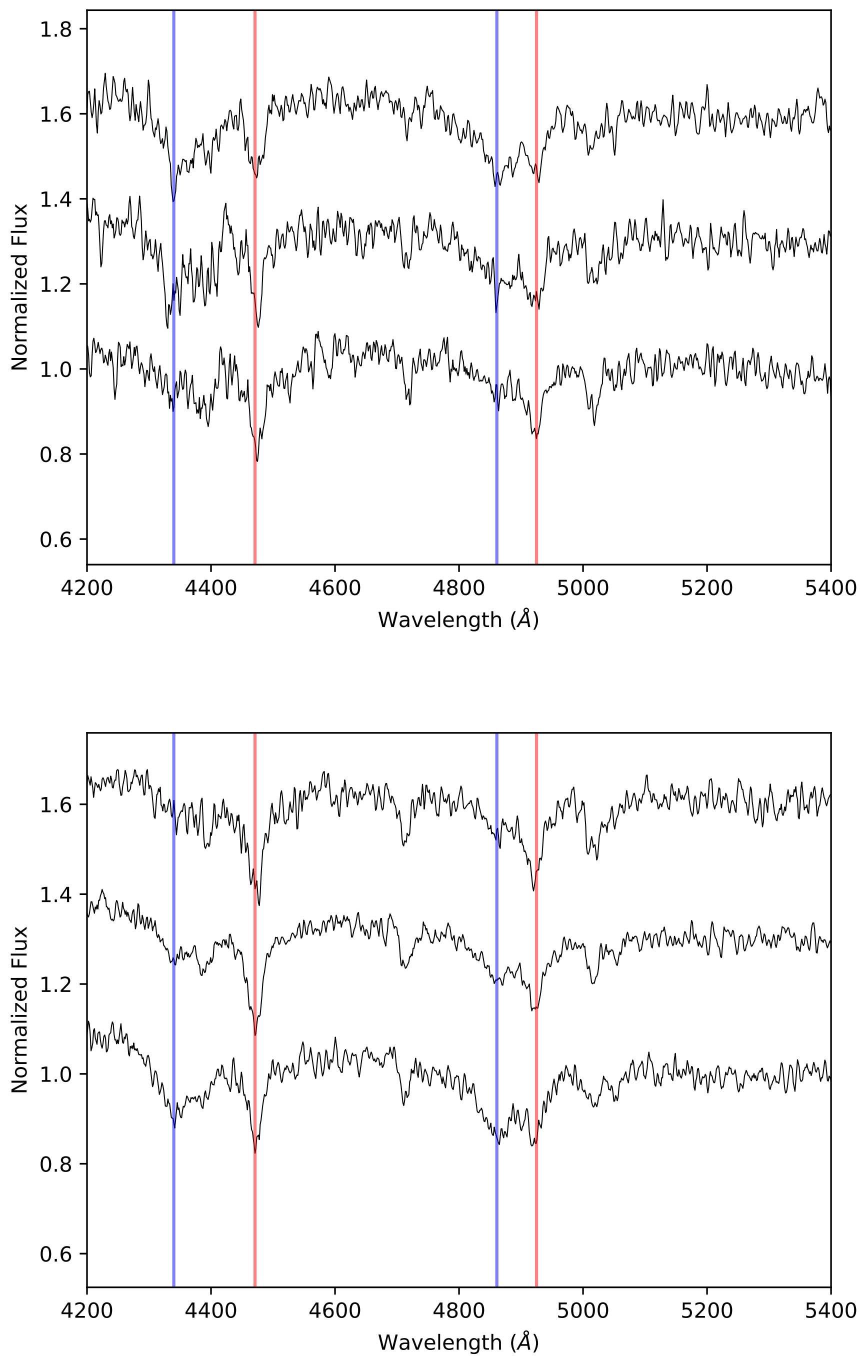

Figure 3.6: Sample of spectra taken at APO on UT 2023 April 13 (top panel) and UT 2023 April 17 (bottom panel). Spectra are plotted in chronological order from bottom to top. The red lines denote the positions of He absorption lines while blue lines denote Hγ and Hβ. The spectra are offset for clarity and smoothed by 3 pixels for display purposes.

3.4. Analysis

3.4.1. The Rotation Period

Our first goal is to determine the rotation period of J0910+2105 by quantifying the variations seen in the H and He lines across all of our data. To accomplish this, we fit a Gaussian profile to both Hβ and He I λ4922 and calculate the equivalent width of these profiles for each spectrum. We use LMFIT, a version of the Levenberg-Marquardt algorithm adapted for Python (Newville et al., 2014), to find the best-fit parameters. We then take the ratio of the equivalent widths to measure how the strength of the H lines vary as a function of time compared to the He lines.

Figure 3.7 shows example fits to spectra at the start and end of our runs on UT 2023 April 13 and UT 2023 April 17. Here the contrast in the Hβ line is stark, which results in very different equivalent width ratios. In this case, the ratio of the equivalent width of the Hβ line to the He I λ4922 line is 0.45 for the first exposure and 2.96 for the final exposure on UT 2023 April 13. For the UT 2023 April 17 data, the ratios are 1.733 and 0.470 for the second and last exposures respectively. The depth of He I λ4922 does not vary significantly across our observations, suggesting a consistent He distribution across the target's surface.

Assuming these variations in the Hβ line are due to an inhomogeneous distribution of H in the atmosphere, we should expect to see similar variations in other H lines. We perform the same fitting process described above on the Hγ line, using the nearby He I λ4471 as a reference. However, there is another He I line at 4388Å that blends with the Hγ line. Attempting to fit a single Gaussian to Hγ produces inferior fits, so we also fit a separate profile to He I λ4388 such that the algorithm clearly distinguishes the two individual profiles and returns a better fit for Hγ. Example fits are shown in Figure 3.8 for the same spectra used in Figure 3.7.

This fitting method alone however does not allow us to sample the errors in our fits. To obtain an error estimate, we use bootstrapping to repeat the fitting process 10,000 times. We then select the ratios corresponding to 15.9 and 84.1% in our distribution of 10,000 values as the $\pm 1\sigma$ lower and upper limit. Figure 3.9 shows the ratios and errors for all our spectra from UT 2023 April 13 and 17 for both Hβ and Hγ. On April 13 we clearly see the H lines gradually increase in strength as a function of time. Conversely, on UT 2023 April 17 we see a gradual decrease in the H line strength.

Knowing that the observed changes in the equivalent width ratios are due to rotation of an inhomogeneous atmosphere, we can use the ratios to constrain the target's rotation period. We generate Lomb-Scargle periodograms using the orbital fit code MPRVFIT (De Lee et al., 2013) in Figure 3.10. Note that we include the equivalent width ratios from all of the APO and MMT data. We generate two separate periodograms, one for each H line. In both cases, we see two strong signals at 0.319 days (7.66 hours) and 0.470 days (11.28 hours). For the Hβ fits, the signal is slightly stronger at 0.319 days. In contrast, the 0.470 day signal is stronger in the Hγ fits. Our

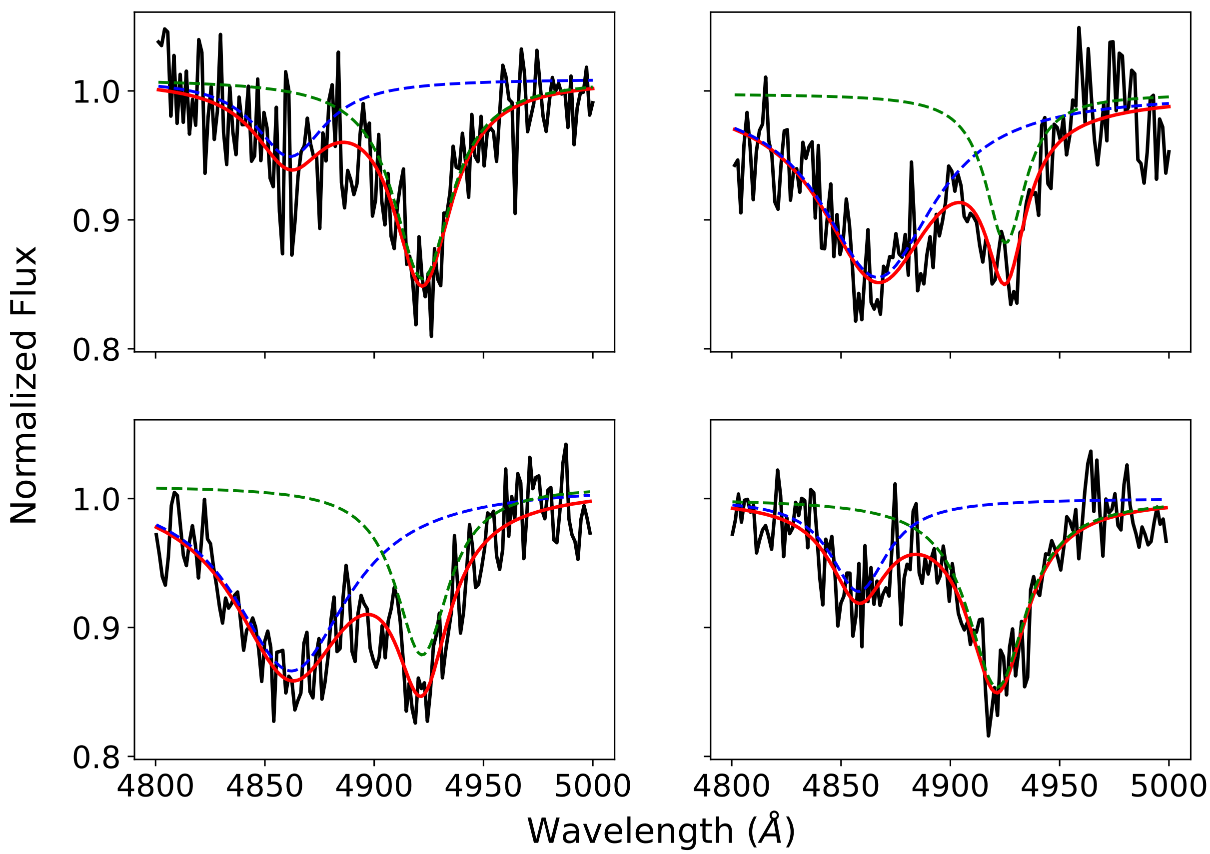

Figure 3.7: *Top row*: Gaussian fits to Hβ and He I λ4922 for the first and last exposure on UT 2023 April 13. The blue line is the best fit Gaussian for Hβ while the green is the best fit for He I λ4922. The red line marks the combined fit of both lines. *Bottom row*: Fits for the second exposure and last exposure on UT 2023 April 17.

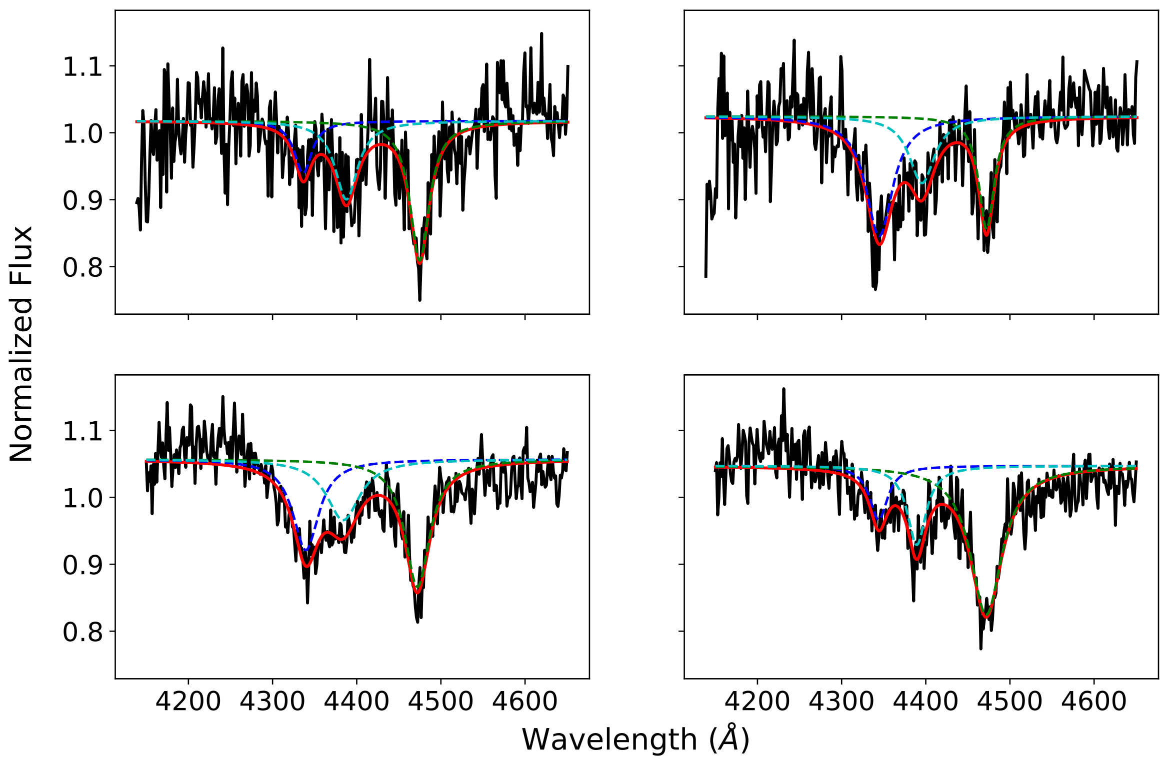

Figure 3.8: *Top row*: Gaussian fits to Hγ (blue), He I λ4388 (cyan), and He I λ4471 (green) for the first and last exposure on UT 2023 April 13. The red line marks the combined fit of all three lines. *Bottom row*: Fits for the second exposure and last exposure on UT 2023 April 17.

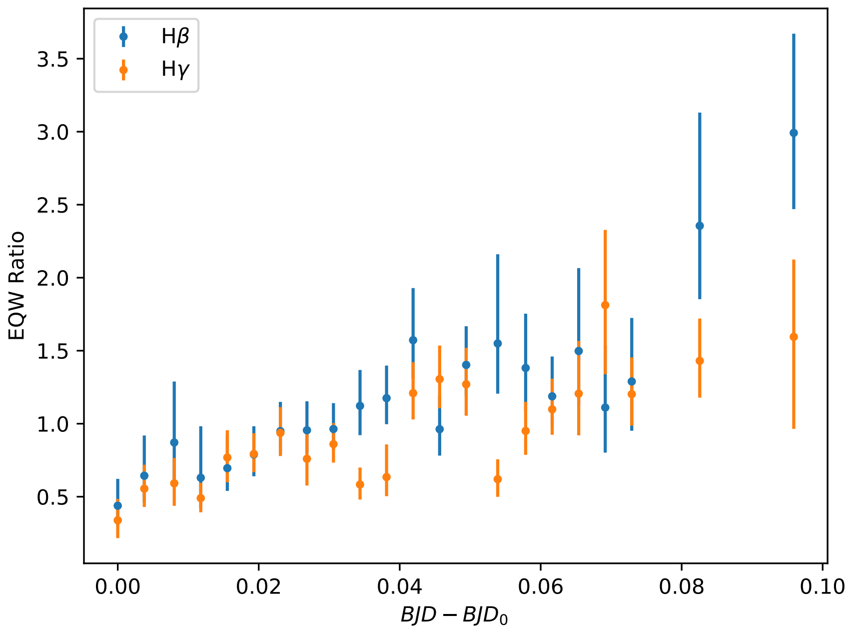

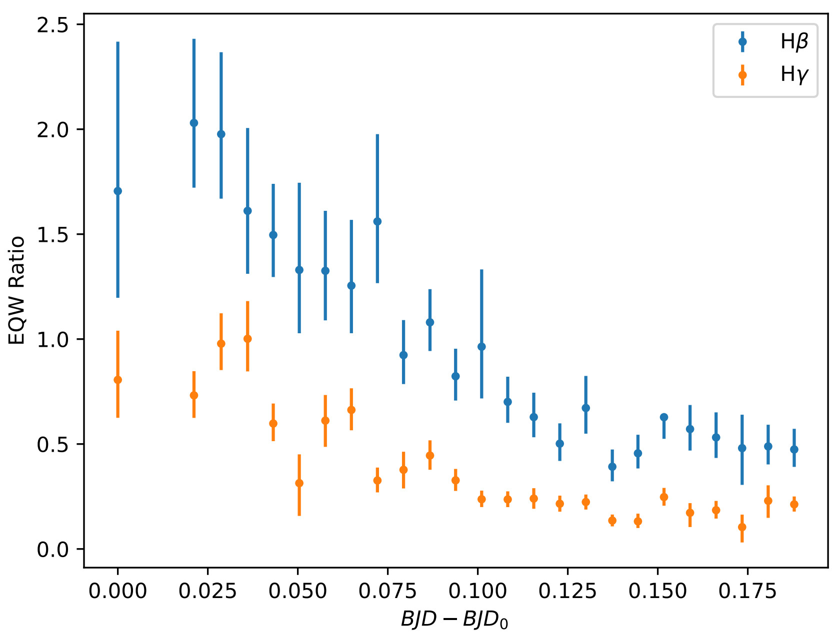

Figure 3.9: Equivalent width ratios for Hβ and Hγ from UT 2023 April 13 (top) and 17 (bottom). The Hγ line tends to be weaker than Hβ due to blending from He I λ4388, so the equivalent width ratios are generally lower. However both lines follow the same trend each night as expected.

observations were obtained over a period of up to ≈ 4 hours on a given night, which limits our ability to discriminate between approximately two cycles and three cycles per day. We conclude that the rotation period is either 7.7 or 11.3 hours, though additional observations while the target is visible the entire night would be useful for removing this degeneracy.

3.4.2. Modelling the Emergent Fluxes

We can see from our spectra that the surface composition of J0910+2105 is modulated over time. Here we attempt to develop the theoretical framework to fit these spectra using models that take into account both inhomogeneous H/He surface abundances and the presence of a magnetic field. We discuss each of these physical ingredients in turn.

We first attempt to model the surface abundance inhomogenity by assuming a particular geometry also used by Beauchamp et al. (1993) and Pereira et al. (2005) in the case of GD 323, which consists of pure H polar caps and a pure He equatorial belt (other geometries are discussed below). We introduce the parameter θ_c to represent the extent of the northern and southern H caps measured from each pole (i.e., $\theta_c = 0°$ means no H caps and thus a pure He atmosphere, while $\theta_c = 90°$ means two full hemispheres and thus a pure H atmosphere). We also denote α as the angle between the magnetic axis and the plane of the sky, as defined in Schnerr et al. (2006, $\alpha = 90°$ means pole-on).

The emergent Eddington flux H_ν is then calculated by numerically integrating the specific intensity I_ν over the visible surface of the disk given the adopted geometry and viewing angle. We adopt pure H and pure He model atmospheres based on the surface composition of each given element. To do so, we fix the $T_{\rm eff}$ and $\log g$ values of both sets of models to the values obtained from the photometric fit, which is certainly a good approximation of the overall physical properties of this star. However, because these parameters have been obtained using homogeneous H/He model atmospheres, we allow them to vary if necessary (our results below indicate that these are appropriate). Sample spectra for these so-called patchy atmospheres are displayed in Figure 3.11 for various values of θ_c, going from a pure He spectrum ($\theta_c = 0°$) to a pure H spectrum ($\theta_c = 90°$). The values in between illustrate how the relative strength between H and He lines varies as a function of the extent of the H caps.

Given the adopted atmospheric parameters based on our photometric fit, $T_{\rm eff} = 16,700$ K and $\log g = 8.30$, our pure H model is fully radiative while our pure He model has a well-developed convective zone. Since it is possible that the presence of the magnetic field inhibits convection, at least partially, we also consider below pure He models with fully radiative atmospheres.

To model the magnetic field of the H and neutral He lines, we use a theoretical approach similar to that described in Bergeron et al. (1992) where the total line opacity is calculated as the sum of the individual Stark-broadened Zeeman components. Here, the line displacements and oscillator strengths of the Zeeman components of Hα through Hδ are taken from the tables of Kemic (1974),

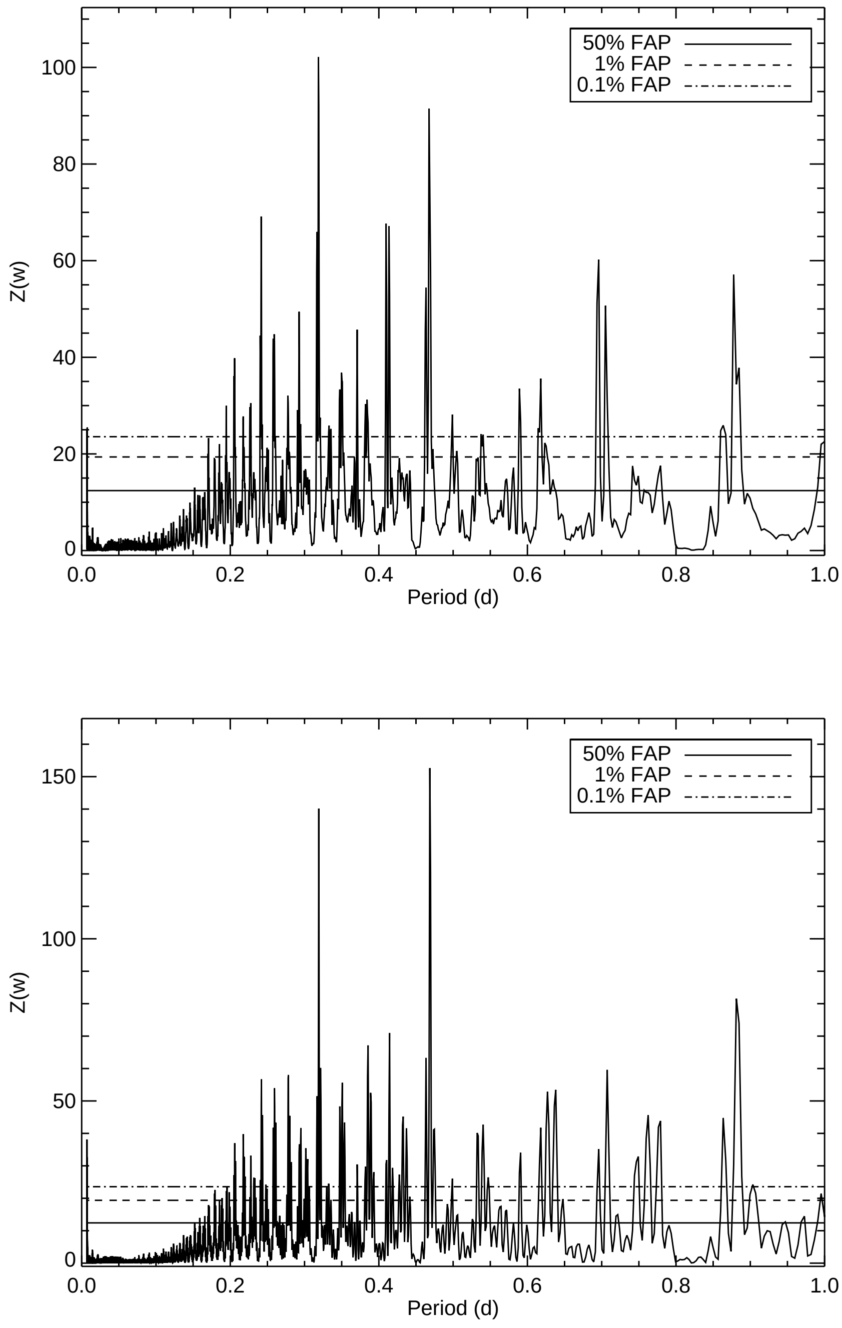

Figure 3.10: Lomb-Scargle periodograms using the Hβ line (top) and Hγ line (bottom). Even though significant aliasing is present, current data strongly favor a period of either 7.7 or 11.3 hours.

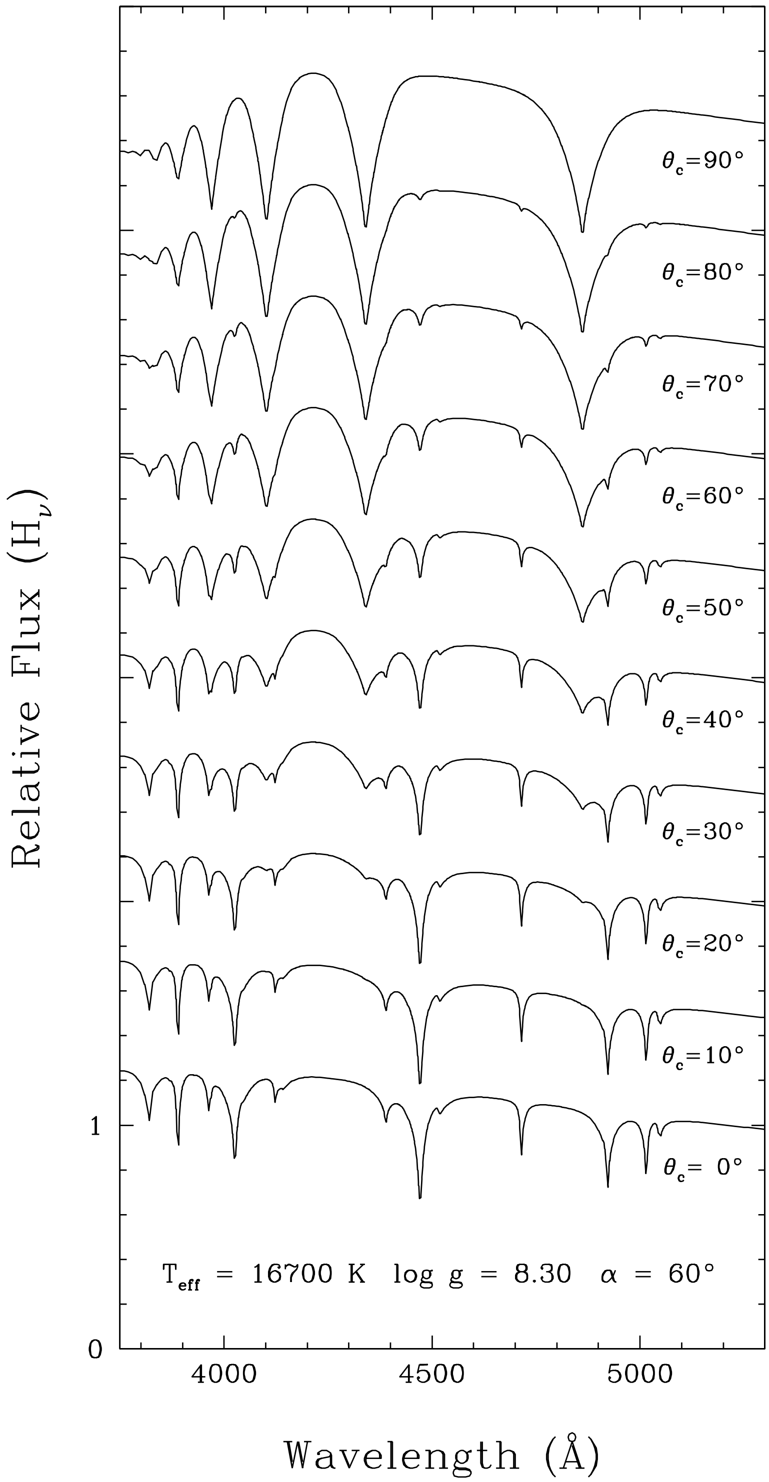

Figure 3.11: Model spectra (Eddington fluxes) for patchy atmospheres with $T_{\rm eff} = 16,700$ K, $\log g = 8.30$, an angle $\alpha = 60°$ between the magnetic axis and the plane of the sky, and various values for the extent of the H caps θ_c indicated in the figure. All spectra are normalized to unity at 5200 Å and offset from each other for clarity.

while for the neutral He lines, we use the detailed calculations from Becken et al. (1999), kindly provided to us by S. Jordan, which have been used successfully in the context of magnetic DB white dwarfs by Hardy et al. (2023b). For both H and He lines, the total line opacity is normalized to that resulting from the zero-field solution. The specific intensities at the surface, $I(\nu, \mu, \tau_\nu = 0)$, are obtained by solving the radiative transfer equation for various field strengths and values of μ ($\mu = \cos\theta$, where θ is the angle between the angle of propagation of light and the normal to the surface of the star). In doing so, the polarization of the radiation field is neglected as we are mainly interested in the total monochromatic intensity. Also, the thermodynamic structures are those obtained from our non-magnetic model atmospheres. Because there is no theory that currently treats magnetic and Stark broadening simultaneously, we make the simple assumption that each magnetic Zeeman component is individually Stark-broadened using an approximate treatment for both H and He lines, instead of relying on the detailed line profile calculations of Tremblay & Bergeron (2009) and Beauchamp et al. (1997) for the H and He lines, respectively. In particular, for the H lines, we rely on the Stark treatment from Kurucz (1970), which is based on Griem's broadening theory (Griem, 1960, 1967), as described in Wesemael et al. (1980), while for the neutral He lines, we used the electron impact shifts and widths and ion broadening parameters taken from Griem (1974), as described in Wesemael (1981). As a test of our overall procedure, we compared our synthetic spectrum calculations with those of Hardy et al. (2023a,b) for magnetic DA and DB white dwarfs, respectively, and found an excellent agreement with their models.

Results from these theoretical calculations are illustrated in Figure 3.12 for H polar caps with $\theta_c = 35°$ (thus a He equatorial belt $110°$ thick), an angle $\alpha = 60°$ between the magnetic axis and the plane of the sky, and the adopted atmospheric parameters taken from the photometric solution. The top spectra compare two non-magnetic models where H and He lines have been treated with detailed Stark profiles (red spectrum), and with our more approximate Stark profiles (black spectrum); we can see the absence of the He I forbidden components with this more approximate treatment. Overall, the comparison between these spectra is excellent, and certainly sufficient for our purposes. The bottom spectrum in Figure 3.12 shows the inclusion of a magnetic field in our calculations with a dipole field strength of $B_d = 1$ MG; here and in the remainder of our analysis, we simply assume a centered dipole model. The splitting of both the H and He lines can be clearly observed in this magnetic spectrum. We conclude that this theoretical framework of magnetic white dwarfs with inhomogeneous surface abundances is perfectly suited for our spectroscopic analysis, which we now consider.

Figure 3.13 shows various fits to one of the SDSS spectra, where we emphasize the blue and red regions of the spectrum. We fit the blue spectrum by considering both the size of the H polar caps θ_c and the angle α as free parameters, while we use the red region near Hα to determine the strength of the magnetic field given that the line splitting is more important there. Our analysis

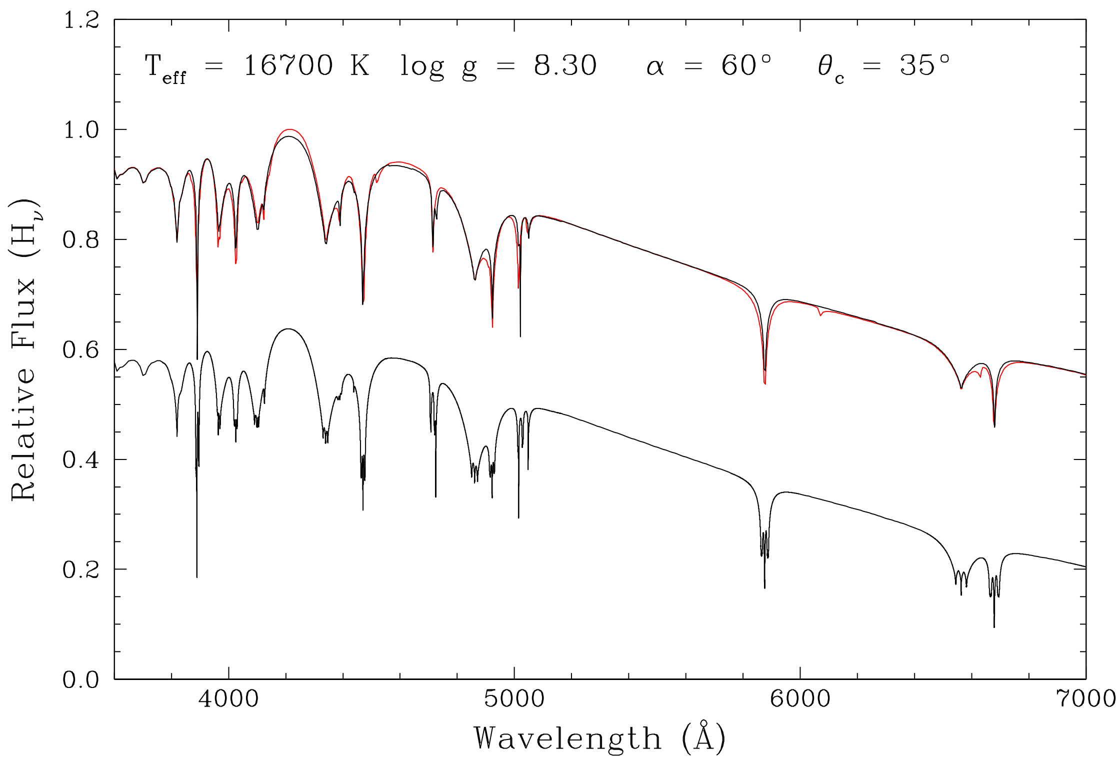

Figure 3.12: Theoretical spectra obtained from model atmospheres with inhomogeneous surface abundances (see text). The top two spectra compare non-magnetic models using detailed (red) and approximate (black) Stark profiles for both the H and He lines. The bottom spectrum (offset for clarity) includes a magnetic field with a dipole field strength of $B_d = 1$ MG.

indicates that a centered dipole model with a dipole field strength of $B_d = 0.55$ MG provides an excellent description of the observed line splitting, which is the value we use throughout our analysis. Because we expect that a field strength of $B_d \sim 0.5$ MG is sufficient to inhibit surface convection based on the findings of Tremblay et al. (2015), who showed that even a field strength of only ∼50 kG can suppress convection, we explore both possibilities in our fits.

Our best fits to the blue spectrum using both radiative and convective atmospheres for the He models are displayed in the top panel of Figure 3.13 (the model spectra are properly convolved with the instrumental profile). A comparison of our best fits with that displayed in Figure 3.5 under the assumption of homogeneous H/He atmospheres indicates that our theoretical framework provides a significant improvement and an excellent match to the observations, giving us confidence in our overall approach. Note that with the exception of the line centers where Zeeman splitting is observed, the improvement in the quality of the fits originates mostly from the treatment of patchy atmospheres rather than the inclusion of the magnetic field.

Even though the fit to the blue spectrum using radiative He model (shown in red) provides a small improvement over that obtained with convective model (shown in blue), as measured by the smaller χ^2 value but also by the overall quality of the fits, the greatest improvement in the radiative fit is for He I λ6678 shown in the bottom panel of Figure 3.13 where we contrast again the convective and radiative solutions. We believe that these results represent a strong indication that the small ∼0.5 MG magnetic field present in J0910+2105 is indeed sufficient to suppress convective energy transport, at least in the atmospheric regions of this star. Consequently, we focus on the radiative fits for the remainder of the analysis.

Note that although our radiative fit of the He I λ4471 line is slightly better than the convective fit, the observed line remains noticeably shallower, which may indicate the limitations of our overall theoretical framework, in particular given the fact that the line core of this particular line is formed high in the atmosphere.

We used this theoretical framework to fit all the spectroscopic observations presented in Section 3, the results of which are discussed in the next subsection. Fits to all of our spectra are presented in the online journal. Although it was possible to reproduce successfully all our spectra using our assumed geometry of H polar caps and He belts, we also explored other surface geometries. For instance, we reversed the abundances and assumed He caps with an equatorial H region. We also assumed a single H (or He) region defined between two predefined polar angles that are not necessarily symmetrical around the equator, as opposed to our previous assumption. This particular geometry could be used to model a white dwarf such as Janus (Caiazzo et al., 2023) with pure H and pure He hemispheres, for instance. Although we do not present the results of these calculations here, we found that we could always achieve good fits to the observations using any of these assumptions. Note that it is always possible that our assumption of H caps and a He equatorial region may not

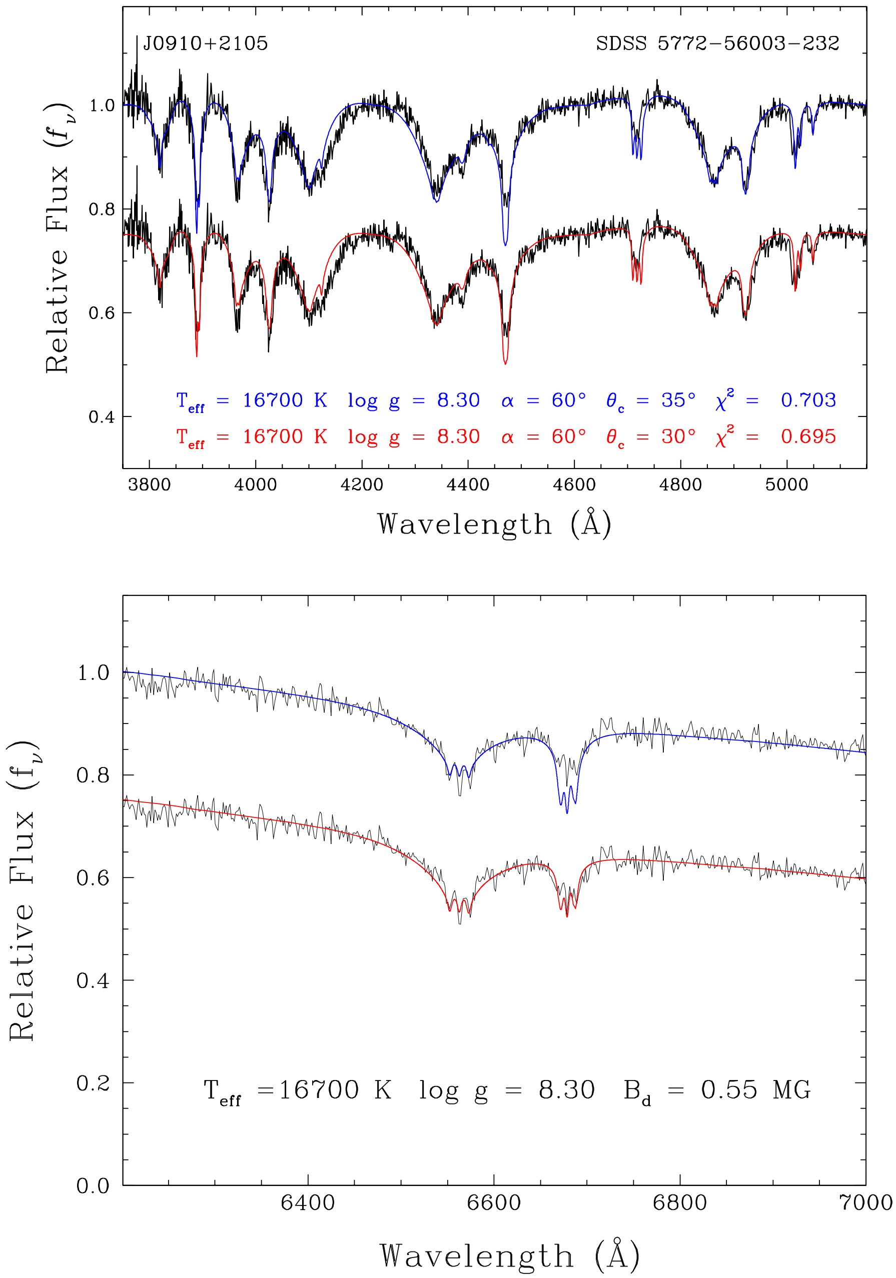

Figure 3.13: *Top*: Best-fitting convective (blue) and radiative (red) atmosphere models to an SDSS spectrum of J0910+2105 using inhomogeneous model atmospheres with H polar caps. The size of the H caps θ_c, the angle between the magnetic axis and the plane of the sky α, and the χ^2 value of the fit are indicated in the figure. *Bottom*: Corresponding fits to Hα and He I λ6678 lines. This portion of the spectrum is used to determine the strength of the magnetic field. Here we find that a centered dipole model with a dipole field strength of $B_d = 0.55$ MG provides the best fit; we also find that the He radiative atmosphere produces a deeper line profile for H and a shallower one for He, yielding a better fit overall.

be representative of the true distribution of H and He of the surface of the stellar disk, but instead only serves as a proxy of the surface area covered by each element. We test our adopted geometry further in the next section using the so-called oblique rotator model.

3.4.3. Model Fits to the Time-Resolved Spectra

A physical model to explain the observed abundance variations in J0910+2105 is the oblique rotator model (Stibbs, 1950; Monaghan, 1973), where the magnetic axis is tilted with respect to the rotation axis. Here, because the two axes are misaligned, the observer would see a different surface abundance (and magnetic field) distribution across the stellar surface due to rotation. The oblique rotator model denotes β as the angle between the two axes, and i as the angle between the line of sight and rotation axis (see Figure 2 of Bailey et al. 2011 for an image of the geometry of this model). This model has been successfully used in the literature to constrain the magnetic field geometry of Ap stars and magnetic white dwarfs based on spectropolarimetry (e.g. Liebert et al., 1977; Borra & Landstreet, 1978; Bailey et al., 2011). For example, Valyavin et al. (2005) analyzed the magnetic white dwarf, WD 0009+501, and found a relatively large $\beta = 117 \pm 24°$ and a viewing angle of $i = 63 \pm 24°$ to explain the spectral variations in that object.

Our optical spectroscopy data on J0910+2105 do not have sufficient signal-to-noise ratio to constrain the change in the average surface magnetic field strength over time. Nevertheless, the observed variations in the H line strengths can be used to constrain the system geometry using the oblique rotator model. Since the lowest χ^2 solutions are typically found for a cap size of 35°, we fix $\theta_c = 35°$ for the following analysis.

Figure 3.14 shows our model fits to several spectra with a fixed H cap size and varying viewing angle α between the plane of the sky and the magnetic axis. The top panels show the model fits to the two SDSS spectra, which are best explained by models with $\alpha = 53°$ and 38°, respectively. Since $\alpha = 90°$ is for a pole-on configuration, more prominent H lines mean a larger α value. We see a broader range of H line depths in the APO spectra, and the example APO data shown in the middle panels are best explained with α values ranging from 51 to 17°, whereas the MMT spectra shown in the bottom panels indicate α values of 54 to 38°. Fitting all available spectra on the system, we find that α ranges from 13 to 55° in this system.

In the oblique rotator model, β is defined as the angle between the magnetic and rotation axes, and i is the angle between the rotation axis and the line of sight. Hence, as the star rotates, the angle between the magnetic axis and the line of sight ranges from $\beta - i$ to $\beta + i$ (see Figure 2 of Bailey et al., 2011). Since α is the angle between the plane of the sky and the magnetic axis, this means that $90 - \alpha$, the angle between the line of sight and the magnetic axis, changes from $\beta - i$ to $\beta + i$ as the star rotates. Hence, the observed range of $\alpha = 13 - 55°$ provides a unique solution for the system geometry, including unique values of β and i.

The lower limit of $\alpha = 13°$ comes from a low S/N spectrum from APO on UT May 26. Instead of relying on a single spectrum to mark its limits, we use all available spectra and fit a sine curve to the best-fitting α values. Figure 3.15 shows the best-fitting α from our first two nights of APO data, which have the longest baseline out of all our data, and the sine curves corresponding to the 7.7 and 11.3 hour solutions. Both solutions match the data relatively well, so we are unable to remove the degeneracy in the rotation period.

For the 7.7 hr solution, the minimum and maximum correspond to $\alpha \approx 25°, 51°$ respectively. For the 11.3 hr solution, the values are $\alpha \approx 23°, 54°$. Combining these values with the definition of α above, we estimate both β and i. The spectroscopic variations seen in J0910+2105 can be explained by the rotation of a star with the polar caps covering $\sim$18% of the surface area (with $\theta_c = 35°$), the angle between the rotation axis and the magnetic axis of $\beta = 52°$, and the angle between the line of sight and the rotation axis of $i = 13°$ for the 7.7 hr solution. For the 11.3 hr period, $\beta = 52°$ and $i = 16°$.

3.5. Discussion

3.5.1. The Patchy Atmosphere

We have successfully applied a magnetic patchy atmosphere model to our time-resolved spectra of J0910+2105. We show that the oblique rotator model with H polar caps provides an excellent match to the observed changes on the strength of the H lines in the spectra. However, there are clear degeneracies in the geometry of these fits, as the surface H distribution may be more complicated than just polar caps. Additionally, the fact that we see H and He at all phases means we require a more complicated distribution than something like Janus in Caiazzo et al. (2023) where the lines completely vanish at specific phases, implying either side is dominated by one element. Regardless, while our fits may not return the exact values or geometry of what the atmosphere of J0910+2105 truly looks like, we have successfully produced a working model that yields excellent fits to the data. It is likely our current interpretation represents only a subsample of the various possible surface H/He abundance distributions.

We can confidently rule out the possibility of J0910+2105 being in a DA+DB binary system. For that scenario to work, both stars would need to be magnetic which is quite rare based on population synthesis calculations from Briggs et al. (2015). We also do not see signs of Doppler shifts in our spectra, and a binary system would not produce the particular variations we see. While Genest-Beaulieu & Bergeron (2019b) obtained a better fit using a DA+DB model than their homogeneous atmosphere model, the predicted He line profiles are consistently deeper compared to what is observed. With our patchy atmosphere model, we obtain significantly better fits to the depths of the line profiles.

Most DBAs can be successfully modelled using a simpler model than the one we invoked here.

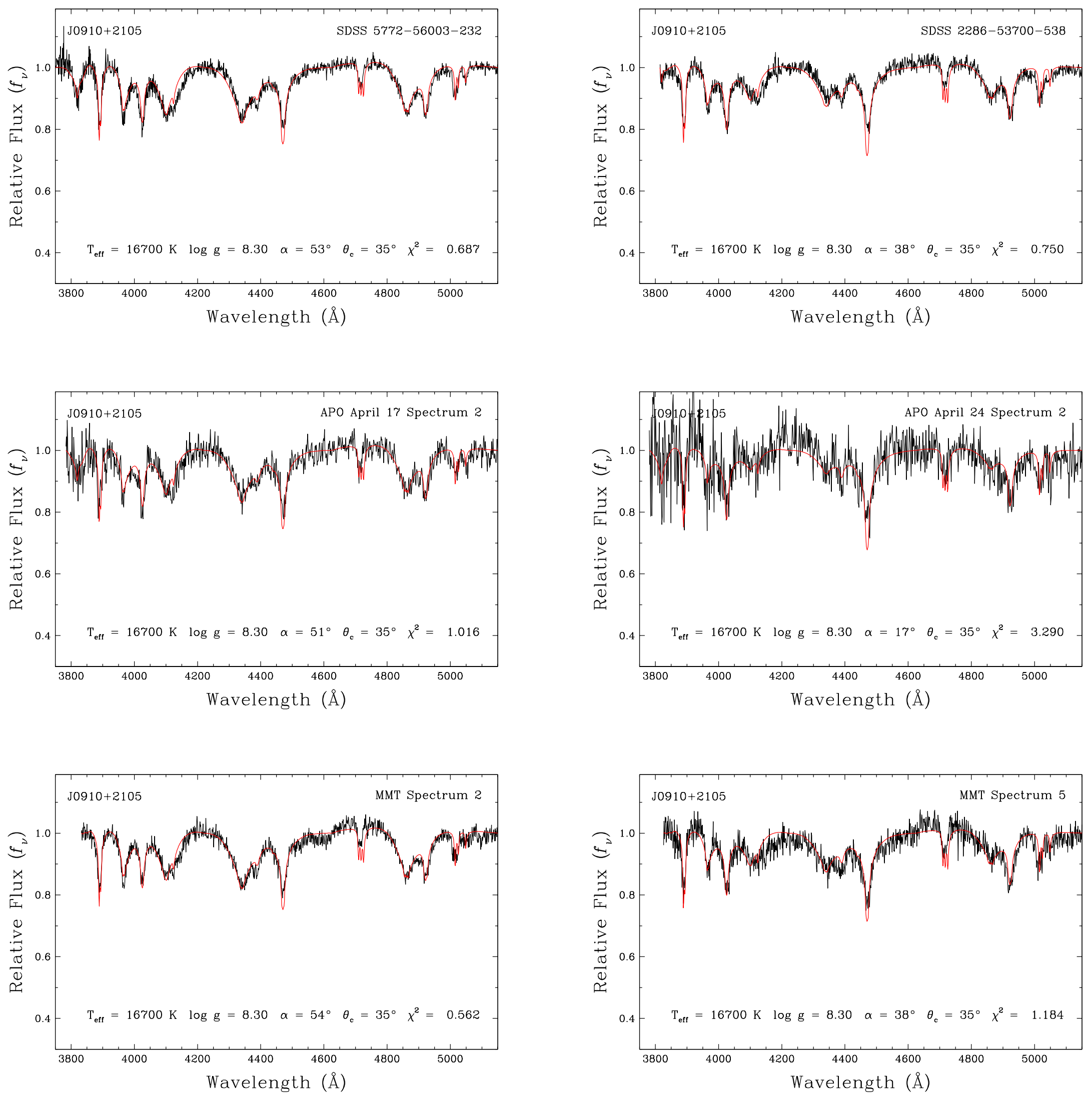

Figure 3.14: *Top row*: Fits to both SDSS spectra using radiative atmospheres and assuming $\alpha = 30°$. *Middle row*: Fits to the second and final spectra from APO on UT 2023 April 17th. *Bottom row*: Fits to the fourth and final spectra from the MMT. Since $\alpha = 90°$ means pole-on, more prominent H lines are explained by a larger α angle.

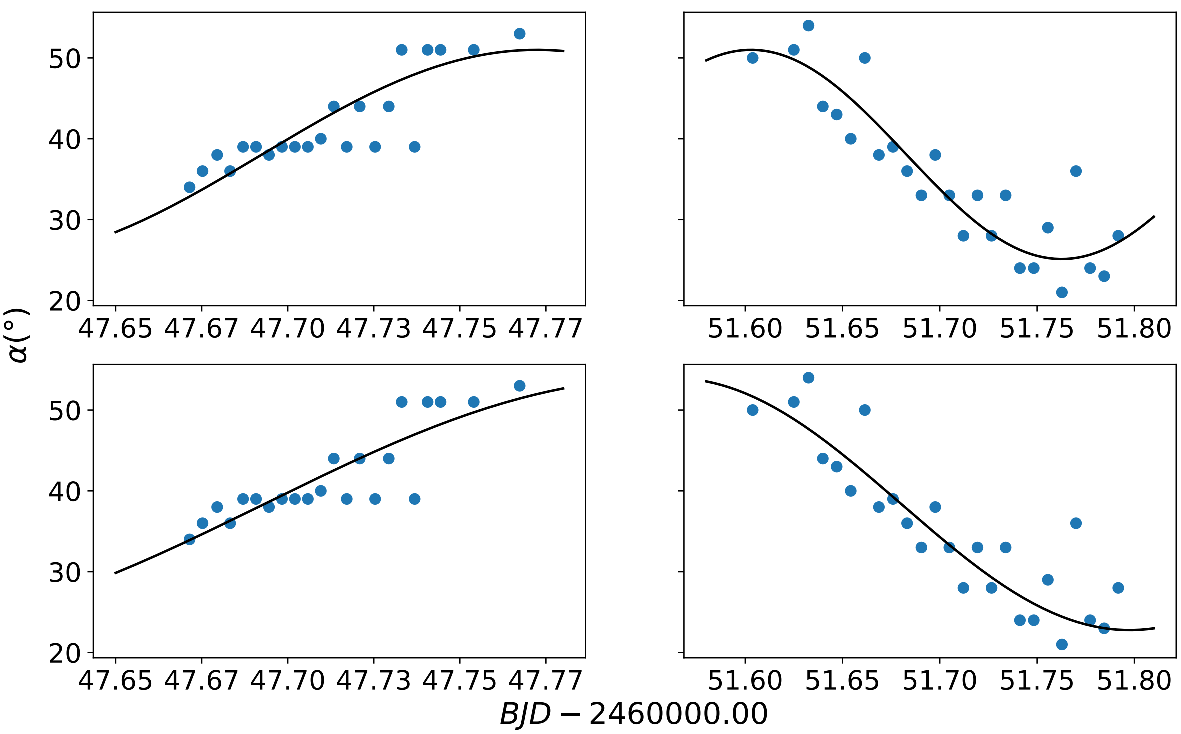

Figure 3.15: *Top row*: Best-fit sine curve (black line) assuming a 7.7 hr rotation period with the α angle values (blue points) from the UT April 13th (left column) and UT April 17th (right column) APO data. *Bottom row*: same as the top row but with a 11.3 hr solution.

A major question is what caused the inhomogeneities in the atmosphere of J0910+2105? The current paradigm to explain the re-appearence of DBs below $T_{\text{eff}} \sim 30,000$ K is that DA white dwarfs with adequately thin surface H layers are converted to DBs through convective instability of the underlying He layer. The He layer mixes in with H above, turning the star into a DBA or DB white dwarf, depending on the total amount of H in the stellar envelope (Bédard et al., 2023).

The question then becomes why this mixing did not occur over the entire surface of the star. Because J0910+2105 is magnetic and because the motions of the material are confined along the magnetic field lines, this field can suppress convection and lead to varying elemental abundances throughout the atmosphere (see for example, Achilleos et al., 1992). Specifically, mixing is expected to be inefficient in regions where the field lines are tangential to the stellar surface (i.e. equatorial regions), and more efficient where the lines are radial to the surface (polar caps). Bédard et al. (2023) successfully reproduced the range of atmospheric H abundances among cool DBAs using a deep H reservoir. With this reservoir, the magnetic field would carry H from the interior to the aforementioned regions where the field lines are radial to the surface. This process would result in H caps, matching the geometry we have invoked to model the atmosphere of J0910+2105.

It is interesting to analyze this target in light of Hardy et al. (2023b), who analyzed all known DBs with signs of Zeeman-splitting in the neutral He lines. In their original sample of 79 objects, only two were classified as DBAs, and were not analyzed as a result. It therefore seems quite rare to find a magnetic DBA despite DBAs themselves making up a large fraction of the DB population. J0910+2105 has given us an opportunity to observe the effects a magnetic field has on the distribution of elements in the mixed H/He atmosphere.

3.5.2. The Rotation Period and Magnetic Field

While we have observed J0910+2105 long enough to detect visible variations in the strength of the H lines, the true rotation period is likely longer than our current baseline, and so we can only partially constrain the target's rotation period. Using the fitting process described in Section 3.1, we obtain a period of 7.7 or 11.3 hours. We expect that our APO observations on UT 2023 April 17th covered approximately half of one rotation given the significant weakening of Hβ throughout the night. Hence a rotation period of roughly twice this baseline is highly likely. This period is also consistent with other magnetic white dwarfs. Kawka (2020) analyzed the distribution of rotation periods for known magnetic white dwarfs and found that the peak is located around $2 - 3$ hours.

The question then becomes: what is the origin of this magnetic field, and how can the rotation period help us narrow it down? There are three potential origins to consider that can result in a magnetic white dwarf. The first is a fossil origin via flux conversion as the progenitor star evolves from a giant star to a white dwarf (Tout et al., 2004). We use the initial-final mass relation from Cummings et al. (2018) to estimate the progenitor mass of J0910+2105. With a white dwarf mass of 0.78 $M_\odot$, we obtain a 3.2 $M_\odot$ progenitor. Hermes et al. (2017b) analyzed the rotation rates of pulsating white dwarfs and found that those with masses from $0.51 - 0.73\ M_\odot$ have an average rotation period of 35 hours, with a large standard deviation of 28 hours. Given J0910+2105's period, a fossil origin of the magnetic field cannot be ruled out.

A second possible origin is via a double-degenerate merger or some form of binary evolution (Liebert et al., 2005b, 2015). Given an average mass of ∼0.8 $M_\odot$ for magnetic white dwarfs, this is a plausible channel to explain the magnetic white dwarfs with strong magnetic fields (Ferrario et al., 2015; Briggs et al., 2015, 2018a). Additionally, a merger product or an isolated white dwarf that had undergone some binary evolution is likely to be spun up (Schwab, 2021). Moss et al. (2023) analyzed seven magnetic white dwarfs and found that three have rotation periods less than an hour, one has a period of only a couple hours, and two are too low mass to have formed via single star evolution. J0910+2105 has an average mass for a magnetic white dwarf and an average period. Hardy et al. (2023b) also found that their magnetic DBs are more massive on average than typical DBs (Genest-Beaulieu & Bergeron, 2019a), so a binary formation channel is also possible.

Finally, core crystallization can trigger a dynamo effect that can then induce a magnetic field (Isern et al., 2017; Schreiber et al., 2021). This does not apply to J0910+2105 though. Based on Figure 17 from Caron et al. (2023), who analyzed the role of crystallization in generating magnetic fields in cool white dwarfs, it is clear that J0910+2105 is much too hot to have begun crystallization for its mass.

Bagnulo & Landstreet (2022) identified two distinct populations of magnetic white dwarfs based on mass. The most massive white dwarfs, with magnetic field strengths on the order of 100 MG, are likely merger products given their high mass and field strength, and tendency to have very short rotation periods. On the other hand, detectable magnetic fields among average mass white dwarfs (0.5 to 0.7 $M_\odot$) are very rare for the first Gyr of cooling, and the fields detected are generally weak, typically tens of kG. The frequency and field strength of these lower mass magnetic white dwarfs actually increases with cooling age. Hence, J0910+2105 is somewhat of an anomaly, being a very young but clearly magnetic white dwarf with a relatively large field, in spite of having a mass not far from the normal white dwarf mass.

3.5.3. Comparison with other Patchy Atmosphere White Dwarfs

Several other white dwarfs are known to show spectroscopic variations due to patchy atmospheres. The first is GD 323, a DAB found to have periodic variations in its line profiles by Pereira et al. (2005). Unlike J0910+2105, the He line strength varies out of phase with the H lines over ∼3.5 hours. Koester et al. (1994) were unable to fit their spectra with homogeneous models, however they did not detect variations in their data. Since GD 323 lies just below the DB gap, Koester et al. (1994) did consider a simple spot model to test the idea of an inhomogeneous atmosphere. Beauchamp et al. (1993) used a more sophisticated model similar to ours, with an equatorial belt and polar caps, and obtained better results overall than the spot model. There are no signs of Zeeman-splitting in the spectra of GD 323 however, suggesting that any inhomogeneities are due to a very weak field, or more likely to the convective dilution process itself.

In contrast, Feige 7 is a DBA with a peculiar atmospheric structure and a strong magnetic field. Achilleos et al. (1992) modelled this white dwarf with a pure He cap, followed by a pure H ring from latitudes $\sim 100°$ and $\sim 130°$ from the He pole, and then a He-dominant region throughout the rest of the atmosphere. The authors initially propose an accretion-based origin for this H ring, but rule it out given the short coupling distance (for the ionized accreting material to couple onto the magnetic field lines) in this region of the white dwarf. Instead, Feige 7 likely began convective dilution as it cooled and exited the DB gap. But due to the magnetic field, the dilution process did not distribute the He across the entire surface as in most DBs. Achilleos et al. (1992) used an offset dipole model to derive a field strength $B_d = 35$ MG, which would clearly suppress convection, and an offset $a_z = 0.15$. The offset nature of the dipole in Feige 7 could further lead to complexities in the atmosphere given that the field strength across the surface is likely to vary significantly. While Feige 7 has a much stronger magnetic field than J0910+2105, the field strength we obtain is still strong enough to inhibit convection and prevent an even distribution of He across the surface.

Caiazzo et al. (2023) discovered both photometric and spectroscopic variations in a rapidly-rotating mixed atmosphere white dwarf, ZTF J203349.8+322901.1 (Janus). Here the H and He lines completely vanish and reappear as Janus rotates with a ~ 15 minute period, suggesting one side is H-dominant and another is He-dominant. Similar to GD 323, there is no evidence of Zeeman-splitting in any of the absorption lines. The authors suggest two possible models to explain the stark differences in the atmosphere. The first is the aforementioned dilution model with a magnetic field strong enough to suppress convection but weak enough to be undetected. Their derived temperature of 34,900 K for the H side and 36,700 K for the He side suggests Janus is exiting the DB gap on the way to becoming a DB and undergoing this dilution process. The second involves the diffusion of H towards regions of high magnetic pressure and low gas pressure. If the magnetic field is stronger on one side, the magnetic pressure would be higher at the pole, and the ion pressure gradient would cause H to diffuse towards the pole. Both models however require a magnetic field that is at least a few tens of kG, which is observationally difficult to detect. Additionally, Caiazzo et al. (2023) derived a large mass of 1.27 $M_\odot$ assuming a carbon-oxygen core and 1.21 $M_\odot$ for an oxygen-neon core. Given the large mass and short spin period, Janus is thus likely a merger product, which could further complicate the process that creates the double-faced atmosphere.

Wesemael et al. (2001) determined that LB 8915 (erroneously called LB 8827), previously known to be a hot DB (Wesemael et al., 1995), is actually a weakly magnetic, variable DBA. Their derived $T_{\rm eff}$ range of 21,300 $-$ 27,700 K places this object within or near the instability strip for pulsating DBs. They did not detect photometric variations, but they do detect changes in the H line strengths. While Wesemael et al. (2001) detect a magnetic field in LB 8915, it is both weak and unconstrained; they made three spectropolarimetric observations of LB 8915, with resulting fields of $B_e = 67 \pm 40, 108 \pm 24$, and 24 ± 13 kG. It is possible the dipole is offset, creating variations in the field strength, however more observations are needed to confirm this.

Lastly, Pshirkov et al. (2020) detected photometric variations in the DBA WD 1832+089 due to rapid rotation. The derived mass of $1.33 \pm 0.01\ M_\odot$ and period of 353 s strongly suggests a past merger occurred to form this white dwarf. Since the variations are due to rotation, it is likely this target also has an inhomogeneous atmosphere, though again no Zeeman splitting is seen in the spectra.

In light of this discussion, it would seem J0910+2105 is most similar to Feige 7 out of the targets we have listed. It is the only one that shows clear Zeeman-splitting alongside J0910+2105. Hardy et al. (2023b) derived an effective temperature of $T_{\rm eff} = 20848 \pm 1077$ K and a mass of 1.13 ± 0.18 $M_\odot$ for Feige 7, although they did not consider H in their models. This puts J0910+2105 at a slightly lower temperature and mass.

Further analysis of magnetic DB or DBA candidates could aid in finding common threads between these objects by expanding this currently small sample. Following up on the the remaining nine unresolved DA+DB candidates from Genest-Beaulieu & Bergeron (2019b) is a natural starting point. Even if Zeeman-splitting is not detectable in the spectra, it is possible these objects have inhomogeneous atmospheres that would manifest as spectral variations with time-series spectroscopy.

3.6. Conclusion

We have detected variations in the strength of the H lines in the DBA white dwarf SDSS J091016.43+210554.2. We obtained time-series spectroscopy at the APO 3.5m telescope and the 6.5m MMT and estimate the rotation period to be either 7.7 or 11.3 hours. We use a magnetic patchy atmosphere model to fit our time-series spectroscopy. We obtain excellent fits using the oblique rotator model, and determine the angle between the magnetic and rotation axis ($\beta = 52°$) and the angle between the rotation axis and line of sight ($i = 13 - 15.5°$). The derived $T_{\rm eff}$ of 16,747 K places this target at a cooler temperature outside of the DB gap. The magnetic field ($B \approx 0.5$ MG) appears to be strong enough to affect convective energy transport in a way that H is brought to the surface from the deep interior more efficiently along the magnetic field lines, thus creating a patchy atmosphere with H polar caps. With the use of our polar cap model, we have successfully shown how the magnetic field affects the distribution of elements in the white dwarf's atmosphere.

CHAPTER 4

Cool Double-Faced White Dwarfs

4.1. Unresolved Binaries? Or Single Stars?

The double-faced objects in the previous chapter are all at $T_{\rm eff} \gtrsim 15,000$ K, such that they have likely formed due to the effects of magnetism on the float-up and convective dilution processes. It then follows that there should be double-faced white dwarfs at cooler temperatures where convective mixing could be impacted by magnetic fields. Perhaps the easiest way to initially detect these unique objects if multi-epoch spectra are not available is by analyzing unresolved binary candidates.

J0910+2105 was identified by Genest-Beaulieu & Bergeron (2019b) as an unresolved binary due to the poor fit obtained with a homogeneous atmosphere model. In this scenario, the system would appear as a single star simply due its distance from Earth and the likely small orbital separation between the two white dwarfs. A model consisting of a DA+DB system provided a much improved fit to their spectrum. Only through the SDSS multi-epoch spectra and detailed follow-up was this system correctly identified as a single star with an inhomogeneous atmosphere. Hence follow-up observations on more unresolved binary candidates can expand the current sample of double-faced white dwarfs.

Rolland & Bergeron (2015) analyzed 16 cool ($T_{\rm eff} < 8000$ K) DAHs and successfully fit six of them using an offset dipole model. However, the remaining ten showed very shallow Hα features compared to what is predicted by models. This over-prediction of the absorption features leads to a discrepancy between the photometric and spectroscopic temperatures obtained by the fits. These differences could be explained by an unresolved companion, so Rolland & Bergeron (2015) obtained effective temperatures for both components as well as the ratio of the radii in their fits, shown in Figure 4.1. Specifically, if the companion has a featureless spectrum (a "DC" white dwarf), then there would be more flux than expected in the Hα region. A white dwarf can have a featureless spectrum if it is at a low enough temperature that atomic transitions in the atmosphere cease ($T_{\rm eff} \lesssim 11,000$ K for helium, $T_{\rm eff} \lesssim 5000$ K for hydrogen), or if a strong magnetic field smears out the absorption features. Since there is no absorption feature, there is more flux received at those wavelengths where lines are usually present such as at 6563 $\mathring{A}$ for Hα. The DA would still contribute less flux due to absorption by the atmosphere, while the DC contributes additional flux since there is no absorption feature. Hence the combined spectrum of both targets shows a weak Hα line, as the DC contribution increases the flux at that wavelength.

The high occurrence of magnetic white dwarfs in binaries from this study is odd, as high field

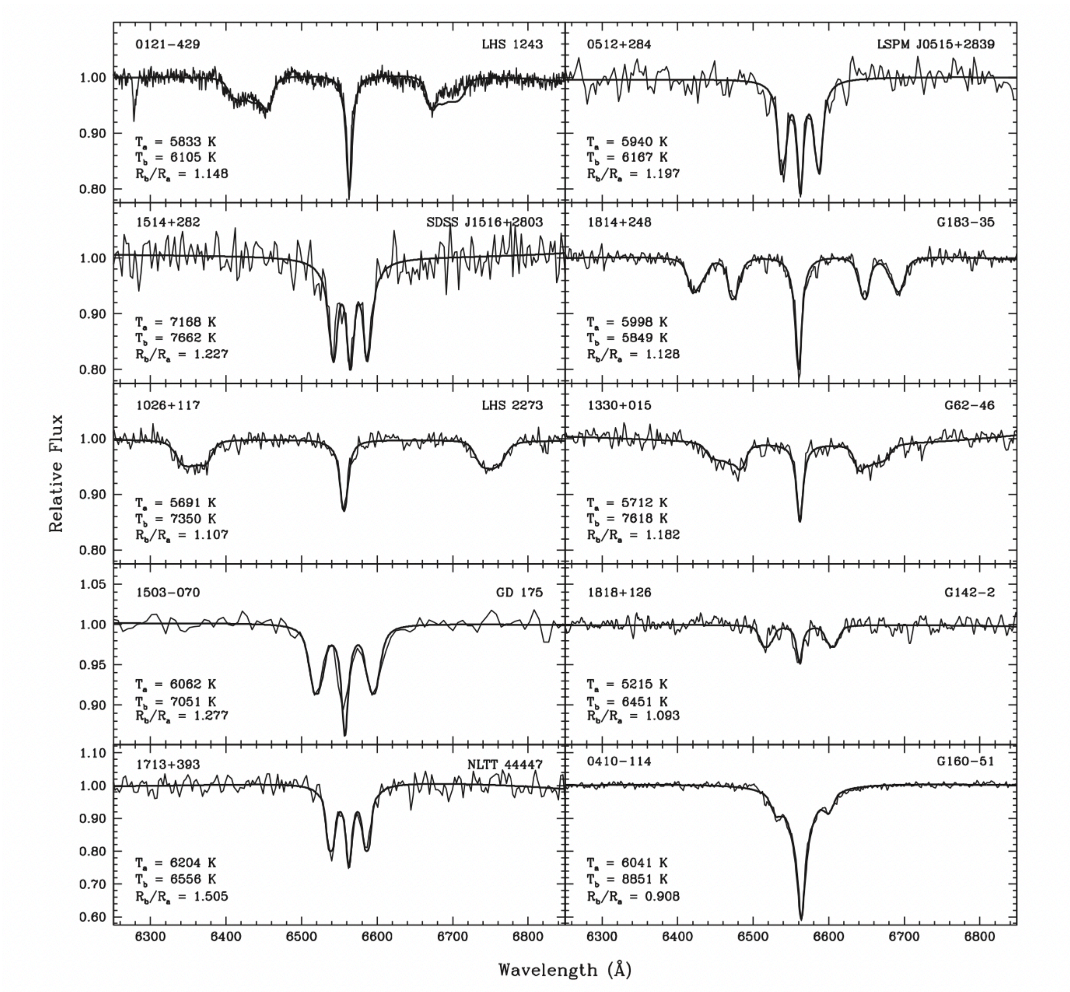

Figure 4.1: Fits to all ten unresolved binary candidates from Rolland & Bergeron (2015). Zeeman-splitting is clear in each system, and excellent fits are obtained assuming an unresolved DC companion.

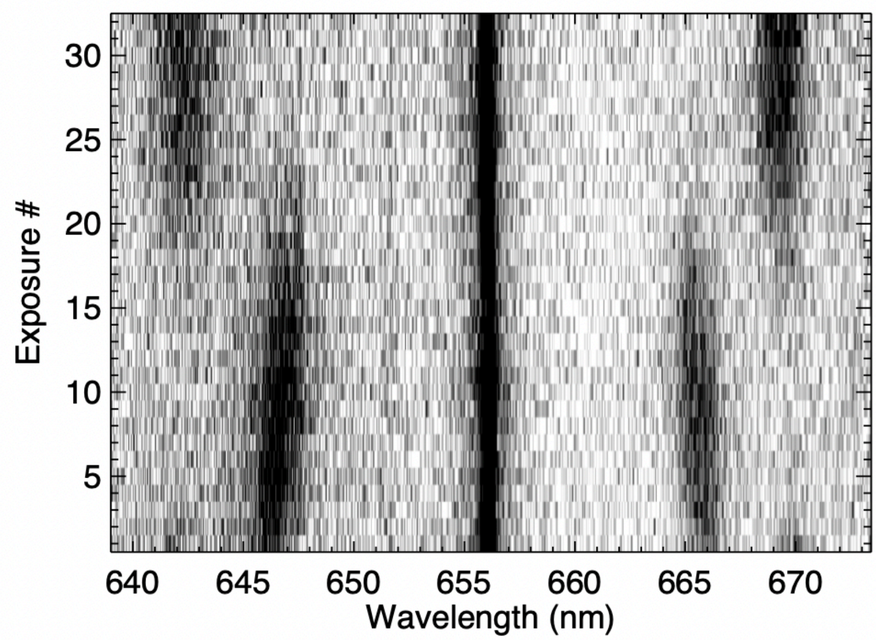

Figure 4.2: Trailed spectrum of G183-35 from Kilic et al. (2019). Individual spectra are represented as pixels, with dark pixels corresponding to the Hα absorption lines. The σ components initially start at $\sim$10 nm away from the π component, but then abruptly shift to $\sim$15 nm away.

white dwarfs in detached binaries are extremely rare (Liebert et al., 2005b, 2015). Follow-up observations on this sample were thus necessary to determine if the systems truly are unresolved binaries. Kilic et al. (2019) obtained time-resolved spectra on one of the candidates, G183-35, and found shifts in the positions of the σ components shown in Figure 4.2. However, these shifts are not due to the radial velocities of a companion in a binary system, as that would cause all three components to be equally blueshifted or redshifted at the same time. Instead, the σ move closer to and further away from the π component. This suggests G183$-$35 is a single star, and as it rotates different regions of the magnetic field come into view. These regions have a varying local field strength, with the polar regions possessing a stronger local field than the equatorial regions. As the white dwarf rotates, the average field integrated over the visible stellar disk changes, which results in the varying line positions.

Another interesting feature of this object is its short rotation period. Kilic et al. (2019) found a rotation period of 3.67 hrs from photometry and 3.98 hrs from spectroscopy. White dwarfs that likely come from single star evolution and do not undergo binary interactions have rotation periods on the order of a day (Hermes et al., 2017b). Hence it is likely this fast-spinning white dwarf has undergone binary evolution, which could also be the source of its magnetic field.

There is also still the issue of the shallow Hα feature. Since G183-35 appears to be a single object, the likely cause of the shallow line profile is an inhomogeneous atmosphere. Since this object is cool ($T_{\rm eff} = 6880$ K), helium lines would not appear in the spectra even if it is present in the atmosphere. Thus it is not as straightforward to analyze the distribution of elements in this target's atmosphere compared to J0910+2105. Regardless, the fact that G183-35 is a single object with a strong field and an inhomogeneous atmosphere is intriguing.

Given the complexities of G183-35, analysis of the remaining 9 targets in the sample is necessary to determine if they also show variations in their spectra and can be classified as isolated objects. If they are indeed single white dwarfs, identifying rapid rotators is important for constraining the source of their fields. In addition, expanding the list of objects with inhomogeneous atmospheres is crucial for understanding the impact of magnetism on the convective processes that lead to spectral evolution. We were awarded time at the Gemini Observatory to obtain time-resolved spectroscopy for all 9 targets and were able to observe 7 of them.

Figure 4.3 shows the location of these 7 targets plus G183-35 in a color-magnitude diagram of the 100 pc white dwarf sample. Interestingly, several of our targets seem to be over-luminous, which is indicative of a low-mass or excess flux from a companion. Here we present our findings for each system. Section 2.2 details our observations, and in Section 2.3 we present our results for each target. We discuss the nature of each object including constraints on their rotation periods and crystallization states, and conclude in Section 2.4.

4.2. Observations

We obtained time-resolved spectroscopy using the 8m Gemini North and South telescopes with the Gemini Multi-Object Spectograph (GMOS) as part of the following programs: GS-2019B-FT-107, GS-2020A-Q-311, GS-2021A-Q-136, GS-2021A-Q-321, GN-2020A-Q-116, GN-2021A-Q-135, and GN-2021A-Q-318. Given the typical short rotation periods of magnetic white dwarfs, our programs were designed to sample periods on the order of minutes and hours. Our observations are summarized in Table 5.1. We used the R831 grating and a 0.5" slit, providing wavelength coverage from 5350 Å to 7710 Å and a resolution of 0.376 Å per pixel. A comparison lamp exposure was taken after every $\sim$15 minutes of science exposures for each target. We used the IRAF Gemini gmos package to reduce these data.

For LHS 1243, our initial sampling was not fine enough to constrain the rotational period. We obtained additional spectra for LHS 1243 at the 6.5m Magellan telescope with the MagE spectrograph. We used the $0.85''$ slit, providing wavelength coverage from about 3400 Å to 7000 Å with a resolving power of R = 4800. Given the short rotational period, we obtained 16×80 s exposures to better sample the period.

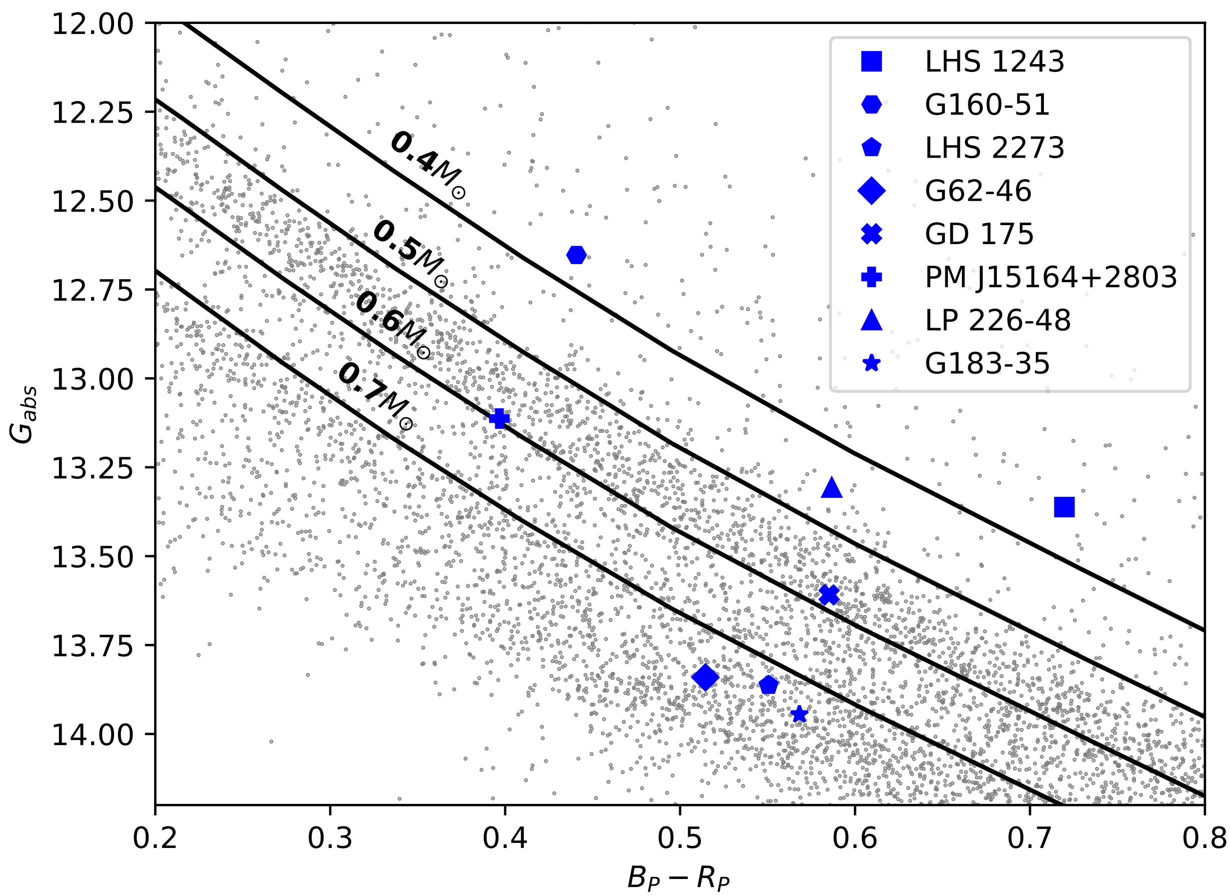

Figure 4.3: Our sample of eight white dwarfs (including G183-35 from Kilic et al. 2019) in the Gaia color-magnitude diagram. Gray points are white dwarfs within 100 pc from the Gentile Fusillo et al. (2021) catalog. Black lines are theoretical cooling models for white dwarfs of various masses (see http://www.astro.umontreal.ca/∼bergeron/CoolingModels).

Table 4.1 Summary of observations for each target. The format for the exposures is (number of exposures) x (exposure duration in min).

Object	RA(J2000)	Dec.(J2000)	Short Exp.	Long Exp.
LHS 1243	01:24:03.9	−42:40:38.4	16 × 1.33 min	27 × 5 min
G160-51	04:12:26.3	−11:17:47.3	None	27 × 5 min
LHS 2273	10:29:07.5	+11:27:19.3	None	25 × 4.1 min
G62-46	13:32:50.7	+01:17:06.3	14 × 2 min	15 × 5 min
GD 175	15:05:49.3	−07:14:40.9	14 × 2 min	55 × 3 min
PM J15164+2803	15:16:25.1	+28:03:20.9	14 × 2 min	15 × 5 min
LP 226-48	17:14:50.8	+39:18:37.4	14 × 2 min	17 × 4 min

Table 4.2 Physical parameters of all 8 white dwarfs in our sample. The effective temperature and masses are derived from the photometric fits from Caron et al. (2023). For the fast rotators, we list the range of magnetic field strengths found in our fits.

ID	T_{eff} [K]	Mass [$M_{\odot}$]	Rotation Period [hr]	B_d [MG]	v_T [km/s]	Cooling Age [Gyr]	DC Offset
LHS 1243	6400	0.430	0.216	10−10.6	53	1.4	1.5
G160-51	7450	0.385	N/A	3.2	47	0.8	0.1
LHS 2273	7041	0.806	0.648	16.0−17.2	78	3.1	1.5
G62-46	7204	0.829	∼hr	6.3−7.7	54	3.1	1.5
GD 175	6889	0.647	N/A	3.2	26	1.9	1.1
PM J15164+2803	8073	0.682	0.576	2.2−3.2	24	1.3	1.5
LP 226-48	6743	0.485	N/A	2.1	38	1.3	1.0
G183-35	6880	0.794	3.98	8.6−10.4	66	3.2	-

4.3. Results

Of our 7 targets, we are able to constrain the rotational period for 3 targets (LHS 1243, LHS 2273, PM J15164+2803) based on the periodic variations in their line centers. We generate Lomb-Scargle periodograms using the orbital fit code MPRVFIT (De Lee et al., 2013) for these 3 targets. One target (G62-46) shows clear variations but we were unable to observe it long enough to constrain its period. The remaining targets do not show variations in their trailed spectra, likely because their rotation periods are longer than a few hours. The analysis of each target is presented in the following subsections.

Before fitting the spectra with an offset dipole model, we construct atmosphere models for each target based on their T_{eff} and $\log g$ as determined from Caron et al. (2023), who used Gaia DR3 parallaxes, Pan-STARRS $grizy$, and near-IR JHK photometry. The physical parameters for each target are given in Table 5.2.

Based on these atmospheric parameters, we construct a grid of magnetic spectra using an offset dipole model to determine the viewing angle i, magnetic field strength B_d, and dipole offset a_z. Figure 1 of Achilleos & Wickramasinghe (1989) shows the 3D model for this geometry, and Figure 4 of Bergeron et al. (1992) demonstrates the magnetic model spectra when varying one of these parameters and holding the other two constant. As the field strength increases, the Zeeman-split components increase in separation from the central Hα line. Changing the dipole offset a_z tends to affect the depth of the split line profiles. Bergeron et al. (1992) demonstrated that it is not possible to constrain the viewing angle from the line profiles alone. As a result, we only allow B_d and a_z to vary as free parameters and manually change inclination to search for the best fit model. Our grid includes various inclination values, but we set the inclination to a fixed value before we begin the fitting process and adjust it if no acceptable solution is found using that inclination value.

Rolland & Bergeron (2015) found that the only way to match the line depths in their spectra was to assume each object was in an unresolved binary with a DC white dwarf, effectively diminishing the depths of the line profiles. Though we assume most of our targets are isolated, we do include this DC offset in our analysis to match line depths between the spectra and our model fits. It is impossible to match the observed line profiles without the addition of this DC component. Our lowest mass targets (LHS 1243, G160-51, and LP 226-48) are likely in binary systems given that they are too low mass ($M < 0.5\ M_{\odot}$) to have formed via single-star evolution. However, this does not rule out the possibility of an inhomogeneous atmospheric composition for these low mass objects. The line profiles simply cannot be fit by magnetic pure H atmosphere models, which is true for all targets in our sample. The new flux when including the DC offset is given by Equation 4.1:

$$\text{Total Flux} = \text{Flux}_{\text{DA}} + \text{DC offset} * \text{Flux}_{\text{DA}} \tag{4.1}$$

Here, Flux_{DA} is the initial flux of the white dwarf. The DC offset term is given in Table 5.2 and is multiplied by Flux_{DA} at a given wavelength which is then added back to the original flux to obtain the new flux, Total Flux. Note that for G183-35, Kilic et al. (2019) allowed the effective temperature to vary in their fits in order to match the depths of the absorption features. Hence there is no corresponding DC offset given for G183-35.

We list several relevant parameters for each white dwarf in Table 5.2, including the effective temperatures and masses from the photometric fits (Caron et al., 2023), as well as the best fit magnetic field strength and rotation period when applicable. We also calculate the transverse velocity and list the cooling ages from the literature, which will be important in the conclusions.

4.3.1. LHS 1243

Figure 4.4 shows the trailed spectra for LHS 1243. Our Gemini observations, shown in the left panel, revealed variations in the split lines. Here we see three split components, with the outer pair abruptly changing wavelength positions from exposure to exposure. Both lines shift away from the central line by ~30 Å before returning to their original location. Given that these shifts are not continuous, we were unable to constrain the period based on the 5 min long exposures from Gemini alone, though it is clear the rotational period should be on the order of ~10 min. Since these exposures were too long to constrain the period, we obtained follow-up spectra at Magellan with 80 s exposures, shown in the right panel of Figure 4.4. The lines still seem to shift abruptly but hold their position for multiple exposures compared to our Gemini data.

In Figure 4.5 (top left) we confirmed the periodicity by using the line centers from the central Hα component to generate a Lomb-Scargle periodogram with the Magellan data. We used the line centers in the first spectrum as the "rest wavelength" and obtained a short rotational period of 12.96

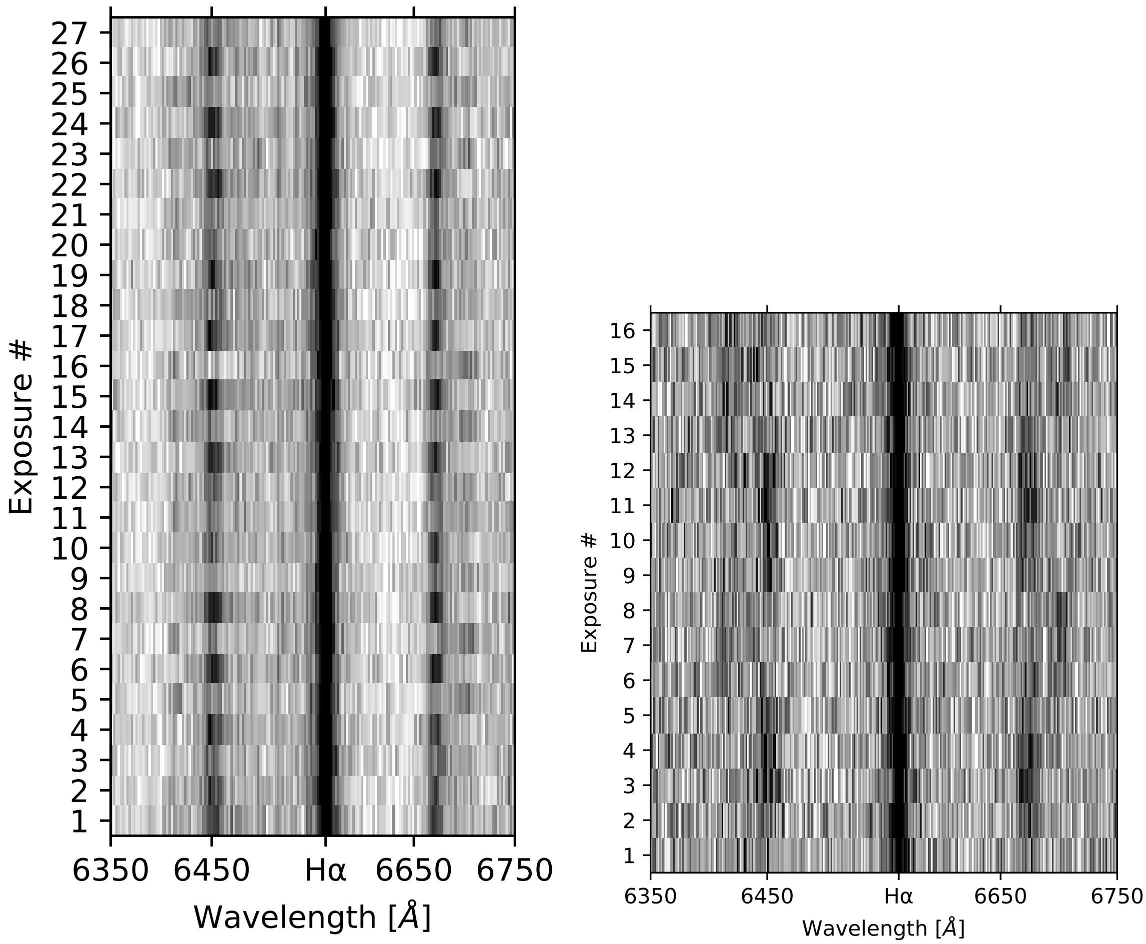

Figure 4.4: *Left:* Gemini time-resolved spectroscopy for LHS 1243 over 2.3 hours. Each exposure is 5 min long. Variations are clear but only hold for one exposure at a time. *Right:* Magellan time-resolved spectroscopy over 26 minutes (16×80 s exposures). Here the starting split line position holds for $\sim$4 exposures, then shifts for $\sim$4 exposures, then shifts back.

$\pm$ 0.2 minutes, with a low velocity semi-amplitude of 9.7 ± 1.6 km/s. This gives a mass function of $f = (8.5 \pm 4.3) \times 10^{-7}\ M_{\odot}$ and a minimum mass companion of $0.005 \pm 0.001\ M_{\odot}$. Given that the outer components of the split Hα line also vary at the same period, the observed variations in the line center is clearly not due to binarity, but because of a complex magnetic field structure resulting in the line position variations as the white dwarf rotates. Note that LHS 1243 could still be in a binary system since it has a relatively low mass of $M = 0.43\ M_{\odot}$.

Figure 4.6 shows the model fits to two of our spectra for LHS 1243. Without incorporating the DC offset (shown as the dotted line), all 3 components of the Hα line are deeper than observed, which would have a significant impact on the best-fit solution. This target was previously studied by Subasavage et al. (2007) who used Johnson V, Kron-Cousins RI, and 2MASS JHK magnitudes to determine its $T_{\rm eff}$ and $\log g$. Their composite spectrum for this object found a solution of $i = 65°$,

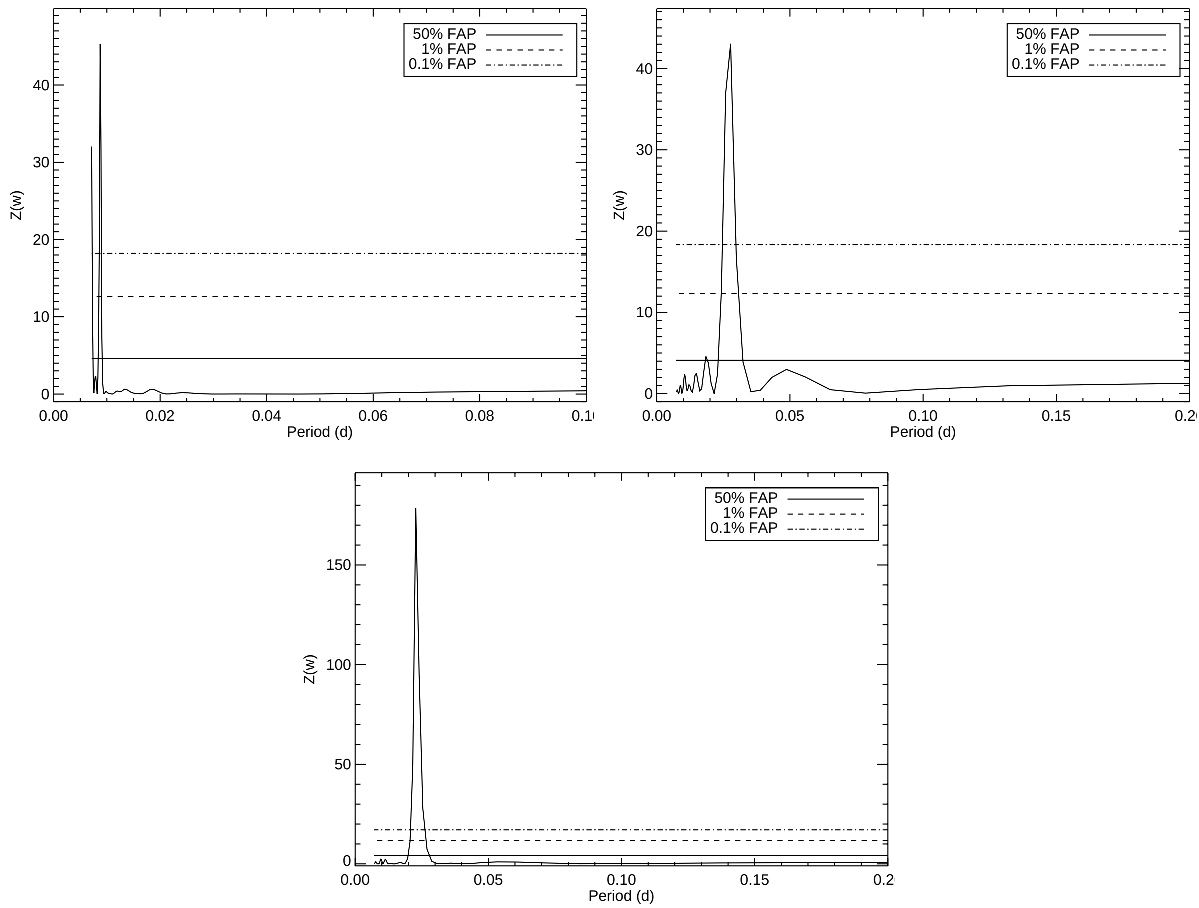

Figure 4.5: Lomb-Scargle periodograms for our three targets that we could constrain the rotational period for. In all three cases, the period is well above the 0.1% False-Alarm Probability limit. The top left, top right, and bottom plots are for LHS 1243, LHS 2273, and PM J15164+2803 respectively.

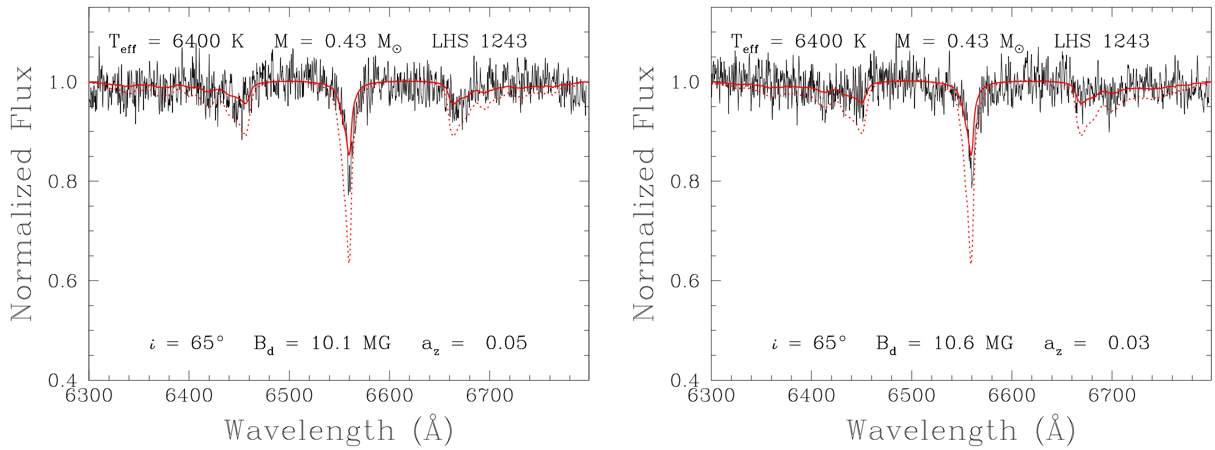

Figure 4.6: Best fits (solid red line) to two separate spectra of LHS 1243 showing the differences in line position and the resulting effect on the dipole field strength. Note that while the offset value is also different and would change the output model, these values are within the uncertainties whereas the magnetic field strengths are not. The dotted red line shows the same model but without the DC offset included. This results in deeper Hα lines that cannot match the observed lines.

$B_d = 9.5$ MG, and $a_z = 0.06$. Given the degeneracies in fitting composite spectra of rapidly rotating magnetic white dwarfs, we assumed the same viewing angle and a positive dipole offset in our fits. B_d is slightly larger in our model fits, but given the rapid rotation in this system, our constraints on the $B-$field strength are superior.

Figure 4.7 (top left) shows how the best fit B_d varies across the Magellan observations. For the first five exposures, the split components are closer to the central line in the trailed spectra, resulting in a lower B_d solution ranging from 10.0 to 10.3 MG. At the sixth exposure, the split lines move further from the central line, resulting in a larger B_d solution of 10.5 MG. The field strength remains high for several exposures before dropping back down to around 10.3 MG for multiple exposures, and then increasing to 10.6 MG for the remaining spectra.

4.3.2. LHS 2273

Figure 4.8 shows the trailed spectra for LHS 2273. Here the variations in the line positions are more gradual compared to LHS 1243. The total shift is ∼60 Å but occurs over the span of nine exposures, where each exposure is 4.13 min long. Figure 4.5 (top right) shows the Lomb-Scargle diagram for LHS 2273 based on the shifts in the central Hα line. Based on this and also the variations seen in the split components, the best-fit period is 38.88 ± 2.53 min.

Figure 4.9 shows fits to two of the spectra for LHS 2273. Here the $B-$field strength changes slightly from 16.0 to 17.2 MG. Figure 4.7 (top right) displays how the best fit magnetic field strength varies over our observations, overall matching the pattern seen in the trailed spectra as the

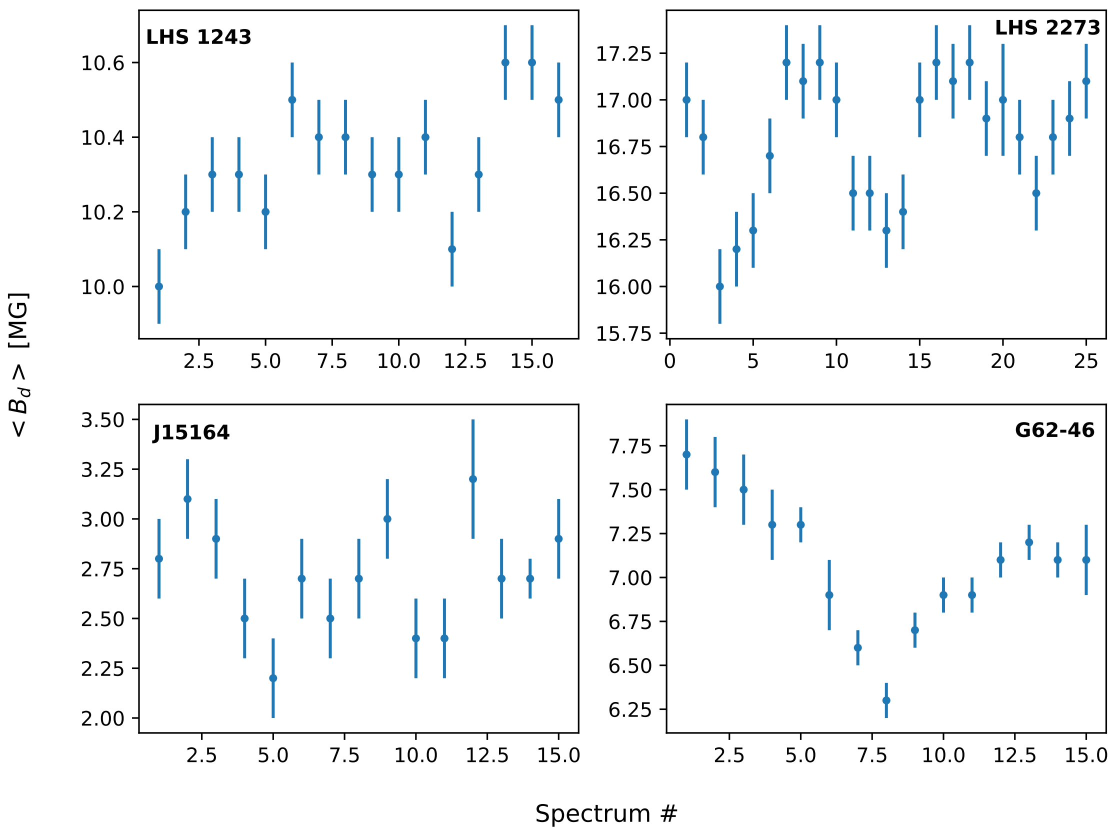

Figure 4.7: The best fit B_d of each spectrum for our four targets that show spectroscopic variability. The changing position of the Zeeman-split Hα lines in the spectra results in a different $B-$field strength. From top left to bottom right: LHS 1243, LHS 2273, PM J15164+2803, and G62-46.

components oscillated from shorter to longer wavelengths. The split lines start out far from the central line, resulting in a higher B_d solution of $\sim$17 MG. The lines then quickly move closer to the central line, dropping the solution to 16 MG. Over the next several spectra, the split lines gradually move away from the central line, resulting in a gradually increasing B_d solution, reaching 17.2 MG. We were able to capture multiple rotations with our Gemini data, so the B_d strength continues to gradually oscillate between 16.0 and 17.2 MG and allows us to easily constrain the period.

Bergeron et al. (1997) previously fit this target using a centered dipole model and found $B_d = 18$ MG and $i = 60°$. However, the predicted Zeeman components were much deeper than observed, hence the initial prediction of an unresolved DC companion. Given that we are using an offset dipole model, and we include the unresolved DC companion to better fit the fluxes of the Zeeman components, our best-fitting model parameters differ slightly. Hardy et al. (2023a) used the SDSS spectrum of this target to fit the same three parameters and found $B_d = 19.18MG$, $a_z = 0.30$, and $i = 46°$. The slight difference in the magnetic field strength and the notable discrepancy in a_z are not surprising given the rapid rotation of this object, the degeneracies in fitting magnetic white dwarf spectra, and that the SDSS spectra are composite of multiple 15 min long exposures.

4.3.3. PM J15164+2803

Figure 4.10 shows the trailed spectrum for our final target we could constrain the period for, PM J15164+2803. The oscillations are clear but the magnetic field strength is low, resulting in smaller overall wavelength shifts of $\sim$10 Å. However the depths of the Hα lines change rapidly as evident by the contrast in darker and lighter pixels from spectrum to spectrum. This does not have a large effect on the B_d solution but does change a_z which should be constant throughout the spectra.

Figure 4.5 (bottom) shows the Lomb-Scargle diagram for PM J15164+2803 based on the split components of the Hα line. The best-fit period is 34.56 ± 1.87 minutes. Figure 4.11 shows fits to two of the spectra for this target. The most notable feature in this figure is that our models have trouble matching the depth of the central Hα component.

Figure 4.7 (bottom left) shows the magnetic field variations, again matching the oscillations in the trailed spectra for this object. The wavelength changes in the trailed spectra are relatively small so the B_d solution similarly changes slightly, though the variations are clear, ranging from 2.2 to 3.2 MG. Here the split components start further from the central line, so the B_d solution is larger, ≈ 2.8 MG. The lines then begin to shift closer to the central line, decreasing the fit B_d to ≈ 2.2 MG. Again we were able to observe multiple rotations of this target, allowing us to easily constrain the period and observe the changes in the best fit B_d.

Hardy et al. (2023a) also analyzed this target, but they found that the absorption lines were too shallow to fit their models and that no combination of parameters could reproduce the observed spectrum. Though they did not definitively arrive at a specific solution, they suggested rapid rotation

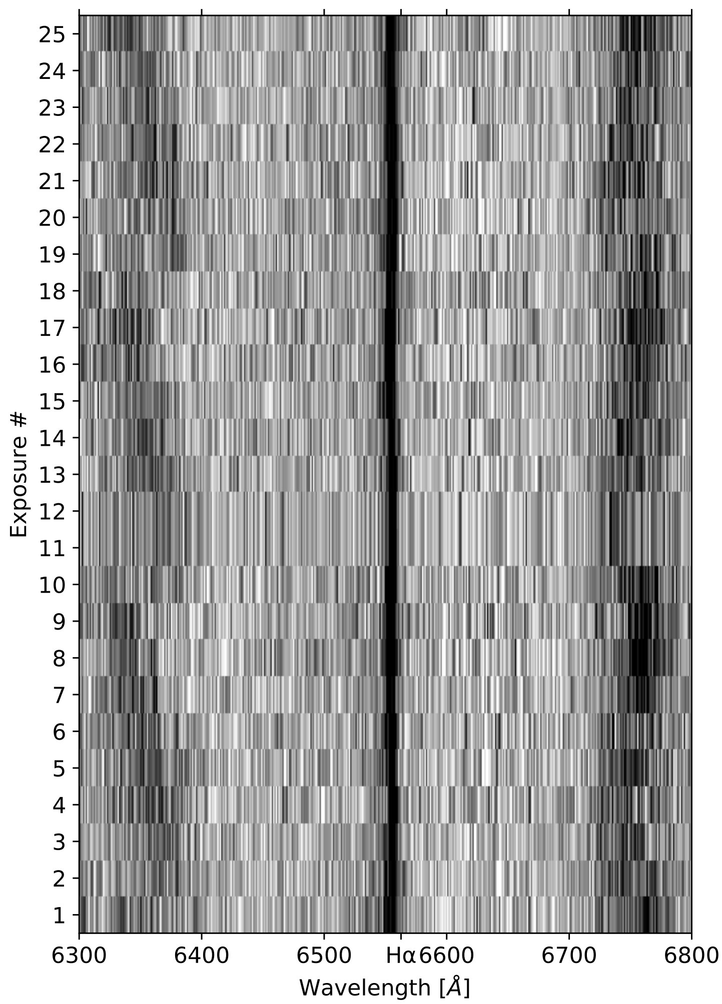

Figure 4.8: Time-resolved Gemini spectra for LHS 2273 over 1.85 hours. The Zeeman split components vary over a period of 39 min.

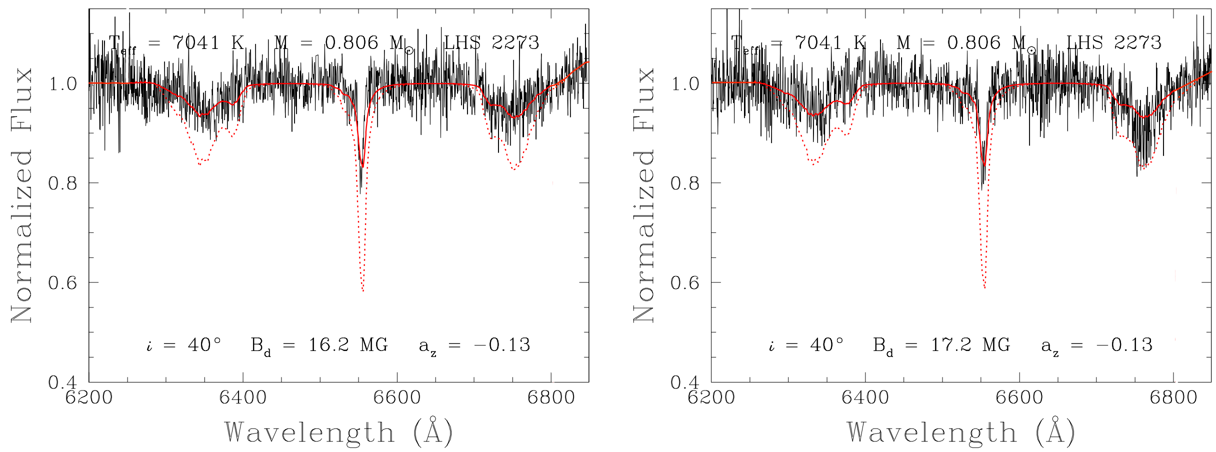

Figure 4.9: Representative fits to two of our LHS 2273 spectra.

of an inhomogeneous atmosphere as the cause. Given that the SDSS spectra are combinations of several 15 min long exposures and that the rotation period of this object is about 35 min, it is not surprising that Hardy et al. (2023a) could not fit the SDSS spectrum.

4.3.4. G62-46

Figure 4.12 shows the trailed spectra for G62-46. Here we were only able to capture ∼1 full rotation so we cannot confidently constrain the period. However, the variations in the split lines are clear, so this target is still likely to have a rotational period on ∼hour timescales. Here we see wavelength shifts of ∼30 Å.

Figure 4.13 shows two of our example fits for G62-46. While we cannot constrain the rotational period, we still fit each individual spectrum. Figure 4.7 (bottom right) shows each best B_d solution for our exposures. Once again the patterns seen in the positions of the split components match what we see in the B_d strength. The line positions start further from the central line then gradually reach their closest position halfway through our observations, then move back towards the end. The B_d similarly starts at its largest value of 7.7 MG and reaches a minimum of 6.3 MG halfway through our observations, then increases back.

4.3.5. The Rest

In Figure 4.14 we show the trailed spectra for our remaining three targets. These three did not show variations in their spectra, so we simply combined the spectra into an average to increase the signal-to-noise, and then fit the combined spectrum. These fits are shown in Figure 4.15. The field strengths for these three targets range from 2.1 to 3.2 MG.

Hardy et al. (2023a) analyzed LP 226-48 and found $B_d = 2.4MG$, $a_z = 0.30$ for $i = 50°$, whereas we found $B_d = 2.1MG$, $a_z = -0.13$ for $i = 30°$. The $B-$field measurements are

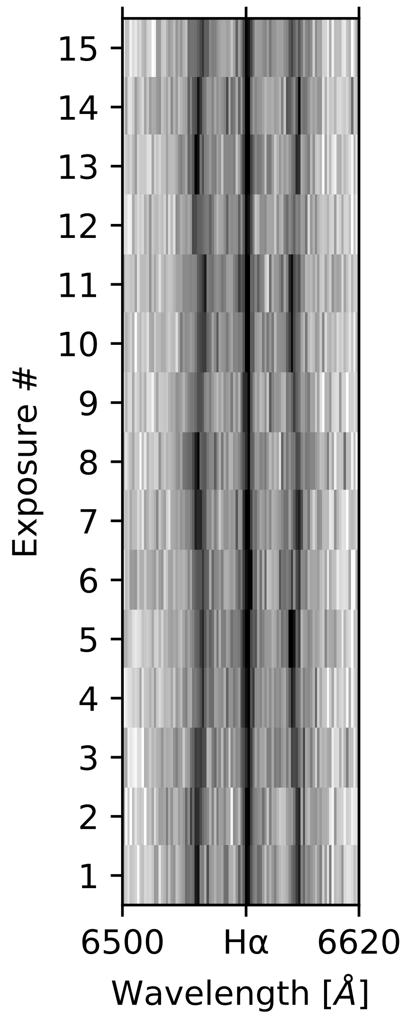

Figure 4.10: Gemini time-resolved spectroscopy for PM J15164+2803. We only plot the longer exposure times here given the higher signal-to-noise. These observations were taken over 1.33 hours.

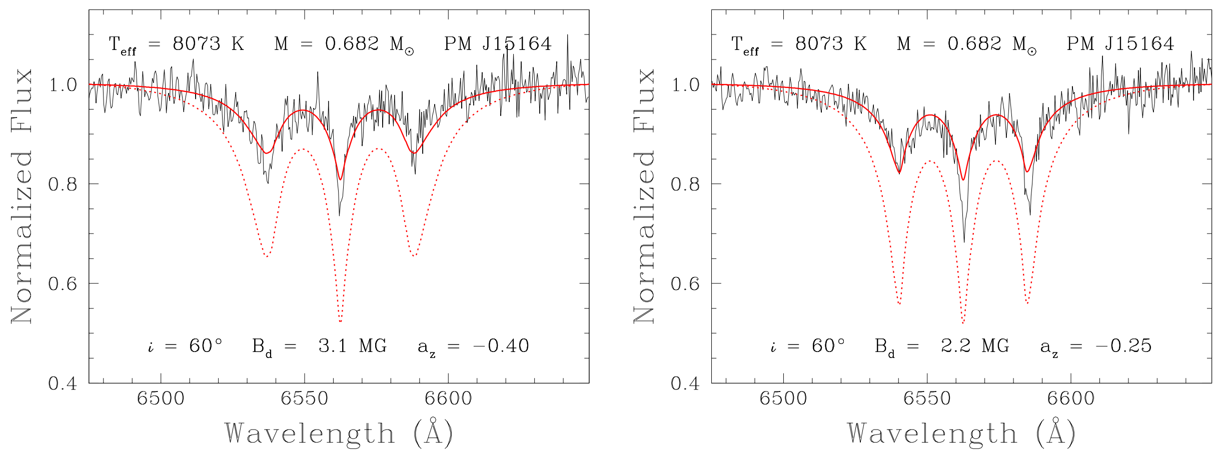

Figure 4.11: Best fits to two of our PM J15164+2803 spectra. Here the depths of the Hα lines vary significantly, resulting in different a_z solutions.

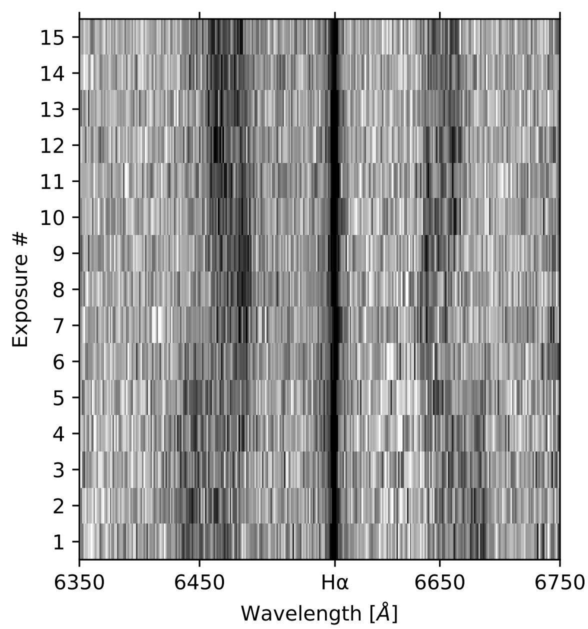

Figure 4.12: Trailed spectra for G62-46. The changes in position are clear, but our observation span of 1.33 hours was too short to observe a full rotation. Regardless, this target is likely to be a fast rotator.

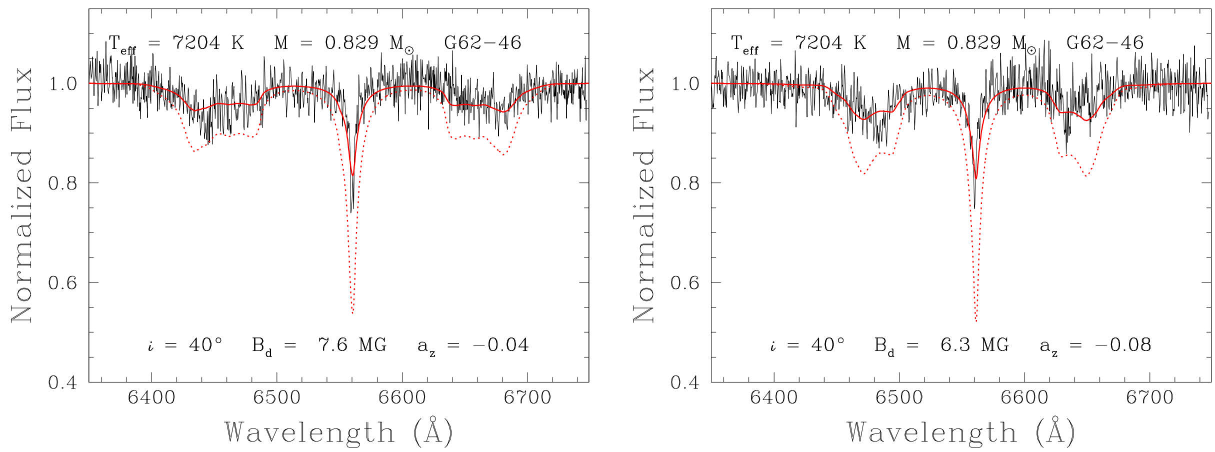

Figure 4.13: Two example fits for G62-46.

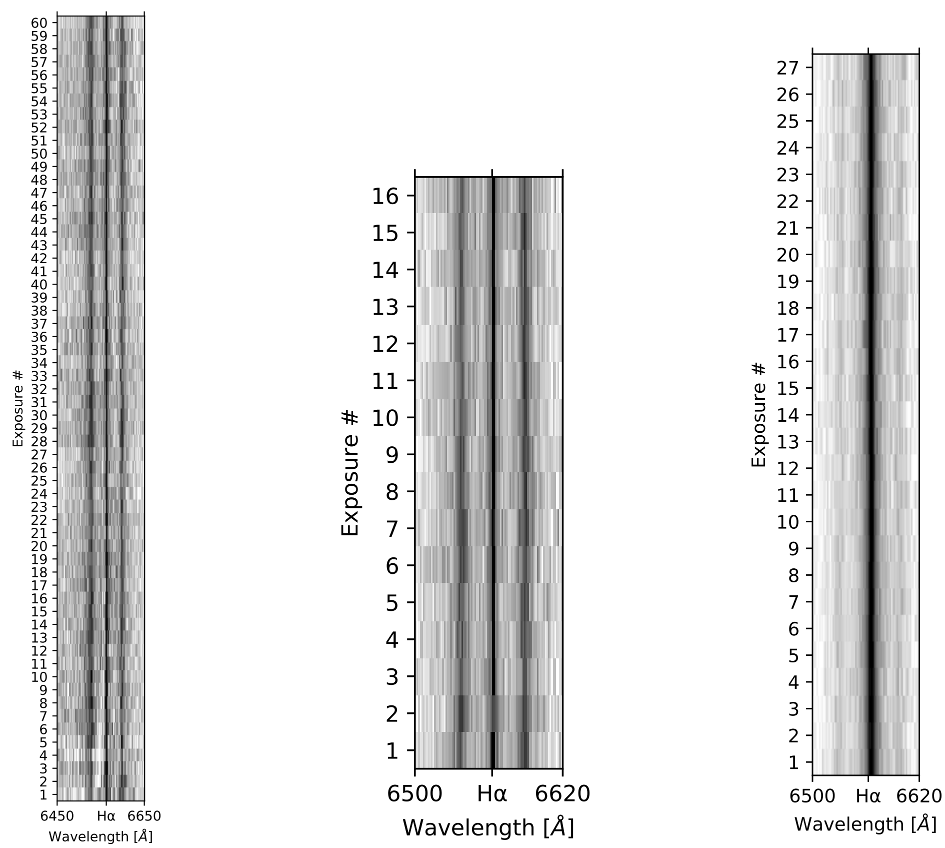

Figure 4.14: Trailed spectra for our remaining targets that do not show significant spectroscopic variations: GD 175, LP 226-48, and G160-51.

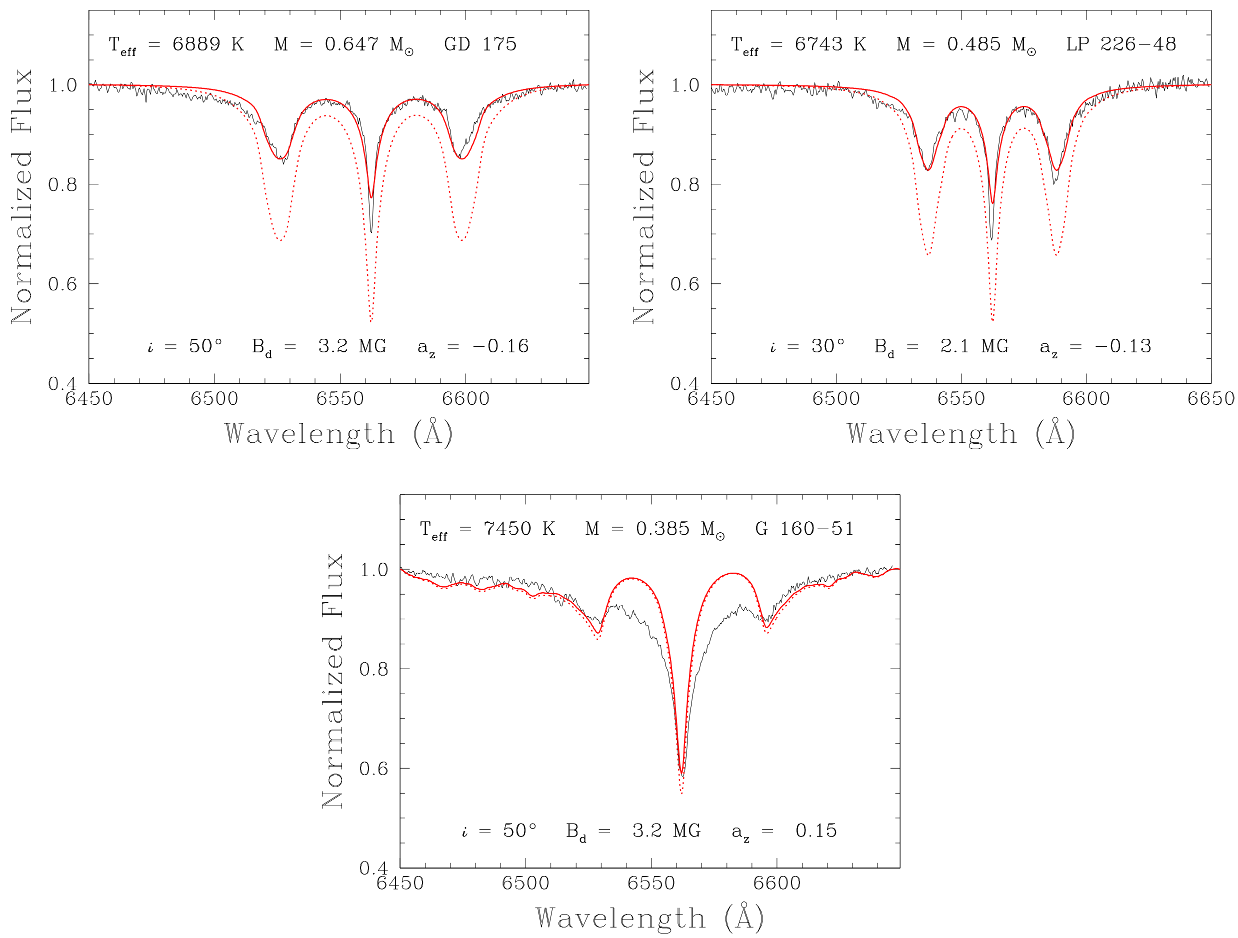

Figure 4.15: Fits for the combined spectra of GD 175, LP 226-48, and G160-51. The poor fit for G160-51 (bottom) suggests this target may be in a binary with a DA companion (though see Section 5.4.3 for a better explanation).

consistent within the errors, but the difference in a_z is likely due to the noticeably different inclination adopted in that work.

We are unable to produce an adequate fit for G160-51. This target is very different from the rest of the sample; the Zeeman-split components separate from the central Hα line, which is deeper and broader on average than the other targets. The low surface gravity obtained from the photometric fit suggests this target is a low-mass white dwarf with $M = 0.385\ M_\odot$ and it is possibly in a binary system with another DA companion that could explain the unusual Hα line profile. However, we will show in the following chapter that we can successfully model this system as a single white dwarf.

4.4. Discussion

4.4.1. Rotational Variability

Of the 10 white dwarfs in proposed unresolved binaries from Rolland & Bergeron (2015), we now have obtained time-resolved spectroscopy on 8 of them (including G183-35 from Kilic et al. 2019), 5 of which show variations in their spectral features on the scale of hours or shorter. In this work we successfully constrained the rotation periods for 3 targets by observing the changing position in their Zeeman-split Hα lines: LHS 1243, LHS 2273, and PM J15164+2803. Each target has a rotation period less than an hour: 12.96 $\pm$ 0.2, 38.88 $\pm$ 2.53, and 34.56 $\pm$ 1.87 min, respectively.

We used an offset dipole model to fit each spectrum to see how the average surface magnetic field strength changes as the white dwarf rotates. The strength for each target varies from 10$-$10.6, 16.0$-$17.2, and 2.2$-$3.2 MG respectively. The magnetic field itself does not change strength, rather with the magnetic axis offset from the rotation axis, we see a different magnetic field distribution across the stellar surface as the objects rotate. G62-46 shows clear variations but the rotation period is longer than our observations, though not by much. The remaining three targets did not show any variations in their spectra, so we simply fit one model to the combined spectrum. It is likely these targets have rotation periods much longer than a few hours.

4.4.2. Patchy Atmospheres

All of our targets require dilution by a hypothetical DC companion (or a likely DA companion in the case of G160-51) in order to match the line profile depths between our models and observations. Without it, our model spectra always produce deeper line profiles that result in poor fits to the observations. However, there is no evidence of significant radial velocity variations in our data. All of the variations seen in the Hα line profiles of our targets can be explained by rotational modulation of a complex magnetic field structure.

In Rolland & Bergeron (2015), under the assumption of an unresolved binary, all of these objects were found to be within the non-DA gap between 5000 and 6000 K (Bergeron et al., 1997). Now with Gaia parallaxes and assuming single objects, our new estimates place them at warmer temperatures between 6400 and 8000 K. It is clear from the discrepancies between the spectroscopic (Rolland & Bergeron, 2015) and photometric temperature estimates (Caron et al., 2023) and also the discrepancies between the predicted and observed line profiles that these atmospheres are not pure H. In fact, rotation of a magnetic white dwarf with a chemically inhomogeneous surface, similar to the Ap/Bp stars, can explain the spectroscopic variations seen in these stars. Note that the three low mass white dwarfs in our sample are likely in unresolved binaries, but can still have inhomogeneous atmospheres.

GD 323 is an excellent example of a white dwarf with an inhomogenous surface composition, where the strengths of the H and He lines change over a period of about 3.5 h (Pereira et al., 2005). GD 323 is hot enough to show both H and He lines, and therefore is classified a DAB, but our targets are too cool to show He absorption lines. In the case of GD 323, Pereira et al. (2005) argued that an inhomogeneous surface composition can be the result of the dilution of a thin hydrogen atmosphere with the underlying helium convection zone. The presence of magnetic fields on MG scales rules out the same scenario for our targets. Tremblay et al. (2015) ran radiative magnetohydrodynamics simulations and found that even a magnetic field of $\sim$50 kG could suppress convection, which was observationally confirmed by Gentile Fusillo et al. (2018). Given that all of our targets have fields stronger than 2 MG, it seems likely that there should be no convective mixing in our targets. Hence, the source of an inhomogenous composition in our targets is currently unclear.

4.4.3. Source of Magnetism

We first consider the fossil origin of the magnetic field from Ap/Bp stars in our rapid rotators. We use the initial-final mass relation from Cummings et al. (2018) to estimate the initial mass of the progenitor stars from our white dwarf masses. LHS 1243 is too low mass (0.430 $M_{\odot}$) to have evolved from single star evolution. It is extremely likely this object underwent some binary interaction in the past, leading to both the short rotation period and the magnetic field. This would involve two common envelope evolutionary phases similar to NLTT 12758 (Kawka et al., 2017) as well as a dynamo driven by differential rotation (Tout et al., 2008; Briggs et al., 2018b), or the expulsion of the majority of the envelope during a common envelope phase merger. PM J15164+2803 has a mass of 0.68 $M_{\odot}$, which yields an initial mass of 2.41 $M_{\odot}$. Our more massive targets, LHS 2273 and G62-46 (0.806 $M_{\odot}$ and 0.829 $M_{\odot}$), yield similar initial masses of 3.33 and 3.45 $M_{\odot}$. Therefore it is possible for our higher mass targets to have originated from these highly magnetic main-sequence stars. However, Hermes et al. (2017b) analyzed the rotation rates of pulsating white dwarfs using asteroseismology and found that white dwarfs that evolved from 1.7 - 3.0 $M_{\odot}$ progenitors typically have $\sim$day rotation periods. These progenitors form average mass

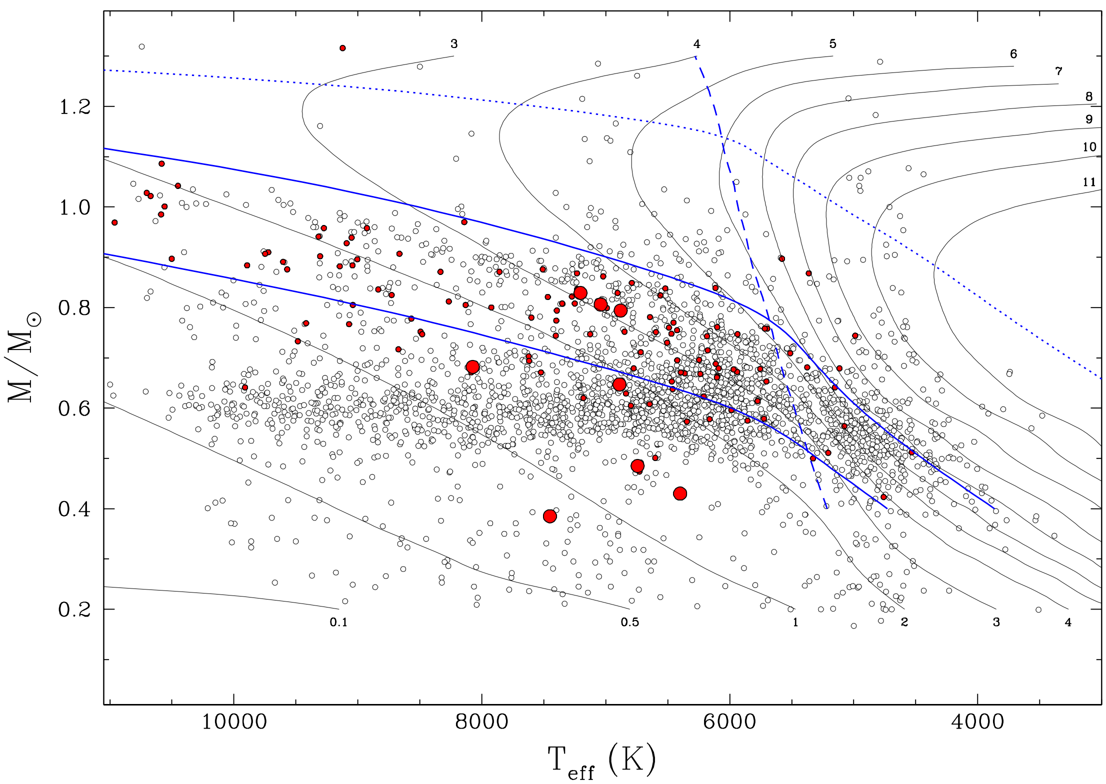

Figure 4.16: Stellar masses as a function of effective temperature for white dwarfs in the Caron et al. (2023) sample. Solid curves are theoretical isochrones, labeled in units of 10^9 yr, obtained from cooling sequences with C/O-core compositions, $q(\mathrm{He}) \equiv M(\mathrm{He})/M_\star = 10^{-2}$, and $q(\mathrm{H}) = 10^{-4}$. The lower blue solid curve indicates the onset of crystallization at the center of evolving models, while the upper one indicates the locations where 80% of the total mass has solidified. The dashed curve indicates the onset of convective coupling, while the dotted curve corresponds to the transition between the classical to the quantum regime in the ionic plasma. Our targets are marked in large red circles.

white dwarfs (0.51 - 0.73 $M_\odot$), and all four of our white dwarfs with $M \geq 0.68\ M_\odot$ in our sample (see Table 5.2) have hour timescale rotation periods. Hence, a fossil origin is unlikely to explain the observed magnetism and rapid rotation in these white dwarfs.

Crystallization, though still not well understood, could also generate magnetic fields via the generation of a dynamo. For example, Ginzburg et al. (2022) show that fields up to 7−10 MG can be generated for a crystallized white dwarf with a spin period of 0.5−1 h (see their Figure 4). Caron et al. (2023) performed a spectrophotometric analysis of 2880 cool white dwarfs within 100 pc. The vast majority of their magnetic objects lie within or near the region where crystallization occurs in Mass-$T_{\rm eff}$ space, shown in their Figure 17. This suggests a strong correlation between the presence of a magnetic field and core crystallization.

Caron et al. (2023) hypothesized that the transition of most cool, He atmosphere white dwarfs to H dominated atmospheres may be due to the crystallization process. In this scenario, the center crystallizes first and the crystallization front propagates outward, generating a dynamo which creates the magnetic field. This field then inhibits convection, allowing H which was originally diluted in the mixed H/He envelope to diffuse upwards, resulting in a H atmosphere. Hence, this scenario could explain the prevalence of H atmosphere white dwarfs below 5200 K.

We reproduce the stellar mass versus effective temperature diagram for the Caron et al. (2023) sample here in Figure 4.16, highlighting our sample of magnetic white dwarfs with large red circles. Among our 8 magnetic DA white dwarf targets, only three have begun crystallization. Based on the evolutionary models (Bédard et al., 2020), we expect LHS 2273, G62-46, G183-35 to have 17, 18, and 46% of their cores crystallized.

Note that the evolutionary models shown in Figure 4.16 assume equal amounts of C and O in the core. If the oxygen abundance in the core is higher (e.g. ~ 0.8, Giammichele et al., 2018, 2022), crystallization would start earlier because the average charge of the ion and the coupling constant are larger. At $0.7\ M_\odot$, a larger oxygen abundance in the core would shift the start of crystallization from $T_{\rm eff} = 7000$ K to 8000 K. Hence, the crystallization region (the area between the two blue lines shown in Figure 4.16) could encompass almost all magnetic white dwarfs included in this Figure, including all but the three lowest mass white dwarfs in our sample.

While crystallization could be the driving force for dynamo generation in five of our targets, three of our targets have not begun crystallizing, nor can crystallization explain the rapid-rotation shown in five of our targets. Binary evolution is the most likely candidate for the observed rapid rotation in addition to the source of the magnetic field. We include the discussion of crystallization-driven dynamos given that it could play a role for five of our targets, but we expect that seven of our targets have undergone some form of binary evolution in the past. Additionally, not every white dwarf that lies within the crystallization region in Figure 4.16 is magnetic, so it would seem crystallization alone cannot produce the dynamo required to generate a magnetic field. It is tantalizing to suggest rapid rotation is also needed to drive up this dynamo and produce magnetism. Only one of our crystallized targets (GD 175) does not show signs of hour timescale rotations, though it could rotate on day-long timescales. Further time-series spectroscopy on these magnetic white dwarfs that lie within the crystallization region could determine what fraction have fast rotation periods and if this rotation aids in producing magnetism in crystallized white dwarfs.

Bagnulo & Landstreet (2022) found two distinct magnetic white dwarf populations based on mass: those above $0.75 M_{\odot}$, which are almost certainly merger products given the high mass and extremely strong magnetic fields ($\sim$ 100 MG); and those below $0.75 M_{\odot}$, likely the products of single-star evolution and fields that actually grow over time, typically in the first 2-3 Gyr of cooling (see also Amorim et al. 2023). The class of hot ($10000 < T_{\rm eff} < 25000$ K) carbon-rich DQs exhibit properties consistent with double-degenerate mergers: large mass ($> 0.8\ M_{\odot}$, Coutu et al., 2019), high transverse velocity, rapid rotation, and magnetism (Dunlap & Clemens, 2015). To determine the progenitors of these objects, Kawka et al. (2023) conducted population synthesis studies for double degenerate mergers and He star mergers with a white dwarf. They found that the double-degenerate mergers produced white dwarfs with larger delay times, higher mass, and older kinematic ages. These findings are consistent with the hot carbon-rich DQs and strongly support the idea that they form via double-degenerate mergers.

Binary mergers can explain a significant fraction of ultramassive white dwarfs (Kilic et al., 2023), however binary evolution is still relevant even for average mass white dwarfs. Binary population synthesis calculations of Temmink et al. (2020) find that the mass distribution of single white dwarfs that form through binary mergers peak at $0.64\ M_{\odot}$, with a median at 0.65 and mean at $0.71\ M_{\odot}$. Briggs et al. (2015) considered only mergers that could generate magnetic white dwarfs and found a mean predicted mass of $0.88 M_{\odot}$ for magnetic white dwarfs compared to $0.64 M_{\odot}$ for all white dwarfs. Observational signatures of a single white dwarf that form through binary evolution may include rapid rotation, magnetism (Tout et al., 2008), or large tangential velocity.

Of our eight targets, three of them (LHS 1243, G160-51, and LP 226-48) are too low mass to have formed via single star evolution ($M < 0.5 M_{\odot}$) given the age of the Universe. Hence, these three stars must have gone through binary evolution. LHS 1243 also happens to be the fastest rotator in our sample. Of the remaining five targets that are more average in mass, four of them (WD 1026+117, PM J15164+2803, G62-46, G183-35) have magnetic field strengths on MG scales and rotate on minute/hour timescales, strong indicators of past binary interactions.

We also calculate the transverse velocity of each target using proper motions and parallaxes from Gaia DR3 to see if any of them are outliers in their kinematics compared to the Galactic disk. Temmink et al. (2020) showed that the ages of single white dwarfs that form through binary evolution are significantly underestimated, and that individual white dwarfs appear ~ 1 Gyr younger than they are if binary evolution is ignored. Hence, some of the single white dwarfs that form through binary evolution may appear as outliers in their kinematics. Kilic et al. (2020) looked at the velocity distributions for DAs with cooling ages below and above 2 Gyrs. For our five targets that are younger than 2 Gyrs, only one (LHS 1243, the fastest rotator) has a notably large velocity of 53 km/s, faster than $\sim$70% of other young DAs. All three of our older targets though have larger transverse velocities than $\sim$60% of the rest of the population older than 2 Gyrs, with LHS 2273 and G183-35 (both fast rotators) in the top $\sim$10 and 20% respectively. This ultimately leaves one object with no particularly noteworthy qualities, GD 175. This object has a mass of $0.65M_{\odot}$, an unremarkable transverse velocity, and no signs of rotation. Hence, 7 of the 8 magnetic white dwarfs in our sample show evidence of past binary evolution that would explain their rapid rotation, magnetism, or low mass.

An emerging class of magnetic white dwarfs dubbed "DAHe" show variable He emission with short rotation periods (Reding et al., 2023; Manser et al., 2023). Their similarities to our sample are noted given the rapid rotation and magnetic field strengths. However, this class of $\sim$25 objects occupy a much narrower range of mass and color, and their formation mechanism is still unclear. Therefore we cannot make any direct connections between that class and our sample besides the idea of binary interactions/mergers. Time-series spectroscopy of additional magnetic white dwarfs across a wider range of effective temperatures and masses will be necessary to detect more systems with variable line profiles and confirm this hypothesis, as well as further advances in the theoretical framework of magnetic field generation.

4.5. Conclusion

To summarize, seven of our eight targets show at least two indicators of binary evolution: magnetism, and either rapid rotation or low mass. LHS 1243 has both a low mass and short rotational period. G160-51 and LP 226-48 do not show signs of rapid rotation but have too low mass to have formed from single-star evolution. LHS 2273, G62-46, PM J15164+2803, and G183-35 are average mass but have rotational periods typical of binary evolution products. Crystallization could play a role in generating a dynamo for five of our targets including GD 175, however this mechanism itself cannot explain the rapid rotation we see in the four other objects. It is possible that the magnetic field of GD 175 is truly a fossil field but we cannot rule out crystallization either.

Each of these objects require dilution by an unseen companion in our fits to reproduce the shallow Hα features. Five of them however appear to be single objects based on the nature of the observed variations, thus an inhomogeneous atmosphere is a more likely solution to explain their unique absorption profiles. These objects all lie in a temperature regime where the magnetic field could have impacted the convective mixing process (as opposed to convective dilution at hotter temperatures). At this point, we have not yet implemented our polar cap model to analyze the specific distribution of elements in the atmospheres of these cooler objects. Regardless, our targeted follow-up of unresolved binary candidates has revealed unique features of the growing class of double-faced white dwarfs. Of course, there are still other candidates ripe for study to improve our understanding of these exotic white dwarfs.

CHAPTER 5

The Emerging Class of Double-Faced White Dwarfs

5.1. Finding More Targets

J0910+2105 was initially identified by Genest-Beaulieu & Bergeron (2019b) as an unresolved binary system based on their poor spectral fit using a homogeneous atmosphere model. Having conducted a comprehensive photometric and spectroscopic analysis on the DB white dwarfs in the SDSS, Genest-Beaulieu & Bergeron (2019b) found nine other unresolved DA+DB binary candidates that exhibit issues similar to those as J0910+2105 in their fits. Figure 5.1 shows the model fits to SDSS J011356.38+301514.62. Similar to J0910+2105, a single-star homogeneous atmosphere model fails to reproduce the observed spectrum. Instead, an unresolved DA+DB binary obtains a better fit to the data. As we have seen with J0910+2105 however, these systems could be single white dwarfs with inhomogeneous atmospheres.

Given that there are nine other unresolved binary candidates in Genest-Beaulieu & Bergeron (2019b), we initiated a time-resolved spectroscopy survey to understand their nature and the emerging class of double-faced white dwarfs. Specifically, as we find more of these double-faced objects, we can begin to understand the range of possible surface geometries (extent of the H and He caps/belts etc), their location on the cooling sequence, the impact of magnetism, and the presence or lack of photometric variability and its significance. In this paper we present our findings on six of the unresolved binary candidates listed in Genest-Beaulieu & Bergeron (2019b), as well as the magnetic DBA white dwarf LB 8915. We detail our observations and target selection in Section 2, followed by the model atmosphere analysis in Section 3. In Section 4 we discuss our findings with respect to other variable mixed-atmosphere white dwarfs, and detail the properties of the emerging class of double-faced white dwarfs. We then conclude in Section 5.

5.2. Observations and Target Selection

Figure 5.2 shows our target selection in the Gaia color-magnitude diagram, along with several inhomogeneous atmosphere white dwarfs with confirmed spectral variations in the literature. We also show isotherms and evolutionary models for various masses assuming pure He atmospheres (Bergeron et al., 2011; Bédard et al., 2020). Seven of the candidates from Genest-Beaulieu & Bergeron (2019b, black and blue symbols) are in fact overluminous; we have time-series spectra for five of these and none show spectroscopic variations over a few hours. We show in Section 3 that these five targets are likely unresolved binaries. Two of the targets however, J0847+4824 and

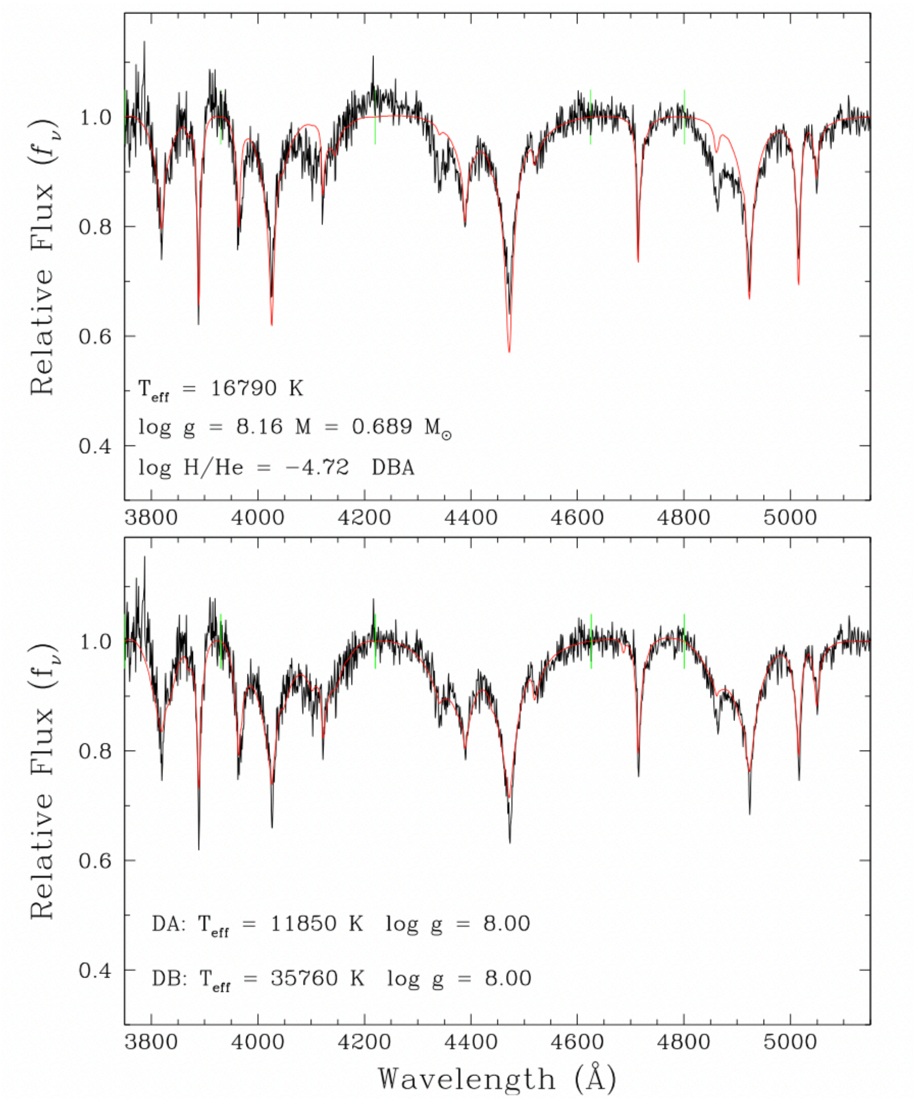

Figure 5.1: *Top*: Homogeneous atmosphere model fit to SDSS J011356.38+301514.62 (Genest-Beaulieu & Bergeron, 2019b). Several helium lines are overpredicted, while the hydrogen lines are extremely underpredicted. *Bottom*: Fit assuming a DA+DB binary system. While not perfect, this fit is an improvement over the single-star fit.

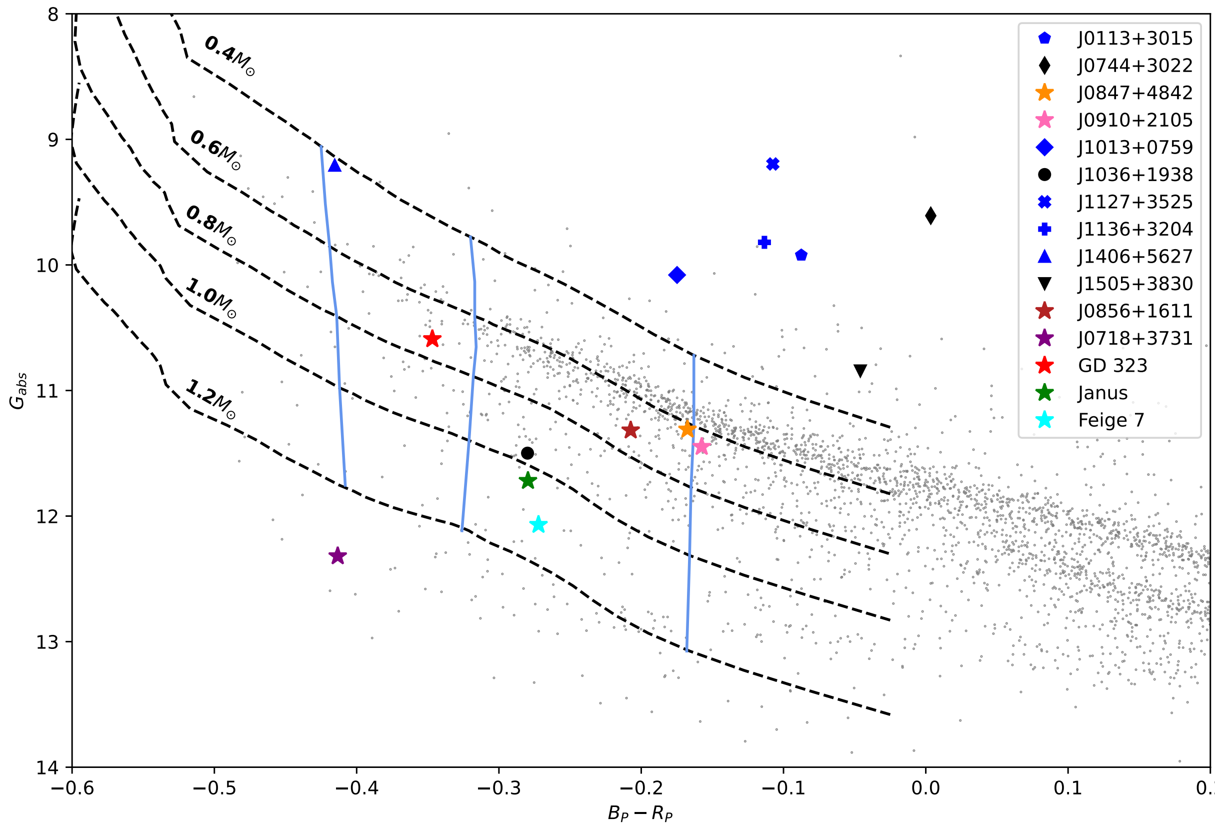

Figure 5.2: Gaia color-magnitude diagram of the unresolved DA+DB binary candidates from Genest-Beaulieu & Bergeron (2019b) along with the 100 pc white dwarf sample (gray points). Blue symbols mark targets that do not show variations in our time-series spectroscopy, whereas the black symbols are the remaining candidates with no follow-up data. Star symbols are the now seven confirmed double-faced white dwarfs, including J0847+4824 and J0856+1611 presented in this work. The evolutionary models for 0.4, 0.6, 0.8, 1.0, and 1.2 $M_\odot$ white dwarfs with pure He atmospheres are also shown. We plot the models down to 11,000 K, below which He lines disappear. The blue lines are isotherms assuming He atmospheres for 35,000, 25,000, and 15,000 K (left to right).

Table 5.1 Observational Details

Object	APO	Gemini	MMT
J0113+3015	11×10 min UT20231108 3×15 min UT20231117	–	–
J0847+4842	9×15 min UT20240305 4×15 min UT20240404 8×15 min UT20240405 16×15 min UT20240417	46×3 min	12 exp UT20240501–UT20240506
J0856+1611	12×10min UT20240305 3×10min UT20240404 7×10min UT20240405	–	10 exp UT20240501–UT20240505
J1013+0759	–	47×3 min	–
J1127+3252	–	8×5 min	–
J1136+3204	–	23×3 min	–
J1406+5627	–	35×4 min	–

J0856+1611, lie close together in the color-magnitude diagram, along with the double-faced white dwarf J0910+2105 (Moss et al., 2024), and we show below that they are also double-faced stars. Among the remaining three candidates from Genest-Beaulieu & Bergeron (2019b) that we could not observe, one of them (J1036+1938) appears to be located close to ZTF J203349.8+322901.1 in the color-magnitude diagram, but follow-up time-series spectroscopy is required to confirm its nature.

Table 5.1 shows our observing summary for each target. We obtained multiple sequences for three targets at the Apache Point Observatory (APO) 3.5m telescope equipped with the Kitt Peak Ohio State Multi-Object Spectrograph (KOSMOS) over multiple nights. We used the 2" slit in the Center position with the Blue disperser and 2x2 binning. The setup covers the wavelength range 3800 - 6600 Å with a resolution of 4.7 Å.

We also obtained additional exposures for two targets at the 6.5m MMT with the Blue Channel Spectrograph. We used the 1.25" slit with the 500 $\mathrm{l\,mm^{-1}}$ grating which yields a resolution of 4.5 Å.

Finally, we obtained back-to-back sequences for five targets using the 8m Gemini North telescope with the Gemini Multi-Object Spectograph (GMOS) as part of the programs GN-2024A-Q-229, GN-2024A-Q-325, and GS-2024A-Q-329. We used the B480 grating with the 1" slit and 4x4 binning, providing wavelength coverage from 3555 - 7300 Å and a resolution of 6.3 Å. All of our spectra were reduced using standard IRAF procedures.

5.3. Analysis

For our variable targets, we start by fitting a Gaussian profile to both Hβ and He 1 λ4922 using LMFIT (Newville et al., 2014) and calculate the equivalent width of these profiles for each spectrum.

We then take the ratio of the equivalent widths to measure how the strength of the H lines vary as a function of time compared to the He lines. To calculate errors, we use bootstrapping to construct a distribution of values. We randomly sample the wavelength-flux pairs of a given spectrum, with replacement, while keeping only the unique pairs. This creates a new spectrum which we then fit as mentioned, repeating this process 10,000 times to generate 10,000 measurements. We then select the values at 15.9 and 84.1% in the distribution as the 1σ errors. We then generate a Lomb-Scargle periodogram with the orbital fit code MPRVFIT (De Lee et al., 2013) to constrain the rotation period using the measured equivalent widths.

Given that homogeneous atmosphere models failed to reproduce the optical spectra in Genest-Beaulieu & Bergeron (2019b) for these objects, we employ a polar cap model to generate fits to our time-resolved spectra, similar to Moss et al. (2024). In this model, the polar cap is made up entirely of H and the equatorial belt of He. We denote $\theta_{\rm c}$ as the extent of the polar cap from the pole down to the equator, such that $\theta_{\rm c} = 90°$ means the entire hemisphere is H. We also denote α as the angle between the magnetic axis and the plane of the sky, as defined in Schnerr et al. (2006, $\alpha = 90°$ means pole-on). The purpose of using this geometry is to provide a physical mechanism for the observed variations. While the total amount of H and He is what determines the strength of each absorption line in our synthetic spectra, this by itself does not explain why we see varying abundances as the objects rotate. The specific use of H polar caps, positioned with respect to the magnetic axis which is misaligned with the rotation axis, accomplishes three goals: it provides excellent fits to our spectra, it explains why we see varying abundances as opposed to a constant ratio, and it fits within our framework of magnetically-inhibited convection at the poles (see Section 5.4.2).

We use the photometric technique described in Bergeron et al. (2019) to obtain precise $T_{\rm eff}$ and $\log g$ values for the variable targets. We use the Gaia DR3 parallaxes, SDSS u, and Pan-STARRS $grizy$ photometry to constrain the effective temperature and solid angle of each object. Since the distance is known, we directly constrain the radius and then calculate the mass using white dwarf evolutionary models.

To generate the spectroscopic fits, the emergent Eddington flux H_ν is calculated by numerically integrating the specific intensity I_ν over the visible surface of the disk given the geometry and viewing angle. We adopt pure H and pure He model atmospheres based on the surface composition of each given element, and fix the $T_{\rm eff}$ and $\log g$ of both sets of models to the values obtained from the photometric fits. The details of our model grid are discussed further in Bergeron et al. (2019) and Genest-Beaulieu & Bergeron (2019b). This approach was successful in reproducing the time-resolved spectra for J0910+2105 (Moss et al., 2024).

With the α values found in our model fits, we then use the oblique rotator model (Stibbs, 1950; Monaghan, 1973) to constrain the orientation of the line of sight and magnetic axis in each target.

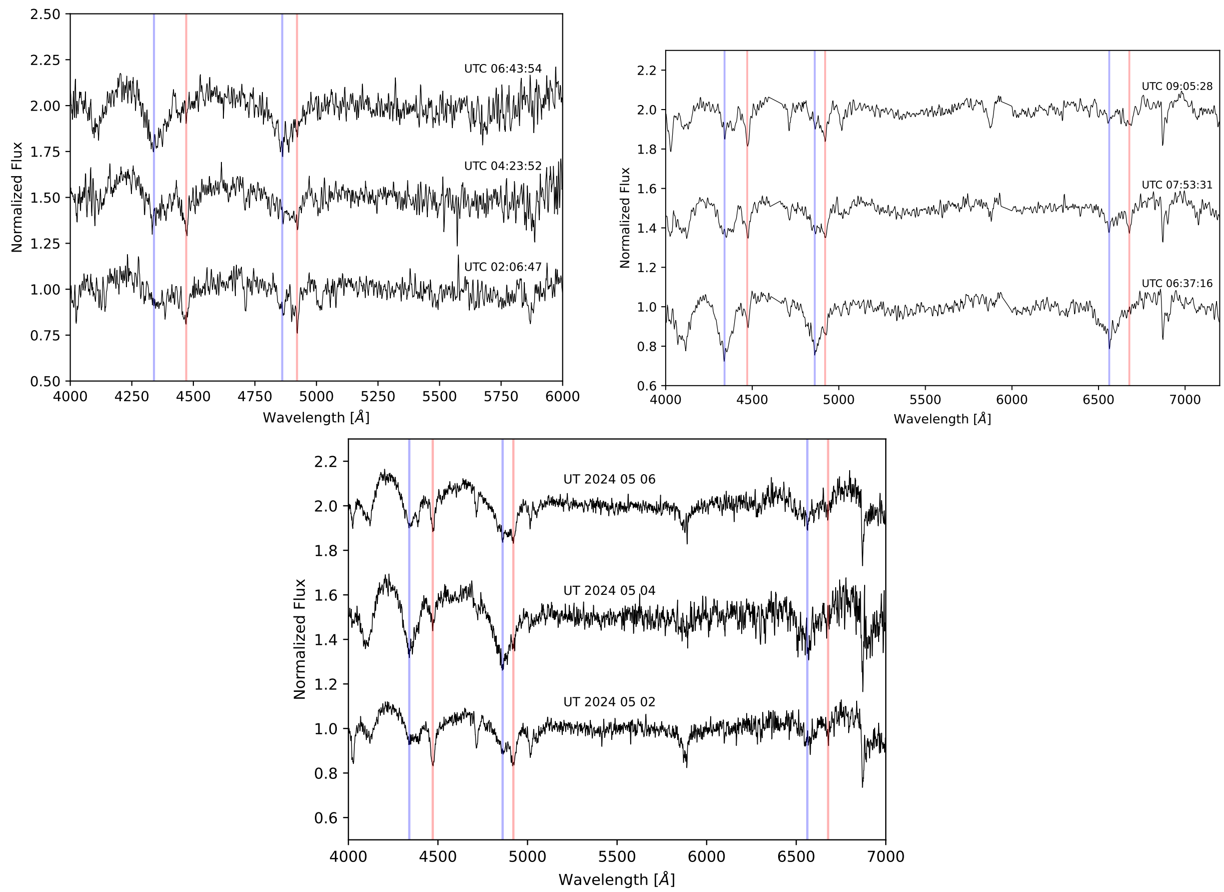

Figure 5.3: J0847+4842 sample spectra from the beginning, middle, and end of the night on UT 2024 March 05 (top left panel, APO) and 2024 February 18 (top right panel, Gemini). Sample spectra from separate nights at the MMT are shown in the bottom panel. The spectra are offset and smoothed for display purposes, and are plotted chronologically from bottom to top. The positions of the Balmer lines are marked with blue lines, and He 1 $\lambda4471$, $\lambda4922$, and $\lambda6678$ are marked with red lines.

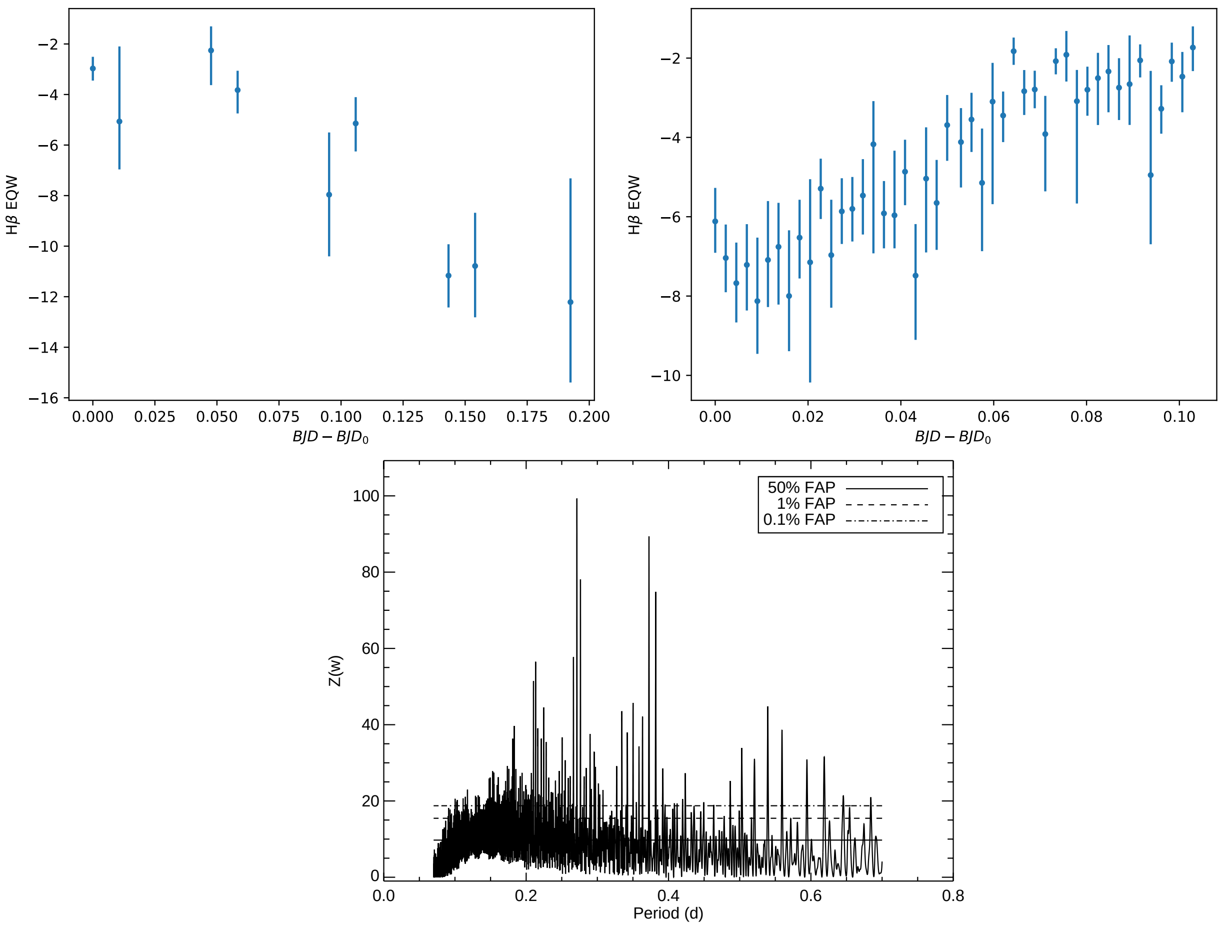

Figure 5.4: Equivalent width of the Hβ line for J0847+4842 from UT 2024 March 05 (top left) and February 18 (top right). The bottom panel shows the Lomb-Scargle periodogram including all of the APO, Gemini, and MMT data on this target. Despite aliasing, current data favor a rotation period of either 6.5 or 8.9 h.

Variations in the spectra occur if the magnetic axis is offset from the rotation axis, so this model is key for providing a physical justification of any variations we observe.

It is important to note two distinctions here. The first is that due to the degeneracies in the model fits (H caps versus He belts, and vice versa), we only use the H polar cap model. While our model only serves as a proxy for the possible geometries, this model provides excellent fits to our data.

Second, Moss et al. (2024) tested both convective and radiative atmospheres for J0910+2105, which has a magnetic field strength of ∼0.5 MG. While radiative atmospheres provided a noticeable improvement in the fit to the He I λ6678 line, the improvement with a radiative atmosphere is negligible outside of this line (see also the discussion in Lecavalier-Hurtubise & Bergeron, 2017). In addition, our model fits are limited to wavelengths shorter than 5150 Å. Our APO data only goes to 6600 Å, which barely covers Hα and does not include the He I λ6678 line. To perform a uniform analysis of all of our APO, Gemini, and MMT data, we restrict our model fits to the wavelengths below 5150 Å, where the majority of the He and H lines are. Hence we use convective atmosphere models in our fits. Fits for our variable targets, as well as all observed data are provided on Zenodo via the DOI https://doi.org/10.5281/zenodo.14232043.

5.3.1. SDSS J084716.21+484220.40

J0847+4842 is the most interesting target in our sample. Figure 5.3 shows sample spectra from the beginning, middle, and end of the night on UT 2024 March 05 (left panel, APO) and 2024 February 18 (right panel, Gemini). We see both H and He lines at the start of the sequence shown in the left panel. As the night progresses, the He lines become much weaker, to the point where the spectrum looks like a DA at the end of the sequence. These variations are clearly due to the rotation of an inhomogeneous mixed atmosphere, and not an unresolved DA+DB binary. We captured the second half of the rotation phase in the Gemini data shown in the right panel. Here the sequence begins with strong H lines, which gradually become weaker while the He lines get stronger.

Figure 5.4 shows the equivalent width measurements from two different nights, along with the Lomb-Scargle diagram (right panel) including all of the data on J0847+4842. Because the He I λ4922 line becomes nearly invisible, here we only use the Hβ line. There is a clear increase in the Hβ line strength (more negative equivalent width) with time in the left panel and a decrease in the right panel. The Lomb-Scargle diagram shown in the right panel reveals two significant peaks at 0.271 days (6.5 hours) and 0.373 days (8.9 hours).

The photometric fit using the Gaia DR3 distance, SDSS u, and Pan-STARRS $grizy$ photometry indicate a relatively cool, average mass DBA white dwarf with ($T_{\rm eff} = 15,000$ K, $\log g = 7.99$, and $M = 0.585\ M_{\odot}$). We assume $\log {\rm H/He} = -3$ for this fit. We use these parameters to generate our spectral fits using the polar cap model. Figure 5.5 shows our fits to the APO and Gemini spectra shown in Figure 5.3. Unlike the homogeneous H/He atmosphere fit shown in Genest-Beaulieu &

Bergeron (2019b), we obtain excellent fits using our H polar cap model. We fix the cap size to $\theta_c = 40°$ since this cap size best fits our entire data set and then allow α to vary.

Several spectra show strong H lines and nearly undetectable He lines, this implies that we see only the H polar caps in some rotation phases, while the He equatorial region is hidden. We obtain $\alpha \approx 90°$ for these spectra. While in other phases, the He lines are stronger, indicating an α value as low as $24°$. We use the oblique rotator model to determine the geometry of this system, in which the magnetic axis is tilted with respect to the rotation axis. The model denotes β as the angle between the two axes, and i as the angle between the line of sight and rotation axis (see Figure 2 of Bailey et al. 2011 for an image of the geometry of this model). As the object rotates, the angle between the magnetic axis and the line-of-sight ranges from $\beta - i$ to $\beta + i$. This angle is equal to $90 - \alpha$, hence the range of α values from our fits constrains the system geometry. The minimum and maximum α values of 24° and 90° result in $\beta = 33°$ and $i = 33°$. This means the magnetic pole and the line of sight angle are aligned, and at certain rotation phases we are looking directly at the magnetic pole. This explains why we see almost exclusively H in some spectra.

5.3.2. SDSS J085618.94+161103.6

J0856+1611 (LB 8915, erroneously referred to as LB 8827 in the literature) is listed as a DBA white dwarf in Genest-Beaulieu & Bergeron (2019b), but it was not identified as a DA+DB binary candidate. Even though the photometric and spectroscopic temperatures agree within the errors, the mass estimates, 0.805 versus $1.060\ M_\odot$ differ significantly. This is likely due to the complications from the changing strengths of the H and He lines in this system. Putney (1997) showed this object to be magnetic, and Wesemael et al. (2001) demonstrated that Balmer line strengths vary with time, though this was based on only three spectra. They concluded that these changes must be due to changes in the apparent H/He abundance ratio or irregularities over the stellar surface.

To significantly improve the physical constraints on this system, we obtained 32 follow-up spectra over several nights. Figure 5.6 shows three of the spectra from a sequence taken at APO on UT 2024 March 05. H lines are relatively weak in all of the spectra, however there are noticeable changes in the line strength throughout the course of the observations. Hγ in particular does not appear at all in several exposures, such as at the start of the sequence shown in this figure, but it is clearly visible later on, whereas He lines stay consistently strong. The middle panel in Figure 5.6 shows the equivalent width ratios of Hβ to He 1 λ4922 from UT 2024 March 05, and the Lomb-Scargle periodogram generated from all of our data on this object. There is a clear increase in the H content as the object rotates, and we recover the 5.7 hour period as measured from K2 photometry (Hermes et al., 2017a, see their Figure 3, labeled PG 0853+164).

Our photometric fit finds $T_{\rm eff} = 17,574$ K, $\log g = 8.29$, and $M = 0.77\ M_\odot$, again assuming $\log \rm H/He = -3$. Figure 5.7 shows example fits for two of the spectra using inhomogeneous

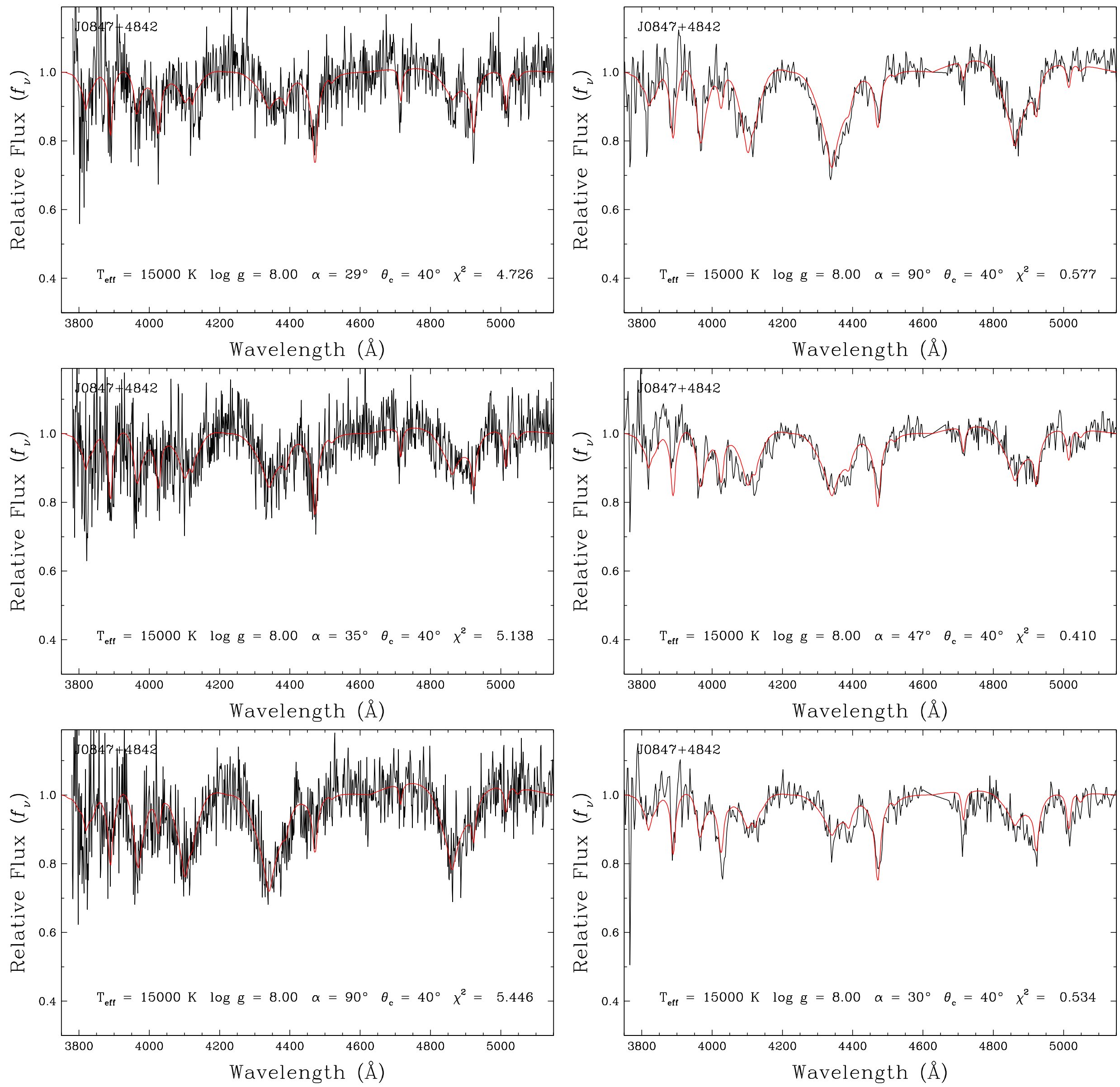

Figure 5.5: Example fits for J0847+4842 spectra from APO (left column) and Gemini (right column). Spectra are chronologically ordered from top to bottom. We fix the cap size to $\theta_c = 40°$ and allow α to vary. An α angle near $90°$ means we are observing towards the pole, which results in stronger H lines in the spectra in our H polar cap model.

atmosphere models with these parameters. Since the H lines are weak, we are unable to fully constrain the polar cap size, though we rule out a cap size greater than $\approx 35°$. Instead we show representative fits with $\theta_c =$ 15, 25, and $35°$. We then use the minimum and maximum α values derived from each of these fixed cap sizes to obtain the best-fit geometry under the assumption of these cap sizes. Table 5.2 shows the derived α, β, and i values assuming these fixed cap sizes.

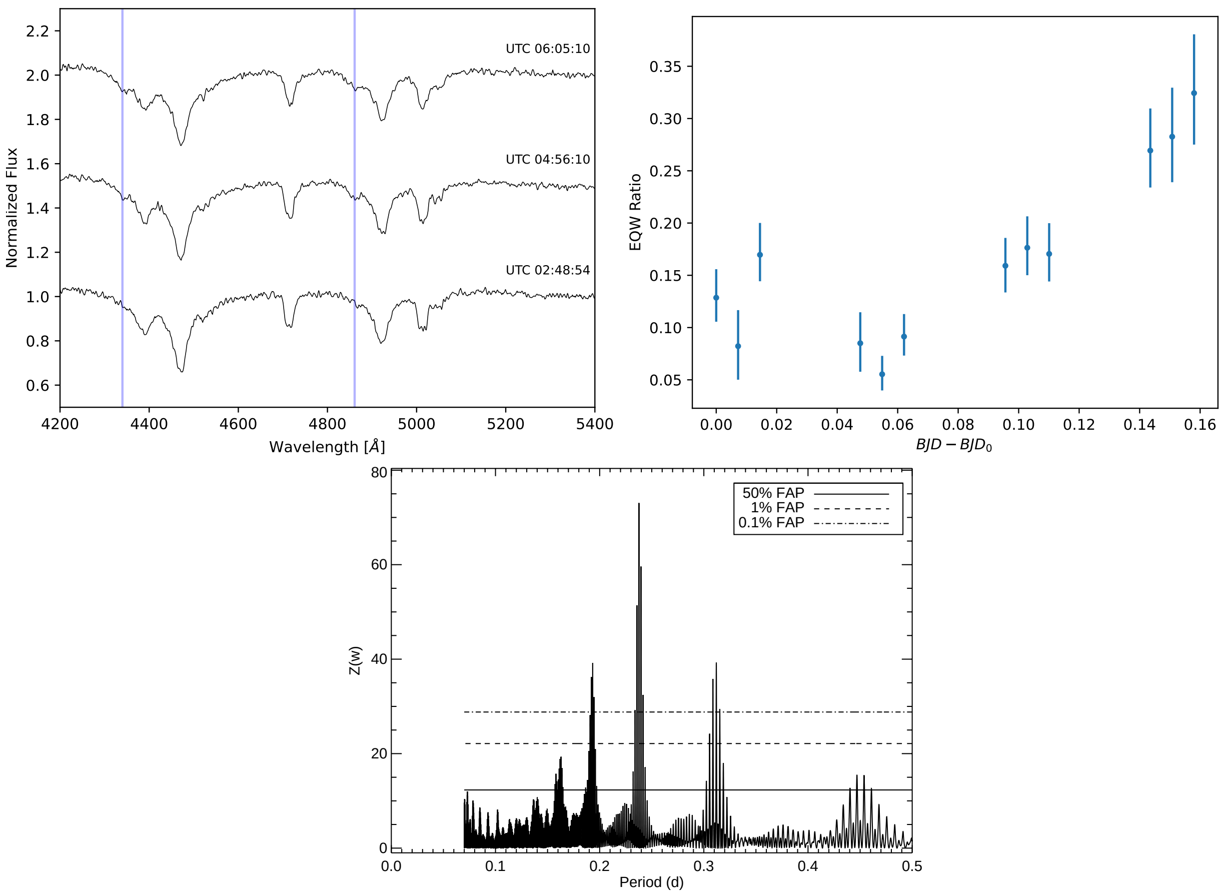

Figure 5.6: *Top Left:* J0856+1611 spectra from the beginning, middle, and end (bottom to top) of the APO sequence on UT 2024 March 05. Blue lines mark Hγ and Hβ. *Top Right:* Equivalent width ratios for the UT 2024 March 05 sequence. *Bottom:* Lomb-Scargle periodogram. We successfully retrieve the 5.7 hour rotation period (Hermes et al., 2017a) from our entire data set.

Table 5.2 Geometry values for J0856+1611 assuming fixed cap sizes. All values are in degrees.

θ_c	α_{min}	α_{max}	β	i
15	16	90	37	37
25	1	37	71	18
35	0	21	75	15

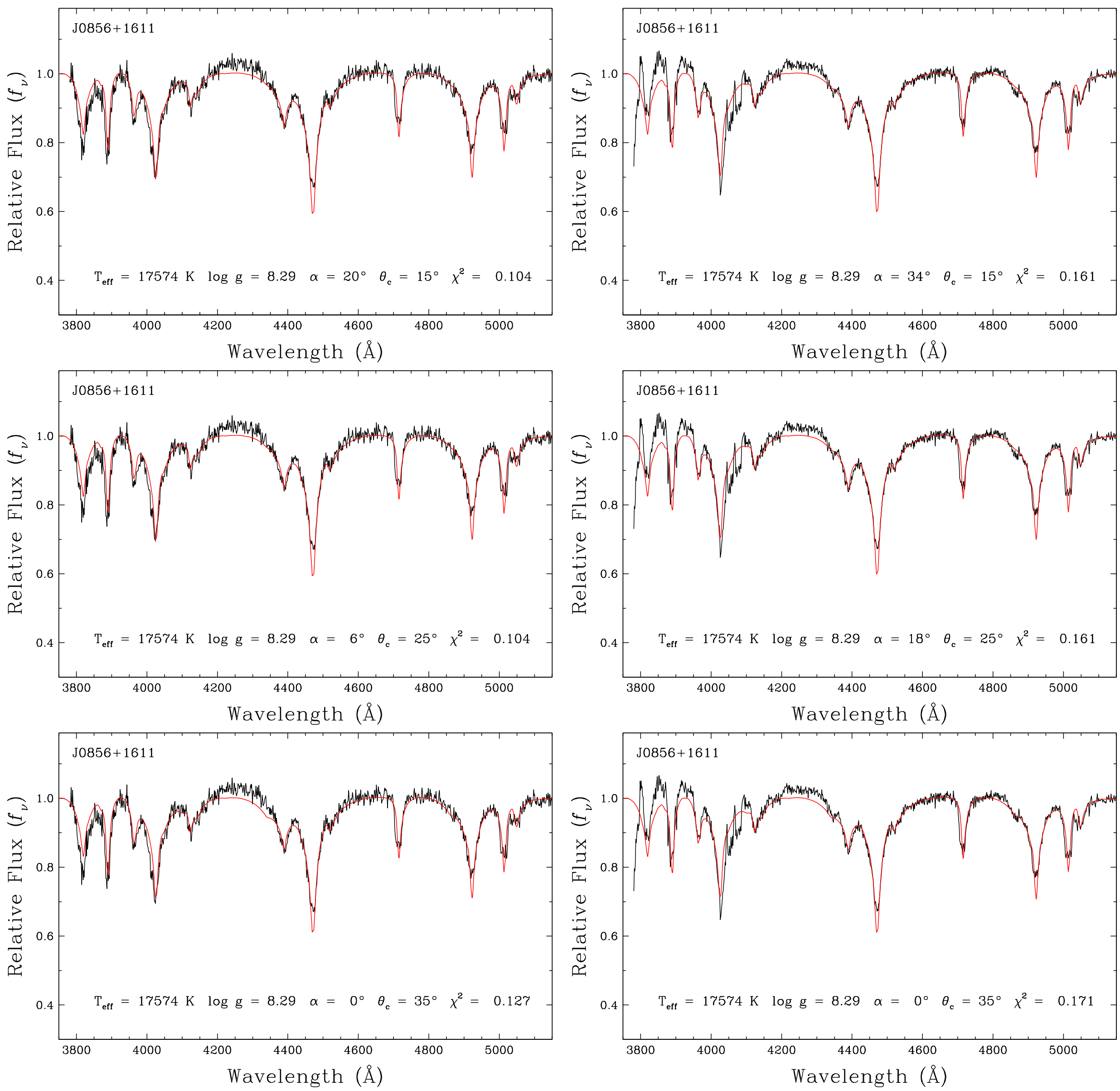

Figure 5.7: Example fits to two J0856+1611 spectra (left and right columns) with $\theta_c = 15$, 25, and 35° (top to bottom rows).

5.3.3. Non-Variable Objects

Of the seven targets we obtained data for, five do not show spectral variations in our back-to-back exposures. Figure 5.8 and Figure 5.9 shows the trailed spectra for these targets. Both hydrogen and helium lines are visible for each system, and there are no significant variations in the strengths of these lines over the course of the sequences. If these white dwarfs have rotation periods longer than a few hours, or if the rotation axis is aligned with the magnetic axis, it may still be possible to hide patchy atmosphere white dwarfs in our data. However, Figure 5.2 shows that all five of these objects are also over-luminous. Hence, they are likely unresolved DA+DB binary systems with periods longer than a few hours. Since Genest-Beaulieu & Bergeron (2019b) obtained excellent fits assuming DA+DB binary systems for these five systems, we do not present any additional modeling of them here.

5.4. Discussion

5.4.1. The Class of Double-faced White Dwarfs

We performed time-series spectroscopy of 7 DBA white dwarfs from Genest-Beaulieu & Bergeron (2019b), and provided a detailed analysis of two double-faced white dwarfs in this sample. J0847+4842 is a new discovery; the observed spectroscopic variations can be explained by a double-faced white dwarf where the H-rich magnetic pole comes into view every 6.5 or 8.9 hours. The second target, J0856+1611, was previously identified as a patchy atmosphere white dwarf by Wesemael et al. (2001) based on only three spectra available. Hermes et al. (2017a) provided a rotation period measurement for J0856+1611 based on K2 photometry, and here we detect spectroscopic variations at the same period. Both J0847+4842 and J0856+1611 are explained well by the oblique rotator model. We now turn our attention to the emerging class of double-faced white dwarfs.

Table 5.3 summarizes the physical parameters for the 7 known double-faced white dwarfs with patchy atmospheres. These double-faced white dwarfs are found over a relatively broad temperature range of 15,000 to 36,000 K. More importantly, their mass distribution is skewed. DB white dwarfs in the solar neighborhood lack the high mass tail seen in DA white dwarfs (Genest-Beaulieu & Bergeron, 2019b). For example, the mass distribution of DB white dwarfs in the 100 pc white dwarf sample and the SDSS footprint is best-explained by a Gaussian with $M = 0.586$ and $\sigma = 0.036\ M_{\odot}$ (Kilic et al., 2025). In addition, there is only a single DB with $M > 0.8\ M_{\odot}$ in that sample, which is also magnetic. The double-faced white dwarf J0856+1611 happens to be the third most massive DB (among 50 objects) in that sample. Jewett et al. (2024) found that there are no normal DBs with $M \geq 0.9\ M_{\odot}$ in the 100 pc sample and the Pan-STARRS footprint, those massive DBs are either magnetic or they rotate rapidly. Hence, besides J0847+4842, all other double-faced white dwarfs in Table 5.3 are unusually massive. Massive white dwarfs tend to be magnetic as well, and four of the

Table 5.3 Physical parameters of the known double-faced white dwarfs.

Object	$T_{\rm eff}$ [K]	Mass [$M_\odot$]	B_d [MG]	Rotation Period [hrs]	References
J0847+4842	14999	0.585	–	6.5 or 8.9	1
J0856+1611	17574	0.773	1.5	5.7	1, 2, 3
J0910+2105	16746	0.778	0.55	7.7 or 11.3	4
ZTF J203349.8+322901.1	∼35800	∼1.24	–	0.25	5
GD 323	26926	0.778	–	3.5	6
Feige 7	18381	1.077	39.45	2.18	3, 7
GALEX J071816.4+373139	33942	1.27	∼8	0.18	7, 8

References. — (1) This Work (2) Hermes et al. (2017a) (3) Hardy et al. (2023b) (4) Moss et al. (2024) (5) Caiazzo et al. (2023) (6) Kilic et al. (2020) (7) Jewett et al. (2024) (8) Cheng et al. (2024)

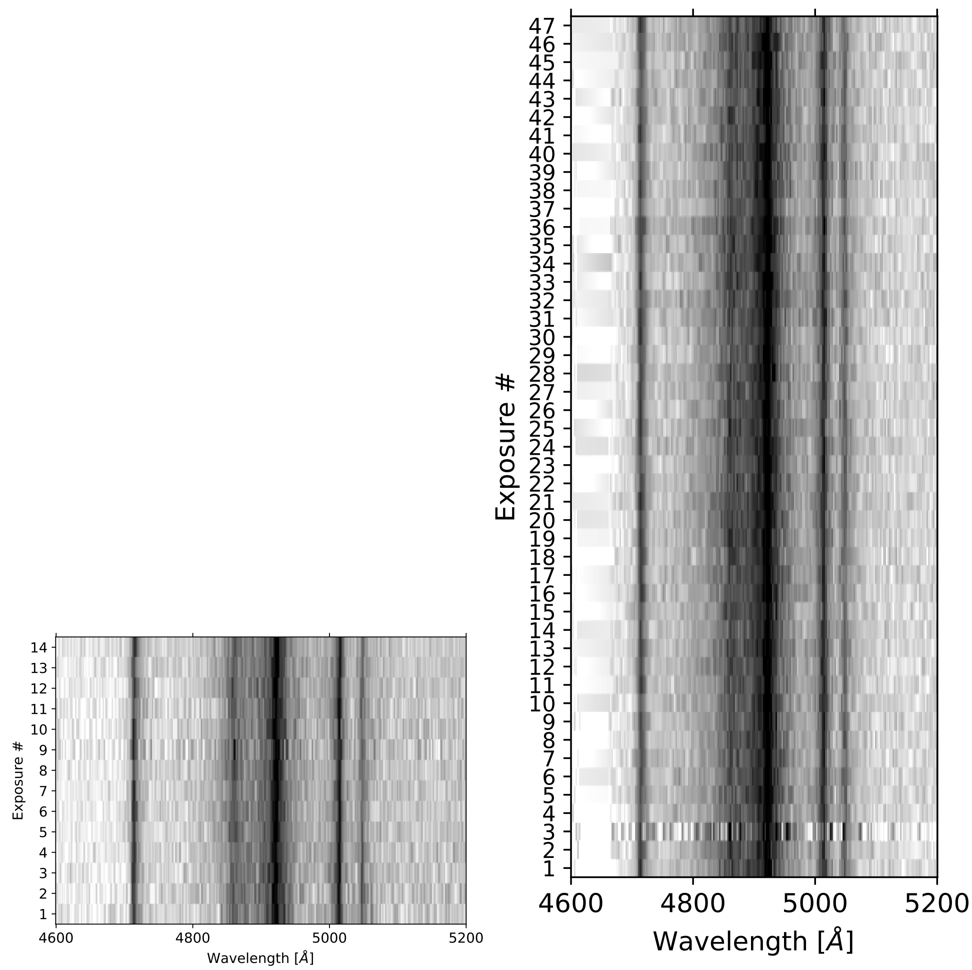

Figure 5.8: Trailed spectra for J0113+3015 (APO, left panel) and J1013+0759 (Gemini, right panel).

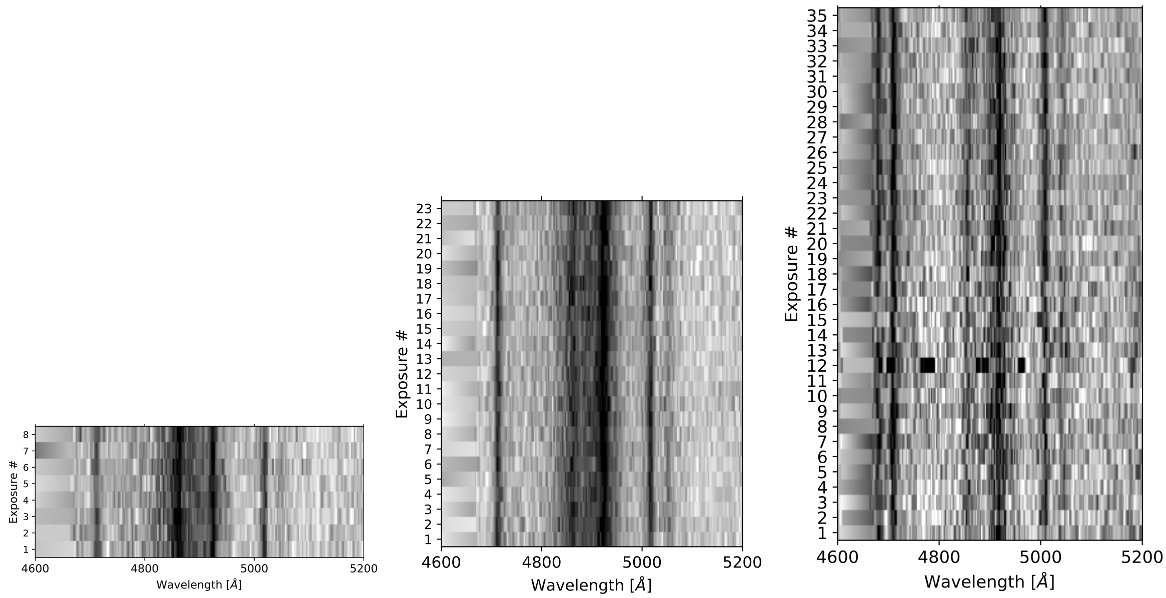

Figure 5.9: Trailed Gemini spectra for our remaining targets that do not show spectral variations: J1127+3525, J1136+3204, and J1406+5627 (from left to right).

seven double-faced objects are confirmed to be strongly magnetic. Despite the diversity of $T_{\rm eff}$ in this sample, it seems that magnetism could be what ties the objects together.

5.4.2. The Role of Magnetism in Double-Faced White Dwarfs

We propose that magnetism is responsible for the emergence of double-faced white dwarfs for two reasons. One is that the frequency of magnetism in this sample is notably higher than that of the DB population. Four out of the seven double-faced targets are confirmed to be magnetic, whereas only 1% of the DBs in the Genest-Beaulieu & Bergeron (2019b) DB sample are magnetic. The second reason is that it is the only plausible way to alter the elemental abundances in such a way that would lead to an inhomogeneous atmosphere. While the float-up and convective dilution/mixing processes greatly alter the surface composition, these impact the entire atmosphere and are expected to lead to well mixed atmospheres. Conversely, the magnetic field should affect any convective processes while still allowing for the flow of material, specifically along the field lines, resulting in surface regions of different abundances. Even in double-faced white dwarfs where Zeeman splitting is not visible in the available low-resolution spectra, magnetism is still invoked to explain patchy atmospheres (e.g., Caiazzo et al., 2023).

In our paradigm, convection is more inhibited at the poles where the magnetic field strength is higher than at the equatorial regions. This leads to H caps as convective dilution would be unable to convert these regions to He. Achilleos et al. (1992) suggested that convection would be inefficient in regions where the field lines are tangent to the surface, thus resulting in He caps and a H ring for

Feige 7 in their model. A similar model was used by Valyavin et al. (2014) to describe temperature variations in WD 1953−011 and suggested convection is less efficient at the equator due to the Lorentz force acting against the direction of gravity. While our H cap model is only a proxy for the possible distribution, Tremblay et al. (2015) showed that for a vertical field (i.e. at the poles) the atmosphere becomes radiative for field strengths above ≈ 50 kG. Hence the strength of the local field matters more than the orientation. Since the local field is stronger at the poles, convection is less efficient there, leading to H caps.

Further supporting this hydrogen cap model is the case of J0856+1611. This target shows strong He lines and weak H lines, hence it has a much larger surface area covered by He. If the polar caps are specifically comprised of He in this target, they would need to be quite large as a result. The more likely explanation is a large He equatorial belt and small H caps. It is possible to have He polar caps of similar size to J0847+4842 while having an orientation where we do not see significant variations. If the magnetic axis is not significantly offset from the rotation axis, the visible stellar disk would not significantly change as the object rotates. However, Wesemael et al. (2001) made three spectropolarimetric measurements and found varying magnetic field strengths between these observations. In addition, the measured polarizations were of opposite sign from Putney (1997). Hence both magnetic poles are visible at different phases, so the magnetic and rotation axes must be offset. Therefore, the variations we detect are likely due to the small H caps coming in and out of view.

While we propose that magnetism is affecting the convective processes in these white dwarfs, we do not suspect that convection is completely shut down. Lecavalier-Hurtubise & Bergeron (2017) compared photometric and spectroscopic fits of cool DAs using radiative and convective atmosphere models and found that the photometric and spectroscopic temperatures using convective atmospheres matched while the radiative models did not. They extended this analysis to two weakly magnetic DAs, G217-37 (100 kG, Schmidt & Smith 1994) and LHS 3501 (∼500 kG, Maxted et al. 2000), and similarly found that the radiative solutions differed, suggesting that convective atmospheres are still prevalent even among magnetic white dwarfs. There is in fact only one particular white dwarf, WD 2105−820, in which only radiative atmosphere models are successful (Bédard et al., 2017; Gentile Fusillo et al., 2018).

The formation of classical DQs (helium-rich atmospheres with traces of carbon) below 10,000 K is attributed to convective dredge-up of carbon from the interior (Pelletier et al., 1986; Bédard et al., 2022a). If magnetism were to fully shut down convection, we would not find any magnetic DQs below 10,000 K, yet there are several confirmed cool magnetic DQs in the 100 pc sample: e.g., GJ 1086, WD 1111+020, and WD 1331+005. GJ 1086 has a field strength of ∼10 MG (Ferrario et al., 2015; Holberg et al., 2016). Neither WD 1111+020 nor WD 1331+005 have measured field strengths but they both show distorted carbon bands and circular polarization (Schmidt et al., 2003).

Hence, the magnetic field does not stop convection fully over the entire surface of the star. However, the strength of convection depends on temperature, and the existence of cool magnetic DQs in principle does not exclude the fact that magnetic fields can successfully inhibit convection at higher temperatures (i.e. WD 2105−820).

Interestingly, none of these seven targets have begun core crystallization, hence crystallization induced dynamos cannot explain magnetism in these sources (Isern et al., 2017; Schreiber et al., 2021). Bagnulo & Landstreet (2022) found two distinct populations of magnetic white dwarfs: those with weaker fields that grow with time and lower mass ($M < 0.75\ M_{\odot}$) which are likely the product of single-star evolution, and those with much stronger fields and higher mass suggesting a merger origin. Two of the double-faced white dwarfs, ZTF J203349.8+322901.1 and J0718+3731, are both ultramassive and have rotation periods of 11-15 min (Caiazzo et al., 2023; Cheng et al., 2024), strongly suggesting a past merger. Feige 7 also has a high mass, is strongly magnetic, and has a rotation period of 2.2 hours (Hernandez et al., 2024). Hence, at least three of these double-faced white dwarfs likely originated in binary white dwarf mergers.

5.4.3. Cooler Double-Faced White Dwarfs

We discussed two mechanisms to convert a DA into a DBA, convective dilution and convective mixing. Convective dilution occurs between $T_{\rm eff} \approx$ 30,000 K and 14,000 K, whereas convective mixing is relevant for temperatures between 14,000 and 6000 K. The seven double-faced white dwarfs presented in Table 5.3 have effective temperatures ranging from about 36,000 down to 15,000 K. Hence, the presence of a magnetic field that affects convective dilution of a DA white dwarf can explain the emergence of this class of double-faced white dwarfs.

The prediction of this model is that there should also be cooler white dwarfs with inhomogeneous atmospheres. Just like the seven double-faced white dwarfs that likely formed through the magnetic field impacting convective dilution, cooler DAs that normally would go through convective mixing between 14,000 and 6000 K could also end up as patchy atmosphere objects under the presence of a surface magnetic field. Here, we suggest that such objects have already been discovered.

Rolland & Bergeron (2015) analyzed 16 magnetic DA white dwarfs with high signal-to-noise ratio optical spectroscopy available and found that 10 of the 16 stars have inconsistent photometric and spectroscopic temperatures. They were able to fit the spectral energy distributions of these magnetic DAs with additional flux from a DC companion, which is needed to explain the relatively shallow Hα lines. Moss et al. (2023) demonstrated that many of these objects are also rapidly rotating, and they also had to include a DC-offset to match the H line profiles.

Figure 5.10 shows our model fits for two of those targets under the assumption of patchy atmospheres: J0412−1117 (G160-51) and J1505−0714 (GD 175). Here we determine the stellar parameters using the Gaia DR3 distance, Pan-STARRS $grizy$, and 2MASS JHK photometry while assuming $\log \mathrm{H/He} = -3$. Moss et al. (2023) used the parameters from Caron et al. (2023) which assumed pure H atmospheres. Hence we obtain different stellar parameters for G160-51 and GD 175: $T_{\text{eff}} = 7463$ K, $\log g = 7.57$ and $T_{\text{eff}} = 6000$ K, $\log g = 7.63$ respectively.

We obtain excellent fits using the polar cap model. The fit for G160-51 is particularly noteworthy, as the strength of the central Hα component is neither over nor under-predicted. The obtained cap size of $\theta_c = 75°$ is much greater than the other targets we have analyzed, as the observed central line profile is quite broad and deep. These fits are superior to the ones presented in the previous chapter and in Moss et al. (2023) where a DC-offset was required to match the relatively shallow Hα line profiles. Hence, these cooler magnetic DAs with shallow Hα lines are likely the cooler versions of the double-faced white dwarfs discussed above.

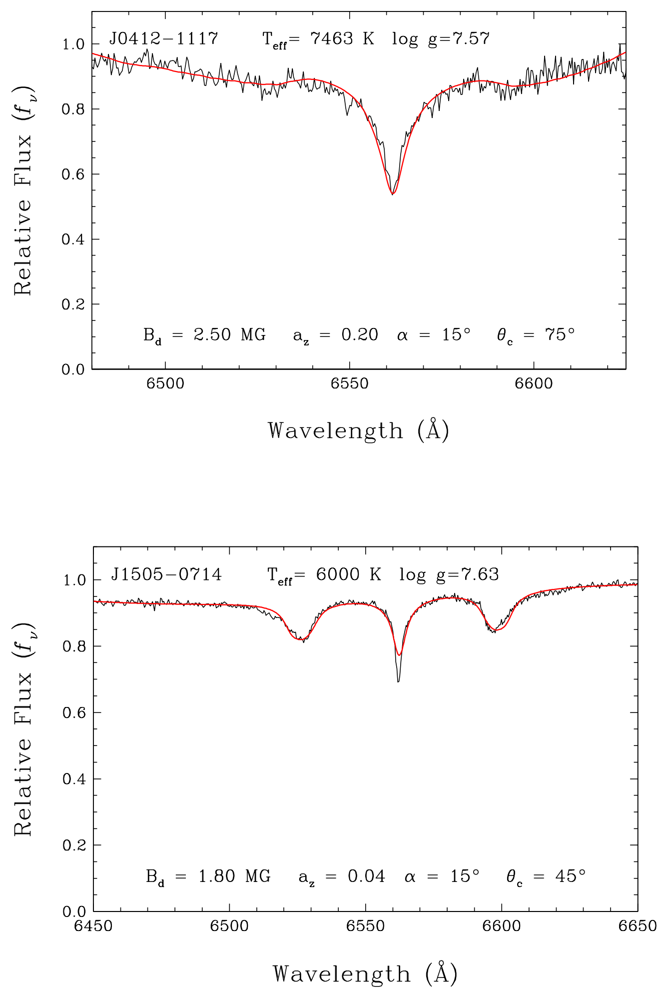

Figure 5.10: Patchy atmosphere fits to the combined spectra of J0412−1117 (top) and J1505−0714 (bottom). We obtain excellent fits without the need of an unresolved binary companion.

Of the eight targets analyzed by Moss et al. (2023), five show signs of rapid rotation via changes in the line position of the Zeeman-split Hα components. The shifts can be interpreted as single stars with their magnetic axis misaligned with the rotation axis, which results in the observer viewing different regions of the complicated magnetic field structure as the object rotates. As we see more of the polar regions, the observed $B_{\rm d}$ is higher, resulting in components that shift further away in wavelength space from the central absorption line.

5.5. Conclusion

In summary, we present time-series spectroscopy of seven DBA white dwarfs, six of which were previously identified as unresolved DA+DB binary candidates. One of these candidates, J0847+4842, shows extreme variations in the absorption lines over the span of our exposure sequences. Hence this unresolved binary candidate is clearly a single white dwarf with an inhomogeneous atmosphere, which results in varying line strength as the object rotates. We constrained the rotation period to either 6.5 or 8.9 hours, and successfully implemented a polar cap model to obtain fits to our spectra. We fix the cap size to 40° and allow the angle between the magnetic axis and plane of the sky to vary in our fits, which lets us constrain the system geometry using the oblique rotator model. We determine that $\beta = 33°$ and $i = 33°$, so the angles between the magnetic axis/line-of-sight and the rotation axis are equal. Hence at certain phases, we are looking directly at the polar cap, which leads to a spectrum that looks effectively like a DA spectrum. As the target rotates, we see more of the equatorial region, which leads to the appearance of He lines.

A separate target we observed is a known variable DBAH, J0856+1611, with a rotation period of 5.7 hours. We detected variations in the strength of the weak H lines, and obtained the same previously determined rotation period. While we do obtain good fits with our polar cap model, the H lines are too weak to put a tight constraint on the cap size. Regardless, it is clear this target has a patchy atmosphere, with likely small caps and an orientation where we mostly view the equatorial region at all phases.

Given the several patchy-atmosphere objects known at this time, we are able to define the class of double-faced objects for the first time. While most objects maintain a homogeneous atmosphere throughout their evolution, this class likely forms as a result of the magnetic field influencing the motion and mixing of either H or He, creating an atmosphere with varying surface abundances. Since magnetism is quite rare in He-dominated white dwarfs, it follows that these inhomogeneous atmospheres are quite rare among the DBA population.

The targets discussed in this work are at effective temperatures where convective dilution is expected to either have already occurred or is currently ongoing. It then follows that double-faced systems could form at cooler temperatures where convective mixing should occur. We identify such a population among the cool magnetic DA white dwarf sample, where the Hα line is shallower than expected based on pure hydrogen atmosphere models.

An important step in analyzing this class is further modeling on how the magnetic field influences convection. If modeling the transport mechanisms can indeed reproduce these atmospheres, that will further solidify the idea that magnetism is the driving force behind the creation of these objects, even if magnetism is not detected in the observations. Of course this also means better modeling of complex fields in general is needed. In our framework, the dipole field is stronger at the polar regions compared to the equatorial regions, with inefficient mixing at the poles. This framework fits well with the traditional dipole field that is used in modeling magnetic white dwarfs. However, the true field structure in these targets could be more complicated, particularly in the case of ZTF J203349.8+322901.1 since it has two opposing faces (Caiazzo et al., 2023). Nevertheless, while the exact nature of the atmosphere geometry cannot be directly confirmed due to the complexities in how magnetism affects convection, we are confident that magnetism is the source of the inhomogeneities in this class of objects.

CHAPTER 6

Conclusions and Future Work

6.1. Summary of this Dissertation

Time-resolved spectroscopy is incredibly expensive in terms of telescope usage, and becomes increasingly difficult when observing white dwarfs given their intrinsic faintness. As a result, the study of white dwarf variability is often constrained to the realm of photometry where signal-to-noise requirements are easier to achieve. This leads to the potential for more rapid sampling, and large photometric surveys such as ZTF and TESS can obtain light curves for thousands of targets simultaneously. But for time-series spectroscopy, we are generally limited to conducting targeted follow-up on a handful of interesting objects.

As we have shown however, performing these intensive observations can yield surprising results and reveal new physics that would otherwise go undetected. We have discovered two hot white dwarfs that show variations in the strength of their spectral lines as they rotate, J0910+2105 and J0847+4842. By analyzing these variations, we have constrained their rotation periods, determined the orientation of their geometries, and implemented a polar cap model to obtain excellent fits to our time-resolved spectra. We have performed similar analysis on a previously known variable white dwarf, J0856+1611, with our work providing significantly improved constraints on the nature of the variations. We have observed seven cool magnetic white dwarfs and found variations in the Zeeman-split line positions for four of them. These four objects are rapidly rotating, and two of the non-variable systems are low mass, indicating that these six objects have likely undergone binary evolution. We initially modeled all seven systems with an unseen companion to dilute their spectra. However, given that the detected variable objects are better explained by rotation, and we achieve excellent fits using inhomogeneous atmospheres for the non-variable objects, these cool systems are instead single stars with inhomogeneous atmospheres similar to the aforementioned hot white dwarfs.

We link the cause of the inhomogeneities in these white dwarf atmospheres to the impact of magnetism on convective processes. All but one of these objects have confirmed magnetic fields, and a field could be strong enough to inhibit convection while being too weak to be detected without polarimetry (Tremblay et al., 2015). ~60% of white dwarfs that begin as DOs will undergo the float-up process at high temperatures ($T_{\rm eff} \gtrsim 30,000$ K) and transition to a DA. As they continue to cool, they will likely undergo either convective dilution or convective mixing depending on the thickness of the newly formed hydrogen layer. Normally, these processes would the turn the DA into a DB or DBA. But instead the magnetic field likely inhibits the convective motion at the polar caps where the local field strength is highest. This would retain the hydrogen atmosphere at the polar regions while allowing the equatorial regions to switch to a helium atmosphere. Given the different temperature regimes where dilution and mixing operate, it is likely that these double-faced white dwarfs at different temperatures form as a result of the different processes. The hot white dwarfs such as J0910+2105 and Feige 7 are in a temperature regime where convective dilution has likely occurred, whereas the cool objects from the Rolland & Bergeron (2015) sample have likely undergone convective mixing. It is also possible that these cooler objects have polar caps that are left over from the magnetic field's effect on the dilution process. These exotic objects make up the ever-growing class of double-faced white dwarfs which we define for the first time.

Given the importance of magnetism on the evolution of white dwarfs, a clearer picture of the origin of these fields is necessary to understand how they form. Here we can take advantage of large spectroscopic surveys like the SDSS to analyze the population of magnetic white dwarfs and obtain excellent statistics. We analyze all magnetic white dwarfs within the 100 pc sample in the SDSS footprint from (Kilic et al., 2025), of which we have 163. We perform a model atmosphere analysis on all 163 objects, and use an offset dipole model to determine the field strength and geometry for 81 newly discovered DAHs. We find statistical evidence of two populations of magnetic white dwarfs that form from different channels: the high mass, young, strongly magnetic objects likely have a significant contribution from binary evolution, while the average mass, old, weakly magnetic objects likely form via single-star evolution. Given the breakout times for a crystallization-induced dynamo (Blatman & Ginzburg, 2024) compared to that of a core-convective dynamo that forms on the main-sequence (Camisassa et al., 2024), our sample of average mass objects can be better explained by the core-convective dynamo.

6.2. The Future

The primary limitation in studying the class of double-faced white dwarfs is the low number of objects. Identifying more variable objects is necessary to determine the possible $T_{\rm eff}$ ranges that these objects occur at, the incidence of magnetism among the objects, and perhaps most importantly the range of possible geometries for the distribution of elements in the atmospheres. For example, Feige 7 was modeled with a ring (Achilleos et al., 1992), while Janus appears to have a thin layer of hydrogen of varying thickness across the entire surface, which yields the double-faced appearance (Caiazzo et al., 2023; Bédard & Tremblay, 2025). Our polar cap model is simply a proxy of the surface area covered by each element, so finding more targets with unique or similar geometries could help inform us on the impacts of the magnetic fields on convection.

Multi-epoch spectroscopy are incredibly valuable in identifying variable targets. We initially found J0910+2105 based on two SDSS spectra obtained in different data releases. Upcoming surveys have the potential to provide more spectra for thousands of white dwarfs, some of which will inevitably show variations between data releases. The Dark Energy Spectroscopic Instrument (DESI, Cooper et al. 2023) will provide spectra for all white dwarfs visible in the Northern hemisphere in the Gaia catalog (Gentile Fusillo et al., 2021). The WHT Enhanced Area Velocity Explorer (WEAVE, Jin et al. 2024) will similarly provide high-quality spectra for ∼100,000 white dwarfs in the Northern hemisphere. Combined with SDSS-V (Almeida et al., 2023), the majority of these white dwarfs will have multi-epoch spectra available. In addition, the 4-metre Multi-Object Spectroscopic Telescope (4MOST, de Jong et al. 2019) survey will obtain spectra for thousands of white dwarfs visible in the Southern hemisphere. In total, these robotic fiber surveys will obtain spectra for over 300,000 white dwarfs from the Gentile Fusillo et al. (2021) catalog. Not only will these surveys detect double-faced white dwarfs, but any variable source such as binaries or magnetic white dwarfs will be found. Targeted follow-up of these variable systems at large telescopes such as Gemini will allow us to fully constrain their nature. And beyond the unique variable systems, these surveys will yield even larger volume-limited samples of magnetic white dwarfs, which will greatly enhance our understanding of the magnetic field origins.

There is also significant information we can obtain about the double-faced white dwarfs from ultraviolet and infrared data. Specifically, the source of hydrogen in these mixed-atmosphere white dwarfs is thought to mostly come from internal processes (Bédard, 2024) but accretion of planetesimals may also contribute (Farihi et al., 2013; Gentile Fusillo et al., 2017). If accretion has occurred or is ongoing, there should be metal lines in the spectra, but these can only be detected in the UV for the hot white dwarfs in this double-faced class, while debris disk signatures are most prominent in the IR. It is important to determine if accretion is ongoing or has occurred in these targets, as this mechanism could be the source of hydrogen rather than the inhibition of internal processes caused by the magnetic field. Two magnetic white dwarfs with uneven distributions of metals in their atmospheres have recently been found (Bagnulo et al., 2024a,b), hence there is evidence that magnetic fields can cause inhomogeneities as material is accreted onto the polar regions. HST and JWST observations of the double-faced white dwarfs would help determine if accretion has a played a role in the generation of their atmospheres.

From a theoretical viewpoint, more work is needed to determine the exact impacts of white dwarf magnetic fields on convection. (Tremblay et al., 2015) conducted the first radiative magneto-hydrodynamic simulations of white dwarf atmospheres and found that field strengths of ∼50 kG can inhibit convection in the photosphere. However, stronger fields ranging from 1 to 100 MG can fully suppress convection in the envelope. Additionally, the simulations specifically used a vertical magnetic field, meaning the physical location on the white dwarf that these calculations simulate is at the poles. A global treatment of the field impacts at different regions of the white dwarf is thus necessary to fully determine if our theory of how these atmospheres form matches the calculations.

Regarding the origin of magnetic fields, the crystallization-induced dynamo seems to be losing favor given the breakout times for this field to reach the surface (Blatman & Ginzburg, 2024) and the convective turnover times needed to generate this field (Montgomery & Dunlap, 2024). The core-convective dynamo proposed by (Camisassa et al., 2024) seems to be successful at reproducing a higher number of magnetic white dwarfs. Since these fields arise at earlier evolution stages, ideally one could detect the fields in stars to confirm their existence. However, since this field is expected to be buried within a star's core, the traditional methods of spectroscopy and polarimetry will fail since these techniques can only detect surface magnetic fields. Asteroseismology can detect these internal fields by analyzing the symmetry breaking of rotational multiplets (Deheuvels et al., 2017), and red giant stars with internal fields have been found with this method (Li et al., 2022, 2023; Deheuvels et al., 2023). However, only a few dozen of these fields have been detected compared to the thousands of red giants that have been searched. It is unlikely that these thousands of stars do not have fields, rather the measurement is very difficult to perform. These fields in red giants have been detected with photometry from the Kepler satellite, which has a baseline of 4 years compared to 27 days for a given TESS sector. Given the $\sim$month long rotation periods of stars, significantly longer baselines are needed to fully characterize the rotation modes and the effects of an internal field.

6.3. Final Thoughts

In the summer before I began my undergraduate degree, I read Carl Sagan's "*The Demon-Haunted World: Science as a Candle in the Dark*". Mind you, I was not much of a reader growing up, and this was simply a recommended book for my "Intro to College" class, not required. For the first time in my life, I was presented with a worldview based on reasoning and facts rather than superstition and emotion. Despite not being a necessary read, I could not put the book down and finished it within three days. In that moment, I was wholly convinced that this outlook on life was the path toward a better future.

Over the last ten years, I have worked to try to emulate this philosophy as best I can and spread the joy of science to others. There is perhaps no greater source of impact we can have on others than by showing them the universe for what it truly is and not what they believe it to be. Throughout my studies, I have been shown a universe far more interesting (and more complex) than what I initially gave it credit for. Although analyzing magnetic white dwarfs, staying up until 7am using a 3.5m telescope from the comfort of my couch, and becoming attached to Oklahoma of all places certainly is not how I envisioned my path going, it has all been worth it. Throughout all of the ups and downs, the setbacks and accomplishments, I need only look up at the stars to remind myself why I keep going.

But also over the past decade, I have witnessed the consequences of not adhering to this philosophy. A global pandemic, wars fought over territory deemed important by religious figureheads, continuously rising temperatures and their related devastating impacts, and the outright denial of basic reality. Oftentimes it feels that we are fighting against forces too great to meaningfully push back against. I (alongside everyone else) am unsure of what the future holds. Will we stay the current course and continue what feels like an almost inevitable descent? Or will something change in the coming years that snaps us back to reality?

I am currently slated to continue on this academic journey I have been on for some time now. My immediate future will naturally involve the usual tasks of academia: publishing papers, writing proposals, presenting at conferences, etc. However, these tasks by themselves do not feel satisfying to me. There is still much more to life than reducing the measurement error of a star's effective temperature by a few hundred Kelvin. If anything, perhaps now more than ever, we need more academics who are able to successfully communicate the value of science to the general public. In an ideal world, I would like to be a positive source for change in what feels like an increasingly maddening world. To show people the same beauty in the stars that I see. In a sense, to be a candle in the dark for others as so many people have been for me.

Bibliography

Achilleos, N., & Wickramasinghe, D. T. 1989, ApJ, 346, 444, doi: 10.1086/168024

Achilleos, N., Wickramasinghe, D. T., Liebert, J., Saffer, R. A., & Grauer, A. D. 1992, ApJ, 396, 273, doi: 10.1086/171715

Adams, W. S. 1915, PASP, 27, 236, doi: 10.1086/122440

Almeida, A., Anderson, S. F., Argudo-Fernández, M., et al. 2023, ApJS, 267, 44, doi: 10.3847/1538-4365/acda98

Amorim, L. L., Kepler, S. O., Külebi, B., Jordan, S., & Romero, A. D. 2023, ApJ, 944, 56, doi: 10.3847/1538-4357/acaf6e

Andrews, J. J., Agüeros, M. A., Gianninas, A., et al. 2015, ApJ, 815, 63, doi: 10.1088/0004-637X/815/1/63

Augustson, K. C., Brun, A. S., & Toomre, J. 2016, ApJ, 829, 92, doi: 10.3847/0004-637X/829/2/92

Bagnulo, S., Farihi, J., Landstreet, J. D., & Folsom, C. P. 2024a, ApJL, 963, L22, doi: 10.3847/2041-8213/ad2619

Bagnulo, S., & Landstreet, J. D. 2021, MNRAS, 507, 5902, doi: 10.1093/mnras/stab2046

Bagnulo, S., & Landstreet, J. D. 2022, ApJL, 935, L12, doi: 10.3847/2041-8213/ac84d3

Bagnulo, S., & Landstreet, J. D. 2024, A&A, 692, A174, doi: 10.1051/0004-6361/202451386

Bagnulo, S., Landstreet, J. D., Farihi, J., et al. 2024b, A&A, 688, L14, doi: 10.1051/0004-6361/202451215

Bagnulo, S., Landstreet, J. D., Mason, E., et al. 2006, A&A, 450, 777, doi: 10.1051/0004-6361:20054223

Bailey, J. D., Landstreet, J. D., Bagnulo, S., et al. 2011, A&A, 535, A25, doi: 10.1051/0004-6361/201117856

Beauchamp, A., Wesemael, F., & Bergeron, P. 1997, ApJS, 108, 559, doi: 10.1086/312961

Beauchamp, A., Wesemael, F., Fontaine, G., & Bergeron, P. 1993, in NATO Advanced Study Institute (ASI) Series C, Vol. 403, White Dwarfs: Advances in Observation and Theory, ed. M. A. Barstow, 281, doi: 10.1007/978-94-011-2020-3_37

Becken, W., Schmelcher, P., & Diakonos, F. K. 1999, Journal of Physics B Atomic Molecular Physics, 32, 1557, doi: 10.1088/0953-4075/32/6/018

Bédard, A. 2024, Ap&SS, 369, 43, doi: 10.1007/s10509-024-04307-5

Bédard, A., Bergeron, P., & Brassard, P. 2022a, ApJ, 930, 8, doi: 10.3847/1538-4357/ac609d

Bédard, A., Bergeron, P., & Brassard, P. 2023, ApJ, 946, 24, doi: 10.3847/1538-4357/acbb62

Bédard, A., Bergeron, P., Brassard, P., & Fontaine, G. 2020, ApJ, 901, 93, doi: 10.3847/1538-4357/abafbe

Bédard, A., Bergeron, P., & Fontaine, G. 2017, ApJ, 848, 11, doi: 10.3847/1538-4357/aa8bb6

Bédard, A., Brassard, P., Bergeron, P., & Blouin, S. 2022b, ApJ, 927, 128, doi: 10.3847/1538-4357/ac4497

Bédard, A., & Tremblay, P.-E. 2025, MNRAS, 538, L69, doi: 10.1093/mnrasl/slaf011

Berdyugin, A., Landstreet, J. D., Bagnulo, S., Piirola, V., & Berdyugina, S. V. 2024, A&A, 690, A10, doi: 10.1051/0004-6361/202450527

Bergeron, P., Dufour, P., Fontaine, G., et al. 2019, ApJ, 876, 67, doi: 10.3847/1538-4357/ab153a

Bergeron, P., Kilic, M., Blouin, S., et al. 2022, ApJ, 934, 36, doi: 10.3847/1538-4357/ac76c7

Bergeron, P., Ruiz, M.-T., & Leggett, S. K. 1992, ApJ, 400, 315, doi: 10.1086/171997

Bergeron, P., Ruiz, M.-T., & Leggett, S. K. 1993, ApJ, 407, 733, doi: 10.1086/172554

Bergeron, P., Ruiz, M. T., & Leggett, S. K. 1997, ApJS, 108, 339, doi: 10.1086/312955

Bergeron, P., Wesemael, F., Dufour, P., et al. 2011, ApJ, 737, 28, doi: 10.1088/0004-637X/737/1/28

Blatman, D., & Ginzburg, S. 2024, MNRAS, 528, 3153, doi: 10.1093/mnras/stae222

Blouin, S., Dufour, P., Thibeault, C., & Allard, N. F. 2019, ApJ, 878, 63, doi: 10.3847/1538-4357/ab1f82

Borra, E. F., & Landstreet, J. D. 1978, ApJ, 222, 226, doi: 10.1086/156138

Brasseur, C. E., Phillip, C., Fleming, S. W., Mullally, S. E., & White, R. L. 2019, Astrocut: Tools for creating cutouts of TESS images, Astrophysics Source Code Library, record ascl:1905.007

Briggs, G. P., Ferrario, L., Tout, C. A., & Wickramasinghe, D. T. 2018a, MNRAS, 478, 899, doi: 10.1093/mnras/sty1150

Briggs, G. P., Ferrario, L., Tout, C. A., & Wickramasinghe, D. T. 2018b, MNRAS, 481, 3604, doi: 10.1093/mnras/sty2481

Briggs, G. P., Ferrario, L., Tout, C. A., Wickramasinghe, D. T., & Hurley, J. R. 2015, MNRAS, 447, 1713, doi: 10.1093/mnras/stu2539

Brinkworth, C. S., Burleigh, M. R., Lawrie, K., Marsh, T. R., & Knigge, C. 2013, ApJ, 773, 47, doi: 10.1088/0004-637X/773/1/47

Brun, A. S., Browning, M. K., & Toomre, J. 2005, ApJ, 629, 461, doi: 10.1086/430430

Burgasser, A. J., Kirkpatrick, J. D., Reid, I. N., et al. 2003, ApJ, 586, 512, doi: 10.1086/346263

Burrow, A., Baron, E., Ashall, C., et al. 2020, ApJ, 901, 154, doi: 10.3847/1538-4357/abafa2

Caiazzo, I., Heyl, J., Richer, H., et al. 2020, ApJL, 901, L14, doi: 10.3847/2041-8213/abb5f7

Caiazzo, I., Burdge, K. B., Tremblay, P.-E., et al. 2023, Nature, 620, 61, doi: 10.1038/s41586-023-06171-9

Camisassa, M., Fuentes, J. R., Schreiber, M. R., et al. 2024, A&A, 691, L21, doi: 10.1051/0004-6361/202452539

Caron, A., Bergeron, P., Blouin, S., & Leggett, S. K. 2023, MNRAS, 519, 4529, doi: 10.1093/mnras/stac3733

Castro-Tapia, M., Zhang, S., & Cumming, A. 2024, ApJ, 975, 63, doi: 10.3847/1538-4357/ad7a6a

Chambers, K. C., Magnier, E. A., Metcalfe, N., et al. 2016, arXiv e-prints, arXiv:1612.05560, doi: 10.48550/arXiv.1612.05560

Chandrasekhar, S. 1931, ApJ, 74, 81, doi: 10.1086/143324

Chen, E. Y., & Hansen, B. M. S. 2011, MNRAS, 413, 2827, doi: 10.1111/j.1365-2966.2011.18355.x

Cheng, S., Cummings, J. D., Ménard, B., & Toonen, S. 2020, ApJ, 891, 160, doi: 10.3847/1538-4357/ab733c

Cheng, S., Schlaufman, K. C., & Caiazzo, I. 2024, arXiv e-prints, arXiv:2408.03985, doi: 10.48550/arXiv.2408.03985

Cooper, A. P., Koposov, S. E., Allende Prieto, C., et al. 2023, ApJ, 947, 37, doi: 10.3847/1538-4357/acb3c0

Coutu, S., Dufour, P., Bergeron, P., et al. 2019, ApJ, 885, 74, doi: 10.3847/1538-4357/ab46b9

Cummings, J. D., Kalirai, J. S., Tremblay, P. E., Ramirez-Ruiz, E., & Choi, J. 2018, ApJ, 866, 21, doi: 10.3847/1538-4357/aadfd6

Cunningham, T., Tremblay, P.-E., Freytag, B., Ludwig, H.-G., & Koester, D. 2019, MNRAS, 488, 2503, doi: 10.1093/mnras/stz1759

Cunningham, T., Tremblay, P.-E., Gentile Fusillo, N. P., Hollands, M., & Cukanovaite, E. 2020, MNRAS, 492, 3540, doi: 10.1093/mnras/stz3638

Day, N. E. 1969, Biometrika, 56, 463, doi: 10.1093/biomet/56.3.463

de Jong, R. S., Agertz, O., Berbel, A. A., et al. 2019, The Messenger, 175, 3, doi: 10.18727/0722-6691/5117

De Lee, N., Ge, J., Crepp, J. R., et al. 2013, AJ, 145, 155, doi: 10.1088/0004-6256/145/6/155

Deheuvels, S., Li, G., Ballot, J., & Lignières, F. 2023, A&A, 670, L16, doi: 10.1051/0004-6361/202245282

Deheuvels, S., Ouazzani, R. M., & Basu, S. 2017, A&A, 605, A75, doi: 10.1051/0004-6361/201730786

Dunlap, B. H., & Clemens, J. C. 2015, in Astronomical Society of the Pacific Conference Series, Vol. 493, 19th European Workshop on White Dwarfs, ed. P. Dufour, P. Bergeron, & G. Fontaine, 547

Euchner, F., Reinsch, K., Jordan, S., Beuermann, K., & Gänsicke, B. T. 2005, A&A, 442, 651, doi: 10.1051/0004-6361:20053038

Farihi, J., Gänsicke, B. T., & Koester, D. 2013, Science, 342, 218, doi: 10.1126/science.1239447

Farihi, J., Robert, A., & Walters, N. 2024, MNRAS, 529, L164, doi: 10.1093/mnrasl/slae014

Ferrario, L., de Martino, D., & Gänsicke, B. T. 2015, SSRv, 191, 111, doi: 10.1007/s11214-015-0152-0

Fontaine, G., Brassard, P., & Bergeron, P. 2001, PASP, 113, 409, doi: 10.1086/319535

Fontaine, G., & Wesemael, F. 1987, in IAU Colloq. 95: Second Conference on Faint Blue Stars, ed. A. G. D. Philip, D. S. Hayes, & J. W. Liebert, 319–326

Fossati, L., Castro, N., Schöller, M., et al. 2015, A&A, 582, A45, doi: 10.1051/0004-6361/201526725

Fuentes, J. R., Castro-Tapia, M., & Cumming, A. 2024, ApJL, 964, L15, doi: 10.3847/2041-8213/ad3100

Fuentes, J. R., Cumming, A., Castro-Tapia, M., & Anders, E. H. 2023, ApJ, 950, 73, doi: 10.3847/1538-4357/accb56

Fuhrmann, K. 2004, Astronomische Nachrichten, 325, 3, doi: 10.1002/asna.200310173

Gaia Collaboration, Prusti, T., de Bruijne, J. H. J., et al. 2016, A&A, 595, A1, doi: 10.1051/0004-6361/201629272

Gaia Collaboration, Brown, A. G. A., Vallenari, A., et al. 2018, A&A, 616, A1, doi: 10.1051/0004-6361/201833051

García-Berro, E., Lorén-Aguilar, P., Aznar-Siguán, G., et al. 2012, ApJ, 749, 25, doi: 10.1088/0004-637X/749/1/25

Genest-Beaulieu, C., & Bergeron, P. 2019a, ApJ, 871, 169, doi: 10.3847/1538-4357/aafac6

Genest-Beaulieu, C., & Bergeron, P. 2019b, ApJ, 882, 106, doi: 10.3847/1538-4357/ab379e

Gentile Fusillo, N. P., Gänsicke, B. T., Farihi, J., et al. 2017, MNRAS, 468, 971, doi: 10.1093/mnras/stx468

Gentile Fusillo, N. P., Tremblay, P. E., Jordan, S., et al. 2018, MNRAS, 473, 3693, doi: 10.1093/mnras/stx2584

Gentile Fusillo, N. P., Tremblay, P. E., Cukanovaite, E., et al. 2021, MNRAS, 508, 3877, doi: 10.1093/mnras/stab2672

Giammichele, N., Charpinet, S., & Brassard, P. 2022, Frontiers in Astronomy and Space Sciences, 9, 879045, doi: 10.3389/fspas.2022.879045

Giammichele, N., Charpinet, S., Fontaine, G., et al. 2018, Nature, 554, 73, doi: 10.1038/nature25136

Ginzburg, S., Fuller, J., Kawka, A., & Caiazzo, I. 2022, MNRAS, 514, 4111, doi: 10.1093/mnras/stac1363

Griem, H. R. 1960, ApJ, 132, 883, doi: 10.1086/146987

Griem, H. R. 1967, ApJ, 147, 1092, doi: 10.1086/149097

Griem, H. R. 1974, Spectral line broadening by plasmas

Hardy, F., Dufour, P., & Jordan, S. 2023a, MNRAS, 520, 6111, doi: 10.1093/mnras/stad196

Hardy, F., Dufour, P., & Jordan, S. 2023b, MNRAS, 520, 6135, doi: 10.1093/mnras/stad197

Hatt, E. J., Ong, J. M. J., Nielsen, M. B., et al. 2024, MNRAS, 534, 1060, doi: 10.1093/mnras/stae2053

Hermes, J. J., Gänsicke, B. T., Gentile Fusillo, N. P., et al. 2017a, MNRAS, 468, 1946, doi: 10.1093/mnras/stx567

Hermes, J. J., Gänsicke, B. T., Kawaler, S. D., et al. 2017b, ApJS, 232, 23, doi: 10.3847/1538-4365/aa8bb5

Hernandez, M. S., Schreiber, M. R., Landstreet, J. D., et al. 2024, MNRAS, 528, 6056, doi: 10.1093/mnras/stae307

Hidalgo, J. P., Käpylä, P. J., Schleicher, D. R. G., Ortiz-Rodríguez, C. A., & Navarrete, F. H. 2024, A&A, 691, A326, doi: 10.1051/0004-6361/202449977

Holberg, J. B., Oswalt, T. D., Sion, E. M., & McCook, G. P. 2016, MNRAS, 462, 2295, doi: 10.1093/mnras/stw1357

Hollands, M. A., Koester, D., Alekseev, V., Herbert, E. L., & Gänsicke, B. T. 2017, MNRAS, 467, 4970, doi: 10.1093/mnras/stx250

Isern, J., García-Berro, E., Külebi, B., & Lorén-Aguilar, P. 2017, ApJL, 836, L28, doi: 10.3847/2041-8213/aa5eae

Isern, J., Mochkovitch, R., García-Berro, E., & Hernanz, M. 1997, ApJ, 485, 308, doi: 10.1086/304425

Jewett, G., Kilic, M., Bergeron, P., et al. 2024, ApJ, 974, 12, doi: 10.3847/1538-4357/ad6905

Jin, S., Trager, S. C., Dalton, G. B., et al. 2024, MNRAS, 530, 2688, doi: 10.1093/mnras/stad557

Kawaler, S. D. 2015, in Astronomical Society of the Pacific Conference Series, Vol. 493, 19th European Workshop on White Dwarfs, ed. P. Dufour, P. Bergeron, & G. Fontaine, 65, doi: 10.48550/arXiv.1410.6934

Kawka, A. 2020, in IAU Symposium, Vol. 357, White Dwarfs as Probes of Fundamental Physics: Tracers of Planetary, Stellar and Galactic Evolution, ed. M. A. Barstow, S. J. Kleinman, J. L. Provencal, & L. Ferrario, 60–74, doi: 10.1017/S1743921320000745

Kawka, A., Briggs, G. P., Vennes, S., et al. 2017, MNRAS, 466, 1127, doi: 10.1093/mnras/stw3149

Kawka, A., Ferrario, L., & Vennes, S. 2023, MNRAS, 520, 6299, doi: 10.1093/mnras/stad553

Kemic, S. B. 1974, JILA Report No. 113

Kepler, S. O., Kleinman, S. J., Nitta, A., et al. 2007, MNRAS, 375, 1315, doi: 10.1111/j.1365-2966.2006.11388.x

Kepler, S. O., Pelisoli, I., Jordan, S., et al. 2013, MNRAS, 429, 2934, doi: 10.1093/mnras/sts522

Kilic, M., Bergeron, P., Blouin, S., et al. 2025, ApJ, 979, 157, doi: 10.3847/1538-4357/ad9bb3

Kilic, M., Bergeron, P., Kosakowski, A., et al. 2020, ApJ, 898, 84, doi: 10.3847/1538-4357/ab9b8d

Kilic, M., Kosakowski, A., Moss, A. G., Bergeron, P., & Conly, A. A. 2021, ApJL, 923, L6, doi: 10.3847/2041-8213/ac3b60

Kilic, M., Rolland, B., Bergeron, P., et al. 2019, MNRAS, 489, 3648, doi: 10.1093/mnras/stz2394

Kilic, M., Moss, A. G., Kosakowski, A., et al. 2023, MNRAS, 518, 2341, doi: 10.1093/mnras/stac3182

Kleinman, S. J., Kepler, S. O., Koester, D., et al. 2013, ApJS, 204, 5, doi: 10.1088/0067-0049/204/1/5

Koester, D., & Kepler, S. O. 2015, A&A, 583, A86, doi: 10.1051/0004-6361/201527169

Koester, D., Liebert, J., & Saffer, R. A. 1994, ApJ, 422, 783, doi: 10.1086/173770

Kolmogorov, A. N. 1933, Annals of Mathematical Statistics, 4, 251

Külebi, B., Jordan, S., Euchner, F., Gänsicke, B. T., & Hirsch, H. 2009, A&A, 506, 1341, doi: 10.1051/0004-6361/200912570

Kurucz, R. L. 1970, SAO Special Report, 309

Landstreet, J. D. 2015, in IAU Symposium, Vol. 307, New Windows on Massive Stars, ed. G. Meynet, C. Georgy, J. Groh, & P. Stee, 311–320, doi: 10.1017/S1743921314007017

Lecavalier-Hurtubise, É., & Bergeron, P. 2017, in Astronomical Society of the Pacific Conference Series, Vol. 509, 20th European White Dwarf Workshop, ed. P. E. Tremblay, B. Gaensicke, & T. Marsh, 169

Lee, Y. S., Beers, T. C., Sivarani, T., et al. 2008, AJ, 136, 2022, doi: 10.1088/0004-6256/136/5/2022

Li, G., Deheuvels, S., Ballot, J., & Lignières, F. 2022, Nature, 610, 43, doi: 10.1038/s41586-022-05176-0

Li, G., Deheuvels, S., Li, T., Ballot, J., & Lignières, F. 2023, A&A, 680, A26, doi: 10.1051/0004-6361/202347260

Liebert, J., Angel, J. R. P., Stockman, H. S., Spinrad, H., & Beaver, E. A. 1977, ApJ, 214, 457, doi: 10.1086/155271

Liebert, J., Bergeron, P., & Holberg, J. B. 2003, AJ, 125, 348, doi: 10.1086/345573

Liebert, J., Bergeron, P., & Holberg, J. B. 2005a, ApJS, 156, 47, doi: 10.1086/425738

Liebert, J., Ferrario, L., Wickramasinghe, D. T., & Smith, P. S. 2015, ApJ, 804, 93, doi: 10.1088/0004-637X/804/2/93

Liebert, J., Wickramasinghe, D. T., Schmidt, G. D., et al. 2005b, AJ, 129, 2376, doi: 10.1086/429639

Limoges, M. M., Bergeron, P., & Lépine, S. 2015, ApJS, 219, 19, doi: 10.1088/0067-0049/219/2/19

López-Sanjuan, C., Tremblay, P. E., Ederoclite, A., et al. 2022, A&A, 658, A79, doi: 10.1051/0004-6361/202141746

MacDonald, J., & Vennes, S. 1991, ApJ, 371, 719, doi: 10.1086/169937

Manser, C. J., Gänsicke, B. T., Inight, K., et al. 2023, MNRAS, 521, 4976, doi: 10.1093/mnras/stad727

Martin, B., & Wickramasinghe, D. T. 1984, MNRAS, 206, 407, doi: 10.1093/mnras/206.2.407

Martin, D. C., Fanson, J., Schiminovich, D., et al. 2005, ApJL, 619, L1, doi: 10.1086/426387

Maxted, P. F. L., Ferrario, L., Marsh, T. R., & Wickramasinghe, D. T. 2000, MNRAS, 315, L41, doi: 10.1046/j.1365-8711.2000.03636.x

McCleery, J., Tremblay, P.-E., Gentile Fusillo, N. P., et al. 2020, MNRAS, 499, 1890, doi: 10.1093/mnras/staa2030

McLachlan, G. J., & Peel, D. 2000, Finite Mixture Models, Wiley Series in Probability and Statistics (John Wiley and Sons)

Mochkovitch, R. 1983, A&A, 122, 212

Monaghan, J. J. 1973, MNRAS, 163, 423, doi: 10.1093/mnras/163.4.423

Montgomery, M. H., & Dunlap, B. H. 2024, ApJ, 961, 197, doi: 10.3847/1538-4357/ad16dc

Moss, A., Bergeron, P., Kilic, M., et al. 2024, MNRAS, 527, 10111, doi: 10.1093/mnras/stad3825

Moss, A., Kilic, M., Bergeron, P., Firgard, M., & Brown, W. 2023, MNRAS, 523, 5598, doi: 10.1093/mnras/stad1835

Newville, M., Stensitzki, T., Allen, D. B., & Ingargiola, A. 2014, LMFIT: Non-Linear Least-Square Minimization and Curve-Fitting for Python, 0.8.0, Zenodo, Zenodo, doi: 10.5281/zenodo.11813

Nordström, B., Mayor, M., Andersen, J., et al. 2004, A&A, 418, 989, doi: 10.1051/0004-6361:20035959

O'Brien, M. W., Tremblay, P. E., Klein, B. L., et al. 2024, MNRAS, 527, 8687, doi: 10.1093/mnras/stad3773

Offner, S. S. R., Moe, M., Kratter, K. M., et al. 2023, in Astronomical Society of the Pacific Conference Series, Vol. 534, Protostars and Planets VII, ed. S. Inutsuka, Y. Aikawa, T. Muto, K. Tomida, & M. Tamura, 275, doi: 10.48550/arXiv.2203.10066

Oliveira da Rosa, G., Kepler, S. O., Soethe, L. T. T., Romero, A. D., & Bell, K. J. 2024, ApJ, 974, 314, doi: 10.3847/1538-4357/ad6987

Ourique, G., Romero, A. D., Kepler, S. O., Koester, D., & Amaral, L. A. 2019, MNRAS, 482, 649, doi: 10.1093/mnras/sty2751

Pedregosa, F., Varoquaux, G., Gramfort, A., et al. 2011, Journal of Machine Learning Research, 12, 2825

Pelletier, C., Fontaine, G., Wesemael, F., Michaud, G., & Wegner, G. 1986, ApJ, 307, 242, doi: 10.1086/164410

Pereira, C., Bergeron, P., & Wesemael, F. 2005, ApJ, 623, 1076, doi: 10.1086/429219

Press, W. H., Flannery, B. P., & Teukolsky, S. A. 1986, Numerical recipes. The art of scientific computing

Pshirkov, M. S., Dodin, A. V., Belinski, A. A., et al. 2020, MNRAS, 499, L21, doi: 10.1093/mnrasl/slaa149

Putney, A. 1997, ApJS, 112, 527, doi: 10.1086/313037

Putney, A., & Jordan, S. 1995, ApJ, 449, 863, doi: 10.1086/176103

Reding, J. S., Hermes, J. J., Clemens, J. C., Hegedus, R. J., & Kaiser, B. C. 2023, MNRAS, doi: 10.1093/mnras/stad760

Richer, H. B., Kerr, R., Heyl, J., et al. 2019, ApJ, 880, 75, doi: 10.3847/1538-4357/ab2874

Robinson, E. L., & Winget, D. E. 1983, PASP, 95, 386, doi: 10.1086/131179

Rolland, B., & Bergeron, P. 2015, in Astronomical Society of the Pacific Conference Series, Vol. 493, 19th European Workshop on White Dwarfs, ed. P. Dufour, P. Bergeron, & G. Fontaine, 53

Rolland, B., Bergeron, P., & Fontaine, G. 2018, ApJ, 857, 56, doi: 10.3847/1538-4357/aab713

Rolland, B., Bergeron, P., & Fontaine, G. 2020, ApJ, 889, 87, doi: 10.3847/1538-4357/ab6602

Schmidt, G. D., & Norsworthy, J. E. 1991, ApJ, 366, 270, doi: 10.1086/169559

Schmidt, G. D., & Smith, P. S. 1994, ApJL, 423, L63, doi: 10.1086/187236

Schmidt, G. D., Harris, H. C., Liebert, J., et al. 2003, ApJ, 595, 1101, doi: 10.1086/377476

Schnerr, R. S., Verdugo, E., Henrichs, H. F., & Neiner, C. 2006, A&A, 452, 969, doi: 10.1051/0004-6361:20054635

Schreiber, M. R., Belloni, D., Gänsicke, B. T., Parsons, S. G., & Zorotovic, M. 2021, Nature Astronomy, 5, 648, doi: 10.1038/s41550-021-01346-8

Schwab, J. 2021, ApJ, 906, 53, doi: 10.3847/1538-4357/abc87e

Serna, J., Hernandez, J., Kounkel, M., et al. 2021, ApJ, 923, 177, doi: 10.3847/1538-4357/ac300a

Shipman, H. L. 1979, ApJ, 228, 240, doi: 10.1086/156841

Shorlin, S. L. S., Wade, G. A., Donati, J. F., et al. 2002, A&A, 392, 637, doi: 10.1051/0004-6361:20021192

Smirnov, N. V. 1939, Annals of Mathematical Statistics, 10, 361

Steen, M., Hermes, J. J., Guidry, J. A., et al. 2024, ApJ, 967, 166, doi: 10.3847/1538-4357/ad3e60

Stevenson, D. J. 1980, Journal de Physique, 41

Stibbs, D. W. N. 1950, MNRAS, 110, 395, doi: 10.1093/mnras/110.4.395

Subasavage, J. P., Henry, T. J., Bergeron, P., et al. 2007, in Astronomical Society of the Pacific Conference Series, Vol. 372, 15th European Workshop on White Dwarfs, ed. R. Napiwotzki & M. R. Burleigh, 53, doi: 10.48550/arXiv.astro-ph/0610946

Temmink, K. D., Toonen, S., Zapartas, E., Justham, S., & Gänsicke, B. T. 2020, A&A, 636, A31, doi: 10.1051/0004-6361/201936889

Torres, S., Cruz, P., Murillo-Ojeda, R., et al. 2023, A&A, 677, A159, doi: 10.1051/0004-6361/202346977

Tout, C. A., Wickramasinghe, D. T., & Ferrario, L. 2004, MNRAS, 355, L13, doi: 10.1111/j.1365-2966.2004.08482.x

Tout, C. A., Wickramasinghe, D. T., Liebert, J., Ferrario, L., & Pringle, J. E. 2008, MNRAS, 387, 897, doi: 10.1111/j.1365-2966.2008.13291.x

Tremblay, P. E., & Bergeron, P. 2008, ApJ, 672, 1144, doi: 10.1086/524134

Tremblay, P. E., & Bergeron, P. 2009, ApJ, 696, 1755, doi: 10.1088/0004-637X/696/2/1755

Tremblay, P. E., Fontaine, G., Freytag, B., et al. 2015, ApJ, 812, 19, doi: 10.1088/0004-637X/812/1/19

Tremblay, P. E., Ludwig, H. G., Steffen, M., Bergeron, P., & Freytag, B. 2011, A&A, 531, L19, doi: 10.1051/0004-6361/201117310

Valyavin, G., Bagnulo, S., Monin, D., et al. 2005, A&A, 439, 1099, doi: 10.1051/0004-6361:20052642

Valyavin, G., & Fabrika, S. 1999, in Astronomical Society of the Pacific Conference Series, Vol. 169, 11th European Workshop on White Dwarfs, ed. S. E. Solheim & E. G. Meistas, 206

Valyavin, G., Antonyuk, K., Plachinda, S., et al. 2011, ApJ, 734, 17, doi: 10.1088/0004-637X/734/1/17

Valyavin, G., Shulyak, D., Wade, G. A., et al. 2014, Nature, 515, 88, doi: 10.1038/nature13836

Vincent, O., Barstow, M. A., Jordan, S., et al. 2024, A&A, 682, A5, doi: 10.1051/0004-6361/202347694

Wegg, C., & Phinney, E. S. 2012, MNRAS, 426, 427, doi: 10.1111/j.1365-2966.2012.21394.x

Wesemael, F. 1981, ApJS, 45, 177, doi: 10.1086/190712

Wesemael, F., Auer, L. H., van Horn, H. M., & Savedoff, M. P. 1980, ApJS, 43, 159, doi: 10.1086/190668

Wesemael, F., Beauchamp, A., Liebert, J., & Bergeron, P. 1995, in White Dwarfs, ed. D. Koester & K. Werner, Vol. 443, 200, doi: 10.1007/3-540-59157-5_208

Wesemael, F., Liebert, J., Schmidt, G. D., et al. 2001, ApJ, 554, 1118, doi: 10.1086/321416

Wickramasinghe, D. T. 1987, in IAU Colloq. 95: Second Conference on Faint Blue Stars, ed. A. G. D. Philip, D. S. Hayes, & J. W. Liebert, 389–399

Wickramasinghe, D. T., & Ferrario, L. 2005, MNRAS, 356, 1576, doi: 10.1111/j.1365-2966.2004.08603.x

Williams, K. A., Hermes, J. J., & Vanderbosch, Z. P. 2022, AJ, 164, 131, doi: 10.3847/1538-3881/ac8543

York, D. G., Adelman, J., Anderson, Jr., J. E., et al. 2000, AJ, 120, 1579, doi: 10.1086/301513